Charge order, Magnetism and Superconductivity In Iron-Based Superconductors And Their Interplay

A THESIS
SUBMITTED TO THE FACULTY OF THE GRADUATE SCHOOL
OF THE UNIVERSITY OF MINNESOTA
BY

Ruiqi Xing

IN PARTIAL FULFILLMENT OF THE REQUIREMENTS
FOR THE DEGREE OF
DOCTOR OF PHILOSOPHY

Andrey V. Chubukov, Adviser

May 2019

Acknowledgements

First and foremost, I would like to express my deepest gratitude to my advisor, Professor Andrey V. Chubukov for his guidance and support during my PhD studies. His insights and immense knowledge in physics helped me greatly with my research. He is always very patient to answer my questions. I also benefited enormously from his taste of physics problems. Besides physics, I also learned a lot from him in other aspects, for example, his passion, his focus, his dedication, his methodology of attacking various problems and so on.

I would like to thank my collaborators Prof. Maxim Khodas and Dr. Laura Classen for our fruitful and pleasant collaborations, Prof. Rafael Fernandes for useful discussions and the help with my letters, and Prof. Oskar Vafek for his insight on renormalization group and great classes in Florida State University.

I would also like to thank my colleges and friends Jian Kang, Xiaoyu Wang, Alberto Hinojosa Alvarado, Mengxing Ye, Yuxuan Wang, Chun Chen, Michael Schuett, Marc Schulz, Morten Christensen, Peter Orth, Tianbai Cui, Yiming Wu, Dmitry Chichinadze, Mengqun Li, Tobias Gulden, Jiashen Cai, Yangmu Li, Daniel Shaffer, Xuzhe Ying, Han Fu, Shao Tang, Luyang Wang and many others for useful discussions on various physical problems. Without them, I would not learn so much physics in such a short time. A lot of the discussions happened during condensed matter journal club, which I enjoyed the most during my graduate study.

My thanks also go to Prof. Turan Birol, Prof. Natalia Perkins and Prof. Ke Wang, who served in my dissertation committee, for their time and effort.

dedicated to the memory of my grandma, Yumei

Abstract

This dissertation focuses on the theoretical understanding of the interesting phases observed in one kind of the high temperature superconductors, iron-based superconductors. In the introduction chapter, I introduce what superconductivity and high temperature superconductors is and the motivation to study them; then I list out some of the basic, important, and relevant experiment results of iron-based superconductors, such as their lattice structures, phase diagrams, superconductivity, magnetic orders and charge orders observed; after that, I give a brief review of motivation, high level summary, and importance of each work being presented in later chapters. I finish the introduction with outlines and an educational introduction for people not that familiar with this area.

The following chapters consist of three topics. First, we attack the issue of methodology of studying the FeSC materials. The approach we use in this entire thesis is itinerant-scenario approach. Our analytical calculation finds out the orders developed for a FeSc model agree with non-biased(though has its own limitations) quantum Monte Carlo calculations. Both of these methods find s^{++} superconductivity and anti-ferro orbital orders as the leading orders. Secondly, we use parquet renormalization group theory to study a 4-pocket and a 5-pocket model for iron-based superconductors to shed more light upon the competing instabilities in these materials. We find amazingly simple behaviors in these complex models. These results can explain the interplay between superconductivity, charge order and magnetism in different kinds of iron-based superconductors. Thirdly, we study the details about the charge order(orbital order) discussed in previous chapters. In FeSe, the orbital order is in d-wave form, i.e., the sign of the orbital order is different between hole and electron pockets. We reproduce this sign difference by including vertex renormalization in d-wave orbital channel. Lastly, the conclusion follows.

Contents

List of Tables

List of Figures

Chapter 1

Introduction

1.1 What are superconductors and why do physicists study them

Superconductivity was first discovered in 1911[1] in mercury below a transition temperature 4.2K. Superconducting phase is a special phase of a material. In this phase, electrical resistance goes to exactly zero and magnetic fields are expelled(Meissner effect[2]). Such properties can make them useful for many possible industrial applications, such as making the magnets in magnetic resonate imaging machines, magnetic-levitated trains and power transmission without energy loss from heat. One obstacle of using these superconductors is that one needs to cool down the material to very low temperature, which has a high cost economically. Since 1911, hundreds of superconductors are discovered or synthesized. Copper-based superconductors discovered [3] in 1986 and iron-based superconductors discovered [4] in 2008 are called high-temperature(high T_c) superconductors. They receive special interests from physicists because their superconducting transition temperature is much higher compared to traditional ones, in some cases higher than the boiling point of liquid nitrogen 77K. Therefore, the cost of keeping them superconducting is significantly lower.

A very successful theory from Bardeen, Cooper and Schrieffer, known as the BCS theory [5], explains traditional superconductors very well. In this theory, electrons attract each other by exchanging phonons and form bound states, called Cooper pairs. Cooper pairs condensate and superconductivity occurs. The part that how electrons attract each other in BCS theory, electron-phonon pairing mechanism, cannot successfully explain the high transition temperature of high T_c superconductors. The consensus is that the pairing "force" is from interactions between electrons themselves instead of interaction between electrons and lattice ions. But the detailed pairing mechanism is still hotly debated, especially for copper-based superconductors, because of the strong correlation between electrons in these materials. Furthermore, some interesting phases emerge in high T_c superconductors and understanding these phases and their interplay with superconductivity is essential for understanding these materials.

My research and this thesis is focused on iron-based superconductors, especially about the phase diagrams and interplay between the various orders.

1.2 Experimental "facts" about iron-based superconductors: their structural properties, phase diagrams, charge order, magnetism and superconductivity

The family of iron-based superconductors includes various iron-pnictides and iron-chalcogenides and people use the pattern of their compositions as the names for the families. There are 1111 systems(eg. LaFeAsO), 111 systems(eg. LiFeAs), 122 systems (eg. $BaFe_2As_2$), 11 systems(eg. FeSe) and so on. The lattice structures(shown in Fig. 1.1) of different families of iron-based superconductors are similar and they all contain square lattice planes made of Fe atoms, with pnictogen or chalcogen atoms being above and below the Fe plane in an puckering pattern(Fig. 1.2).

There are several kinds of typical phase diagrams for iron-based superconductors. Phase diagrams are usually plotted with two axes for iron-based superconductors. One axis is doping or pressure – electron doping, pressure or "chemical pressure"(isovalent replacement such as Se by S), and the other axis is temperature. By tuning parameters along these two axis, various phases/orders are observed in all kinds of experiments. Some of them are charge order(nematic), magnetic order and superconductivity. Fig. 1.4 shows the phase diagram of two typical compounds of two typical kinds of iron-based superconductors, $Ba(Fe_{1-x}Co_x)_2As_2$ for the 122 system and $FeSe_{1-x}S_x$ for 11 system. Both materials are metallic. When lowering the temperature, various phases emerge. For 122 systems, at zero doping(x=0), the parent compounds develop a specific type of magnetic order – stripe spin density wave(SDW)(Fig. 1.3), where the spin degree of freedom of electrons align ferromagnetically along one direction and align antiferro-magnetically along the other direction of the iron square lattice. This phase is still metallic and it is in contrast with localized spin order, where the spins are localized in space. Before entering SDW phase when temperature is lowered, there is a phase occupying narrow spaces in the phase diagram, the nematic phase. In this phase, the tetragonal structure become orthorhombic; dc resistivity, optical conductivity, magnetic susceptibility and other measurements along the iron plane have found that the "macroscopic" C_4 symmetry is broken for the iron plane. The name "nematic" comes from liquid crystals. In liquid crystal, nematic phase breaks rotational symmetry but preserves translational symmetry. Nematic phase in FeSc is similar by analogy. Increasing the doping level, SDW order get suppressed and SDW phase gives way to superconducting phase. The superconducting phase often has a dome-like shape. At optimal doping, the transition temperature reaches the highest value. For 11 systems, there

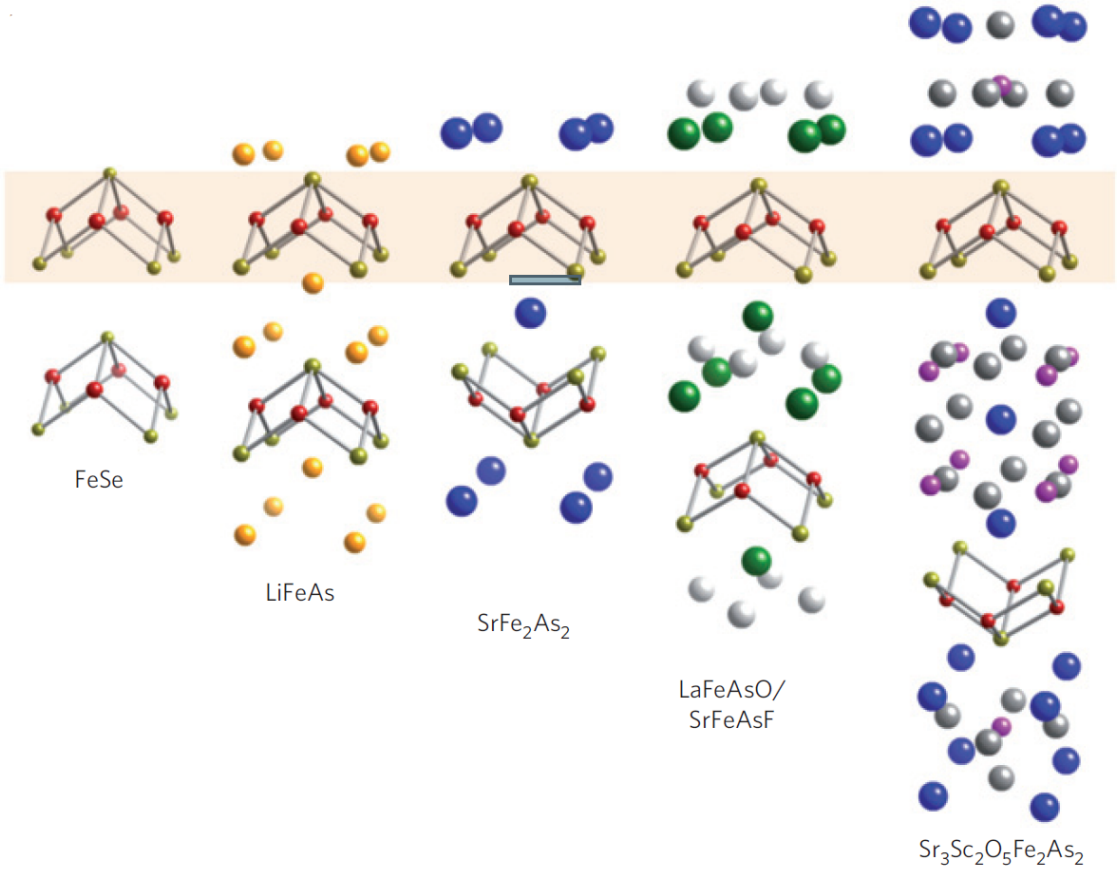

Figure 1.1: Crystal structure for FeSe, LiFeAs, $BaFe_2As_2$, and LaOFeAs. The iron atoms are shown in red and the pnictogen/chalcogen atoms are shown in gold. Figure reprinted by permission from RightsLink: Springer, Nature physics [6]

is no long range magnetic order such as SDW phase at zero doping. Instead, there is a large area of nematic phase. Upon doping, the nematic phase goes away near 15% of S substitution. Superconductivity appears even without doping. There has been no definite evidence to settle the issue of the symmetry of the superconducting order parameter, but the majority of researchers, both theorists and experimentalists believe that it is s_{+-} symmetry. s_{+-} means the phase of a U(1) superconducting order parameter change π between hole and electron pockets. One of the strong evidences supporting this symmetry comes from angle-resolved photoelectron spectroscopy(ARPES) experiments, where the superconducting gap on the hole pockets doesn't have nodes on the Fermi surface. Only s-wave symmetry is consistent with this ARPES observation. Also, there are several experiments

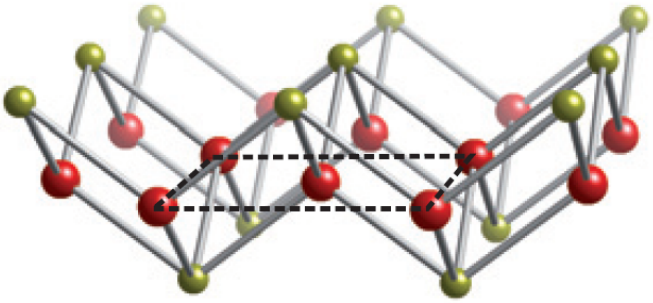

Figure 1.2: The iron plane common to all iron-based superconducting compounds, with iron ions shown in red and pnictogen/chalcogen anions shown in gold. Figure reprinted by permission from RightsLink: Springer, Nature physics [6]

such as neutron scattering finding observations [7] that are consistent with the π phase shift between hole and electron pockets. Piecing these evidences together, the most reasonable symmetry is s_{+-}.

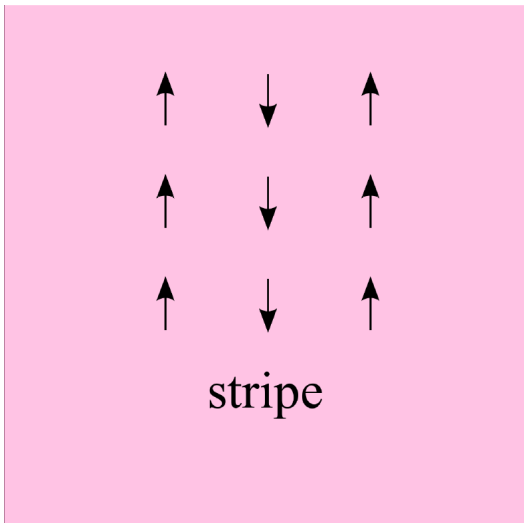

Figure 1.3: Schematic figure for spin density wave with order parameter (π,0) The spins align ferromagnetically along y direction and anti-ferromagentically along x direction. Figure from [8]. IOP Publishing. Reproduced with permission. All rights reserved.

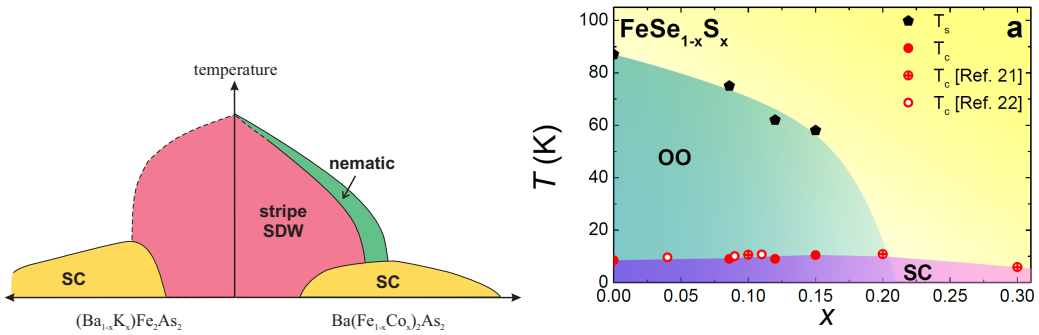

(a) (b)

Figure 1.4: Phase diagram of 122 and 11 systems. Left: Schematic phase diagram for a typical compound, $BaFe_2As_2$, in 122 system. It contains stripe spin-density wave (SDW) order, nematic order, and superconductivity (SC).Figure from [8]. IOP Publishing. Reproduced with permission. All rights reserved. Right: Phase diagram for a typical compound, $FeSe_{1-x}S_x$, in 11 system. It contains nematic order(OO) and superconductivity (SC). Contrast to 122 systems, there is no magnetic order and SC merges at zero doping. Figure reprinted with permission from [9] Copyright (2015) by the American Physical Society

1.3 The theoretical works being presented

Various orders emerge at low temperature in iron-based superconductors. These results about orders can be summarized in phase diagrams. One of the most important steps to understand a material is to understand why the phase diagrams look like what they are and what is the cause or origin of the orders. Nematic order, magnetism and superconductivity are some of the orders occur in the phase diagrams of iron-based superconductors. In this dissertation, I focus on our theoretical models that can explain these phase diagrams and details of these orders.

There are long-lasting debates about whether one should view iron-based superconductors as itinerant electronic systems or electrons from some localized orbitals. These two approaches are called itinerant scenario approach and localized electrons approach. Recent applications of Quantum Monte Carlo (QMC) technique to iron-based superconductors opened a way to directly verify the applicability of the itinerant scenario for these systems. Iron-based superconductors undergo various instabilities upon lowering temperature (magnetism, superconductivity, nematicity/orbital order), and one can check whether the hierarchy of instabilities obtained within the itinerant approach is the same as in unbiased QMC simulations. In a recent paper [10] the authors considered the simplest two-band model with interaction tailored to favor orbital order. The type of the orbital order found

in QMC is different from the one found in earlier itinerant analysis. We report the results of our calculations within the itinerant scenario and argue that they are in perfect agreement with QMC. The itinerant scenario approach serves as our basis for more complex models to understand the phase diagrams in the following.

Interestingly, phase diagrams of different families of iron-based superconductors are vastly different even with similar chemical components and lattice structures, which is not straightforward to understand. In principle, one can come up with different models to explain different families of materials. However, one of the beauty of physics is its generality/unification. The most beautiful theories in physics can explain different phenomenon within one model, such as Maxwell's 4 equations describing electric and magnetic phenomenon and electroweak theory as unified description of electromagnetic forces and weak forces. CKF (A.V. Chubukov, M. Khodas, and R.M. Fernandes [11]) is such a framework. It unifies descriptions for different families of iron-based superconductors. Within this CKF framework, we study 4-pocket and 5-pocket models. Our works presented here extend the framework and make it more general and realistic and being able to explain more experiments.

The results of a parquet renormalization group (RG) study of competing instabilities in the full 2D 4-pocket, three orbital low-energy model for iron-based superconductors are given. We derive and analyze the RG flow of the couplings, which describe all symmetry-allowed interactions between low-energy fermions. Despite that the number of the couplings is large, we argue that there are only two stable fixed trajectories of the RG flow and one weakly unstable fixed trajectory with a single unstable direction. Each fixed trajectory has a finite basin of attraction in the space of initial system parameters. On the stable trajectories, either interactions involving only d_{xz} and d_{yz} or only d_{xy} orbital components on electron pockets dominate, while on the weakly unstable trajectory interactions involving d_{xz} (d_{yz}) and d_{xy} orbital states on electron pockets remain comparable. The behavior along the two stable fixed trajectories has been analyzed earlier [11]. Here we focus on the system behavior along the weakly unstable trajectory and apply the results to FeSe. We find, based on the analysis of susceptibilities along this trajectory, that the leading instability upon lowering the temperature is towards a *three-component* d-wave orbital nematic order. Two components are the differences between fermionic densities on d_{xz} and d_{yz} orbitals on hole pockets and on electron pockets, and the third one is the difference between the densities of d_{xy} orbitals on the two electron pockets. We argue that this order is consistent with the splitting of band degeneracies, observed in recent photoemission data on FeSe by A. Fedorov et al [12].

Then the results of the parquet renormalization group (RG) analysis of the phase diagram of the most general 5-pocket model for Fe-based superconductors are presented. We use as an input the orbital structure of excitations near the five pockets made out of d_{xz}, d_{yz}, and d_{xy} orbitals and argue that there are 40 different interactions between low-energy fermions in the orbital basis. All interactions flow under RG, as one progressively integrates out fermions with higher energies. We find that the low-energy behavior is amazingly simple, despite the large number of interactions. Namely, at low-energies the full 5-pocket model effectively reduces either to a 3-pocket model made of one d_{xy} hole pocket and two electron pockets, or a 4-pocket model made of two d_{xz}/d_{yz} hole pockets and two electron pockets. The leading instability in the effective 4-pocket model is a spontaneous orbital (nematic) order, followed by s^{+-} superconductivity. In the effective 3-pocket model orbital fluctuations are weaker, and the system develops either s^{+-} superconductivity or stripe SDW. In the latter case, nematicity is induced by composite spin fluctuations.

Nematic order/orbital order is often seen together with superconductivity in the phase diagram of iron-based superconductors and certainly worth detailed study. We study the structure of the d-wave orbital order in FeSe in light of recent STM and ARPES data, which detect the shapes of hole and electron pockets in the nematic phase. The geometry of the pockets indicates that the sign of the orbital order $\Gamma = \langle d^\dagger_{xz} d_{xz} - d^\dagger_{yz} d_{yz} \rangle$ is different between hole and electron pockets (Γ_h and Γ_e). We argue that this sign change cannot be reproduced if one solves for the orbital order within mean-field approximation, as the mean-field analysis yields either no orbital order, or order with the same sign of Γ_e and Γ_h. We argue that another solution with the opposite signs of Γ_e and Γ_h emerges if we include the renormalizations of the vertices in $d-$wave orbital channel. We show that the ratio $|\Gamma_e/\Gamma_h|$ is of order one, independent on the strength of the interaction. We also compute the temperature variation of the energy of d_{xz} and d_{yz} orbitals at the center of electron pockets and compare the results with ARPES data.

1.4 Outlines

The outline of the thesis is as following.

In the remaining of chapter 1, I will give an introduction in layman's terms for educational purposes, starting with basics of superconductivity and then BCS theory and finally overview of our works being presented later.

In chapter 2, we attack the issue of methodology of studying the FeSC materials. There are many debates on whether one should use itinerant-scenario approach or localized-

scenario approach for FeSC. Itinerant models start from free moving electrons under the background of lattice and then add in the interactions between them as perturbation, whereas localized models treat electrons as localized and then add in kinetic energies as perturbation. Our calculations using itinerant approach on one of the model for FeSC agrees with non-biased(though has its own limitations) quantum Monte Carlo calculations. Both of these methods find s^{++} superconductivity and anti-ferro orbital orders as the leading orders. This aligning is an indication that interesting low temperature properties such as superconductivity and orbital orders observed in the experiments can be properly accounted for in itinerant models. The results presented in this chapter have been published in [13]. Copyrighted by the American Physical Society.

In chapter 3, a 4-pocket model for iron-based superconductors is studied to shed more light upon the competing instabilities in these materials, especially orbital ordering and splitting of band degeneracy in FeSe systems. We use itinerant-scenario approach and adopt a realistic band structure, and then resort to powerful parquet renormalization group theory to deal with interactions between electrons. Parquet renormalization group analysis is one of the most unbiased treatment for competing orders in itinerant-scenario approach. What we find is that, under renormalization group flow, the interactions follows three fixed trajectories. It means that we can describe a very complex model with a huge parameter space using only these three simple fixed trajectories. Two of them are stable and already analyzed in previous work, and the third fixed trajectory features a specific form of orbital order, which may have already been observed in experiments related to splitting of band degeneracy. The results presented in this chapter have been published in [14]. Copyrighted by the American Physical Society.

In chapter 4, we expand to a more general model, a 5-pocket model for iron-based superconductors. Once again, we find amazingly simple behaviors in complex models. At low temperature, it reduces to 2 possible scenarios depends on where the parameters resides in the parameter space. One scenario is an effective 4-pockets model, where a spontaneous orbital (nematic) order develops upon lowering temperature, followed by s^{+-} superconductivity. While the other scenario is an effective 3-pockets model, where the system develops either s^{+-} superconductivity or stripe spin density wave, and nematic order is partially melted stripe spin density wave order in this case. These results can explain the interplay between superconductivity, nematic order and magnetism in different kinds of iron-based superconductors. The results presented in this chapter have been published in [15]. Copyrighted by the American Physical Society.

In chapter 5, we study the details about the nematic order discussed in previous chapters.

In FeSe, the orbital order is in d-wave form, i.e., the sign of the orbital order is different between hole and electron pockets. We reproduce this sign difference by including vertex renormalization in d-wave orbital channel. The results presented in this chapter have been published in [16]. Copyrighted by the American Physical Society.

1.5 Introduction in plain English

In this section, I will rephrase the introduction in plain English for educational purposes, as a helper for newcomers in this field. First, an introduction of superconductivity and the mechanism of traditional superconductors is given. Challenges and problems that motivate our research on iron-based high-temperature superconductors are presented. We systematically study why different non-superconducting states of matter(phases), observed experimentally in the iron-based high-temperature superconductors, develop, and what the relation of these phases is to superconductivity. We do this using one of the most unbiased approaches, called renormalization group theory. Through our model and calculations, we identify different classes of iron-based superconductors and find unified description of these materials.

Superconductors can conduct electricity without energy loss and thus have important applications. Under normal conditions (for example, at room temperature), metals such as aluminum and copper can conduct electricity, but they all have some electrical resistance. When a voltage is applied to a metal, electrons move in a certain direction and current forms. It is inevitable that a moving electron hits other objects, like impurities (no material is absolutely pure) or other electrons. Then the energy will be lost as these collisions convert electron energy into heat. Resistance is the quantity that characterizes the energy loss. Superconductors has exactly zero electrical resistance. Since there is no heat produced when an electric current flows through, superconductors are used to make powerful magnets in MRI machines. If normal wires with non-zero resistance were used in these machines, they would be melted by the heat produced by the huge electric current. Another potential application of superconductors in the future is electric power transmission. Imagine the energy saved by using zero-resistance wires for electric transmission!

The reason that we still use normal metal for electric transmission is that superconductivity emerges only at very low temperatures. Mercury, the first superconductor, discovered [1] by K. Onnes in 1911, becomes superconducting below 4.2K(Fig. 1.5). Aluminum become superconductor below 1.2K. The temperature for the transition between superconducting and normal metal is called superconducting transition temperature T_c. The Holy Grail

for many physicists is to find room-temperature superconductors, i.e., metals that become superconductors already above room temperature.

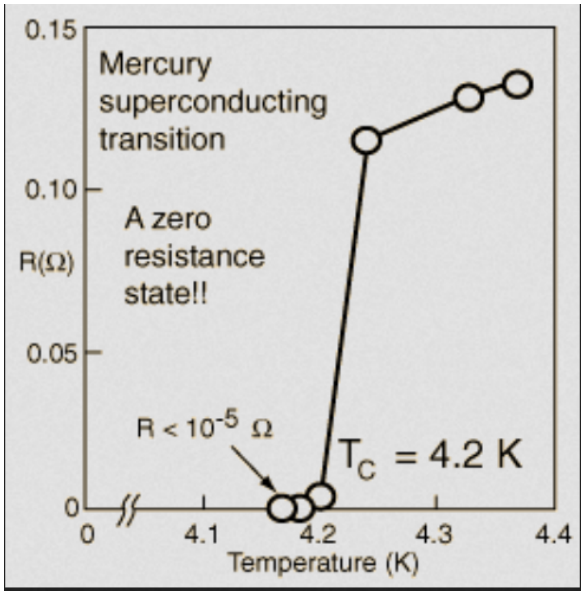

Figure 1.5: Mercury becomes superconducting when temperature lowers to 4.2K. The resistance measured is less than 10^{-5} Ohm, due to limitation of sensitivity of instruments. We know now it's exactly zero. The figure is from [1]

A history-making discovery was made in 1986, when a new family of copper-based materials was found [3], which have much higher T_c. In a certain material of this family, superconductivity has been observed at a record high T_c over 150K. In 2008, another class of superconductors with high T_c, called iron-based superconductors [4], has been discovered. These two families of materials are known as high-temperature superconductors. At the moment, it is not completely understood what causes superconductivity in copper- and iron-based systems. Understanding the mechanism of high-temperature superconductivity in these materials may help to unveil the route to discover room temperature superconductors suitable for practical use.

Before we look at the challenges that motivate our research, let us look at what has already been known. For traditional superconductors, Bardeen-Cooper-Schrieffer (BCS) theory [5] explains most of their properties. The BCS theory states that, as long as there is attraction between electrons, no matter how small, two electrons can form a bound state, a so called "Cooper pair". All these Cooper pairs act together (like people holding hands), and this protects electrons from losing energy due to collisions with impurities etc. Consequently,

the electric current flows without dissipation. The origin of attraction between electrons is a tricky issue, as we know that electrons repel each other due to Coulomb force. In BCS theory, the attraction comes from the underlying positively charged ions, which form a periodic structure, called ionic lattice. Positively charged ions and negatively charged electrons attract each other. When an electron moves through, it drags the nearby ions towards it. Since these ions have much larger mass than the electrons, they are still in the dragged, distorted position for a while even after an electron has left, thus preserving a higher positive charge density in this area. A new electron is then attracted into this area by these distorted ions (Fig. 1.6). As a result, effectively, the first and the second electron attract each other. At low enough temperatures, the attraction mediated through ions is larger than the direct repulsion between electrons due to Coulomb force, so that there is net attraction between electrons. Then Cooper pairs form and superconductivity occurs.

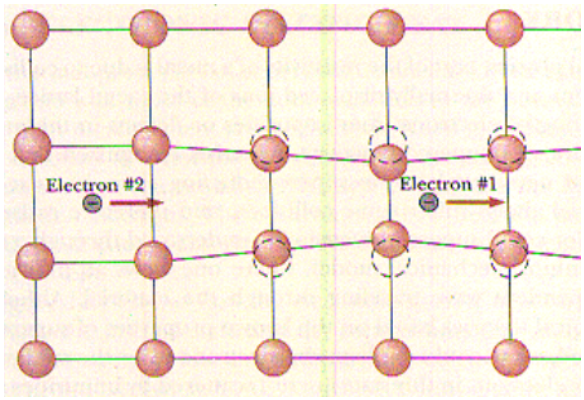

Figure 1.6: To show the attraction between electrons mediated by ions. The red circles are ions with positive charge. When electron 1 move through, these ions are attracted by the electron and thus form a region with higher positive charge density. Electron 2 is attracted to the region with these squeezed ions. The figure is from *http* : *//www.owlnet.rice.edu/ hkic/superconductors/*

Despite the huge success that BCS theory had in explaining the physics of traditional superconductors, the theory fails to explain high-temperature superconductors. Through calculations, people found that the attraction through ions is too small to be able to account for such high T_c. Also, exotic phases have been found in these high-temperature superconductors, which also cannot be explained by the ion-mediated interaction between electrons. (A phase is a particular state of matter, e.g., water and ice are two phases of H_2O). Some examples of exotic phases in iron-based superconductors are the nematic phase (Fig. 1.7) and the spin density wave phase. Naturally, the questions that need to be addressed are

not only what causes superconductivity, but also why these additional phases appear and what is the relation between those phases and superconductivity (which is also a phase). That motivates us to study all relevant phases in high-temperature superconductors in a systematic way. We focus on one family – iron-based superconductors.

To systematically study the phases in iron-based superconductors, theorists need to choose an appropriate model. Since the property of the material is similar to that of a metal, the widely used starting point is the so-called itinerant scenario, which means that the electrons are treated as moving almost freely in the entire material (as in the case of metal), instead of moving in a small region near some specific ions (as in the case of insulators). At the next step, we consider the Coulomb forces (termed as interactions) between the electrons and analyze how these forces give rise to various phases, including superconductivity. If the interactions between electrons are treated as weak, we can do almost perfect calculations to explain or even predict the behaviors of electrons and understand all the phases in the materials. However, the interactions are intermediate to strong in iron-based superconductors. We run into the famous open question of how to deal with strongly interacting electrons. We use one of the most unbiased analytical methods, renormalization group (RG) theory, to study it. As we can see in the case of water and ice, temperature plays a crucial role in forming phases. The idea of RG is that, as temperature gets lower, electrons are less and less probable to be in a state of high energy; therefore, one can discard(integrate out, mathematically) the states with higher energy when going to lower temperature. The rigorous procedure to do this is called RG method.

In chapter 2, we dig deep into the applicability of the itinerant-scenario approach, our starting point as discussed above, by comparing with Quantum Monte Carlo(QMC) calculations. QMC, though has its own drawbacks, is considered one of the most unbiased numerical methods to cope with strongly interacting electrons. The recent QMC results shows superconductivity and a so-called Anti-Ferro-orbital (AFO) phase in a simplified model for iron-based superconductors as the leading instabilities. We demonstrated that our results with the itinerant-scenario approach are in perfect agreement with QMC calculations. This study shows the applicability of itinerant-scenario approach for iron-based superconductors, giving us more confidence in our starting point.

In chapter 3 and 4, after establishing the starting point, we used the itinerant model and analyzed if we can obtain and understand all the phases observed in iron-based superconductors from pure theoretical calculations with the most general model (Analogy to this is that trying to understand what happens when we cool down water below 0 degree Celsius and to understand why ice looks like the way it is). For example, for one kind of

iron-based superconductor, $FeSe$, the nematic phase and the superconducting phase have been observed. The nematic phase is a phase where originally equivalent directions in the material (Fig. 1.7 Left), X and Y, become nonequivalent. This can result from ionic lattice distortion (Fig. 1.7 Middle), orbital order (Fig. 1.7 Right), or something else. From our unbiased RG calculation, we find that, when the temperature is lowered, the first instability occurs is orbital order, that gives rise to nematic phase (as in Fig. 1.7 Right), and that superconductivity develops at a lower temperature, as the second phase. This scenario is in full agreement with the experimental data; specifically, we calculated the order parameter – the quantity that characterizes the nematic phase, and found that it matches with spectroscopic experiments. Other kinds of iron-based superconductor (e.g. $LaFeAsO$) and their phases can also be understood within our framework in a simple and unified way. The most general model for iron-based superconductors we studied is a 5-pocket model in chapter 4.

In chapter 5, we study the details of the orbital order mentioned previously, specifically, about the opposite signs of orbital order for two different kinds of the electrons(electrons near eletron pockets and near hole pockets) in the FeSe materials. We reproduce the opposite signs by considering a modified interaction between electrons from RG theory.

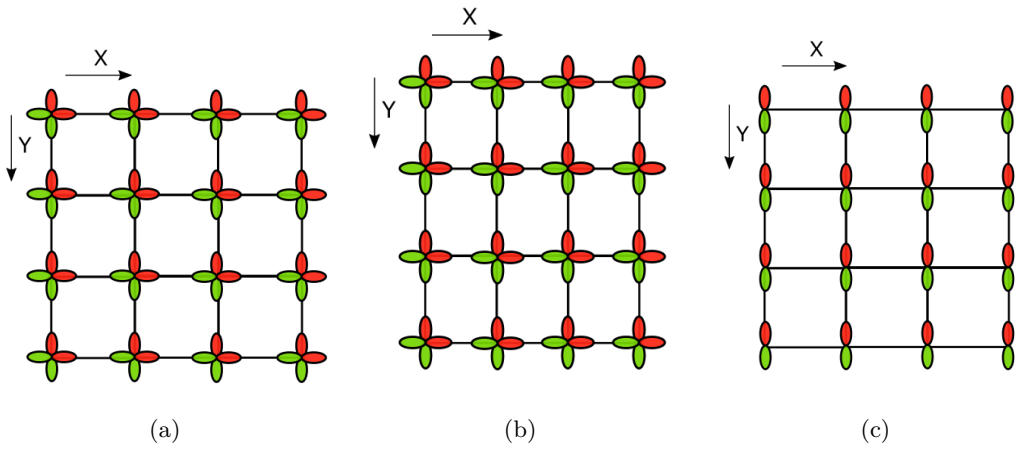

Figure 1.7: Schematics of nematic phase. Each two head-to-tail ellipses represent an orbital of an electron, and the underlying black lines (ions lie on the intersections) represent the ionic lattice. Left: normal phase, direction X is the same as direction Y. Middle: nematic phase, caused by ionic lattice distortion. Direction X becomes different from Y. Right: nematic phase, caused by orbital order (only one kind of orbital is left). Direction X becomes different from Y.

Chapter 2

Itinerant scenario and comparison with quantum Monte Carlo

2.1 Introduction.

The issue whether Fe-based (FeSCs) can be viewed as fully itinerant electronic systems, or electrons from some of the orbitals are localized, has been at the center of the debates on FeSCs right from their discovery[17, 18, 19, 20, 21, 22, 23, 24, 25, 26, 27, 28, 29, 30, 31, 32]. The itinerant scenario is justified when the interactions are smaller than the fermionic bandwidth, and it treats various instabilities in FeSCs, such as magnetism, superconductivity (SC), Ising-nematic spin order and spontaneous orbital order, as low energy instabilities are determined by carriers located near hole and/or electron Fermi surfaces (FSs) (Refs. [19, 20, 21, 22, 23, 24]). Localized scenario, on the other hand, is justified when the density-density (Hubbard) interactions are larger than the bandwidth, and within this scenario instabilities in FeSCs involve carriers from everywhere in the Brillouin zone [25, 26, 27, 28, 29, 30, 31]. The third, Hund metal scenario, has also been put forward [32] – it assumes that Hund interaction is large enough, in which case the system retains a metallic behavior but becomes a bad metal.

The FeSCs are metals for all dopings and compositions, and this would generally place them in the category of itinerant systems. At the same time the values of the Hubbard and Hund interactions in FeSCs, obtained from first-principle calculations, are comparable to the bandwidth, and some measurements of magnetic excitations in parent compounds have been reasonably well reproduced in calculations based on both itinerant [33] and localized [34] scenario. Measurements of the specific heat in strongly hole-doped FeSCs (specifically in K_x Ba_{1-x} Fe_2 As_2 for $x \to 1$, Refs. [35]) have been interpreted both within the itinerant scenario [36], and by assuming that electrons on some of the Fe-orbitals get localized [30, 31], and mid-infrared optical data have been interpreted within the Hund metal scenario [37]. Furthermore, weak coupling and strong coupling scenarios for FeSCs yield the same set of ordered states – magnetism, SC, etc. This all makes it difficult to settle on the approach. It also raises the fundamental issue whether FeSCs can be viewed as the "systems in the intermediate regime", which can be gradually reached starting from weak coupling, but some of the features they display are inherently strong coupling and are completely missed in weak coupling calculations.

To the best of our knowledge, there are no experimental data for weakly/moderately doped Fe-pnictides, which could not be reproduced, at least qualitatively, within the weak coupling scenario. In Fe-selenades, the situation is a bit more involved as magnetism in FeTe – the parent compound of $FeTe_{1-x}Se_x$ family, is qualitatively different from that in other parent compounds of FeSCs (double stripe or plaquette [38] in FeTe vs single stripe

in other systems [39]) and is only reproduced within the localized scenario [38]. Still, an orbital order at $x \approx 1$ and SC at $x \geq 0.5$ in this material and also in 245 family of FeSCs are all reproduced within the itinerant approach [24, 40, 11, 41, 42]. This is in line with the idea that FeSCs, with the exception of FeTe, can be viewed as itinerant systems, adiabatically extended to intermediate coupling.

However, the ability to qualitatively explain the data may be misleading and one needs another tool to verify whether the behavior of a given FeSC, particularly the hierarchy of the instabilities upon lowering temperature or changing parameters, differs in any fundamental way from that in a weakly coupled metal with the same topology of the FS as in a FeSC. Recent application of Quantum Monte Carlo (QMC) method to FeSCs (Refs. [43, 10]) provide such a tool as they allow one to compare the actual behavior in a fermionic system with comparable strength of kinetic and potential energies with the one obtained by using weak coupling perturbative schemes for various topologies of Fermi surfaces and structures of multi-band excitations. In Ref. [10], Dumitrescu et al applied QMC to the simplest toy model for FeSCs – the two band model with Fe d_{xz} and d_{yz} orbitals, first considered by Raghu et al [44]. Although this model does not reproduce the correct topology of low-energy electronic states in FeSCs (one of the two hole FSs is in wrong place in the 1 Fe Brillouin zone), it nevertheless is the simplest toy model with two hole and two electron Fermi surfaces. Dumitrescu et al further tailored 4-fermion interaction to be local and in the form $-g(n_{xz} - n_{yz})^2$, where $n_i = d_i^\dagger d_i$ is fermionic density on a given orbital, and $g > 0$. This last condition is difficult to justify on microscopic grounds because it implies that intra-orbital Hubbard interaction is attractive, in variance with first-principle calculations [46]. Nevertheless, the model considered in [10] and in earlier works [47] is quite interesting for our purpose to compare QMC and perturbation theory as it favors an orbital order (a spontaneous development of a non-zero $< n_{xz} - n_{yz} >$). An orbital order is a threshold phenomenon, i.e., it appears only when g exceeds a certain critical value g_c, which is generally of order of the bandwidth, W. Weak coupling analysis is an expansion in g, and there is no a'priori guarantee that the type of orbital order obtained by using weak coupling approximation and extending g to critical g_c will be the right one.

Different types of orbital order in the two-pocket model include ferro-orbital (FO) order (a Pomeranchuk instability), which can be in $s-$wave or $d-$wave channel, antiferro-orbital (AFO) order with momentum (π, π), and stripe-type orbital order with momentum $(0, \pi)$ or $(\pi, 0)$. Dumitrescu et al argued that strong coupling analysis (an expansion in $1/g$) favors AFO order, and they did find the same type of order in QMC. Earlier itinerant calculations, on the other hand found numerically a different, FO order (Ref. [47]).

2.1.1 Summary of our results

In this paper we report the results of our analytical analysis of the orbital order and SC within the itinerant scenario.

In the particle-hole channel we found that weak coupling calculation shows that the system chooses to develop AFO order, the same one as found in QMC calculations. Moreover, we argue that some of the particle-hole polarization bubbles involved in the renormalizations of the orbital order parameters are logarithmical at intermediate energies and, as a result, the critical coupling $g = g_c$ for the orbital instability is small compared to fermionic bandwidth, W, and is within the range of applicability of weak coupling expansion. The smallness of g_c/W is due to small sizes of hole and electron pockets and holds in $1/\log \frac{W}{\epsilon_0}$, where ϵ_0 is of order of Fermi energy. We found logarithms in both AFO and FO channels, but the prefactor in the AFO channel is larger, hence the leading instability is towards AFO order.

In the particle-particle channel we found the leading instability in s^{++} channel (ordinary $s-$wave) and subleading instability in the $d-$wave channel. The renormalizations in both channels contain series of conventional Cooper-type $\frac{g}{W} \log \frac{W}{T}$ terms, but also contain terms of order g/ϵ_0, due to the presence of two weakly dispersing bands, whose energies remain of order ϵ_0 over a wide range of momenta. S-wave channel wins over $d-$wave both at truly weak coupling, when $T_c \ll \epsilon_0$ and only the conventional logarithmical terms matter, while at larger g, terms of order g/ϵ_0 play the leading role.

We compared critical g for the instabilities in the particle-hole and particle-particle channels. Within the ladder approximation, when particle-particle and particle-hole channels do not couple to each other, the comparison of the eigenvalues in the AFO and s^{++} channels shows that the overall prefactor in the AFO channel is larger than in s^{++} channel, but the combination of polarization operators is larger in the SC channel. We went beyond the ladder approximation and used renormalization group (RG) to include the flow of the intra-orbital and inter-orbital interactions between high and low energies due to the actual presence of the couplings between particle-hole and particle-particle channels. We found that, due to the flow, the overall prefactor in the AFO channel is reduced and becomes the same as in s^{++} channel. Because polarization operator is larger in the SC channel, the leading instability upon, e,g., increasing g at a certain non-zero temperature is definitely towards s^{++} SC. The AFO order develops, but at a larger g. This fully agrees with QMC calculations.

Another result of RG is that couplings in both s^{++} and AFO channels get enhanced by

coupling to stripe magnetic fluctuations. This enhancement is the strongest around half-filling, when there is nesting between hole and electron pockets [20]. Accordingly, both s^{++} SC and AFO order are the strongest near half-filling. This again agrees with QMC results.

The structure of the paper is the following. In the next section we introduce the model. In Sec. 3.4 we consider instabilities in the particle-hole and particle-particle channels and the interplay between them. In Sec. 2.3.1 we analyze instabilities towards FO and AFO orders within the ladder approximation. In Sec. 2.3.2 we analyze the pairing instabilities within the same approximation. In Sec. 2.3.3 we compare the instabilities in the particle-hole and particle-particle channels first in the ladder approximation and then by adding RG analysis. We present our conclusions in Sec. 2.4.

2.2 The model

We consider the same two-orbital model as in earlier works, with hoping between dxz and d_{yz} orbitals at nearest and next-nearest neighbors. The kinetic energy is

$$\begin{aligned} \mathcal{H} &= \sum_k A_{x,k} d^\dagger_{xz,k} d_{xz,k} + A_{y,k} d^\dagger_{yz,k} d_{yz,k} + \\ & V_k \left(d^\dagger_{xz,k} d_{yz,k} + d^\dagger_{yz,k} d_{xz,k} \right) \end{aligned} \tag{2.1}$$

where the summation over spin components is assumed and

$$\begin{aligned} A_{x,k} &= A_0 + t_1 \cos k_x + t_2 \cos k_y + t_3 \cos k_x \cos k_y, \\ A_{y,k} &= A_0 + t_2 \cos k_x + t_1 \cos k_y + t_3 \cos k_x \cos k_y, \\ V_k &= V \sin k_x \sin k_y. \end{aligned}$$

The dispersions $A_{x,k}$ and $A_{y,k}$ along different directions in momentum space are presented in Fig. 2.1. The two dispersions are obviously degenerate at $(0,0)$ and at (π,π). The V term does not remove the degeneracy, but it mixes d_{xz} and d_{yz} orbitals away from these points. The kinetic energy in the presence of the V term can be easily diagonalized. Near $(0,0)$ and (π,π) there are two low-energy modes, each with mixed d_{xz}/d_{yz} character. Out of two low-energy modes near $(0,0)$, one crosses the chemical potential and creates a hole pocket, while the other remains above the chemical potential. The same holds near (π,π), where the second hole pocket develops.

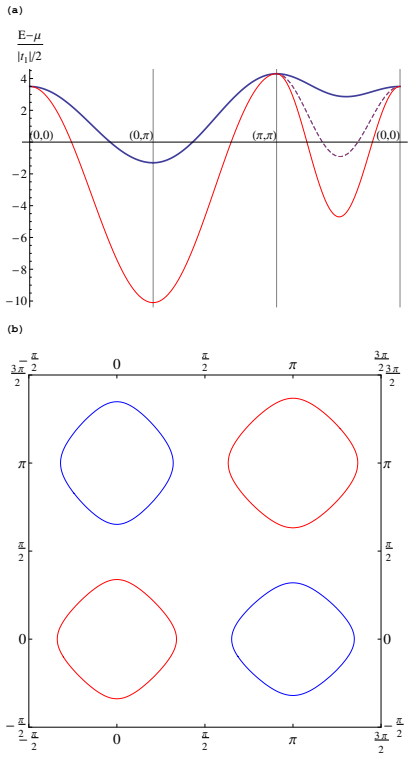

Figure 2.1: (a)Dispersion along $(0,0)$-$(0,\pi)$-(π,π)-$(0,0)$ measured from μ. The solid red line shows $E_a(k)$; the thick blue line shows $E_b(k)$; the purple dashed line shows $A_{x,k} = A_{y,k}$ from (π,π) to $(0,0)$. $A_{x,k}$ coincides with $E_a(k)$ (and $A_{y,k}$ coincides with $E_b(k)$) along $(0,0)$-$(0,\pi)$ and $(0,\pi)$-(π,π) directions. We used $t_1 = 2.0$, $t_2 = -2.4$, $t_3 = 4.8$, $V = 3.8$ and $\mu = 0.9$. (b)the Fermi surface of the two-orbital model. The red circles are hole pockets and the blue ones are electron pockets.

Near $\mathbf{k} = 0$, $A_{x,k}$, $A_{y,k}$ and V_k are approximated by

$$\begin{aligned} A_{x,k} &= \epsilon_0 - ak^2 - c(k_x^2 - k_y^2), \\ A_{y,k} &= \epsilon_0 - ak^2 + c(k_x^2 - k_y^2), \\ V_k &= Vk_xk_y, \end{aligned}$$

where

$$\epsilon_0 = A_0 + t_1 + t_2 + t_3, a = \frac{t_1 + t_2 + 2t_3}{4}, c = \frac{t_1 - t_2}{4}.$$

The diagonalization near $\mathbf{k} = 0$ yields

$$\mathcal{H} = E_a(k) a_k^\dagger a_k + E_b(k) b_k^\dagger b_k,$$

and the two dispersions are

$$E_{a,b}(k) = \epsilon_0 - ak^2 \mp \sqrt{c^2(k_x^2 - k_y^2)^2 + V^2 k_x^2 k_y^2}.$$

To simplify the analysis we set $V = 2c$, in which case the two dispersions near $\mathbf{k} = 0$ are isotropic: $\mathcal{H} = E_a(k) a_k^\dagger a_k + E_b(k) b_k^\dagger b_k$, where $E_{a,b}(k) = \epsilon_0 - (a \pm |c|)k^2$. The transformation from d_{xz}/d_{yz} orbital operators to a and b band operators is a pure rotation [45]

$$d_{xz} = a\cos\phi + b\sin\phi, d_{yz} = b\cos\phi - a\sin\phi, \tag{2.2}$$

where ϕ is the angle between $\mathbf{k}$ and x-axis. Like in earlier works we set $\epsilon_0 > 0$, $a > 0$, and $a \sim |c|$. For these parameters, E_a crosses zero at $k = k_F = (\epsilon_0/(a + |c|))^{1/2}$, while E_b remains approximately equal to E_0 at small k.

A similar analysis for $\mathbf{k} \approx (\pi, \pi)$ yields the similar form of $\mathcal{H}$ as near $\mathbf{k} = 0$, i.e.,

$$\mathcal{H} = E_{\tilde{a}}(k) \tilde{a}_k^\dagger \tilde{a}_k + E_{\tilde{b}}(k) \tilde{b}_k^\dagger \tilde{b}_k,$$

where $\mathbf{k}$ is counted from (π, π), and

$$E_{\tilde{a},\tilde{b}}(k) = \tilde{\epsilon}_0 - (a \pm |c|)k^2$$

where $\epsilon_0 = A_0 - t_1 - t_2 + t_3$. Again, the $\tilde{a}$ band crosses the chemical potential and forms a hole pocket, while the energy of the $\tilde{b}$ band remains approximately equal to $\tilde{\epsilon}_0$. The dispersions near (π, π) become identical to those near $(0, 0)$ when $t_1 + t_2 = 0$. The transformation from d_{xz}/d_{yz} orbital operators to $\tilde{a}$ and $\tilde{b}$ band operators is

$$d_{xz} = \tilde{b}\cos\phi - \tilde{a}\sin\phi, d_{yz} = \tilde{a}\cos\phi + \tilde{b}\sin\phi, \tag{2.3}$$

where ϕ is again the angle between small $\tilde{k}$ and x-axis. We emphasize that (5.3) is not obtained from (5.2) by rotating ϕ by 90^o, one needs to invoke an additional reflection around, say, x axis.

Near$(0, \pi)$ ($(\pi, 0)$), only $A_{x,k}$ ($A_{y,k}$) becomes soft, other branch has a larger gap, comparable to the full bandwidth. The hybridization term V_k vanishes at $(\pi, 0)$ and $(0, \pi)$, hence

low-energy excitations near $(0,\pi)$ ($(\pi,0)$) can be safely approximated as pure d_{xz} (d_{yz}). These pure excitations form two electron pockets (see Fig. 2.1). We label corresponding low-energy fermions as $f_{1,k}$ ($f_{2,k}$) with momentum counted from $(0,\pi)$ ($(\pi,0)$).

We follow Refs. [10, 47] and set the interaction term to be $\mathcal{H}_{int} = -g\sum_{r,\alpha}(n_{xz,\alpha}(r) - n_{yz\alpha}(r))^2$, where $n_{xz,\alpha}(r) = d^\dagger_{xz,\alpha}(r)d_{xz,\alpha}(r)$ and $n_{yz,\alpha}(r) = d^\dagger_{yz,\alpha}(r)d_{yz,\alpha}(r)$. This interaction can be cast into more familiar $U-U'$ Hubbard form with intra-pocket and inter-pocket terms:

$$\begin{aligned}\mathcal{H} &= \sum_{r,\alpha,\beta}\frac{U}{2}\left(n_{xz,\alpha}(r)n_{xz,\beta}(r) + n_{yz,\alpha}(r)n_{yz,\beta}(r)\right) + \\ &\quad U' n_{xz,\alpha}(r)n_{yz,\beta}(r)\end{aligned} \tag{2.4}$$

with $U = -2g$ and $U' = 2g$. Like in earlier works, we set g to be positive, in which case the interaction favors orbital order with $n_{xz,\alpha}(r) \neq n_{yx,\alpha}(r)$. The model with a positive g is somewhat artificial as it implies that intra-orbital Hubbard interaction U is attractive, but, like we said, this model allows one to compare QMC results with analytical results at weak and strong coupling.

The interaction (2.4) is momentum independent in the orbital basis, but acquires the dependence on $\cos\theta$ and $\sin\theta$ of individual fermions, when re-expressed in the band basis. Namely, each time d_{xz} or d_{yz} operator is re-expressed in terms of $a, b, \tilde{a}$, or $\tilde{b}$ fermions, the interaction term acquires the corresponding coherence factor from the transformation from orbital to band basis.

2.3 Instabilities in the particle-hole and particle-particle channels within the itinerant approach

2.3.1 Orbital ordering

At large g, the potential energy well exceeds the kinetic energy. The $-g(n^2_{xz} - n^2_{yz})$ is minimized when all fermions accumulate in one band, breaking the orbital symmetry. However, the potential energy is local and it alone does not specify the momentum of the orbital order. To understand what kind of orbital ordering develops, one needs to include the leading corrections in t/g. These terms favor a checkerboard, AFO order with momentum (π,π) (Ref.[49]). The same AFO order has been found in QMC analysis [10]. Like we said, our goal is to understand what kind of orbital order emerges at weaker couplings, when potential energy can be treated as a perturbation and the instability comes from low-energy

fermions, located near the Fermi surfaces.

We compare two types of orbital orders $\Delta(r) = \sum_q \Delta(q) e^{iqr}$: uniform FO order $\Delta(q) = \Delta_{fo}\delta(q)$ and staggered anti-FO order $\Delta(q) = \Delta_{afo}\delta(q-(\pi,\pi))$. In terms of low-energy band fermions,

$$\Delta_{fo} = \sum_k \left[< f^\dagger_{1,k} f_{1,k} - f^\dagger_{2,k} f_{2,k} >\right] \tag{2.5}$$
$$+ \sum_k \left[\left(< a^\dagger_k a_k - b^\dagger_k b_k >\right)\cos 2\theta_k + \left(< a^\dagger_k b_k + b^\dagger_k a_k >\right)\sin 2\theta_k\right]$$
$$- \sum_k \left[\left(< \tilde{a}^\dagger_k \tilde{a}_k - \tilde{b}^\dagger_k \tilde{b}_k >\right)\cos 2\theta_k + \left(< \tilde{a}^\dagger_k \tilde{b}_k + \tilde{b}^\dagger_k \tilde{a}_k >\right)\sin 2\theta_k\right]$$

and

$$\Delta_{afo} = \sum_k \left[\left(< a^\dagger_k \tilde{b}_k + \tilde{b}^\dagger_k a_k >\right) - \left(< b^\dagger_k \tilde{a}_k + \tilde{a}^\dagger_k b_k >\right)\right], \tag{2.6}$$

where the integration over k is confined to the FS and this reduces the integration over position of k on the FS specified by θ_k. In both terms the summation is restricted to small k. There is no contribution to Δ_{afo} from electron pockets because out of two fermions from the same orbital, one has high energy.

To understand when (and if) the system develops an instability towards any of these orbital orders, we add to the Hamiltonian infinitesimally small order parameters $\Delta^{(0)}_{fo}$ and $\Delta^{(0)}_{afo}$ and compute the full susceptibilities. The divergence of a certain susceptibility would signal an instability towards the corresponding spontaneous order.

2.3.1.1 Ferro-orbital order

We first do calculations in the ladder approximation and then include RG renormalizations of U and U'. In the ladder approximation (also often called random phase approximation) one assumes that the dominant contribution to the renormalization of $\Delta^{(0)}_{fo}$ and $\Delta^{(0)}_{afo}$ comes from series of ladder and bubble diagrams with repeated insertions of the interactions in the same channel, in our case particle-hole channel with momentum transfer either zero or (π,π), while coupling to other channels (e.h., particle-particle channel) are neglected. Within this approximation, the fully renormalized order parameters Δ_{fo} and Δ_{afo} are expressed via the bare ones as $\Delta_{fo} = \Delta^{(0)}_{fo}/(1-I_{fo})$ and $\Delta_{afo} = \Delta^{(0)}_{afo}/(1-I_{afo})$. The instability in a given channel develops when the corresponding $I = 1$. To obtain when (and if) this condition is satisfied, one can neglect the bare values, find eigenvalues of the self-consistent equations

for Δ_{fo} and Δ_{afo} and check when the highest eigenvalue reaches one.

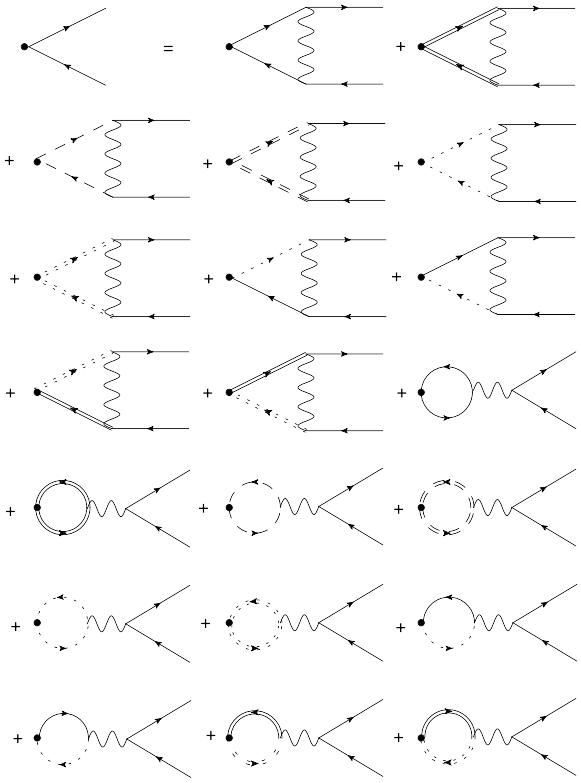

Figure 2.2: Diagrams for the renormalization of the components of ferro-orbital order parameter. Only diagrams for Δ_{fo}^{aa} are shown; the diagrams for the renormalization of other order parameters Δ_{fo}^{bb}, Δ_{fo}^{ab}, $\Delta_{fo}^{\tilde{a}\tilde{a}}$, $\Delta_{fo}^{\tilde{b}\tilde{b}}$, $\Delta_{fo}^{\tilde{a}\tilde{b}}$, $\Delta_{fo}^{f_1 f_1}$ and $\Delta_{fo}^{f_2 f_2}$ are obtained in a similar way. Solid lines, dotted lines and dashed lines label a, $\tilde{a}$, f_1 respectively; double solid lines, dotted lines and dashed lines label b, $\tilde{b}$, f_2 respectively.

The set of self-consistent equations for Δ_{fo} is presented in Fig. 2.2. Because coherence factors depends separately on $\cos\theta$ and $\sin\theta$, one has to introduce a more generic $q = 0$ order parameter with components

$$\begin{aligned}
&\Delta_{fo}^{aa}\cos^2\theta, \quad \bar{\Delta}_{fo}^{aa}\sin^2\theta, \quad \Delta_{fo}^{\tilde{a}\tilde{a}}\cos^2\theta, \quad \bar{\Delta}_{fo}^{\tilde{a}\tilde{a}}\sin^2\theta, \\
&\Delta_{fo}^{ab}\cos\theta\sin\theta, \quad \Delta_{fo}^{\tilde{a}\tilde{b}}\cos\theta\sin\theta, \\
&\Delta_{fo}^{f_1 f_1}, \quad \Delta_{fo}^{f_2 f_2},
\end{aligned} \tag{2.7}$$

where $\Delta_{fo}^{aa} = \sum_k a_k^\dagger a_k$ and so on. These 8 order parameters are all coupled in the ladder

approximation, however the 8×8 secular equation decouples between $s-$wave and two $d-$wave harmonics. Assume momentarily that $t_1 + t_2 = 0$, i.e., the pockets at $(0,0)$ and $\pi,\pi)$ are identical. Then in the $d_{x^2-y^2}$ channel (the one we need)

$$\begin{aligned}
&\Delta_{fo}^{aa} = -\bar{\Delta}_{fo}^{aa} = -\Delta_{fo}^{\tilde{a}\tilde{a}} = \bar{\Delta}|_{fo}^{\tilde{a}\tilde{a}} = \Delta_1 \\
&\Delta_{fo}^{ab} = -\Delta_{fo}^{\tilde{a}\tilde{b}} = \Delta_2, \\
&\Delta_{fo}^{f_1 f_1} = -\Delta_{fo}^{f_2 f_2} = \Delta_3
\end{aligned} \tag{2.8}$$

The three equations on Δ_i, $i = 1-3$ are identical up to a factor 2:

$$\begin{aligned}
\Delta_1 &= \frac{-U+2U'}{2}\left[\Delta_1\Pi_{aa} + 2\Delta_2\Pi_{ab} + 2\Delta_3\Pi_{ff}\right] \\
\Delta_2 &= \frac{-U+2U'}{2}\left[\Delta_1\Pi_{aa} + 2\Delta_2\Pi_{ab} + 2\Delta_3\Pi_{ff}\right] \\
\Delta_3 &= 2\frac{-U+2U'}{2}\left[\Delta_1\Pi_{aa} + 2\Delta_2\Pi_{ab} + 2\Delta_3\Pi_{ff}\right]
\end{aligned} \tag{2.9}$$

where Π_{ij} are polarization operators defined such that $\Pi_{ij} > 0$. The solution of (2.9) is, obviously, $\Delta_1 = \Delta_2 = \Delta_3/2 = \Delta$. Substituting this into (2.5) we obtain $\Delta_{fo} = 6\Delta$. The eigenvalue for this solution is $\lambda_{fo} = (-U/2 + U')\left(\Pi_{aa} + 2\Pi_{ff} + 2\Pi_{ab}\right)$. For a more generic case when hole pockets are not equivalent, the calculations are a bit more involved, but the result is the expected one:

$$\lambda_{fo} = \frac{-U+2U'}{4}\left[\left(\Pi_{aa} + \Pi_{\tilde{a}\tilde{a}}\right) + 4\Pi_{ff} + 2\left(\Pi_{ab} + \Pi_{\tilde{a}\tilde{b}}\right)\right] \tag{2.10}$$

We recall that in our model $U = -2g$ and $U' = 2g$, i.e. $-U + 2U' = 6g > 0$. Then, at some critical g, the system becomes unstable against FO order.

2.3.1.2 Antiferro-orbital order

We now consider AFO order. The set of self-consistent equations for Δ_{afo} is presented in Fig. 2.3.

Like before, we have to introduce more general $q = (\pi, \pi)$ order parameters

$$\begin{aligned}
&\Delta_{afo}^{a\tilde{b}}\cos^2\theta, \quad \bar{\Delta}_{afo}^{a\tilde{b}}\sin^2\theta, \quad \Delta_{afo}^{\tilde{a}b}\cos^2\theta, \quad \bar{\Delta}_{afo}^{\tilde{a}b}\sin^2\theta, \\
&\Delta_{afo}^{a\tilde{a}}\cos\theta\sin\theta, \quad \Delta_{afo}^{f_1 f_2}.
\end{aligned}$$

Again, $s-$wave and $d-$wave harmonics decouple. One can straightforwardly verify that only

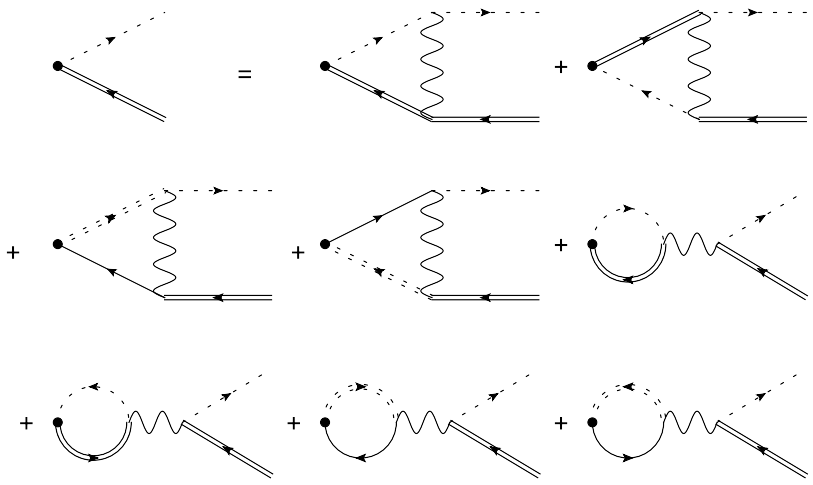

Figure 2.3: Diagrams for the renormalization of the components of antiferro-orbital order parameter. Only diagrams for $\Delta^{\tilde{a}b}_{afo}$ are shown; the diagrams for the renormalization of $\Delta^{a\tilde{b}}_{afo}$ are obtained in a similar way. The notations are the same as in Fig. 2.2.

the first four parameters contribute to $d_{x^2-y^2}$ harmonics, and, moreover, in this channel

$$\Delta^{a\tilde{b}}_{afo} = \bar{\Delta}^{a\tilde{b}}_{afo} = \Delta_{1a},$$
$$\Delta^{\tilde{a}b}_{afo} = \bar{\Delta}^{\tilde{a}b}_{afo} = \Delta_{2a}.$$

The coupled equations on Δ_{1a} and Δ_{2a} are

$$\Delta_{1a} = \left[-\left(U-2U'\right)\Delta_{1a} + \left(U-2U'\right)\Delta_{2a}\right]\Pi_{a\tilde{b}}$$
$$\Delta_{2a} = -\left[-\left(U-2U'\right)\Delta_{1a} + \left(U-2U'\right)\Delta_{2a}\right]\Pi_{a\tilde{b}}$$

where we used that $\Pi_{a\tilde{b}} = \Pi_{\tilde{a}b}$. Like before, we defined polarization operator such that $\Pi_{a\tilde{b}} > 0$. For $U < 0$ and $U' > 0$ the only positive eigenvalue is

$$\lambda_{afo} = 2\left(-U+2U'\right)\Pi_{a\tilde{b}} \tag{2.11}$$

The corresponding eigenfunction has $\Delta_{1a} = -\Delta_{2a} = \Delta_a$. Substituting into (2.6) we obtain $\Delta_{afo} = 8\Delta_a$. For $U = -2g$, $U' = 2g$, $\lambda_{afo} = 12g\Pi_{a\tilde{b}}$

We now compare λ_{fo} and λ_{afo}. The point for comparison is that for small hole pockets, i.e., for small ratios $E_{a,b;0}/W = \epsilon_0/W$ and $E_{\tilde{a},\tilde{b};0}/W = \tilde{\epsilon}/W$, polarization operators Π_{ab}, $\Pi_{\tilde{a}\tilde{b}}$, and $\Pi_{a\tilde{b}}$ are logarithmically enhanced as $\log W/\epsilon_0 \sim \log W/\tilde{\epsilon}_0$, because they are made

out of fermions which over wide momentum range have opposite signs of dispersion, i.e., a particle-hole bubble effectively behaves as a particle-particle bubble, up to an overall sign. As a result, each of these bubbles behaves as $\log W/\epsilon_0$. At the same time, Π_{aa} and Π_{ff} are ordinary zero-momentum polarization bubbles, and both are of order $1/W$. Without Π_{ab} and other cross-terms, λ_{afo} would vanish, while λ_{fo} would be positive, but of order g/W, i.e., there would be no instability at $g \ll W$, where weak coupling approach is justified. Because of cross-terms, the situation is quite different in two aspects. First, the instability occurs at $g \sim W/\log \frac{W}{\epsilon_0} \ll W$, where calculations are under control. Second, the prefactor for the logarithm is by a factor of two larger in λ_{afo} than in λ_{fo}, hence the leading orbital instability is actually towards the AFO order. That $\lambda_{afo} > \lambda_{fo}$ is consistent with QMC results [10]. QMC calculations show that susceptibility in both channels increases as g increases and, at a critical g_c, diverges in the AFO channel, while the susceptibility in the FO channel remains finite at g_c. The QMC study also found that AFO order develops only at filling when hole pockets are small but finite, and disappears at higher and smaller fillings. This is also consistent with our analysis because at larger electron filling electron pockets grow, and the range where a and $\tilde{b}$ dispersions have opposite sign shrinks, hence $\Pi_{a\tilde{b}}$ decreases. At large hole doping, ϵ_0 and $\bar{\epsilon}_0$ increase and $\Pi_{a\tilde{b}}$ again decreases, this time because logarithmic enhancement gets weaker.

2.3.2 Superconductivity

The same interaction Hamiltonian, Eq. (2.4), also gives rise to the SC instability, and it becomes an issue whether this instability develops before or after AFO order sets in.

The dominant contribution to SC at weak coupling, when T_c is small enough, comes from states immediately close to the Fermi surface, i.e., from a, $\tilde{a}$, f_1 and f_2 fermions. However, when T_c is higher, one needs to include the contributions to the pairing from b and $\tilde{b}$ fermions, i.e., particle-particle polarization bubbles Π_{bb}, $\Pi_{a,b}$ and other terms of the same type. In the analysis below we keep all contributions in the SC channel. The calculations are performed in the same way as before(Fig. 2.4), by introducing order parameters

$$\Delta_{SC}^{aa} \cos^2\theta, \quad \Delta_{SC}^{aa} \sin^2\theta, \quad \Delta_{SC}^{ab} \cos\theta \sin\theta \tag{2.12}$$

and so on, where $\Delta_{SC}^{aa} = \sum_k a_{k,\alpha} a_{k\beta} (i\sigma^y_{\alpha\beta})$, etc. Like before, we derive self-consistent equations on Δ_{SC}^{ij} in the ladder approximation and obtain eigenvalues. Only the U term contributes to the renormalization of the pairing vertex, U' term doesn't play a role. In total, there are 16 gap components (if we count Δ_{ab} and Δ_{ba} as separate variables), i.e., there

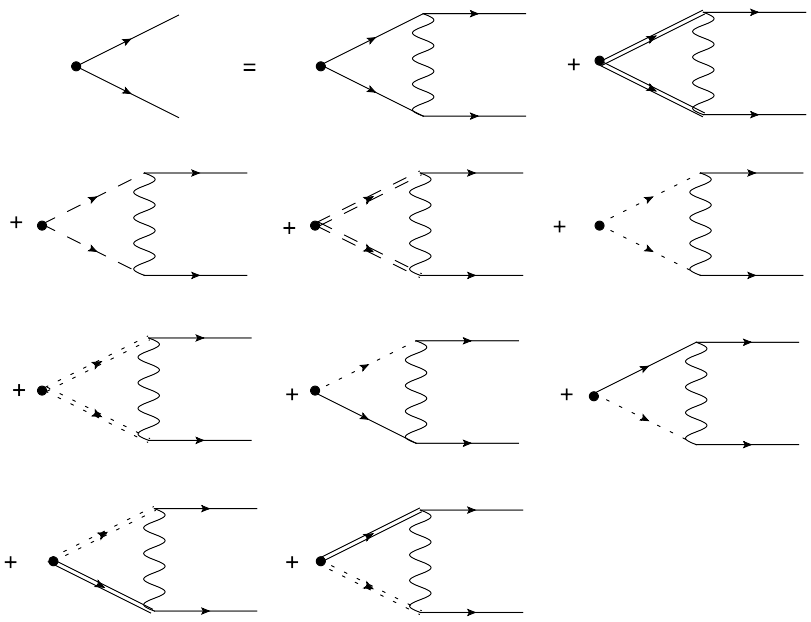

Figure 2.4: Diagrams for the renormalization of the components of pairing order parameter. Only diagrams for Δ_{SC}^{aa} are shown; the diagrams for the renormalization of other order parameters Δ_{SC}^{bb}, $\Delta_{SC}^{f_1 f_1}$, $\Delta_{SC}^{f_2 f_2}$, $\Delta_{SC}^{\tilde{a}\tilde{a}}$, $\Delta_{SC}^{\tilde{b}\tilde{b}}$, $\Delta_{SC}^{\tilde{a}\tilde{b}}$ and Δ_{SC}^{ab} are obtained in a similar way. The notations are the same as in Fig. 2.2.

are 16 coupled equations. By obvious reasons, the equations decouple between $s-$wave and $d-$wave channels. With our choice of variables in Eq. (2.12), $d-$wave component necessary has $d_{x^2-y^2}$ symmetry. [To analyze the coupling in d_{xy} channel one has to introduce different set of variables like $\Delta_{SC}^{aa} \sin\theta\cos\theta$, etc.]

The presence of large number of components normally implies that there exist non-zero eigenvalues in different subsets of $s-$wave and $d_{x^2-y^2}$ channels (e.g., s^{++} and s^{+-}), and one has to verify which sub-channel wins. However, we found that in in our case there is no such competition as eigenvalues are non-zero only in the s^{++} and $d_{x^2-y^2}$ channels. These two non-zero eigenvalues are

$$\lambda_{s^{++}} = -2U \left[\frac{\Pi_{pp}^{aa} + \Pi_{pp}^{\tilde{a}\tilde{a}} + 2\Pi_{pp}^{ff}}{4} + \frac{\Pi_{pp}^{bb} + \Pi_{pp}^{\tilde{b}\tilde{b}}}{4} \right]$$

$$\lambda_{d_{x^2-y^2}} = -U \left[\frac{\Pi_{pp}^{aa} + \Pi_{pp}^{\tilde{a}\tilde{a}} + 4\Pi_{pp}^{ff}}{4} + \frac{\Pi_{pp}^{bb} + \Pi_{pp}^{\tilde{b}\tilde{b}}}{4} + \frac{\Pi_{pp}^{ab} + \Pi_{pp}^{\tilde{a}\tilde{b}}}{2} \right] \qquad (2.13)$$

where Π_{pp}^{ij} are particle-particle susceptibilities made out of fermions from band i and j with momenta $\mathbf{k}$ and $-\mathbf{k}$, defined such that $\Pi_{pp}^{ij} > 0$. Note that cross-terms $\Delta_{SC}^{ab} \cos\theta \sin\theta$ only contribute to $d-$wave channel, and for this channel $\Delta_{SC}^{ab} = -\Delta_{SC}^{\tilde{a}\tilde{b}}$. We recall that $U = -2g$ for the model of Eq. (2.4). Then $\lambda_{s^{++}}$ and $\lambda_{d_{x^2-y^2}}$ are both positive, i.e., both channels are attractive. For small g, the pairing instability occurs at small T_c, and the largest contributions to λ in both channels comes from Π_{pp}^{aa}, $\Pi_{pp}^{\tilde{a}\tilde{a}}$, and Π_{pp}^{ff}, which scale as $\frac{1}{W}\log(\frac{W}{T})$. Other Π_{pp}^{ij} do not diverge at $T = 0$, however, because b and $\tilde{b}$ bands are flat over a wide range of momenta, and the band energies in this flat region are of order $\epsilon_0 \ll W$, Π_{pp}^{bb} and $\Pi_{pp}^{\tilde{b}\tilde{b}}$ both scale as $\frac{1}{\epsilon_0} \sim \frac{1}{W}\frac{W}{\epsilon_0} \gg \frac{1}{W}$. The other two polarization bubbles Π_{pp}^{ab} and $\Pi_{pp}^{\tilde{a}\tilde{b}} \sim \frac{1}{W}$, i.e., are much smaller. Keeping only $\frac{1}{W}\log(\frac{W}{T})$ terms, we find that $\lambda_{s^{++}} > \lambda_{d_{x^2-y^2}}$, i.e., the leading instability in the particle-particle channel is towards s^{++} state. The $d_{x^2-y^2}$ channel is attractive, but subleading to s^{++}. This result holds when we include Π_{pp}^{bb} and $\Pi_{pp}^{\tilde{b}\tilde{b}}$, because the prefactor for Π_{pp}^{bb} and $\Pi_{pp}^{\tilde{b}\tilde{b}}$ is larger in the s^{++} channel. Then, the attraction in the s^{++} channel is stronger than in $d_{x^2-y^2}$ channel, no matter what is T_c, as long as $T_c \ll W$.

2.3.3 Interplay between AFO order and s-wave SC, the role of RG

Comparing λ_{afo} and $\lambda_{s^{++}}$ we find that at the smallest g the system only develops an instability towards s^{++} SC at an exponentially small T_c. If the system is probed by varying g at a given $T \sim \epsilon_0$, the selection is less obvious because the prefactor $-2U + 4U'$ in the AFO channel (Eq. (2.11)) is larger than $-2U$ for $\lambda_{s^{++}}$ in (2.13), while the combination of the polarization operators is obviously larger in the SC channel. This uncertainty goes away once we include the renormalizations neglected in the ladder approximation. Specifically, if we apply parquet RG technique for multi-band superconductors [20], we find that inter-orbital repulsion $U' > 0$ gets renormalized in the particle-particle channel (but not in particle-hole channel) and flows to zero under RG. This is similar to McMillan-Tolmachev renormalization in conventional phonon superconductor [50]. As the consequence, the prefactor in λ_{afo} becomes the same $-2U$ as in $\lambda_{s^{++}}$. The polarization operators are larger in the SC channel, hence in the ladder approximation, but with running U and U', $s-$wave pairing instability has to develop first, i.e., at a smaller g than AFO order. This is consistent with the results of QMC analysis. Another result of RG is that U, and, hence, the couplings in both s^{++} and AFO channels get enhanced by the coupling to $(\pi, 0)/(0, \pi)$ magnetic fluctuations [20, 48]. This enhancement is the strongest in the doping range when both hole and electron pockets are small in size. Hence, the instability temperatures are maximized in this region. This

again agrees with QMC results. We caution, however, that using Eqs. (2.11) and (2.13) with the running couplings is an approximation not controlled by a small parameter. [11].

2.4 Summary

In this paper we analyzed instablities towards orbital order and superconductivity within the two-orbital model for FeSCs, which has been recently studied in detail by QMC. We used itinerant approach and argued that it is applicable because critical coupling g for orbital and superconducting instabilities is parameterically smaller than the bandwidth. We found that the leading instability in the orbital channel is towards AFO order with momentum (π, π), while the one in the pairing channel is towards s^{++} SC, while $d_{x^2-y^2}$ SC is close second. We argued that, as g increases at a fixed T, the system first develops s^{++} SC order and then, at a larger g, develops AFO order. The latter is confined to the range of fillings when hole and electron pockets are small in size. The same two orders and the same phase diagram has been recently detected in QMC studies. We view the agreement with unbiased QMC as the indication that orbital and superconducting orders in FeSCs can be properly accounted for within the itinerant scenario.

Chapter 3

Competing instabilities of a 4-pocket model for iron-based superconductors: application to FeSe

3.1 Introduction

The interplay and competition between different types of electronic order is at the focus of the research on iron based superconductors (FeSCs) [51, 53, 34, 52, 109]. In most FeSCs superconductivity (SC) emerges out of a stripe spin-density-wave (SDW) state upon either hole or electron doping, application of pressure, or by isovalent substitution of one pnictogen atom by the other (e.g., As by P). The SDW phase is often preceded by the nematic phase, in which the system breaks C_4 rotational symmetry down to C_2 but keeps spin-rotational symmetry intact.

The nematic phase has been extensively studied both experimentally and theoretically [55, 27, 26, 31, 25, 43, 56, 132, 58, 59, 60, 40, 61, 10, 62, 63, 64]. The manifestations of spontaneous C_4 symmetry breaking include the anisotropy of resistivity [65, 66, 67], spin susceptibility [68, 69, 70], and optical conductivity [71, 72], orthorhombic lattice distortion [73, 74], and unequal occupation of Fe d_{xz} and d_{yz} orbitals [75, 76]. The majority of researchers believe that nematicity is driven by electronic degrees of freedom rather than by the lattice. There is no agreement, however, on the mechanism of the nematic order. It can be a composite Ising-nematic magnetic order [129], preceding stripe SDW order, or a quantum-disordered spin state, which breaks C_4 symmetry [78] or a spontaneous orbital order [55, 27, 26, 25, 43, 58, 10]. The Ising-nematic scenario likely applies to Fe-pnictides, in which the nematic phase is located in a close proximity to a stripe SDW phase. However, the application of this scenario to Fe-chalcogenide FeSe is questionable because in FeSe at ambient pressure the nematic transition occurs at $T_s = 85$K, but there is no SDW transition down to $T = 0$. The Ising-nematic scenario, particularly when combined with the idea of a weak dispersion of spin excitations along one direction in momentum space [79], can still be the explanation because T_s and T_{SDW} do not have to be close to each other. However, NMR [80, 81] and neutron scattering [82] experiments have found that the magnetic correlation length does not show any notable enhancement around T_s, which would be generally expected in the Ising-nematic scenario. Substantial SDW fluctuations have been detected only at lower temperatures [83], or upon applying pressure [84], when the system eventually develops an SDW order.

The fact that in FeSe at ambient pressure nematic order emerges without magnetism fuelled speculations that in this system nematicity may be due to a spontaneous orbital ordering. The most natural C_4 symmetry-breaking orbital order is associated with unequal occupation of d_{xz} and d_{yz} orbitals. In FeSe, these two orbitals are the building blocks for the low-energy states near both hole and electron pockets. The electronic structure of FeSe

consists of two $\Gamma-$centered hole pockets and two electron pockets centered at $X = (\pi, 0)$ and $Y = (0, \pi)$ in the 1Fe Brillouin zone (BZ) (see Fig. 5.1). The $\Gamma-$centered hole pockets are made out of d_{xz} and d_{yz} orbitals. The electron pockets are made out of these two orbitals and the d_{xy} orbital. More precisely, the pocket near X is made out of d_{yz} and d_{xy} orbitals, and the one near Y is made out of d_{xz} and d_{xy} orbitals. Accordingly, one can introduce three C_4 breaking orbital order parameters. Two involve d_{xz} and d_{yz} orbitals: $\Gamma_{1,h} = \sum_k d^\dagger_{xz}(k)d_{xz}(k) - d^\dagger_{yz}(k)d_{yz}(k)$ and $\Gamma_{1,e} = \sum_k d^\dagger_{xz}(k+Y)d_{xz}(k+Y) - d^\dagger_{yz}(k+X)d_{yz}(k+X)$, and the third one, $\Gamma_{2,e} = \sum_k d^\dagger_{xy}(k+Y)d_{xy}(k+Y) - d^\dagger_{xy}(k+X)d_{xy}(k+X)$, describes unequal occupation of the d_{xy} orbital near X and Y electron pockets and induces an X/Y anisotropy of the hopping integral for the d_{xy} orbital [85]. Here and below the summation over k is restricted to small k.

All three order parameters, $\Gamma_{1,h}$, $\Gamma_{1,e}$, and $\Gamma_{2,e}$ belong to the same B_{1g} representation of the point group D_{4h} [45] and break the same C_4 symmetry. The order parameter $\Gamma_{1,h}$ gives rise to elliptical elongation of the two hole pockets and splits the two hole dispersions at the Γ point. The order parameters $\Gamma_{1,e}$ and $\Gamma_{2,e}$ change the shape of electron pockets and split the dispersions of d_{xz}/d_{yz} and d_{xy} orbitals between X and Y pockets.

Recent ARPES experiments [12, 87, 88, 86] analyzed relative signs and magnitudes of the three order parameters $\Gamma_{1,h}$, $\Gamma_{1,e}$, and $\Gamma_{2,e}$, and the results of these experiments place constraints on theoretical considerations. The ARPES data is taken in the 2-Iron Brillouin Zone (2FeBZ), which is the physical BZ, because Se atoms in FeSe are located above and below the Fe plane in a ches-type order. In the 2FeBZ, both electron pockets are located at the M point ($k_x = k_y = \pi$). Above T_s, d_{xz} and d_{yz} dispersions are degenerate at M, even in the presence of spin-orbit coupling [45]. A non-zero $\Gamma_{1,e}$ splits the two dispersions by $\pm\Gamma_{1,e}$. Similarly, the two d_{xy} dispersions from X and Y pockets are degenerate at the M point above T_s, but split in the nematic phase by $\pm\Gamma_{2,e}$. The authors of Refs. [[12]] reported that they detected the splitting of both, d_{xz}/d_{yz} and d^X_{xy}/d^Y_{xy}, bands at the M-point. Both splittings are found to be around 15meV, what implies that the magnitudes of $\Gamma_{1,e}$ and $\Gamma_{2,e}$ are nearly equal ($|\Gamma_{1,e}| \sim |\Gamma_{2,e}| \sim 7.5$ meV). These authors also reported that they detected a 20 meV spin-orbit induced splitting of d_{xz} and d_{yz} bands at the Γ-point above T_s, and that this splitting increases to 25 meV in the nematic phase. The full splitting at Γ is $\pm\sqrt{\Gamma^2_{so} + \Gamma^2_{1,h}}$ (Ref. [85]). Using this formula, one extracts from the data $|\Gamma_{so}| = 10$ meV and $|\Gamma_{1,h}| = 7.5$ meV. The outcome is that all three order parameters, $\Gamma_{1,h}$, $\Gamma_{1,e}$, and $\Gamma_{2,e}$ have about the same magnitude of 7.5 meV. Other ARPES groups [87, 88, 86] interpreted their data somewhat differently, and some reported larger $\Gamma_{1,e}$, and $\Gamma_{2,e}$. In a separate development, the authors of Ref. [89] argued, based on their ARPES results, that $\Gamma_{1,h}$ and

$\Gamma_{1,e}$ have opposite signs.

In this paper we analyze whether the near-equivalence of the magnitudes of $\Gamma_{1,h}$, $\Gamma_{1,e}$, and $\Gamma_{2,e}$ and the sign difference between $\Gamma_{1,h}$ and $\Gamma_{1,e}$ can be understood theoretically. In our theory, we obtain the ratios of the order parameters near T_s, when the magnitudes of all condensates are small. We do find the near-equivalence of $\Gamma_{1,e}$ and $\Gamma_{2,e}$ and the sign change between $\Gamma_{1,h}$, and $\Gamma_{1,e}$. The ratio of $\Gamma_{1,h}$ and $\Gamma_{1,e}$ comes out larger in our analysis than in the ARPES data, but we caution that our calculations do not include spin-orbit coupling, which by itself splits d_{xz} and d_{yz} orbitals at the Γ point.

Our analysis is build on recent parquet renormalization group (RG) studies of orbital order in FeSCs. In Ref. [11], Chubukov, Khodas, and Fernandes (CKF) analyzed the interplay between SDW, SC, and orbital order in two approximate 4-pocket models for FeSe. In both models the hole pockets were treated without an approximation, but the electron pockets were assumed to be made entirely out of d_{xz}/d_{yz} orbitals (model I), or entirely out of d_{xy} orbitals (model II). This was done to reduce the number of running RG couplings to 14, down from 30 in the full model (see below). For both models, CKF found that the leading instability upon lowering the temperature is towards an orbital order, the subleading one is towards s^{+-} superconductivity, and SDW order does not develop, despite that the SDW susceptibility is the largest at the beginning of the RG flow. This hierarchy of instabilities holds if the pockets are small enough and RG has a "space" to run, i.e., there is enough energy scales to integrate out.

CKF did find that the sign of $\Gamma_{1,h}$ is opposite to that of $\Gamma_{1,e}$, in agreement with the ARPES analysis in [89]. However, they could not explain the observed near-equivalence between $\Gamma_{1,e}$ and $\Gamma_{2,e}$ at the M point because, by construction, in the two approximate models studied by CKF, either $\Gamma_{2,e} = 0$ (model I) or $\Gamma_{1,e} = 0$ (model II).

In this paper we extend the analysis of CKF to the full 4-pocket, 3-orbital model of FeSCs. The goal is two-fold: (1) verify whether the hierarchy of instabilities remains the same as in the approximate models studied by CKF, and (2) see whether the relations between $\Gamma_{1,e}, \Gamma_{1,h}$, and $\Gamma_{2,e}$ reproduce the ones extracted from the ARPES measurements. The 4-pocket, 3-orbital low-energy model has been introduced by Cvetkovic and Vafek in Ref. [45]. These authors have shown that the number of different symmetry-allowed interactions between low-energy fermions is equal to 30. The initial values of all 30 couplings are expressed via local Hubbard and Hund interactions U, U', J, J'. But the couplings evolve differently as one progressively integrates out fermions with higher energies, i.e., in the process of the RG flow the system self-generates longer-range interactions. We derive and analyze, both analytically and numerically, the set of 30 coupled parquet RG equations,

which describe the flow of the couplings. We show that the flow is towards universal fixed trajectories, along which the ratios between the couplings tend to fixed values. We then derive another set of RG equations for the susceptibilities in different channels (SDW, SC, orbital) and solve them using the running couplings as inputs [116, 120, 92, 118, 119]. We identify the channel in which the system first develops an instability as the one where the susceptibility diverges at the highest T, and, if critical T are the same in several channels, as the one where the divergent susceptibility has the largest exponent.

We show that two of the universal fixed trajectories are stable, and that they are separated by several unstable fixed trajectories. [The system approaches a stable fixed trajectory from all directions within its basin of attraction, it approaches an unstable fixed trajectory from some directions and moves away from it along other directions]. We argue that on a stable fixed trajectory the system behavior effectively reduces to that of one of the two models considered by CKF. Specifically, on one stable trajectory, interactions involving d_{xy} components of the electron pockets vanish compared to the interactions involving d_{xz} (or d_{yz}) components (same as in model I of CKF), while along the other stable fixed trajectory interactions involving d_{xz} (or d_{yz}) orbital components vanish compared to the interactions involving d_{xy} components (model II of CKF). Like we said, each of these two models yields the same hierarchy of orderings (orbital order, then SC, but no SDW, if the pockets are small enough). However, neither model I, nor model II, reproduces the observed near-equivalence of $\Gamma_{1,e}$ and $\Gamma_{2,e}$.

We next analyze the unstable fixed trajectories. In general, these trajectories are irrelevant for the RG analysis, because the RG flow moves the system away from these trajectories towards the stable ones. In our case, however, the system behavior is more nuanced. Namely, we show that there are several truly unstable fixed trajectories and one "weakly unstable" fixed trajectory with just one direction, along which the system eventually moves away from it (i.e., the stability analysis yields one positive exponent). This weakly unstable fixed trajectory is located in between the two stable fixed trajectories. We argue that under RG the system first flows away from truly unstable trajectories towards the weakly unstable trajectory, and then flows towards one of the two stable fixed trajectories. However, the positive exponent, which characterizes how fast the system moves away from this trajectory, is quite small. This implies that the weakly unstable fixed trajectory behaves as a stable one nearly up to the very end of the RG flow, when the hierarchy of susceptibilities is already established. We analyze the system behavior on this weakly unstable fixed trajectory and obtain the same sequence of orderings as the two stable trajectories, i.e., the leading instability is towards C_4-breaking orbital order, the subleading is towards s^{+-} SC, and SDW

order does not develop. In distinction to the stable fixed trajectories, however, now the interactions involving $d_{xz}(d_{yz})$ and d_{xy} orbital components on electron pockets are of the same order. Therefore $\Gamma_{1,h}$, $\Gamma_{1,e}$, and $\Gamma_{2,e}$ all become non-zero once the orbital order sets in. We solve the set of coupled equations for $\Gamma_{1,h}, \Gamma_{1,e}$, and $\Gamma_{2,e}$ on the weakly unstable fixed trajectory and find that the magnitudes of $\Gamma_{1,e}$, and $\Gamma_{2,e}$ are nearly equal, and the signs of $\Gamma_{1,h}$ and $\Gamma_{1,e}$ are opposite. This is fully consistent with the ARPES data [12, 87, 89]. We view the agreement as an indication that the parquet RG analysis of the full 4-pocket, 3-orbital model is capable to reproduce not only the sequence of phase transitions in FeSe upon lowering of temperature, but also the ARPES results for the magnitudes and signs of the nematic orbital order parameters. At the same time, our analysis yields a larger ratio of $\Gamma_{1,h}/\Gamma_{1,e}$ than in the data. This may reveal a limited validity of the RG analysis. But the discrepancy may also be due to the fact that, according to ARPES [12], the largest splitting of d_{xz} and d_{yz} orbitals on hole pockets comes from spin-orbit coupling, which we did not include into the analysis. We conjecture that the feedback from spin-orbit-induced band splitting reduces the value of the orbital order parameter on hole pockets compared to our result, which, we reiterate, is obtained neglecting spin-orbit interaction.

The paper is organized as follows. In Sec. 3.2 we discuss the generic 4-band, 3-orbital model for FeSCs. We first present the kinetic energy and then introduce the 30 different C_4-symmetric interactions between low-energy fermions. We argue that the structure of the interaction Hamiltonian remains invariant under RG, but the values of the couplings flow. In Sec. 3.3 we derive and solve the set of 30 coupled differential RG equations for the flow of the couplings. In Sec. 3.3.2 we analyze the fixed trajectories resulting from the solution of the RG equations. Because the system behavior along the two stable fixed trajectories is the same as in the two approximate models studied by CKF, we do not re-derive the results here and instead focus on the system behavior along the weakly unstable fixed trajectory. In Sec. 3.4 we discuss the RG flow of the susceptibilities in different channels and analyze the hierarchy of the instabilities on the weakly unstable fixed trajectory. In Sec. 3.5 we discuss the interplay between the three orbital order parameters $\Gamma_{1,h}, \Gamma_{1,e}$, and $\Gamma_{2,e}$ and compare our results with the ARPES data. We present our conclusions in Sec. 3.6. Technical details of the RG analysis are presented in the supplementary material.

In the complimentary work [15], we applied parquet RG to 5-band, 3-orbital model with an additional d_{xy} pocket at (π, π) in the 1Fe BZ (at Γ in the 2Fe BZ). We argued that in some range of input parameters the fifth pocket does not affect the low-energy behavior, and remains the same as in the 4-pocket, 3-orbital model.

3.2 The Model

We consider a four-band model with two hole pockets at the center of the 1FeBZ and two electron pockets at the zone edges, and keep the actual orbital content of low-energy excitations near each pocket (See Fig. 5.1). Each of the two hole pockets have orbital character alternating between d_{xz} and d_{yz}, with negligible contribution from d_{xy} and other orbitals. Of the two symmetry-related electron pockets, one is constructed from d_{xz} and d_{xy} orbitals, the other from d_{yz} and d_{xy} orbitals, again with negligible contribution from other orbitals. Below we first consider the effective model for the low-energy band structure and then construct the interactions, consistent with the tetragonal crystal symmetry above the nematic transition.

3.2.1 Effective model of the band structure

We follow the approach by Cvetkovic and Vafek, [45] who used Luttinger's method of invariants (also known as $k{\cdot}p$ theory) and symmetry constraints to construct the effective low energy model of the band structure. We neglect spin-orbit coupling, assuming that is does not affect the RG flow at energies above E_F, and perform calculations in the unfolded 1FeBZ. Because we are interested in the low-energy theory, fermions near different pockets are treated as different species. Namely, we introduce a 6-component spinor $\psi = (\psi_1, \ldots, \psi_6)$ (See Fig. 5.1). The components $\psi_1(\boldsymbol{k})$ and $\psi_2(\boldsymbol{k})$ are the Bloch states of pure d_{xz} and d_{xy} orbital character, respectively, with momentum near Y (spin indices are omitted for clarity). The components $\psi_3(\boldsymbol{k})$ and $\psi_4(\boldsymbol{k})$ are the Bloch states of pure d_{yz} and d_{xy} orbital character near X, and $\psi_5(\boldsymbol{k})$ and $\psi_6(\boldsymbol{k})$ are the Bloch states of pure d_{yz} and d_{xz} orbital character near Γ. We list pocket and orbital "affiliations" of ψ_i in Table 5.1 (see also Fig.5.1). The

ψ_i	Pocket	Orbital
ψ_1	Y	d_{xz}
ψ_2	Y	d_{xy}
ψ_3	X	d_{yz}
ψ_4	X	d_{xy}
ψ_5	Γ	d_{yz}
ψ_6	Γ	d_{xz}

Table 3.1: Affiliation of ψ_i with a pocket and an orbital.

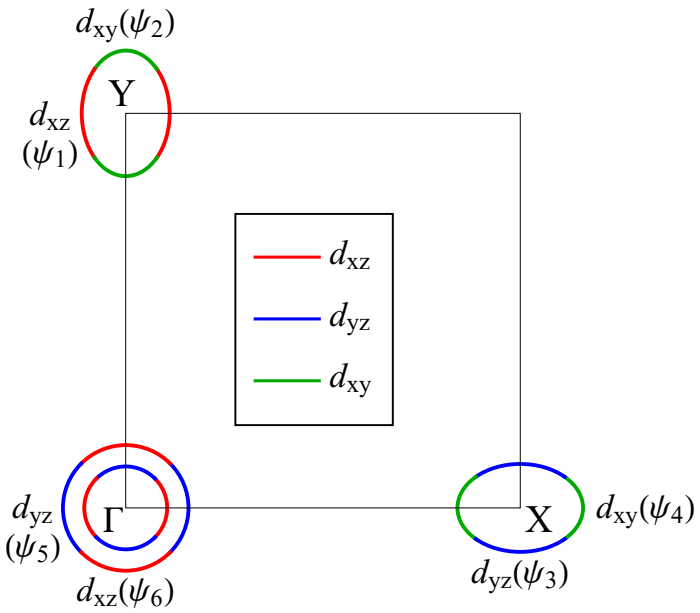

Figure 3.1: The Fermi surfaces in 1Fe BZ with the orbital content of the interactions. The six ψ fields are introduced in the text.

non-interacting part of the effective Hamiltonian is expressed as

$$H_0 = \sum_{\boldsymbol{k},\sigma} \psi^\dagger_\sigma(\boldsymbol{k}) \begin{pmatrix} h_Y(\boldsymbol{k}) & & \\ & h_X(\boldsymbol{k}) & \\ & & h_\Gamma(\boldsymbol{k}) \end{pmatrix} \psi_\sigma(\boldsymbol{k})\,, \tag{3.1}$$

In Eq. (3.1) and in what follows all momenta $\boldsymbol{k}$ are counted relative to the respective high symmetry points Γ, X, or Y. The d_{xz} dispersion at Y and the d_{yz} dispersion at X are doubly degenerate, and the d_{xy} dispersions at X and Y are also degenerate (see left panel in Fig. 3.16). These two degeneracies can be traced to the fact that chalcogen atoms in Fe-chalcogenides (Se in FeSe) or pnictogen atoms in Fe-pnictides are located above or below the Fe plane in chess-like order. In group theory language, this "up-down" location of chalcogen/pnictogen atoms implies that the symmetry group P4/nmm contains a glide plain symmetry element. The corresponding symmetry operation is a mirror reflection about the iron plane, followed by a translation by one lattice side along X or Y directions in the 1FeBZ or, equivalently, along the half of the unit cell diagonal in the actual 2FeBZ (see e.g., Ref. [45]). The symmetry group P4/nmm containing this glide plain symmetry is a nonsymmorphic group and therefore all physical irreducible representations are two-

dimensional at M point (X and Y point in 1FeBZ map to M point in 2FeBZ; see left panel of Fig. 3.15), implying any states are doubly degenerate at M point. This is reflected in the expressions for h_X and h_Y in Eq. (3.1). We have

$$h_{Y,X}(\boldsymbol{k}) = \begin{pmatrix} \epsilon_1 + \frac{k^2}{2m_1} \pm a_1(k_y^2 - k_x^2) & -iv_\pm(k) \\ iv_\pm(k) & \epsilon_2 + \frac{k^2}{2m_2} \pm a_2(k_y^2 - k_x^2) \end{pmatrix} \tag{3.2}$$

where the upper sign is for the Y pocket and the lower one is for the X pocket, $v_+(k) = v(2k_x) + O(k^3)$, $v_-(k) = v(-2k_y) + O(k^3)$, and $v, \epsilon_{1,2}$, $a_{1,2}$, and $m_{1,2}$ are parameters, which can be determined by fitting the band structure to ARPES data. The two pockets are interchangeable under a 90° rotation, $h_X(k_x, k_y) = h_Y^*(-k_y, k_x)$.

The hole pockets are described by the effective Hamiltonian

$$h_\Gamma(\boldsymbol{k}) = \begin{pmatrix} \epsilon_3 - \frac{k^2}{2m_3} + b(k_y^2 - k_x^2) & 2ck_xk_y \\ 2ck_xk_y & \epsilon_3 - \frac{k^2}{2m_3} - b(k_y^2 - k_x^2) \end{pmatrix}. \tag{3.3}$$

The parameters ϵ_3, m_3, b and c are again determined by fitting the band structure to ARPES data. Note that these parameters generally differ from the ones obtained by taking tight-binding LDA dispersion and expanding it near Γ, X, and Y points, as Eqs. (5.5) and (5.1) include regular self-energy corrections coming from high-energy fermions.

The band dispersions are obtained by diagonalizing the effective Hamiltonian Eq. (3.1). The result is

$$\begin{aligned} H_0 = \sum_{k,\sigma} [&\epsilon_c(k) c_{k\sigma}^\dagger c_{k\sigma} + \epsilon_d(k) d_{k\sigma}^\dagger d_{k\sigma} \\ &+ \epsilon_{f_1}(k) f_{1,k\sigma}^\dagger f_{1,k\sigma} + \epsilon_{f_2}(k) f_{2,k\sigma}^\dagger f_{2,k\sigma}] \\ &+ \epsilon_{g_1}(k) g_{1,k\sigma}^\dagger g_{1,k\sigma} + \epsilon_{g_2}(k) g_{2,k\sigma}^\dagger g_{2,k\sigma}] \end{aligned} \tag{3.4}$$

The dispersions are

$$\begin{aligned} \epsilon_c(k) &= \epsilon_3 - \frac{k^2}{2m_3} + \sqrt{b^2 \left(k_x^2 - k_y^2\right)^2 + 4c^2 k_x^2 k_y^2} \\ \epsilon_d(k) &= \epsilon_3 - \frac{k^2}{2m_3} - \sqrt{b^2 \left(k_x^2 - k_y^2\right)^2 + 4c^2 k_x^2 k_y^2} \\ \epsilon_{f_1}(k) &= \frac{\epsilon_{1,Y} + \epsilon_{2,Y}}{2} + \sqrt{\left(\frac{\epsilon_{1,Y} - \epsilon_{2,Y}}{2}\right)^2 + 4v^2 k_x^2} \\ \epsilon_{g_1}(k) &= \frac{\epsilon_{1,Y} + \epsilon_{2,Y}}{2} - \sqrt{\left(\frac{\epsilon_{1,Y} - \epsilon_{2,Y}}{2}\right)^2 + 4v^2 k_x^2} \end{aligned}$$

$$\epsilon_{f_2}(k) = \frac{\epsilon_{1,X} + \epsilon_{2,X}}{2} + \sqrt{\left(\frac{\epsilon_{1,X} - \epsilon_{2,X}}{2}\right)^2 + 4v^2k_y^2}$$
$$\epsilon_{g_2}(k) = \frac{\epsilon_{1,X} + \epsilon_{2,X}}{2} - \sqrt{\left(\frac{\epsilon_{1,X} - \epsilon_{2,X}}{2}\right)^2 + 4v^2k_y^2} \tag{3.5}$$

where

$$\epsilon_{1,Y(X)} = \epsilon_1 + \frac{k^2}{2m_1} \pm a_1(k_y^2 - k_x^2)$$
$$\epsilon_{2,Y(X)} = \epsilon_2 + \frac{k^2}{2m_2} \pm a_2(k_y^2 - k_x^2) \tag{3.6}$$

(upper sign for Y, lower for X). The transformation from orbital basis to band basis is a generalized rotation,

$$\begin{pmatrix}\psi_1(\boldsymbol{k})\\ \psi_2(\boldsymbol{k})\end{pmatrix} = \begin{pmatrix}\cos\phi_{e,\boldsymbol{k}} & -i\sin\phi_{e,\boldsymbol{k}}\\ -i\sin\phi_{e,\boldsymbol{k}} & \cos\phi_{e,\boldsymbol{k}}\end{pmatrix}\begin{pmatrix}f_{1,\boldsymbol{k}}\\ g_{1,\boldsymbol{k}}\end{pmatrix} \tag{3.7}$$
$$\begin{pmatrix}\psi_3(\boldsymbol{k})\\ \psi_4(\boldsymbol{k})\end{pmatrix} = \begin{pmatrix}\cos\phi'_{e,\boldsymbol{k}} & -i\sin\phi'_{e,\boldsymbol{k}}\\ -i\sin\phi'_{e,\boldsymbol{k}} & \cos\phi'_{e,\boldsymbol{k}}\end{pmatrix}\begin{pmatrix}f_{2,\boldsymbol{k}}\\ g_{2,\boldsymbol{k}}\end{pmatrix} \tag{3.8}$$
$$\begin{pmatrix}\psi_5(\boldsymbol{k})\\ \psi_6(\boldsymbol{k})\end{pmatrix} = \begin{pmatrix}\cos\phi_{h,\boldsymbol{k}} & \sin\phi_{h,\boldsymbol{k}}\\ -\sin\phi_{h,\boldsymbol{k}} & \cos\phi_{h,\boldsymbol{k}}\end{pmatrix}\begin{pmatrix}c_{\boldsymbol{k}}\\ d_{\boldsymbol{k}}\end{pmatrix} \tag{3.9}$$

The rotation angles $\phi_{e,\boldsymbol{k}}$, $\phi'_{e,\boldsymbol{k}}$ and $\phi_{h,\boldsymbol{k}}$ depend on the parameters in h_X, h_Y, and h_Γ as

$$\tan 2\phi_{e,\boldsymbol{k}} = \frac{-4vk_x}{\epsilon_{1,Y} - \epsilon_{2,Y}}$$
$$\tan 2\phi'_{e,\boldsymbol{k}} = \frac{4vk_y}{\epsilon_{1,X} - \epsilon_{2,X}}$$
$$\tan 2\phi_{h,\boldsymbol{k}} = \frac{2ck_xk_y}{b(k_x^2 - k_y^2)} \tag{3.10}$$

Fermions labeled by f_1 and f_2 cross the Fermi level and form the electron pockets near Y and X, respectively. Fermions labeled by c and d form the two hole pockets near Γ. We call these fermions low-energy excitations. Fermions labeled by g_1 and g_2 are gapped and do not cross the Fermi level. In principle, $g_{1,2}$ fermions have to be included into the

parquet RG analysis as the gap in their excitation spectrum is of order E_F, which is the lower edge of parquet RG analysis. To avoid dealing with too many couplings, we assume that parameters are such that the gap in the spectra of g_1 and g_2 fermions is numerically much larger than E_F and treat these fermions as high-energy, in which case they are not subjects of RG.

We make two additional assumptions to simplify the evaluation of the integrals below. First, we assume that the hole pockets are circular rather than just C_4-symmetric. This is the case when $c = b$ in Eq. (5.1). For circular hole pockets

$$\epsilon_{c,d}(\boldsymbol{k}) = \mu_h - \frac{k^2}{2m_{c,d}}, \tag{3.11}$$

where $\mu_h = \epsilon_3$, $m_c = m_3(1 - 2m_3 b), m_d = m_3(1 + 2m_3 b)$, and the rotation angle $\phi_{h,\boldsymbol{k}}$ in (3.9) coincides with the angle θ_h between $\boldsymbol{k}$ and X axis along the hole Fermi surfaces. Second, on electron pockets we set $\cos\phi_{e,k} = A_0 \cos\theta_e$, $\sin\phi_{e,k} = \sqrt{1 - A_0^2 \cos^2\theta_e}$, and $\cos\phi'_{e,k} = -A_0 \sin\theta_e$, $\sin\phi'_{e,k} = \sqrt{1 - A_0^2 \sin^2\theta_e}$, where θ_e is the angle between $\boldsymbol{k}$ and X direction on both electron Fermi surfaces and $1/\sqrt{2} < A_0 < 1$. This parametrization is indeed an approximation, but it is consistent with symmetry, and we verified numerically (see Fig. 3.2) that it matches quite accurately the actual $\phi_{e,\boldsymbol{k}}$ and $\phi'_{e,\boldsymbol{k}}$ from Eq. (3.10), at least for the parameters of the tight-binding dispersion listed in Ref. [45]. The condition $A_0 > 1/\sqrt{2}$ follows from the fact that $\epsilon_{1,Y(X)}$ and $\epsilon_{2,Y(X)}$ must cross at some value of θ_e to ensure that over some range along each of the electron pockets the largest spectral weight comes from the $d_{xz}(d_{yz})$ orbital, while over the rest of the pockets the largest spectral weight comes from d_{xy} orbital. (A larger value of A_0 would mean a larger total weight of the $d_{xz}(d_{yz})$ orbital on an electron pocket). These two approximations simplify the evaluation of angular integrals later in the paper, but they do not affect the structure of RG equations and the interplay between susceptibilities in different channels. Expanding the dispersions of f_1 and f_2 fermions in Eq. (3.5) in powers of momenta, we find that electron pockets are elliptical, and the dispersions near these pockets are

$$\epsilon_{f_1,f_2}(\boldsymbol{k}) = \frac{k_x^2}{2m_{x,y}} + \frac{k_y^2}{2m_{y,x}} - \mu_e. \tag{3.12}$$

The parameters $m_{x,y}$ and μ_e are determined by Eqn. (3.5).

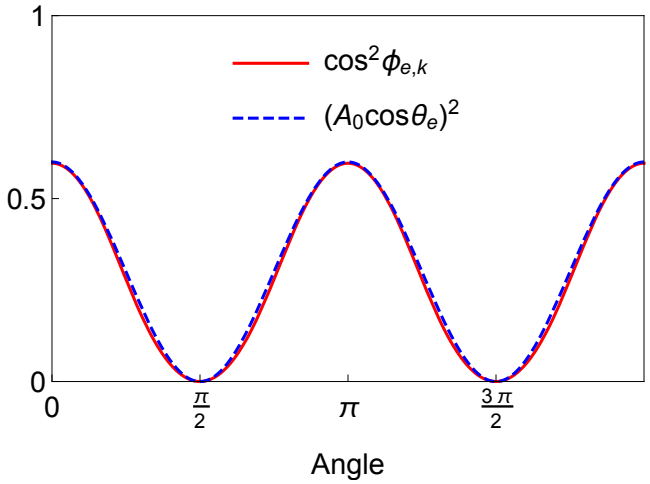

Figure 3.2: Approximation for the transformation matrix between orbital and band basis. Solid line – the actual $\cos^2\phi_{e,k}$ from Eq. (3.10). Dashed line – $(A_0\cos\theta_e)^2$, where θ_e is the angle along an electron pocket.

3.2.2 The interactions

We now move to the interaction part of the Hamiltonian. We can either derive the 4-fermion part of the Hamiltonian by using symmetry arguments, or just depart from the model with local Hubbard-Hund interactions. In the notations of Ref. [19], we have

$$\begin{aligned} H_{int} =& \frac{U}{2}\sum_{i,\mu} n_{i,\mu}n_{i,\mu} + \frac{U'}{2}\sum_{i,\mu\neq\mu'} n_{i\mu}n_{i\mu'} \\ &+ \frac{J}{2}\sum_{i,\mu'\neq\mu}\sum_{\sigma\sigma'} \psi^\dagger_{i\mu\sigma}\psi^\dagger_{i\mu'\sigma'}\psi_{i\mu\sigma'}\psi_{i\mu'\sigma} + \\ &+ \frac{J'}{2}\sum_{i,\mu'\neq\mu} \psi^\dagger_{i\mu\sigma}\psi^\dagger_{i\mu\sigma'}\psi_{i\mu'\sigma'}\psi_{i\mu'\sigma}\,. \end{aligned} \tag{3.13}$$

Here $\psi^\dagger_{i\mu\sigma}$ creates an electron on iron site $\boldsymbol{R}_i$, in orbital state μ, and in spin state σ. The operator $n_{i,\mu} = \psi^\dagger_{i,\mu}\psi_{i,\mu}$ is the density operator at an orbital μ at site i. U and U' are Hubbard intra-orbital and inter-orbital density interactions, J is the Hund's exchange coupling, and J' is the amplitude of the inter-orbital pair hopping. The Hamiltonian H_{int} is invariant under SU(2) spin rotations.

The relation between the local operators, $\psi_{i\mu\sigma}$ and orbital operators $\psi_{a\sigma}(\boldsymbol{k})$ near Γ, X,

and Y is

$$\begin{aligned}
\psi_{i,xz,\sigma} &= \frac{1}{\sqrt{N}} \sum_{\boldsymbol{k}} e^{i\boldsymbol{k}\boldsymbol{R}_i} \big[\psi_{1\sigma}(\boldsymbol{k}) e^{i\boldsymbol{Q}_y \boldsymbol{R}_i} + \psi_{6\sigma}(\boldsymbol{k})\big], \\
\psi_{i,yz,\sigma} &= \frac{1}{\sqrt{N}} \sum_{\boldsymbol{k}} e^{i\boldsymbol{k}\boldsymbol{R}_i} \big[\psi_{3\sigma}(\boldsymbol{k}) e^{i\boldsymbol{Q}_x \boldsymbol{R}_i} + \psi_{5\sigma}(\boldsymbol{k})\big], \\
\psi_{i,xy,\sigma} &= \frac{1}{\sqrt{N}} \sum_{\boldsymbol{k}} e^{i\boldsymbol{k}\boldsymbol{R}_i} \big[\psi_{2\sigma}(\boldsymbol{k}) e^{i\boldsymbol{Q}_y \boldsymbol{R}_i} + \psi_{4\sigma}(\boldsymbol{k}) e^{i\boldsymbol{Q}_x \boldsymbol{R}_i}\big].
\end{aligned} \tag{3.14}$$

Substituting Eq. (3.14) in Eq. (3.13), we obtain the interaction Hamiltonian in the orbital representation:

$$\begin{aligned}
&H_{int} \\
=&U_1 \sum{}' \left[\psi^\dagger_{1\sigma}\psi_{1\sigma}\psi^\dagger_{6\sigma'}\psi_{6\sigma'} + \psi^\dagger_{3\sigma}\psi_{3\sigma}\psi^\dagger_{5\sigma'}\psi_{5\sigma'}\right] + \bar{U}_1 \sum{}' \left[\psi^\dagger_{1\sigma}\psi_{1\sigma}\psi^\dagger_{5\sigma'}\psi_{5\sigma'} + \psi^\dagger_{3\sigma}\psi_{3\sigma}\psi^\dagger_{6\sigma'}\psi_{6\sigma'}\right] \\
+&\tilde{U}_1 \sum{}' \left[\psi^\dagger_{2\sigma}\psi_{2\sigma}\psi^\dagger_{6\sigma'}\psi_{6\sigma'} + \psi^\dagger_{4\sigma}\psi_{4\sigma}\psi^\dagger_{5\sigma'}\psi_{5\sigma'}\right] + \tilde{\bar{U}}_1 \sum{}' \left[\psi^\dagger_{4\sigma}\psi_{4\sigma}\psi^\dagger_{6\sigma'}\psi_{6\sigma'} + \psi^\dagger_{2\sigma}\psi_{2\sigma}\psi^\dagger_{5\sigma'}\psi_{5\sigma'}\right] \\
+&U_2 \sum{}' \left[\psi^\dagger_{1\sigma}\psi_{6\sigma}\psi^\dagger_{6\sigma'}\psi_{1\sigma'} + \psi^\dagger_{3\sigma}\psi_{5\sigma}\psi^\dagger_{5\sigma'}\psi_{3\sigma'}\right] + \bar{U}_2 \sum{}' \left[\psi^\dagger_{1\sigma}\psi_{5\sigma}\psi^\dagger_{5\sigma'}\psi_{1\sigma'} + \psi^\dagger_{3\sigma}\psi_{6\sigma}\psi^\dagger_{6\sigma'}\psi_{3\sigma'}\right] \\
+&\tilde{U}_2 \sum{}' \left[\psi^\dagger_{2\sigma}\psi_{6\sigma}\psi^\dagger_{6\sigma'}\psi_{2\sigma'} + \psi^\dagger_{4\sigma}\psi_{5\sigma}\psi^\dagger_{5\sigma'}\psi_{4\sigma'}\right] + \tilde{\bar{U}}_2 \sum{}' \left[\psi^\dagger_{2\sigma}\psi_{5\sigma}\psi^\dagger_{5\sigma'}\psi_{2\sigma'} + \psi^\dagger_{4\sigma}\psi_{6\sigma}\psi^\dagger_{6\sigma'}\psi_{4\sigma'}\right] \\
+&\frac{U_3}{2} \sum{}' \left[\psi^\dagger_{1\sigma}\psi_{6\sigma}\psi^\dagger_{1\sigma'}\psi_{6\sigma'} + \psi^\dagger_{3\sigma}\psi_{5\sigma}\psi^\dagger_{3\sigma'}\psi_{5\sigma'} + h.c.\right] \\
+&\frac{\bar{U}_3}{2} \sum{}' \left[\psi^\dagger_{1\sigma}\psi_{5\sigma}\psi^\dagger_{1\sigma'}\psi_{5\sigma'} + \psi^\dagger_{3\sigma}\psi_{6\sigma}\psi^\dagger_{3\sigma'}\psi_{6\sigma'} + h.c.\right] \\
+&\frac{\tilde{U}_3}{2} \sum{}' \left[\psi^\dagger_{2\sigma}\psi_{6\sigma}\psi^\dagger_{2\sigma'}\psi_{6\sigma'} + \psi^\dagger_{4\sigma}\psi_{5\sigma}\psi^\dagger_{4\sigma'}\psi_{5\sigma'} + h.c.\right] \\
+&\frac{\tilde{\bar{U}}_3}{2} \sum{}' \left[\psi^\dagger_{2\sigma}\psi_{5\sigma}\psi^\dagger_{2\sigma'}\psi_{5\sigma'} + \psi^\dagger_{4\sigma}\psi_{6\sigma}\psi^\dagger_{4\sigma'}\psi_{6\sigma'} + h.c.\right] \\
+&\frac{U_4}{2} \sum{}' \left[\psi^\dagger_{5\sigma}\psi_{5\sigma}\psi^\dagger_{5\sigma'}\psi_{5\sigma'} + \psi^\dagger_{6\sigma}\psi_{6\sigma}\psi^\dagger_{6\sigma'}\psi_{6\sigma'}\right] + \frac{\bar{U}_4}{2} \sum{}' \left[\psi^\dagger_{5\sigma}\psi_{6\sigma}\psi^\dagger_{5\sigma'}\psi_{6\sigma'} + \psi^\dagger_{6\sigma}\psi_{5\sigma}\psi^\dagger_{6\sigma'}\psi_{5\sigma'}\right] \\
+&\tilde{U}_4 \sum{}' \psi^\dagger_{5\sigma}\psi_{5\sigma}\psi^\dagger_{6\sigma'}\psi_{6\sigma'} + \tilde{\bar{U}}_4 \sum{}' \psi^\dagger_{5\sigma}\psi_{6\sigma}\psi^\dagger_{6\sigma'}\psi_{5\sigma'} \\
+&\frac{U_5}{2} \sum{}' \left[\psi^\dagger_{1\sigma}\psi_{1\sigma}\psi^\dagger_{1\sigma'}\psi_{1\sigma'} + \psi^\dagger_{3\sigma}\psi_{3\sigma}\psi^\dagger_{3\sigma'}\psi_{3\sigma'}\right] \\
+&\frac{\bar{U}_5}{2} \sum{}' \left[\psi^\dagger_{1\sigma}\psi_{3\sigma}\psi^\dagger_{1\sigma'}\psi_{3\sigma'} + h.c.\right] + \tilde{U}_5 \sum{}' \psi^\dagger_{1\sigma}\psi_{1\sigma}\psi^\dagger_{3\sigma'}\psi_{3\sigma'} + \tilde{\bar{U}}_5 \sum{}' \psi^\dagger_{1\sigma}\psi_{3\sigma}\psi^\dagger_{3\sigma'}\psi_{1\sigma'} \\
+&\frac{U_6}{2} \sum{}' \left[\psi^\dagger_{2\sigma}\psi_{2\sigma}\psi^\dagger_{2\sigma'}\psi_{2\sigma'} + \psi^\dagger_{4\sigma}\psi_{4\sigma}\psi^\dagger_{4\sigma'}\psi_{4\sigma'}\right] + \frac{\bar{U}_6}{2} \sum{}' \left[\psi^\dagger_{2\sigma}\psi_{4\sigma}\psi^\dagger_{2\sigma'}\psi_{4\sigma'} + h.c.\right] \\
+&\tilde{U}_6 \sum{}' \psi^\dagger_{2\sigma}\psi_{2\sigma}\psi^\dagger_{4\sigma'}\psi_{4\sigma'} + \tilde{\bar{U}}_6 \sum{}' \psi^\dagger_{2\sigma}\psi_{4\sigma}\psi^\dagger_{4\sigma'}\psi_{2\sigma'}
\end{aligned}$$

$$
\begin{aligned}
&+\frac{\bar{U}_7}{2}\sum{}'\left[\psi^\dagger_{1\sigma}\psi_{2\sigma}\psi^\dagger_{1\sigma'}\psi_{2\sigma'}+\psi^\dagger_{3\sigma}\psi_{4\sigma}\psi^\dagger_{3\sigma'}\psi_{4\sigma'}+h.c.\right]\\
&+\tilde{U}_7\sum{}'\left[\psi^\dagger_{1\sigma}\psi_{1\sigma}\psi^\dagger_{2\sigma'}\psi_{2\sigma'}+\psi^\dagger_{3\sigma}\psi_{3\sigma}\psi^\dagger_{4\sigma'}\psi_{4\sigma'}\right]+\tilde{\tilde{U}}_7\sum{}'\left[\psi^\dagger_{1\sigma}\psi_{2\sigma}\psi^\dagger_{2\sigma'}\psi_{1\sigma'}+\psi^\dagger_{3\sigma}\psi_{4\sigma}\psi^\dagger_{4\sigma'}\psi_{3\sigma'}\right]\\
&+\frac{\bar{U}_8}{2}\sum{}'\left[\psi^\dagger_{1\sigma}\psi_{4\sigma}\psi^\dagger_{1\sigma'}\psi_{4\sigma'}+\psi^\dagger_{2\sigma}\psi_{3\sigma}\psi^\dagger_{2\sigma'}\psi_{3\sigma'}+h.c.\right]\\
&+\tilde{U}_8\sum{}'\left[\psi^\dagger_{1\sigma}\psi_{1\sigma}\psi^\dagger_{4\sigma'}\psi_{4\sigma'}+\psi^\dagger_{2\sigma}\psi_{2\sigma}\psi^\dagger_{3\sigma'}\psi_{3\sigma'}\right]\\
&+\tilde{\tilde{U}}_8\sum{}'\left[\psi^\dagger_{1\sigma}\psi_{4\sigma}\psi^\dagger_{4\sigma'}\psi_{1\sigma'}+\psi^\dagger_{2\sigma}\psi_{3\sigma}\psi^\dagger_{3\sigma'}\psi_{2\sigma'}\right], \qquad (3.15)
\end{aligned}
$$

where

$$
\begin{aligned}
&U_1=U_2=U_3=U_4=U_5=U_6=\bar{U}_6=\tilde{U}_6=\tilde{\tilde{U}}_6=U,\\
&\bar{U}_1=\tilde{U}_1=\tilde{\tilde{U}}_1=\tilde{U}_4=\tilde{U}_5=\tilde{U}_7=\tilde{U}_8=U',\\
&\bar{U}_2=\tilde{U}_2=\tilde{\tilde{U}}_2=\tilde{\tilde{U}}_4=\tilde{\tilde{U}}_5=\tilde{\tilde{U}}_7=\tilde{\tilde{U}}_8=J,\\
&\bar{U}_3=\tilde{U}_3=\tilde{\tilde{U}}_3=\bar{U}_4=\bar{U}_5=\bar{U}_7=\bar{U}_8=J'. \qquad (3.16)
\end{aligned}
$$

In Eq. (3.15) the momentum arguments of the fermion operators $\boldsymbol{k}_i$, $i=1,2,3,4$ are omitted and the summation is over spin indices σ, σ' and momenta, subject to the momentum conservation condition $\sum_{i=1}^4 \boldsymbol{k}_i=0$.

The next step is to realize that Eq. (3.15) with *arbitrary* prefactors is the most general form of the interaction for the 4-band, 3-orbital model, consistent with the C_4 lattice symmetry. The C_4 symmetry implies that the four-fermion Hamiltonian must be invariant under the transformation $\psi_1\leftrightarrow\psi_3$, $\psi_2\leftrightarrow\psi_4$, $\psi_5\leftrightarrow\psi_6$. One can easily check that each term in (3.15) is C_4-symmetric on its own. Then the coupling constants do not have to be bound by the relations (5.14).

This reasoning implies that Eq. (3.15) is the most generic form of fermion-fermion interaction for a model with not necessarily local interactions. The total number of different terms in Eq. (3.15) is 30, hence there are 30 independent coupling constants. This number was first reported in Ref. [45]. At a bare level, the couplings may be related, as in Eq. (5.14). However, once we integrate out fermions with energies above a certain cutoff, all 30 coupling constants renormalize differently. As a result the conditions set by Eq. (5.14) do not hold for the running couplings. We also verified explicitly that no new interactions are generated by the RG flow, i.e., the terms which we present in Eq. (3.15) exhaust all possible symmetry allowed interactions between low-energy fermions. In RG language this implies that the theory is renormalizable.

3.3 Renormalization group (RG) analysis

Like we said, we will use the parquet RG technique to analyze the flow of the couplings. The RG technique is generally applicable when interactions in some channels evolve logarithmically with the running energy. Ladder RG is applicable when there is only one channel with logarithmic interactions (e.g, the Cooper channel). The parquet RG is applied when there is more than one channel, in which the renormalization of the coupling is logarithmic.

Parquet RG was first introduced in field-theory [95]. In condensed matter it was successfully used to map the phase diagram of one-dimensional systems, where logarthmic renormalizations are present in both particle-particle and particle-hole channels [96], and was also applied to several 2D systems, e.g., to the 2D σ-model [97], fermions near a van-Hove singularity in the dispersion [98], and bilayer graphene [99]. The leading logarithmic contributions at each order of perturbation are represented by the so-called parquet diagrams. The RG technique allows one to express infinite series of logarithmic renormalizations by differential equations for fully renormalized vertices.

The application of parquet RG to FeSCs has been discussed before [100]. Like we said, the new key element of our analysis is the inclusion of the orbital content of the excitations around the Fermi pockets. We refer to earlier literature for details and here just state the two main reasons to use parquet RG for FeSCs. First, the very fact that hole and electron dispersions have opposite signs implies that the renormalizations in the particle-hole channel at momenta separating hole and electron pockets are logarithmic at energies between the bandwidth and the Fermi energy. Nesting does not play a crucial role here as the two dispersions have opposite sign with or without nesting. Nesting (the near equivalence between hole and electronic dispersions, up to a sign) extends the logarithmic renormalizations in the particle-hole channel to energies smaller than E_F (down to energies of order $|\mu_h - \mu_e|$), but at such low energies parquet RG is already not applicable as particle-particle and particle-hole channels no longer "talk" to each other. Second, the logarithm in the particle-particle channel is not the Cooper logarithm (which comes from fermions in the near vicinity of the Fermi surfaces), but the one associated with the renormalization of the scattering amplitude in 2D (Ref. [101]). In this respect, the pairing instability within the parquet RG is actually towards a bound state formation of two particles. In a one-band 2D system, the actual superconducting T_c would be much smaller than this temperature [102] However, in our case, when hole and electron bands are both present, the temperature, at which bound pairs develop, and the actual superconducting T_c are of the same order [103]. By this reason we will not distinguish between a bound state formation (which develops

within parquet RG) and a true superconductivity.

In the calculations below we assume that the bare values of the interactions are small compared to the bandwidth and restrict the analysis to one loop parquet RG. We show that some interactions grow in the process of the RG flow, i.e., the system flows towards strong coupling. If we set the bare interactions to be larger, the system will more rapidly flow towards strong coupling, and the temperature of the leading instability will increase. In FeSe the leading instability is at $T_s = 85K \sim 8$ meV. This temperature is two orders of magnitude smaller than the bandwidth $W \sim 1$ eV. We consider the smallness of T_s/W as at least partial justification to apply the RG procedure. At the same time we caution that our approximation of the dispersions of the bands which cross the Fermi level by parabolas is not well justified, as other bands hybridize with d_{xz}, d_{yz}, and d_{xy} bands already at energies below W. These additional bands, however, affect only the value of the upper cutoff for parquet RG, but not the outcome of the RG flow.

3.3.1 RG equations for the interactions

In this Section we derive and solve the set of parquet RG equations for the interactions. The derivation of 30 coupled RG equations is a cumbersome but straightforward procedure. As we said, solving one-loop parquet RG equations is equivalent to summing up all leading logarithmic contributions originating from both particle-particle and particle-hole channels. Like in BCS theory, logarithms come from internal energies larger, in logarithmic sense, than the external ones. To logarithmic accuracy we set all external frequencies to be of the same order E and set external momenta k_{ext} to be of order $(2mE)^{1/2}$. We obtain the interactions $U_i(k_{ext})$ by integrating first over internal frequency and then over internal momentum between $\sqrt{2mW}$ and $(2mE)^{1/2}$.

As an example, we derive the RG equations for the interactions $\tilde{U}_4$ and $\tilde{\tilde{U}}_4$. The renormalizations of these couplings are given by diagrams shown in Fig. 3.3. Evaluating the diagrams, we obtain

$$\begin{aligned}\tilde{U}_4(k_{ext}) = &-\int_{k_{ext}}^{\sqrt{2mW}} \frac{d^2\boldsymbol{k}}{4\pi^2}(\tilde{U}_4^2(\boldsymbol{k}) + \tilde{\tilde{U}}_4^2(\boldsymbol{k})) \\ &\times \int \frac{d\epsilon}{2\pi} G_{\psi_5;\psi_5}(i\epsilon, \boldsymbol{k}) G_{\psi_6;\psi_6}(-i\epsilon, -\boldsymbol{k}) \\ &-\int_{k_{ext}}^{\sqrt{2mW}} \frac{d^2\boldsymbol{k}}{4\pi^2} 2\tilde{U}_4(\boldsymbol{k})\tilde{\tilde{U}}_4(\boldsymbol{k})\end{aligned}$$

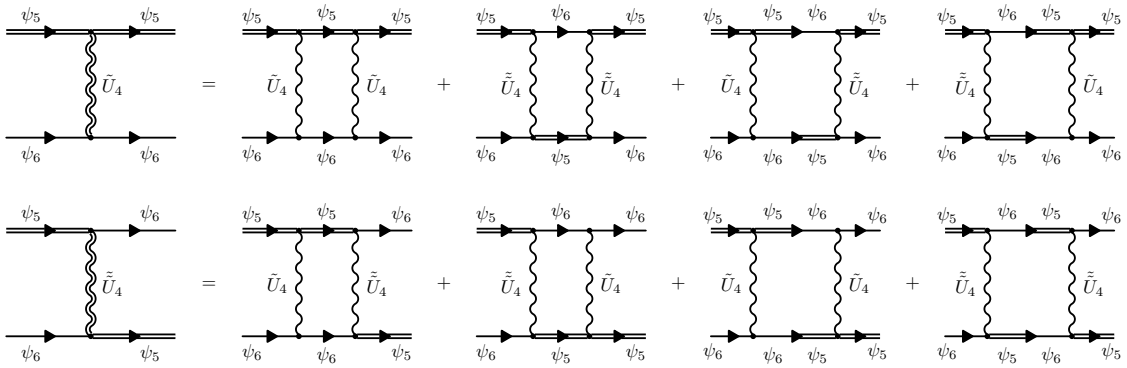

Figure 3.3: The diagrams for the renormalizations of $\tilde{U}_4$ and $\tilde{\tilde{U}}_4$. The propagators are identified by their label. Note that there are contributions involving Green's functions which are non-diagonal in the orbital index.

$$\times \int \frac{d\epsilon}{2\pi} G_{\psi_5;\psi_6}(i\epsilon, \boldsymbol{k}) G_{\psi_6;\psi_5}(-i\epsilon, -\boldsymbol{k}), \tag{3.17}$$

$$\begin{aligned}
\tilde{\tilde{U}}_4(k_{ext}) = &- \int_{k_{ext}}^{\sqrt{2mW}} \frac{d^2\boldsymbol{k}}{4\pi^2} 2\tilde{U}_4(\boldsymbol{k})\tilde{\tilde{U}}_4(\boldsymbol{k}) \\
&\times \int \frac{d\epsilon}{2\pi} G_{\psi_5;\psi_5}(i\epsilon, \boldsymbol{k}) G_{\psi_6;\psi_6}(-i\epsilon, -\boldsymbol{k}) \\
&- \int_{k_{ext}}^{\sqrt{2mW}} \frac{d^2\boldsymbol{k}}{4\pi^2} (\tilde{U}_4^2(\boldsymbol{k}) + \tilde{\tilde{U}}_4^2(\boldsymbol{k})) \\
&\times \int \frac{d\epsilon}{2\pi} G_{\psi_5;\psi_6}(i\epsilon, \boldsymbol{k}) G_{\psi_6;\psi_5}(-i\epsilon, -\boldsymbol{k}).
\end{aligned} \tag{3.18}$$

where $G_{\psi_i;\psi_j}(i\epsilon, \boldsymbol{k}) = -i\langle T\psi_i(\epsilon, \boldsymbol{k})\psi_j^\dagger(\epsilon, \boldsymbol{k})\rangle$. To select the logarithms, we use Eq. (3.9) and re-express $G_{\psi_i;\psi_j}(i\epsilon, \boldsymbol{k})$ in terms of Green's functions of band operators (in this case operators c and d), $G_{c,d}(i\epsilon, \boldsymbol{k}) = 1/(i\epsilon - \epsilon_{c,d}(\boldsymbol{k}))$. Integrating over frequency, introducing the logarithmic variable

$$L = \log \frac{W}{k_{ext}^2/2m} = \log \frac{W}{E} \tag{3.19}$$

and combing the equations (3.17) and (3.18), we obtain

$$\tilde{U}_4(L) \pm \tilde{\tilde{U}}_4(L) = -A_\pm \int_0^L dL' \frac{(\tilde{U}_4(L') \pm \tilde{\tilde{U}}_4(L'))^2}{4\pi} \tag{3.20}$$

where

$$A_\pm = \left[\frac{1}{8}(m_c + m_d) + \frac{3}{8}\frac{4m_c m_d}{m_c + m_d} \pm \frac{1}{8}\frac{(m_c - m_d)^2}{m_c + m_d} \right] . \tag{3.21}$$

Note that $A_\pm > 0$. Differentiating in (3.20) over the upper limit, we obtain

$$4\pi \frac{d(\tilde{U}_4 \pm \tilde{\tilde{U}}_4)}{dL} = -A_\pm (\tilde{U}_4 \pm \tilde{\tilde{U}}_4)^2 \tag{3.22}$$

Solving the equations for $\tilde{U}_4 + \tilde{\tilde{U}}_4$ and $\tilde{U}_4 - \tilde{\tilde{U}}_4$, we find that both interactions flow to zero under RG, provided that at the bare level $\tilde{U}_4 > \tilde{\tilde{U}}_4$. Using Eq. (5.14) for the bare couplings, we see that this holds if $U' > J$. We assume in this paper that this condition is satisfied. If it is not satisfied, the conclusions will be different [104].

Because both $\tilde{U}_4$ and $\tilde{\tilde{U}}_4$ vanish under RG for any A_+ and A_-, i.e., for any ratio of m_c/m_d, as long as both masses are non-zero, below we set $m_c = m_d = m_h$ to reduce the number of parameters in the RG equations. By the same reason we also set $m_x = m_y = m_e$, i.e., approximate electron pockets as circular. Keeping $m_c \neq m_d$ and $m_x \neq m_y$ only complicates the formulas but does not lead to any novel system behavior. With these approximations, Eq. (3.22) simplifies to

$$4\pi \frac{d(\tilde{U}_4 \pm \tilde{\tilde{U}}_4)}{dL} = - A_h (\tilde{U}_4 \pm \tilde{\tilde{U}}_4)^2 \tag{3.23}$$

where $A_h = m_h$.

Using the same reasoning, we obtain eight similar-looking RG equations

$$\begin{aligned}
4\pi \frac{d\tilde{U}_5}{dL} &= - A_e^{'} (\tilde{U}_5^2 + \tilde{\tilde{U}}_5^2) \\
4\pi \frac{d\tilde{\tilde{U}}_5}{dL} &= -2A_e^{'} \tilde{U}_5 \tilde{\tilde{U}}_5 \\
4\pi \frac{d\tilde{U}_6}{dL} &= - A_e^{''} (\tilde{U}_6^2 + \tilde{\tilde{U}}_6^2) \\
4\pi \frac{d\tilde{\tilde{U}}_6}{dL} &= -2A_e^{''} \tilde{U}_6 \tilde{\tilde{U}}_6
\end{aligned}$$

$$
\begin{aligned}
4\pi\frac{d\tilde{U}_7}{dL} =& 4\pi\frac{d\tilde{\tilde{U}}_7}{dL} = -\tilde{A}_e(\tilde{U}_7+\tilde{\tilde{U}}_7)^2,\\
4\pi\frac{d\tilde{U}_8}{dL} =& -A_e^{'''}(\tilde{U}_8^2+\tilde{\tilde{U}}_8^2)\\
4\pi\frac{d\tilde{\tilde{U}}_8}{dL} =& -2A_e^{'''}\tilde{U}_8\tilde{\tilde{U}}_8,
\end{aligned}
\tag{3.24}
$$

where

$$
\begin{aligned}
\tilde{A}_e &= m_e\int\frac{d\theta_e}{2\pi}\cos^2\phi_{e,k}\sin^2\phi_{e,k}\\
A_e^{'} &= m_e\int\frac{d\theta_e}{2\pi}\cos^2\phi_{e,k}\cos^2\phi_{e,k}^{'}\\
A_e^{''} &= m_e\int\frac{d\theta_e}{2\pi}\sin^2\phi_{e,k}\sin^2\phi_{e,k}^{'}\\
A_e^{'''} &= m_e\int\frac{d\theta_e}{2\pi}\cos^2\phi_{e,k}\sin^2\phi_{e,k}^{'}\,.
\end{aligned}
\tag{3.25}
$$

and we remind that we set $\cos\phi_{e,k} = A_0\cos\theta_e$, $\sin\phi_{e,k} = \sqrt{1-A_0^2\cos^2\theta_e}$, and $\cos\phi_{e,k}^{'} = -A_0\sin\theta_e$, $\sin\phi_{e,k}^{'} = \sqrt{1-A_0^2\sin^2\theta_e}$, where $1/\sqrt{2} < A_0 < 1$. The different A's in Eq. (3.25) all scale as m_e and are functions of A_0. One can easily see from Eq. (3.24) that the couplings $\tilde{U}_j$ and $\tilde{\tilde{U}}_j$ with $j = 5, 6, 8$ flow to zero (upper panel in Fig. 3.4) if the bare values $\tilde{U}_j$ and $\tilde{\tilde{U}}_j$ are positive and bare $\tilde{U}_j \geq \tilde{\tilde{U}}_j$, which is the case when $U' > J$. Like we said, we assume that this holds.

The RG equations for $\tilde{U}_7$ and $\tilde{\tilde{U}}_7$ are somewhat different compared to the other six equations in Eq. (3.24). The reason is that the couplings $\tilde{U}_7$ and $\tilde{\tilde{U}}_7$ are density-density and exchange couplings for d_{xz} and d_{xy} (or d_{yz} and d_{xy}) orbital components on the same pockets. Because only one combination of these orbitals forms the band which crosses the Fermi level, the difference $\tilde{U}_7 - \tilde{\tilde{U}}_7$ does not flow under RG. [The situation is similar to the case of RG flow of $\tilde{U}_4$ and $\tilde{\tilde{U}}_4$ when one of the masses vanishes and A_- becomes equal to zero]. Solving the RG equations for $\tilde{U}_7$ and $\tilde{\tilde{U}}_7$, we find that these two couplings tend to finite values under RG, $\tilde{U}_7 = -\tilde{\tilde{U}}_7 = const$. We will see that the other couplings increase under RG, and in comparison the couplings $\tilde{U}_7$ and $\tilde{\tilde{U}}_7$ become negligible (compare the lower panel in Fig. 3.4 and Fig. 3.5).

Performing an analogous diagrammatic analysis for the remaining 20 couplings, we obtain 20 coupled RG equations. We write these equations below for dimensionless couplings, which we introduce as follows:

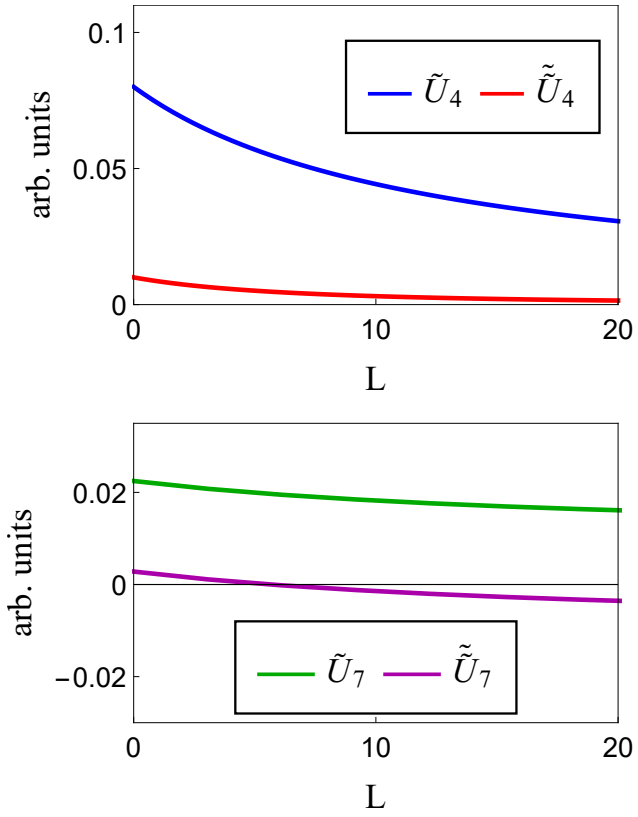

Figure 3.4: Representatrive RG flow of some of 10 decoupled interactions. The upper panel shows the flow of $\tilde{U}_4$ and $\tilde{\tilde{U}}_4$. Both flow to zero under RG. The flow of $\tilde{U}_5$ and $\tilde{\tilde{U}}_5$, $\tilde{U}_6$ and $\tilde{\tilde{U}}_6$, and $\tilde{U}_8$ and $\tilde{\tilde{U}}_8$ are similar. The lower panel shows the flow of $\tilde{U}_7$ and $\tilde{\tilde{U}}_7$. Both flow to small but finite values under RG.

$$
\begin{aligned}
u_{1,2} &= \frac{A}{4\pi} U_{1,2}\,, \bar{u}_{1,2} = \frac{\bar{A}}{4\pi}\bar{U}_{1,2}\,,\\
\tilde{u}_{1,2} &= \frac{\tilde{A}}{4\pi}\tilde{U}_{1,2}\,, \tilde{\tilde{u}}_{1,2} = \frac{\tilde{A}}{4\pi}\tilde{\tilde{U}}_{1,2}\,,\\
u_3 &= \frac{AC}{4\pi} U_3\,, \bar{u}_3 = \frac{\bar{A}\bar{C}}{4\pi}\bar{U}_3\,, \tilde{u}_3 = \frac{\tilde{A}\tilde{C}}{4\pi}\tilde{U}_3\,, \tilde{\tilde{u}}_3 = \frac{\tilde{A}\tilde{C}}{4\pi}\tilde{\tilde{U}}_3\,,\\
u_4 &= \frac{A_h}{4\pi} U_4\,, \bar{u}_4 = \frac{A_h}{4\pi}\bar{U}_4\,, u_5 = \frac{A_e}{4\pi} U_5\,, \bar{u}_5 = \frac{A_e}{4\pi}\bar{U}_5\,,\\
u_6 &= \frac{\bar{A}_e}{4\pi} U_6\,, \bar{u}_6 = \frac{\bar{A}_e}{4\pi}\bar{U}_6\,,
\end{aligned}
$$

$$\bar{u}_7 = \frac{\sqrt{A_e \bar{A}_e}}{4\pi} \bar{U}_7 \, , \bar{u}_8 = \frac{\sqrt{A_e \bar{A}_e}}{4\pi} \bar{U}_8 \, , \tag{3.26}$$

where

$$\begin{aligned} A = \bar{A} &= \frac{2m_e m_h}{m_e + m_h} \int \frac{d\theta}{2\pi} cos^2 \phi_{e,k} \\ \tilde{A} &= \frac{2m_e m_h}{m_e + m_h} \int \frac{d\theta}{2\pi} sin^2 \phi_{e,k} \\ A_e &= m_e \int \frac{d\theta}{2\pi} \cos^4 \phi_{e,k} \\ \bar{A}_e &= m_e \int \frac{d\theta}{2\pi} \sin^4 \phi_{e,k} \end{aligned} \tag{3.27}$$

and

$$\begin{aligned} C = \bar{C} &= \frac{\sqrt{A_h A_e}}{A} = \frac{m_e + m_h}{2\sqrt{m_e m_h}} \frac{\sqrt{\int \frac{d\theta}{2\pi} \cos^4 \phi_{e,k}}}{\int \frac{d\theta}{2\pi} \cos^2 \phi_{e,k}} \\ \tilde{C} &= \frac{\sqrt{A_h \bar{A}_e}}{\tilde{A}} = \frac{m_e + m_h}{2\sqrt{m_e m_h}} \frac{\sqrt{\int \frac{d\theta}{2\pi} \sin^4 \phi_{e,k}}}{\int \frac{d\theta}{2\pi} \sin^2 \phi_{e,k}} \end{aligned} \tag{3.28}$$

We also introduce the ratio

$$E = \frac{\tilde{A}_e}{\sqrt{A_e \bar{A}_e}} = \frac{\int \frac{d\theta}{2\pi} \cos^2 \phi_{e,k} \sin^2 \phi_{e,k}}{\sqrt{\int \frac{d\theta}{2\pi} \cos^4 \phi_{e,k} \int \frac{d\theta}{2\pi} \sin^4 \phi_{e,k}}} \, . \tag{3.29}$$

With these notations the 20 coupled RG equations read

$$\begin{aligned} \dot{u}_1 &= u_1^2 + u_3^2/C^2 \\ \dot{\bar{u}}_1 &= \bar{u}_1^2 + \bar{u}_3^2/C^2 \\ \dot{\tilde{u}}_1 &= \tilde{u}_1^2 + \tilde{u}_3^2/\tilde{C}^2 \\ \dot{\tilde{\bar{u}}}_1 &= \tilde{\bar{u}}_1^2 + \tilde{\bar{u}}_3^2/\tilde{C}^2 \\ \dot{u}_2 &= 2u_1 u_2 - 2u_2^2 \\ \dot{\bar{u}}_2 &= 2\bar{u}_1 \bar{u}_2 - 2\bar{u}_2^2 \\ \dot{\tilde{u}}_2 &= 2\tilde{u}_1 \tilde{u}_2 - 2\tilde{u}_2^2 \\ \dot{\tilde{\bar{u}}}_2 &= 2\tilde{\bar{u}}_1 \tilde{\bar{u}}_2 - 2\tilde{\bar{u}}_2^2 \end{aligned}$$

$$
\begin{aligned}
\dot{u}_3 &= -\bar{u}_3\bar{u}_5 - u_3u_5 - \tilde{u}_3\bar{u}_7 - \tilde{\bar{u}}_3\bar{u}_8 \\
&\quad - E(\tilde{u}_3u_5 + \tilde{\bar{u}}_3\bar{u}_5 + u_3\bar{u}_7 + \bar{u}_3\bar{u}_8) \\
&\quad - u_3u_4 - \bar{u}_3\bar{u}_4 + 4u_1u_3 - 2u_2u_3 \\
\dot{\bar{u}}_3 &= -\bar{u}_3u_5 - u_3\bar{u}_5 - \tilde{\bar{u}}_3\bar{u}_7 - \tilde{u}_3\bar{u}_8 \\
&\quad - E(\tilde{u}_3\bar{u}_5 + \tilde{\bar{u}}_3u_5 + \bar{u}_3\bar{u}_7 + u_3\bar{u}_8) \\
&\quad - u_3\bar{u}_4 - \bar{u}_3u_4 + 4\bar{u}_1\bar{u}_3 - 2\bar{u}_2\bar{u}_3 \\
\dot{\tilde{u}}_3 &= -u_3\bar{u}_7 - \bar{u}_3\bar{u}_8 - \tilde{u}_3u_6 - \tilde{\bar{u}}_3\bar{u}_6 \\
&\quad - E(u_3u_6 + \bar{u}_3\bar{u}_6 + \tilde{u}_3\bar{u}_7 + \tilde{\bar{u}}_3\bar{u}_8) \\
&\quad - \tilde{u}_3\bar{u}_4 - \tilde{\bar{u}}_3u_4 + 4\tilde{u}_1\tilde{u}_3 - 2\tilde{u}_2\tilde{u}_3 \\
\dot{\tilde{\bar{u}}}_3 &= -\bar{u}_3\bar{u}_7 - u_3\bar{u}_8 - \tilde{\bar{u}}_3u_6 - \tilde{u}_3\bar{u}_6 \\
&\quad - E(\bar{u}_3u_6 + u_3\bar{u}_6 + \tilde{\bar{u}}_3\bar{u}_7 + \tilde{u}_3\bar{u}_8) \\
&\quad - \tilde{u}_3u_4 - \tilde{\bar{u}}_3\bar{u}_4 + 4\tilde{\bar{u}}_1\tilde{\bar{u}}_3 - 2\tilde{\bar{u}}_2\tilde{\bar{u}}_3 \\
\dot{u}_4 &= -u_3^2 - \bar{u}_3^2 - \tilde{u}_3^2 - \tilde{\bar{u}}_3^2 - E(2u_3\tilde{u}_3 + 2\bar{u}_3\tilde{\bar{u}}_3) - u_4^2 - \bar{u}_4^2 \\
\dot{\tilde{u}}_4 &= -2u_3\bar{u}_3 - 2\tilde{u}_3\tilde{\bar{u}}_3 - E(2u_3\tilde{\bar{u}}_3 + 2\bar{u}_3\tilde{u}_3) - 2u_4\bar{u}_4 \\
\dot{u}_5 &= -u_5^2 - \bar{u}_5^2 - \bar{u}_7^2 - \bar{u}_8^2 - E(2u_5\bar{u}_7 + 2\bar{u}_5\bar{u}_8) - u_3^2 - \bar{u}_3^2 \\
\dot{\tilde{u}}_5 &= -2u_5\bar{u}_5 - 2\bar{u}_7\bar{u}_8 - E(2\bar{u}_5\bar{u}_7 + 2u_5\bar{u}_8) - 2u_3\bar{u}_3 \\
\dot{u}_6 &= -\bar{u}_7^2 - \bar{u}_8^2 - u_6^2 - \bar{u}_6^2 - E(2u_6\bar{u}_7 + 2\bar{u}_6\bar{u}_8) - \tilde{u}_3^2 - \tilde{\bar{u}}_3^2 \\
\dot{\tilde{u}}_6 &= -2\bar{u}_7\bar{u}_8 - 2u_6\bar{u}_6 - E(2\bar{u}_6\bar{u}_7 + 2u_6\bar{u}_8) - 2\tilde{u}_3\tilde{\bar{u}}_3 \\
\dot{\tilde{u}}_7 &= -u_5\bar{u}_7 - \bar{u}_5\bar{u}_8 - \bar{u}_6\bar{u}_8 - u_6\bar{u}_7 \\
&\quad - E(u_5u_6 + \bar{u}_5\bar{u}_6 + \bar{u}_7^2 + \bar{u}_8^2) - u_3\tilde{u}_3 - \bar{u}_3\tilde{\bar{u}}_3 \\
\dot{\tilde{u}}_8 &= -u_5\bar{u}_8 - \bar{u}_5\bar{u}_7 - \bar{u}_6\bar{u}_7 - u_6\bar{u}_8 \\
&\quad - E(u_5\bar{u}_6 + \bar{u}_5u_6 + 2\bar{u}_7\bar{u}_8) - u_3\tilde{\bar{u}}_3 - \bar{u}_3\tilde{u}_3.
\end{aligned}
\tag{3.30}
$$

where $\dot{u} = \frac{du}{dL}$. The three parameters in this RG set, C, $\tilde{C}$, and E depend on the ratio of hole and electron masses m_h/m_e and on A_0. We remind that A_0 determines over which portion of the electron Fermi surface the d_{xy} orbital component is stronger than the d_{xz} (d_{yz}) component.

The analysis of the set shows that couplings grow under the RG and diverge at a finite critical $L = L_0$ (see Fig. 3.5). Physically this scale can be seen as a temperature of order We^{-L_0}. This signals an instability of the normal state. The symmetry that is actually broken at L_0 has to be determined by comparing the susceptibilities in different channels.

We will do this after we analyze the flow of the couplings.

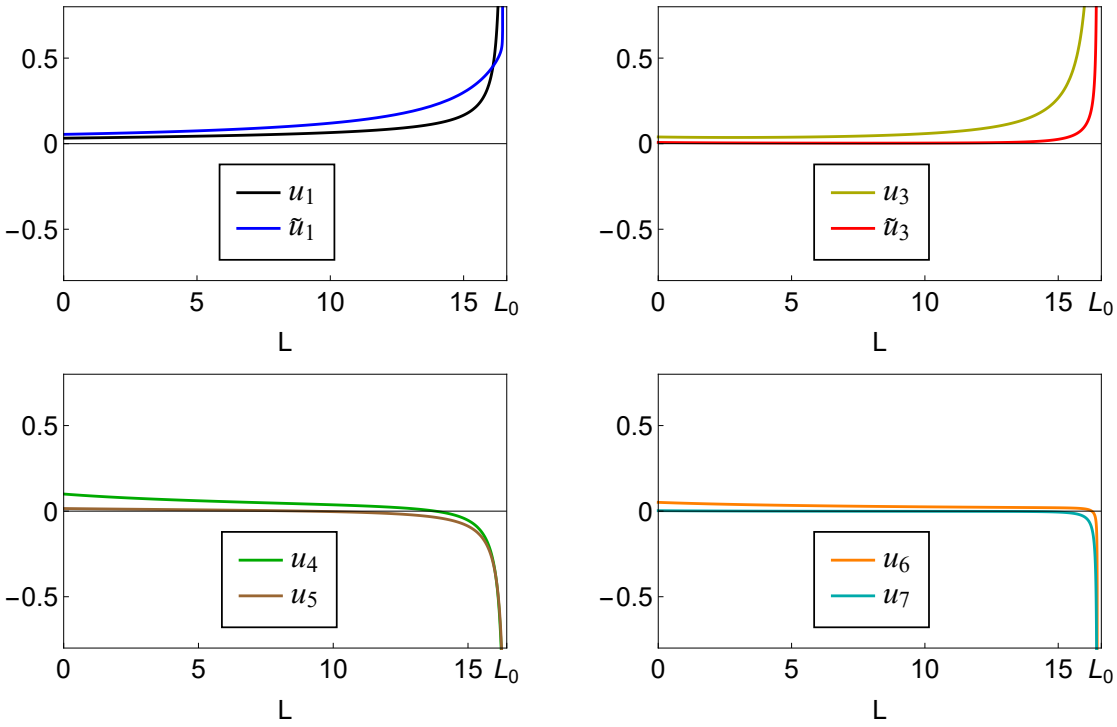

Figure 3.5: Representative RG flows of some of the 20 coupled interactions. The flow of eight couplings is shown. All couplings diverge at $L = L_0$. In the particular case we show here $L_0 = 16.47$.

3.3.2 Fixed trajectories of the RG equations

A stable fixed trajectory is the solution for u_i, to which the system flows from all directions as L tends to the critical value L_0. Each fixed trajectory has a basin of attraction in the space of bare interactions. A fixed trajectory is universal in the sense that the system behavior on this trajectory does not depend on the initial conditions. The latter only determine how fast the system approaches a given fixed trajectory. We will show that in our case there are two stable fixed trajectories.

An unstable fixed trajectory is approached from some directions, but along other directions the system moves away from it (i.e., the stability analysis for deviations from an unstable fixed trajectory yields at least one positive exponent). Unstable fixed trajectories are located in between stable fixed trajectories and in general are irrelevant for the RG analysis because the RG flow moves the system away from these trajectories towards the

stable ones. In our case, however, we show that there is one weakly unstable fixed trajectory with just one positive exponent, whose value is small. In this situation, a weakly unstable fixed trajectory behaves, for practical purposes, as a stable one because deviations from it become relevant only near the end of the RG flow, when the hierarchy of susceptibilities is already established. By this reason, below we treat the two stable and one weakly unstable fixed trajectories on equal footing.

As a first step, we verified, both analytically and numerically, that along stable and weakly unstable trajectories

$$\begin{aligned} &u_1 = \bar{u}_1, \tilde{u}_1 = \tilde{\bar{u}}_1, u_2 = \bar{u}_2, \tilde{u}_2 = \tilde{\bar{u}}_2, \\ &u_3 = \bar{u}_3, \tilde{u}_3 = \tilde{\bar{u}}_3, u_4 = \bar{u}_4, u_5 = \bar{u}_5, \\ &u_6 = \bar{u}_6, \bar{u}_7 = \bar{u}_8 \equiv u_7. \end{aligned} \tag{3.31}$$

Specifically, we verified that if we set initially $u_1 \neq \bar{u}_1$, the difference between the two running couplings will decrease in the process of the RG flow.

Eq. (3.31) allows one to reduce the 20 RG equations from Eq. (3.30) to 10 equations:

$$\begin{aligned} \dot{u}_1 &= u_1^2 + u_3^2/C^2 \quad \dot{\tilde{u}}_1 = \tilde{u}_1^2 + \tilde{u}_3^2/\tilde{C}^2 \\ \dot{u}_2 &= 2u_1u_2 - 2u_2^2 \qquad \dot{\tilde{u}}_2 = 2\tilde{u}_1\tilde{u}_2 - 2\tilde{u}_2^2 \\ \dot{u}_3 &= -2u_3u_5 - 2\tilde{u}_3u_7 - E(2\tilde{u}_3u_5 + 2u_3u_7) \\ &\quad - 2u_3u_4 + 4u_1u_3 - 2u_2u_3 \\ \dot{\tilde{u}}_3 &= -2u_3u_7 - 2\tilde{u}_3u_6 - E(2u_3u_6 + 2\tilde{u}_3u_7) \\ &\quad - 2\tilde{u}_3u_4 + 4\tilde{u}_1\tilde{u}_3 - 2\tilde{u}_2\tilde{u}_3 \\ \dot{u}_4 &= -2u_3^2 - 2\tilde{u}_3^2 - E(4u_3\tilde{u}_3) - 2u_4^2 \\ \dot{u}_5 &= -2u_5^2 - 2u_7^2 - E(4u_5u_7) - 2u_3^2 \\ \dot{u}_6 &= -2u_7^2 - 2u_6^2 - E(4u_6\bar{u}) - 2\tilde{u}_3^2 \\ \dot{u}_7 &= -2u_5u_7 - 2u_6u_7 - E(2u_5u_6 + 2u_7^2) - 2u_3\tilde{u}_3. \end{aligned} \tag{3.32}$$

Along the fixed trajectories, the couplings grow (and diverge at $L = L_0$), but their ratios tend to universal constant values. We introduce such ratios by selecting, say, u_1, and writing $u_i = \gamma_i u_1$, $\tilde{u}_i = \tilde{\gamma}_i u_1$, etc. We then set γ_i to be constants and solve the algebraic equations for γ_i. The solutions yield non-divergent γ_i if u_1 is one of the most strongly divergent couplings. If some γ_i come out infinite, we select another coupling as the primary one and repeat the procedure until all γ_i are non-divergent. We then check the stability of

the solution by expanding around it to linear order and solving for the deviations δu_j. The deviations behave as $\delta\gamma_j = \sum_m A_{mj}(\frac{1}{L_0-L})^{\beta_m}$ $(m = 1, 2, ..., 10)$. If all β_m are negative, the trajectory is fully stable. If one or more $\beta_m > 0$, the trajectory is unstable. Like we said, we call a trajectory weakly unstable if only one $\beta_m > 0$ and its value is numerically small.

Carrying out this procedure, we obtain two stable fixed trajectories and one weakly unstable trajectory. We present technical details of our analysis in the supplementary material (see Sec. 3.7.1). For the two stable fixed trajectories, we find

$$\begin{aligned}
&u_1(L) = \frac{1}{1+\gamma_3^2/C^2}\frac{1}{L_0-L},\\
&\tilde{\gamma}_1 = \gamma_2 = \tilde{\gamma}_2 = \tilde{\gamma}_3 = \gamma_6 = \gamma_7 = 0,\\
&\gamma_3 = +C\sqrt{-1+8C^2+4\sqrt{1-C^2+4C^4}},\\
&\gamma_4 = \gamma_5 = 1-2C^2-\sqrt{1-C^2+4C^4}
\end{aligned} \tag{3.33}$$

for the one and

$$\begin{aligned}
&\tilde{u}_1(L) = \frac{1}{1+\tilde{\gamma}_3^2/\tilde{C}^2}\frac{1}{L_0-L},\\
&\gamma_1 = \gamma_2 = \tilde{\gamma}_2 = \gamma_3 = \gamma_5 = \gamma_7 = 0,\\
&\tilde{\gamma}_3 = +\tilde{C}\sqrt{-1+8\tilde{C}^2+4\sqrt{1-\tilde{C}^2+4\tilde{C}^4}},\\
&\gamma_4 = \gamma_6 = 1-2\tilde{C}^2-\sqrt{1-\tilde{C}^2+4\tilde{C}^4}.
\end{aligned} \tag{3.34}$$

for the other.

Along the first fixed trajectory, the interactions $\tilde{U}_1$, U_2, $\tilde{U}_2$, $\tilde{U}_3$, U_6, and U_7 become negligible compared to interactions U_1, U_3, U_4, and U_5. Going back to Eq. (3.15), we find that this separation between the couplings implies that the interactions involving d_{xy} components on electron pockets vanish compared to interactions involving d_{xz} or d_{yz} components. In other words, the electron pockets can be effectively approximated as pure d_{xz} (the Y pocket) and pure d_{yz} (the X pocket). Along the second fixed trajectory, the situation is opposite – the interactions involving d_{xz} or d_{yz} orbital components on electron pockets vanish compared to interactions involving d_{xy} components. In this case, both electron pockets can be effectively approximated as pure d_{xy}. These two situations correspond to the two approximate models, considered in Ref. [11] – model I and II, respectively.

Additionally, we found a new fixed trajectory not present in the approximate models. This new fixed trajectory is formally an unstable one, but it is weakly unstable, with only one unstable direction. Furthermore the corresponding positive exponent is numerically small, e.g., $\beta_1 = 0.10$ for $m_h/m_e = 1$ and $A_0 = 0.8$. On this fixed trajectory the couplings behave as

$$\begin{aligned}
&\tilde{u}_1 = u_1 = \frac{1}{1+\gamma_3^2/C^2}\frac{1}{L_0 - L} > 0, \\
&\gamma_2 = \tilde{\gamma}_2 = 0 \\
&\gamma_3/C = \tilde{\gamma}_3/\tilde{C}, \\
&\gamma_4, \gamma_5, \gamma_6, \gamma_7 < 0
\end{aligned} \tag{3.35}$$

The values of the couplings γ_3, γ_4, γ_5, γ_6 and γ_7 depend on the three parameters C, $\tilde{C}$, and E, defined in Eqs. (3.28) and (3.29), which in turn depend on the ratios of hole and electron masses and on A_0. The analytical formulas for γ_i are somewhat involved and we present them in the supplementary material (see Sec. 3.7.1). For $m_h/m_e = 1$ and $A_0 = 0.8$, the numbers are $\gamma_3 = 9.62$, $\gamma_4 = -14.69$, $\gamma_5 = -5.50$, $\gamma_6 = -3.74$, $\gamma_7 = -4.56$.

The key feature of this fixed trajectory is that now interactions involving d_{xz}/d_{yz} and d_{xy} orbital components of the electron pockets remain of the same order and both grow under RG. We will see below that, as a consequence, an instability towards orbital order leads to simultaneous appearance of three order parameters, two involving d_{xz}/d_{yz} orbitals on hole pockets and on electron pockets, and one involving d_{xy} orbitals on the electron pockets. We argue below that all three orbital order parameters are required to explain recent ARPES data on FeSe [12].

3.4 Scaling of susceptibilities and the hierarchy of phase transitions

In this section we analyze the hierarchy of instabilities, which break different symmetries. For this we introduce auxiliary order parameter fields in different channels. We obtain the RG equations for the vertices, which couple the corresponding auxiliary fields to fermions, and solve them using the running couplings as inputs. We then express the running susceptibilities $\chi_i(L)$ in terms of running vertices and obtain the expressions for $\chi_i(L)$ in different channels. Similar procedure was applied to other problems [99, 128]. The divergence of the susceptibility in a particular channel signals an instability towards developing a long-range

order in this channel. We will see that not all susceptibilities diverge as L approaches L_0. For divergent susceptibilities, we compare the exponents and select the channel, in which the the exponent is the largest, as the one where the leading instability occurs.

Below we consider SDW, charge-density-wave (CDW), superconducting, and orbital channels. The interplay between the susceptibilities in these channels on the the two stable fixed trajectories is the same as in the two approximate models considered in Ref. [11]. We will not repeat the analysis here and focus on the system behavior along the weakly unstable fixed trajectory.

3.4.1 SDW and CDW order parameters

The SDW order introduces a spatial modulation at wave-vectors $X = (\pi, 0)$ and/or $Y = (0, \pi)$ and breaks spin SU(2) symmetry. If SDW order develops at a single wave-vector, X or Y, it in addition breaks the C_4 lattice rotational symmetry (the stripe order). If the modulations at X and Y wave-vectors coexist, the resulting checkerboard SDW order preserves the C_4 lattice symmetry. In the RG approach we perform a linear stability analysis of the paramagnetic state, i.e. we analyze the behavior of susceptibilities at temperatures above the one for the leading instability. By symmetry, SDW susceptibilities at X and Y are equivalent in the paramagnetic (non-nematic) phase. To distinguish between stripe and checkerboard orders one has to include non-linear couplings between the X and Y SDW order parameters [132]. This analysis is beyond the scope of our RG analysis.

In a multi-orbital system, the orbital content must be included in the classification of different order parameters in terms of irreducible representations of the symmetry group of the lattice. Specifically, for a tetragonal lattice, the SDW order parameters must come in degenerate pairs because an SDW order parameter at the wave-vector X transforms into an SDW order parameter at the wave-vector Y under a rotation by $\pi/2$. In addition, SDW order parameters split into two distinct groups, depending on whether the order parameter is diagonal or off-diagonal in the orbital index [45]. The SDW order in the first group gives rise to a finite magnetization on Fe ions, while for the order in the second group the magnetization vanishes on Fe sites, but is finite on pnictogen or chalcogen ions (on Se ions in FeSe). In our case the first group contains two elements (SDW involving d_{xz} or d_{yz} orbitals) and the second group contains six elements (between d_{xz} at Γ and d_{yz} at X, or d_{xy} at X or d_{xy} at Y, and between d_{yz} at Γ and d_{xz} at Y, or d_{xy} at Y or d_{xy} at X). Accordingly, we introduce eight auxiliary fields $\boldsymbol{s}^{(0)}_{i(i')}$, $i = 1, \ldots, 4$, choose them to be along the z direction

for definiteness, and couple them to fermions as

$$
\begin{aligned}
&H_{SDW} = \\
&\sum_k [\boldsymbol{s}_1^{(0)} \cdot \psi_{1,\alpha}^\dagger(k)\boldsymbol{\sigma}_{\alpha,\beta}\psi_{6,\beta}(k) + \boldsymbol{s}_{1'}^{(0)} \cdot \psi_{1,\alpha}^\dagger(k)\boldsymbol{\sigma}_{\alpha,\beta}\psi_{5,\beta}(k) \\
&+ \boldsymbol{s}_2^{(0)} \cdot \psi_{2,\alpha}^\dagger(k)\boldsymbol{\sigma}_{\alpha,\beta}\psi_{5,\beta}(k) + \boldsymbol{s}_{2'}^{(0)} \cdot \psi_{2,\alpha}^\dagger(k)\boldsymbol{\sigma}_{\alpha,\beta}\psi_{6,\beta}(k) \\
&+ \boldsymbol{s}_3^{(0)} \cdot \psi_{3,\alpha}^\dagger(k)\boldsymbol{\sigma}_{\alpha,\beta}\psi_{5,\beta}(k) + \boldsymbol{s}_{3'}^{(0)} \cdot \psi_{3,\alpha}^\dagger(k\boldsymbol{\sigma}_{\alpha,\beta}\psi_{6,\beta}(k) \\
&+ \boldsymbol{s}_4^{(0)} \cdot \psi_{4,\alpha}^\dagger(k)\boldsymbol{\sigma}_{\alpha,\beta}\psi_{6,\beta}(k) + \boldsymbol{s}_{4'}^{(0)} \cdot \psi_{4,\alpha}^\dagger(k)\boldsymbol{\sigma}_{\alpha,\beta}\psi_{5,\beta}(k) \\
&+ h.c.]
\end{aligned}
\tag{3.36}
$$

We recall that in our notations $\psi_1(\boldsymbol{k})$ and $\psi_6(\boldsymbol{k})$ are Bloch states of pure d_{xz} character at Y and at Γ, $\psi_3(\boldsymbol{k})$ and $\psi_5(\boldsymbol{k})$ are the Bloch states of pure d_{yz} character at X and at Γ, and $\psi_2(\boldsymbol{k})$ and $\psi_4(\boldsymbol{k})$ are the Bloch states of pure d_{xy} character at Y and at X, respectively. The field $\boldsymbol{s}_1^{(0)}$ ($\boldsymbol{s}_3^{(0)}$) couples to intra-orbital SDW order parameters on d_{xz} (d_{yz}) Fe orbitals, The intra-orbital SDW at Y and at X are related by C_4 lattice rotation, and the susceptibilities with respect to $\boldsymbol{s}_1^{(0)}$ and $\boldsymbol{s}_3^{(0)}$ must be equal by symmetry. The other four auxiliary fields couple to inter-orbital SDW. By symmetry, the susceptibilities with respect to $\boldsymbol{s}_{1'}^{(0)}$ and $\boldsymbol{s}_{3'}^{(0)}$ and with respect to $\boldsymbol{s}_{2(2')}^{(0)}$ and $\boldsymbol{s}_{4(4')}^{(0)}$ must coincide.

The RG equations for the flow of the running auxiliary fields $\boldsymbol{s}_{i(i')}$ away from the bare values $\boldsymbol{s}_{i(i')}^{(0)}$ from Eq. (3.36) are obtained in the same way as the flow of the couplings – by analyzing diagrams with renormalizations of $\boldsymbol{s}_{i(i')}^{(0)}$ due to the interactions. In general, $\boldsymbol{s}_{i(i')}^{(0)}$ are complex fields, whose real part Re $\boldsymbol{s}_{i(i')}$ describes the actual SDW, and whose imaginary part Im $\boldsymbol{s}_{i(i')}$ describes spin currents. We analyzed RG flows for both Re $\boldsymbol{s}_{i(i')}$ and Im $\boldsymbol{s}_{i(i')}$ and found that the RG equations for the two decouple, and in the process of the RG flow, Re $\boldsymbol{s}_{i(i')}$ becomes larger than Im $\boldsymbol{s}_{i(i')}$, even if the bare values of the two are comparable. For brevity, we then only consider the flow of Re $\boldsymbol{s}_{i(i')}$ and skip "Re" in the formulas below.

The RG equations describing the renormalization of $\boldsymbol{s}_1$, $\boldsymbol{s}_{1'}$, $\boldsymbol{s}_2$, and $\boldsymbol{s}_{2'}$ are (see Fig. 3.6)

$$
\begin{aligned}
\frac{ds_1}{dL} &= s_1\left(u_1 + \frac{u_3}{C}\right) \\
\frac{ds_2}{dL} &= s_2\left(\tilde{u}_1 + \frac{\tilde{u}_3}{\tilde{C}}\right) \\
\frac{ds_{1'}}{dL} &= s_{1'}\left(\bar{u}_1 + \frac{\bar{u}_3}{C}\right)
\end{aligned}
$$

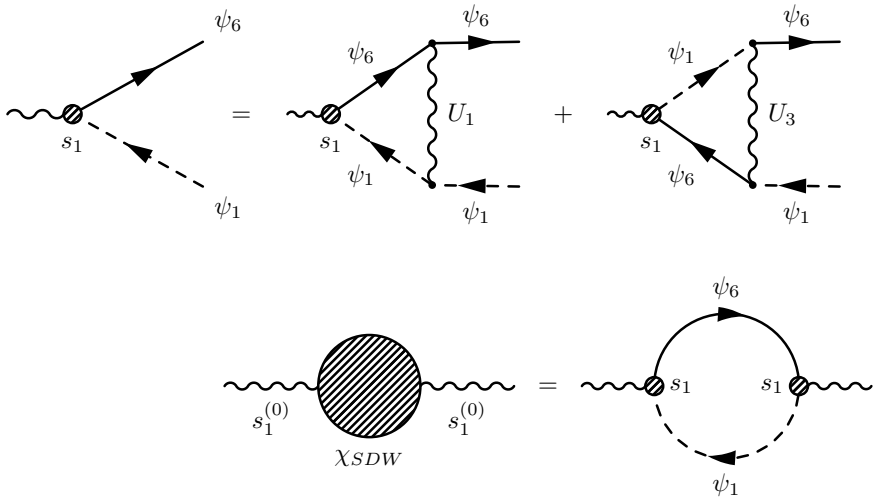

Figure 3.6: The diagrams for the renormalization of the SDW vertex(upper panel) and the susceptibility(lower panel).

$$\frac{ds_{2'}}{dL} = s_{2'}\left(\tilde{\tilde{u}}_1 + \frac{\tilde{\tilde{u}}_3}{\tilde{C}}\right). \tag{3.37}$$

On the fixed trajectories, the running couplings satisfy Eq. (3.31), and the RG equations for s_i and $s_{i'}$ become identical. We emphasize that this equivalence is the property of the fixed trajectories of the RG flow of the couplings rather than the consequence of tetragonal symmetry. The latter only guarantees that the vertices $s_{3(3')}$ and $s_{4(4')}$ satisfy the same parquet RG equations as $s_{1(1')}$ and $s_{2(2')}$, respectively.

On the weakly unstable fixed trajectory the couplings are related by Eq. (3.35). Expressing $u_3(L)$ in terms of $u_1(L)$ and using $u_1(L) = \frac{1}{1+\gamma_3^2/C^2}\frac{1}{L_0-L}$ we obtain from the first equation in (3.37)

$$s_1(L) \propto s_1^{(0)}(\frac{1}{L_0-L})^{\frac{1+\gamma_3/C}{1+\gamma_3^2/C^2}}. \tag{3.38}$$

The running susceptibility $\chi_{SDW,1}(L)$ is represented within RG by the bubble diagram with fully renormalized side vertices. We emphasize that both vertices should be treated as the running ones (see Fig. 3.6). The RG equation for $\chi_{SDW,1}(L)$ is then

$$(s_1^{(0)})^2\frac{d\chi_{SDW,1}}{dL} = s_1^2. \tag{3.39}$$

Solving this equation we obtain

$$\chi_{SDW,1}(L) = (\frac{1}{L_0 - L})^{\alpha_{SDW,1}}\,, \tag{3.40}$$

where the scaling exponent $\alpha_{SDW,1}$ is given by

$$\alpha_{SDW,1} = 2\frac{1+\gamma_3/C}{1+\gamma_3^2/C^2} - 1. \tag{3.41}$$

Performing the same calculations for $\chi_{SDW,2}(L)$ we obtain

$$\chi_{SDW,2}(L) \propto (\frac{1}{L_0 - L})^{\alpha_{SDW,2}} \tag{3.42}$$

with

$$\alpha_{SDW,2} = 2\frac{1+\tilde{\gamma}_3/\tilde{C}}{1+\tilde{\gamma}_3^2/\tilde{C}^2} - 1 \tag{3.43}$$

Using the fact that on the weakly unstable fixed trajectory $\gamma_3/C = \tilde{\gamma}_3/\tilde{C}$ (see Eq. (3.35)), we find

$$\alpha_{SDW,2} = \alpha_{SDW,1} \equiv \alpha_{SDW}. \tag{3.44}$$

By C_4 symmetry, the other susceptibilities $\chi_{SDW,i(i')}(L)$ have the same exponent $\alpha_{SDW,1'} = \alpha_{SDW,3} = \alpha_{SDW,3'} = \alpha_{SDW,2'} = \alpha_{SDW,4} = \alpha_{SDW,4'} = \alpha_{SDW}$. We plot α_{SDW} along with the exponents in other channels in Fig. 3.10.

We also analyzed the susceptibility in the CDW channel at the same momentum X and Y. We found (see Sec. 3.7.3.1 in the supplementary material) that along the weakly unstable fixed trajectory different CDW components are degenerate and the susceptibility exponent in the CDW channel is the same as in the SDW channel, i.e.,

$$\alpha_{CDW} = \alpha_{SDW}\,. \tag{3.45}$$

3.4.2 Superconducting order parameters

To study superconductivity we analyze the response to the auxiliary intra-orbital pairing fields $\Delta_i^{(0)}$, $i = 1, \ldots, 6$ and inter-orbital pairing fields $\Delta_{1,2}^{(0)}$, $\Delta_{3,4}^{(0)}$, $\Delta_{5,6}^{(0)}$. These 12 auxiliary fields couple to 12 distinct singlet superconducting order parameters which one can construct

out of d_{xz}, d_{yz}, and d_{xy} orbitals:

$$
\begin{aligned}
&H_{SC}^{(0)} = \\
&\sum_{k\sigma}[\Delta_1^{(0)}\psi_{1,\sigma}^\dagger(k)\psi_{1,-\sigma}^\dagger(-k) + \Delta_2^{(0)}\psi_{2,\sigma}^\dagger(k)\psi_{2,-\sigma}^\dagger(-k) \\
&+ \Delta_3^{(0)}\psi_{3,\sigma}^\dagger(k)\psi_{3,-\sigma}^\dagger(-k) + \Delta_4^{(0)}\psi_{4,\sigma}^\dagger(k)\psi_{4,-\sigma}^\dagger(-k) \\
&+ \Delta_5^{(0)}\psi_{5,\sigma}^\dagger(k)\psi_{5,-\sigma}^\dagger(-k) + \Delta_6^{(0)}\psi_{6,\sigma}^\dagger(k)\psi_{6,-\sigma}^\dagger(-k) \\
&+ \Delta_{1,2}^{(0)}\psi_{1,\sigma}^\dagger(k)\psi_{2,-\sigma}^\dagger(-k) + \Delta_{3,4}^{(0)}\psi_{3,\sigma}^\dagger(k)\psi_{4,-\sigma}^\dagger(-k) \\
&+ \Delta_{5,6}^{(0)}\psi_{5,\sigma}^\dagger(k)\psi_{6,-\sigma}^\dagger(-k) + h.c.]
\end{aligned}
\tag{3.46}
$$

The parameters $\Delta_i^{(0)}$ and $\Delta_{ij}^{(0)}$ play the role of bare superconducting vertices with zero total momenta in the particle-particle channel. We label the full vertices as Δ_i and $\Delta_{i,j}$, without the superscript.

Like we did in the SDW case, we first obtain and solve the RG equations for the vertices and then use the results to obtain the exponents for superconducting susceptibilities. For symmetry analyses it is useful to introduce the symmetrized combinations $\Delta_1 \pm \Delta_3$, $\Delta_2 \pm \Delta_4$, and $\Delta_5 \pm \Delta_6$. These combinations transform as A_{1g} (B_{1g}) representations of the D_{4h} point group of a tetragonal lattice. Similarly, the combinations $\Delta_{1,2}^{re(im)} = \Delta_{1,2} \pm \Delta_{1,2}^*$, $\Delta_{3,4}^{re(im)} = \Delta_{3,4} \pm \Delta_{3,4}^*$ and $\Delta_{5,6}^{re(im)} = \Delta_{5,6} \pm \Delta_{5,6}^*$ transform as A_{2g} (B_{2g}) representations of the D_{4h} group. Because the interaction is a D_{4h} scalar, renormalizations do not mix vertices from different representations. As a result, all symmetrized combinations, belonging to different representations, decouple and flow separately under RG.

The derivation of RG equations proceeds in the same way as for SDW vertices. We show the corresponding diagrams in Fig. 3.7. The RG equations for particle-particle vertices in the A_{1g} channel on the weakly unstable fixed trajectory are

$$
\frac{d}{dL}\begin{pmatrix}\Delta_1+\Delta_3\\ \Delta_2+\Delta_4\\ \Delta_5+\Delta_6\end{pmatrix} = M\begin{pmatrix}\Delta_1+\Delta_3\\ \Delta_2+\Delta_4\\ \Delta_5+\Delta_6\end{pmatrix}, \tag{3.47}
$$

where

$$M = \begin{pmatrix} -2(u_5 + Eu_7) & -2(\sqrt{\frac{\bar{A}_e}{A_e}}u_7 + \sqrt{\frac{\bar{A}_e}{A_e}}Eu_5) & -2(\sqrt{\frac{A_h}{A_e}}u_3) \\ -2(\sqrt{\frac{A_e}{\bar{A}_e}}u_7 + \sqrt{\frac{A_e}{\bar{A}_e}}Eu_6) & -2(u_6 + Eu_7) & -2(\sqrt{\frac{A_h}{\bar{A}_e}}\tilde{u}_3) \\ -2(\sqrt{\frac{A_e}{A_h}}u_3 + \sqrt{\frac{A_e}{A_h}}E\tilde{u}_3) & -2(\sqrt{\frac{\bar{A}_e}{A_h}}\tilde{u}_3 + \sqrt{\frac{\bar{A}_e}{A_h}}Eu_3) & -2u_4 \end{pmatrix} \tag{3.48}$$

We solve the RG equations by taking the interactions u_i to be on the weakly unstable

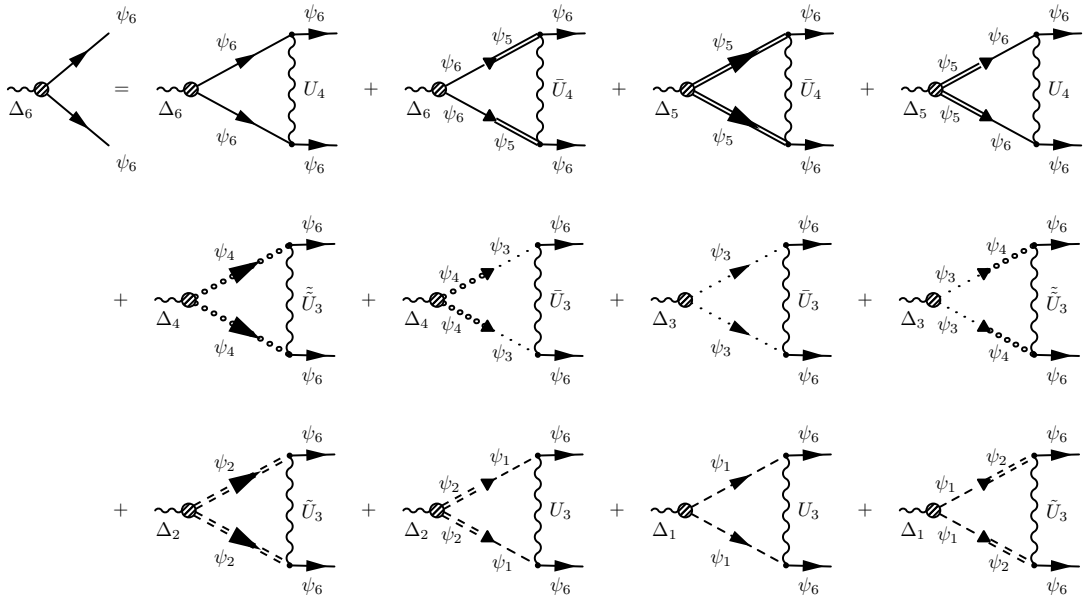

Figure 3.7: The diagraamatic representation of the renormalizations of the vertices in SC channel.

fixed trajectory, (3.35). The diagonalization of the 3×3 matrix yields three independent combinations of A_{1g} vertices, corresponding to three eigenvalues: $e_\alpha u_1$, $e_\beta u_1$ and $e_\gamma u_1$. Solving the three independent RG equations we obtain

$$\Delta_\mu(L) \propto \left(\frac{1}{L_0 - L}\right)^{\frac{e_\mu}{1+\gamma_3^2/C^2}} , \tag{3.49}$$

where $\mu = \alpha, \beta, \gamma$. We choose the solution with the largest exponent, which corresponds to the largest eigenvalue $e_{SC} = \max\{e_\alpha, e_\beta, e_\gamma\}$. For the corresponding susceptibility we then

obtain $\chi_{SC}(L) \propto 1/(L_0 - L)^{\alpha_{SC}}$, where

$$\alpha_{SC} = 2\frac{e_{SC}}{1+\gamma_3^2/C^2} - 1\,. \tag{3.50}$$

The values $e_{\alpha,\beta,\gamma}$ depend on our three parameters $C, \tilde{C}$, and E, which, we recall, depend on A_0 and m_h/m_e. We obtain the largest exponent α_{SC} numerically and show it in Fig. 3.10 as a function of A_0 along with the exponents in the other channels. The corresponding A_{1g} order parameter is plotted in Fig. 3.12 as a function of the angle along the Fermi surfaces. The order parameter has opposite signs on electron and hole Fermi surfaces, i.e. the gap structure is s^{+-}.

We also analyzed the three other superconducting channels B_{1g}, A_{2g} and B_{2g}, and found that the vertices and susceptibilities in these channels do not diverge. In the B_{1g} channel, the analog of the 3×3 matrix for $\Delta_1 - \Delta_3$, $\Delta_2 - \Delta_4$, and $\Delta_5 - \Delta_6$ vanishes on the weakly unstable fixed trajectory, because the corresponding couplings vanish (see Eq. (3.31)). The vertices in A_{2g} and B_{2g} channels describe inter-orbital pairing. These vertices are renormalized via the interactions $\tilde{U}_4$, $\tilde{\tilde{U}}_4$, $\tilde{U}_7$ and $\tilde{\tilde{U}}_7$. For our choice $U' > J$, these interactions renormalize to zero under RG, hence the corresponding vertices do not increase.

3.4.3 Orbital order parameters

We consider orbital order parameters with zero transferred momentum. In the band basis, an instability leading to condensation of any of such orbital order parameters is a Pomeranchuk instability. A non-s-wave Pomeranchuk order breaks the rotational symmetry of the lattice but does not break the translational invariance. The reconstruction of the Fermi surfaces for a d-wave (B_{1g}) Pomeranchuk order is shown in Fig. 3.11.

To analyze the susceptibilities in the orbital channel we again introduce auxiliary fields, this time real charge fields $\Gamma_i^{(0)}$ and complex charge fields $\Gamma_{i,j}^{(0)}$. The coupling of auxiliary fields to fermions is described by

$$\begin{aligned} H_{Pom} = \sum_{k\sigma} \Big[& \Gamma_1^{(0)} \psi_{1,\sigma}^\dagger(k)\psi_{1,\sigma}(k) + \Gamma_2^{(0)} \psi_{2,\sigma}^\dagger(k)\psi_{2,\sigma}(k) \\ & + \Gamma_3^{(0)} \psi_{3,\sigma}^\dagger(k)\psi_{3,\sigma}(k) + \Gamma_4^{(0)} \psi_{4,\sigma}^\dagger(k)\psi_{4,\sigma}(k) \\ & + \Gamma_5^{(0)} \psi_{5,\sigma}^\dagger(k)\psi_{5,-\sigma}^\dagger(k) + \Gamma_6^{(0)} \psi_{6,\sigma}^\dagger(k)\psi_{6,\sigma}(k) \\ & + (\Gamma_{1,2}^{(0)} \psi_{1,\sigma}^\dagger(k)\psi_{2,\sigma}(k) + \Gamma_{3,4}^{(0)} \psi_{3,\sigma}^\dagger(k)\psi_{4,\sigma}(k) \end{aligned}$$

$$+\Gamma^{(0)}_{5,6}\psi^{\dagger}_{5,\sigma}(k)\psi_{6,\sigma}(k)+h.c.)\Big]\,. \tag{3.51}$$

The coefficients $\Gamma^{(0)}_{i}$ and $\Gamma^{(0)}_{i,j}$ are bare vertices with zero momentum in the particle-hole charge channel. We label dressed vertices by the same Γ_i and $\Gamma_{i,j}$, but without the superscript. We introduce symmetrized combinations $\Gamma_1 \pm \Gamma_3$, $\Gamma_2 \pm \Gamma_4$, and $\Gamma_5 \pm \Gamma_6$, which transform as A_{1g} (B_{1g}) representations of the D_{4h} group, and the combinations $\Gamma^{re(im)}_{1,2} = \Gamma_{1,2} \pm \Gamma^{*}_{1,2}$, $\Gamma^{re(im)}_{3,4} = \Gamma_{3,4} \pm \Gamma^{*}_{3,4}$ and $\Gamma^{re(im)}_{5,6} = \Gamma_{5,6} \pm \Gamma^{*}_{5,6}$, which transform as A_{2g} (B_{2g}). Combinations belonging to different representations again decouple in the RG equations.

The renormalization of the vertices in the orbital (Pomeranchuk) channels is different from the ones in SDW and superconducting channels, because the particle-hole susceptibility at zero momentum transfer is non-logarithmical. Still, the renormalization involves the running couplings $u_i(L)$. One can demonstate (see Ref. [106]) for details), that the renormalization of $\Gamma_i(L)$ and $\Gamma_{ij}(L)$ comes from internal energies comparable to L. As a consequence, the vertices at a scale L are expressed in terms of interactions u_i *at the same* scale L.

We now need to select diagrammatic series for Γ_i. In SDW and superconducting channels the RG flow of the vertices is given by series of ladder diagrams. The selection of these diagrams is rigorously justified within the one-loop RG. For the Pomeranchuk vertices, there are no logarithms and hence no parameter to select a particular set of diagrams. We choose, without proof, the same set of ladder diagrams as for SDW and superconducting channels (see Fig. 3.8). Within this approximation, the equations for the dressed Pomeranchuk vertices are

$$\begin{pmatrix}\Gamma_1-\Gamma_3\\ \Gamma_2-\Gamma_4\\ \Gamma_5-\Gamma_6\end{pmatrix} = \boldsymbol{M}_{B_{1g}}\begin{pmatrix}\Gamma_1-\Gamma_3\\ \Gamma_2-\Gamma_4\\ \Gamma_5-\Gamma_6\end{pmatrix} + \begin{pmatrix}\Gamma^{(0)}_1-\Gamma^{(0)}_3\\ \Gamma^{(0)}_2-\Gamma^{(0)}_4\\ \Gamma^{(0)}_5-\Gamma^{(0)}_6\end{pmatrix} \tag{3.52}$$

$$\begin{pmatrix}\Gamma_1+\Gamma_3\\ \Gamma_2+\Gamma_4\\ \Gamma_5+\Gamma_6\end{pmatrix} = \boldsymbol{M}_{A_{1g}}\begin{pmatrix}\Gamma_1+\Gamma_3\\ \Gamma_2+\Gamma_4\\ \Gamma_5+\Gamma_6\end{pmatrix} + \begin{pmatrix}\Gamma^{(0)}_1+\Gamma^{(0)}_3\\ \Gamma^{(0)}_2+\Gamma^{(0)}_4\\ \Gamma^{(0)}_5+\Gamma^{(0)}_6\end{pmatrix} \tag{3.53}$$

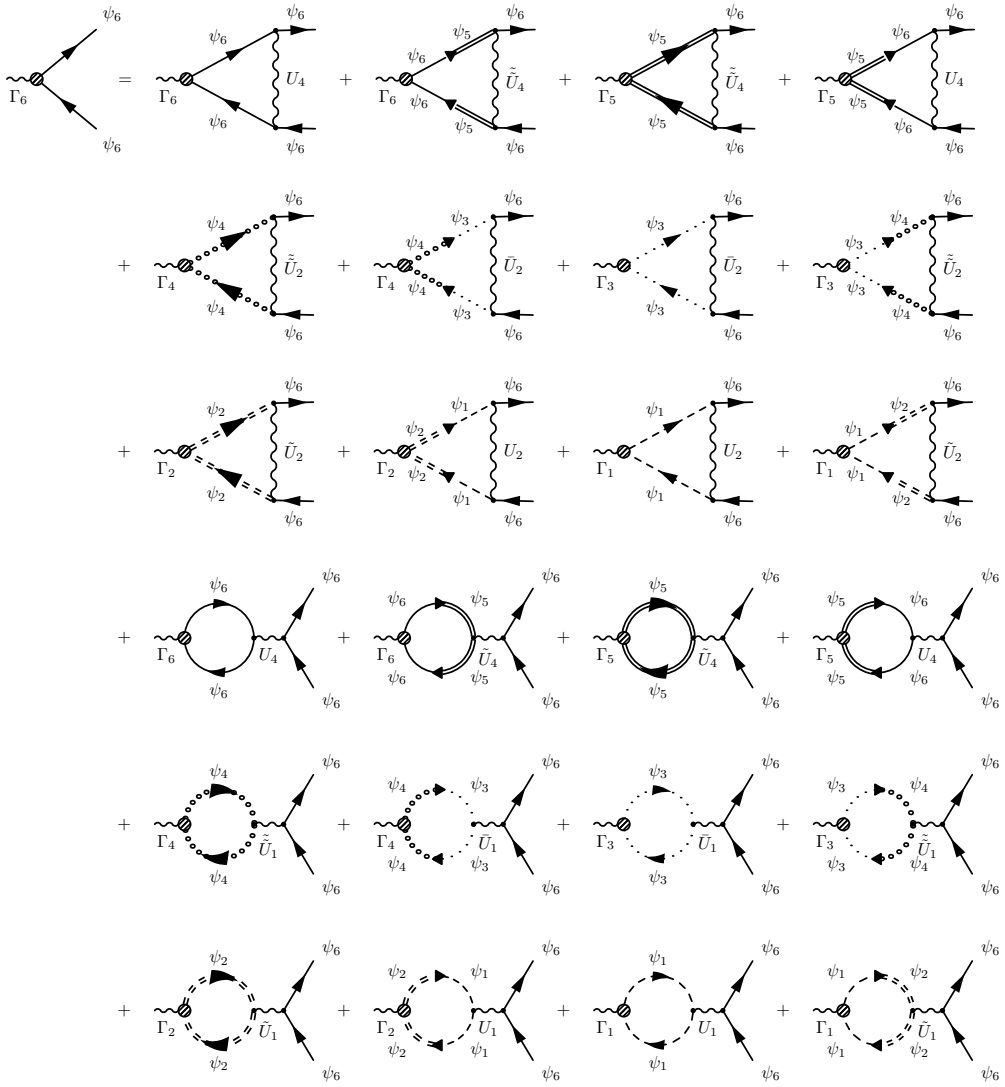

Figure 3.8: The diagramatic representation of the renormalization of the vertices in the Pomeranchuk channel.

where

$$\boldsymbol{M}_{B_{1g}} = \begin{pmatrix} -2u_5 & -2\frac{\tilde{A}_e}{A_e}u_5 & -2\frac{A_h}{A}\epsilon_1 \\ -2\frac{\tilde{A}_e}{A_e}u_6 & -2u_6 & -2\frac{A_h}{A}\epsilon_2 \\ -2\frac{A_e}{A}\epsilon_1 - 2\frac{\tilde{A}_e}{\tilde{A}}\epsilon_2 & -2\frac{\tilde{A}_e}{A}\epsilon_1 - 2\frac{\bar{A}_e}{\tilde{A}}\epsilon_2 & -2u_4 \end{pmatrix} \tag{3.54}$$

and

$$\boldsymbol{M}_{A_{1g}}=\begin{pmatrix} -2u_5 & -2\frac{\tilde{A}_e}{A_e}u_5 & -8\frac{A_h}{A}u_1 \\ -2\frac{\tilde{A}_e}{A_e}u_6 & -2u_6 & -8\frac{A_h}{A}\tilde{u}_1 \\ -8(\frac{A_e}{A}u_1+\frac{\tilde{A}_e}{A}\tilde{u}_1) & -8(\frac{A_e}{A}u_1+\frac{\tilde{A}_e}{A}\tilde{u}_1) & -2u_4 \end{pmatrix}. \tag{3.55}$$

In Eqs. (3.54) and (3.55) we introduced

$$\begin{aligned} \epsilon_1 &= u_2 - \bar{u}_2 - 2(u_1 - \bar{u}_1) \\ \epsilon_2 &= \tilde{u}_2 - \tilde{\bar{u}}_2 - 2(\tilde{u}_1 - \tilde{\bar{u}}_1)\,. \end{aligned} \tag{3.56}$$

The ratios A_e/A, etc. are functions of A_0 and m_h/m_e.

In what follows, we focus on the instability in the B_{1g} channel, which gives rise to a true C_4 breaking orbital order. Solving the 3×3 matrix equation for the three order parameters $\Gamma_{1,e}=\Gamma_1-\Gamma_3$, $\Gamma_{2,e}=\Gamma_2-\Gamma_4$, $\Gamma_{1,h}=-(\Gamma_5-\Gamma_6)$, we obtain

$$\Gamma_{1,e},\Gamma_{2,e},\Gamma_{1,h}\propto 1/(1-\lambda u_1)\propto (L_{B_{1g}}-L)^{-1}\,, \tag{3.57}$$

where λu_1 is the largest eigenvalue of $\mathbf{M}_{B_{1g}}$ and

$$L_{B_{1g}}=L_0-\frac{\lambda}{1+\gamma_3^2/C^2}\,. \tag{3.58}$$

We verified that the largest eigenvalue of $\mathbf{M}_{B_{1g}}$ is positive. Then $L_{B_{1g}}<L_0$, i.e., the instability in the orbital channel occurs at a larger T than the one in the superconducting channel. This, however, may be the artefact of our approximation, because the correction to L_0 in (3.58) is non-logarithmical and, strictly speaking, the difference between L_0 and $L_{B_{1g}}$ is outside of the applicability of the one-loop RG analysis. Put it differently – at $L=L_{B_{1g}}$, the running couplings become of order of one, i.e., one-loop RG is at the border of its applicability. In this respect, the ladder approximation is a bit biased towards a Pomeranchuk order (for a similar discussion of RG analysis for the 2D Hubbard model, see Refs. [107, 108] We note, however, that, even if we neglect the difference between L_0 ad $L_{B_{1g}}$, we still find that the exponent for the B_{1g} Pomeranchuk vertices is $\beta_{Pom}=1$. Evaluating then the susceptibility in the Pomeranchuk channel we obtain

$$\chi_{B_{1g}}\propto (L_0-L)^{-1}, \tag{3.59}$$

i.e. the susceptibility exponent $\alpha_{Pom} = 1$.

For completeness, we also considered A_{1g}, A_{2g} and B_{2g} Pomeranchuk channels. The divergence of the Pomeranchuk susceptibility in the A_{1g} channel gives rise to a shift of the chemical potential, with different magnitudes on hole and electron pockets [11]. It does not, however, give rise to a true symmetry breaking as A_{1g} symmetry is the same as the symmetry of the tetragonal phase. In practice it implies that the divergence of the A_{1g} Pomeranchuk susceptibility is very likely cut by terms beyond RG. The order parameters Γ_{ij} in A_{2g} and B_{2g} channels are inter-pocket ones and do not break symmetry between x and y directions. We discuss these orders in Sec. 3.7.3.3 in the supplementary material.

3.4.4 Comparative analysis of susceptibilities

The explicit results for the RG flow of susceptibilities in SC, SDW, and d-wave (B_{1g}) Pomeranchuk channels are presented in Fig. 3.9. We obtained this flow by selecting a particular set of initial conditions, for which the RG flow moves the system towards the weakly unstable fixed trajectory, solving for $u_i(L)$, and using these running couplings to obtain L dependencies first of the vertices and then of the susceptibilities. We see the same behavior as we obtained by analyzing the fixed trajectories. Namely, the susceptibility in the Pomeranchuk channel becomes the largest at $L \approx L_0$ (even if we neglect the difference between L_0 ad $L_{B_{1g}}$). The susceptibility in the SC channel increases, but not as fast as the Pomeranchuk susceptibility, and the susceptibility in SDW channel does not diverge at $L = L_0$.

To see more accurately the scaling behavior of various susceptibilities we compared the exponents α in $\chi(L) \propto 1/(L_0 - L)^\alpha$ in SDW, SC, and Pomeranchuk channels for u_i on the weakly unstable fixed trajectory. We plot α_i in Fig. 3.10 as function of A_0 at fixed m_h/m_e and as function of m_h/m_e at fixed A_0. The value of $\alpha_{Pom} = 1$ is independent on the m_h/m_e mass ratio and the parameter A_0. The values of $\alpha_{SDW} = \alpha_{CDW}$ and α_{SC} weakly depend on on A_0 (and on m_h/m_e). We see that α_{SC} is positive, but smaller than one, and $\alpha_{SDW} = \alpha_{CDW}$ is negative. This is fully consistent with Fig. 3.9. The conclusion from both figures is then that, upon increasing L (i.e., lowering the temperature), the first instability occurs in the B_{1g} Pomeranchuk channel and leads to a spontaneous orbital order which breaks C_4 rotational symmetry. Superconducting order develops at a lower temperature (which will be further reduced due to a negative feedback from the orbital order), and SDW and CDW orders do not develop down to $T = 0$.

We caution that this result only applies to systems for which $L_0 \leq L_F = \log W/E_F$.

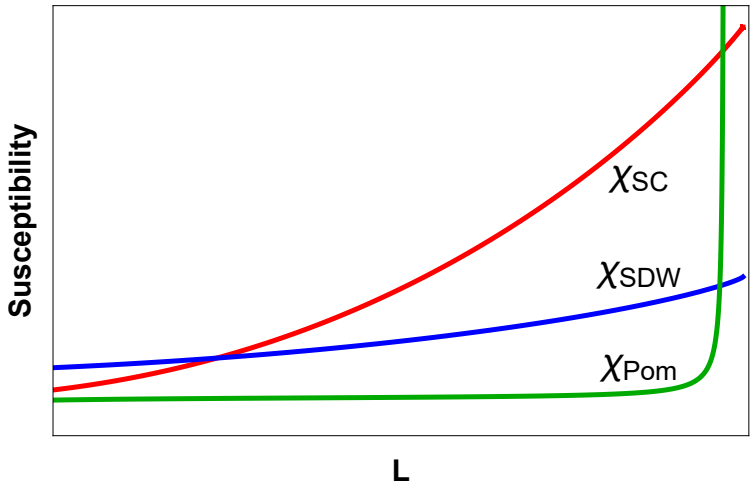

Figure 3.9: The RG flow of susceptibilities as functions of the RG parameter L. The susceptibilities in the superconducting and Pomeranchuk channels diverges, while the one in the SDW channel initially increases but remains finite as L approaches L_0, which is slightly to the right from the right boundary of the figure.

When $L_F < L_0$, the one-loop parquet RG runs up to $L = L_F$, and the system generally develops an instability in the channel in which the susceptibility is the largest at $L = L_F$ (see Refs. [52, 11, 106]).

3.5 The structure of superconducting and orbital order parameters and implications for the experiments

The susceptibility analysis reveals instabilities towards superconducting and orbital order. In this section we determine the structure of the corresponding order parameters and discuss the implications of the orbital order for the band structure.

The magnitudes of different order parameters at $T \to 0$ can only be obtained by solving the full set of non-linear gap equations, which include a non-linear coupling between orbital and superconducting orders. This accounts for the fact that, once orbital order develops first, it tends to suppress the onset of superconducting order. This analysis is beyond the scope of our RG study, in which we approach the instabilities from the disordered state at higher T. Nevertheless, the RG analysis allows one to detect the symmetry of superconducting and orbital orders, and also find the ratios between different components of superconducting and orbital order parameters near their onsets, i.e. between superconduct-

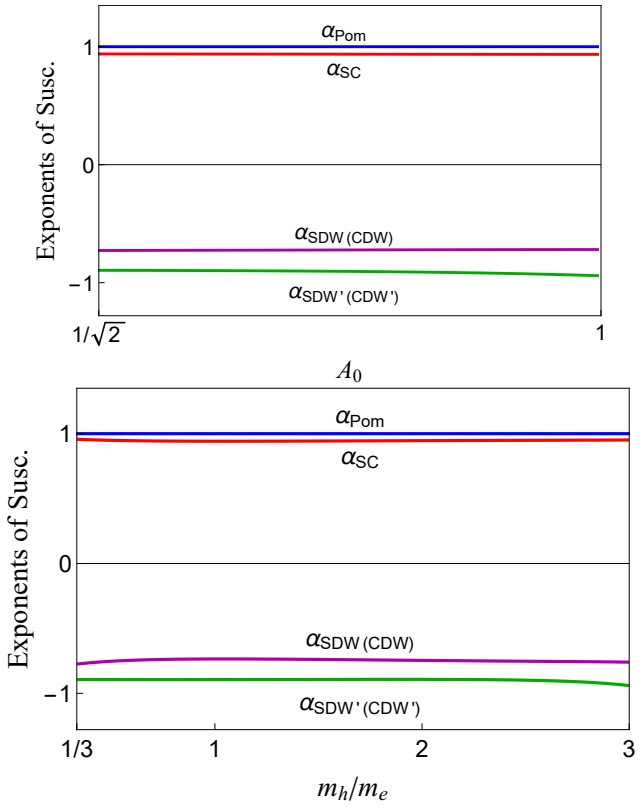

Figure 3.10: The exponents α_i for susceptibilities $\chi_0 \propto 1/(L_0 - L)^{\alpha_i}$ in SDW, SC, and d-wave Pomeranchuk channels for interactions on the weakly unstable fixed trajectory, Eq. (3.35). Upper panel – α_i as functions of A_0 at fixed $m_h/m_e = 1$. Lower panel – α_i as functions of m_h/m_e at fixed $A_0 = 0.8$. A larger exponent means a faster divergence of the susceptibility. We recall that A_0^2 determines a relative weight of $d_{xz}(d_{yz})$ and d_{xy} orbitals along the electron pockets.

ing gaps on hole and electron pockets and between various xy and xz/yz components of the orbital order parameter. We assume that the vertices Δ_i for superconductivity and Γ_i for orbital order ($i = 1-6$) in the equations Eqs. (3.47), (3.52), and (3.53), are proportional to the corresponding condensates in the ordered phases. Furthermore we assume that, with one exception, which we discuss below, the ratios between the components of Δ_i and Γ_i do not change between the onset of the order and lower T, at which they are measured by ARPES and other techniques.

We consider the superconducting channel first and then analyze the orbital channel.

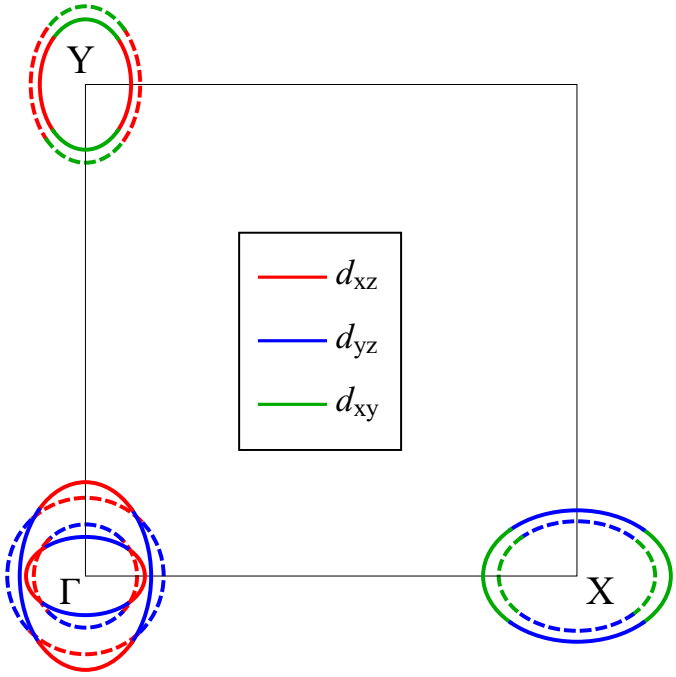

Figure 3.11: Electron structure in the nematic state above and below the onset of B_{1g} Pomeranchuk instability. The two originally circular hole pockets (dashed lines) are distorted into ellipses with orthogonal directions of elongation (solid lines). The electron pockets at X and Y, originally of the same size and form (dashed lines), become inequivalent in the presence of a nematic order (solid lines).

3.5.1 Superconducting order parameter

The vertices Δ_i represent fermionic bilinears in the particle-particle channel in the orbital basis. To obtain the superconducting order parameters on different pockets, we need to convert these Δ_i into band basis using the orbital-to-band transformation from Eq. (3.9). For the SC order parameter on hole pockets we obtain

$$\begin{aligned}\langle c_k c_{-k}\rangle &= \langle \cos^2\theta_h \psi_5(k)\psi_5(-k) + \sin^2\theta_h \psi_6(k)\psi_6(-k) \\ &\quad + \frac{1}{2}\sin 2\theta_h(\psi_5(k)\psi_6(-k) + \psi_6(k)\psi_5(-k))\rangle \\ &= \cos^2\theta_h \Delta_5 + \sin^2\theta_h \Delta_6 + \frac{1}{2}\sin 2\theta_h\,(\Delta_{5,6} + \Delta_{6,5}) \\ &= \Delta_5 \equiv \Delta_h \end{aligned} \tag{3.60}$$

and

$$\begin{aligned}\langle d_k d_{-k}\rangle &= \langle \sin^2\theta_h \psi_5(k)\psi_5(-k) + \cos^2\theta_h \psi_6(k)\psi_6(-k) \\ &+ \frac{1}{2}\sin 2\theta_h(\psi_5(k)\psi_6(-k) + \psi_6(k)\psi_5(-k))\rangle \\ &= \sin^2\theta_h \Delta_5 + \cos^2\theta_h \Delta_6 + \frac{1}{2}\sin 2\theta_h\,(\Delta_{5,6} + \Delta_{6,5}) \\ &= \Delta_5 \equiv \Delta_h \end{aligned} \tag{3.61}$$

The A_{1g} SC order parameter on the electron pocket near Y is

$$\begin{aligned}\langle f_{1,k} f_{1,-k}\rangle &= \langle \cos^2\phi_{e,k}\psi_1(k)\psi_1(-k) + \sin^2\phi_{e,k}\psi_2(k)\psi_2(-k) \\ &+ \frac{1}{2}\sin 2\phi_{e,k}(\psi_1(k)\psi_2(-k) + \psi_2(k)\psi_1(-k))\rangle \\ &= \cos^2\phi_{e,k}\Delta_1 + \sin^2\phi_{e,k}\Delta_2 \\ &= A_0^2\cos^2\theta_e\Delta_1 + (1 - A_0^2\cos^2\theta_e)\Delta_2 \\ &= (\frac{A_0^2}{2}\Delta_1 + (1 - \frac{A_0^2}{2})\Delta_2) + A_0^2\frac{\Delta_1 - \Delta_2}{2}\cos 2\theta_e \\ &= \Delta_{a,e} + \Delta_{b,e}\cos 2\theta_e, \end{aligned} \tag{3.62}$$

where $\Delta_{a,e} = \Delta_1 A_0^2/2 + \Delta_2(1 - A_0^2/2)$ and $\Delta_{b,e} = (\Delta_1 - \Delta_2)A_0^2/2$. The order parameter on the electron pocket near X is obtained from (3.62) by $\pi/2$ rotation:

$$\langle f_{2,k} f_{2,-k}\rangle = \Delta_{a,e} - \Delta_{b,e}\cos 2\theta_e, \tag{3.63}$$

The ratios of Δ_h, $\Delta_{a,e}$, and $\Delta_{b,e}$ are determined by extracting the components $\Delta_1 = \Delta_3, \Delta_2 = \Delta_4$, and $\Delta_5 = \Delta_6$ from the matrix equation (3.47), i.e. from the solution which corresponds to the largest eigenvalue of this matrix. We show the results for SC gaps on hole and electron pockets on the weakly unstable fixed trajectory in Fig. 3.12. We see that all three components $\Delta_h, \Delta_{a,e}$, and $\Delta_{b,e}$ are non-zero and of the same order. The two angle-independent components Δ_h and $\Delta_{a,e}$ have opposite signs, i.e., the A_{1g} order parameter has s^{+-} structure, as expected. We also see that $\Delta_{a,e} > \Delta_{b,e}$, i.e., there are no accidental nodes on the electron pockets. We note by passing that on the stable fixed trajectories the angular dependence of the gaps on the electron pockets becomes more pronounced.

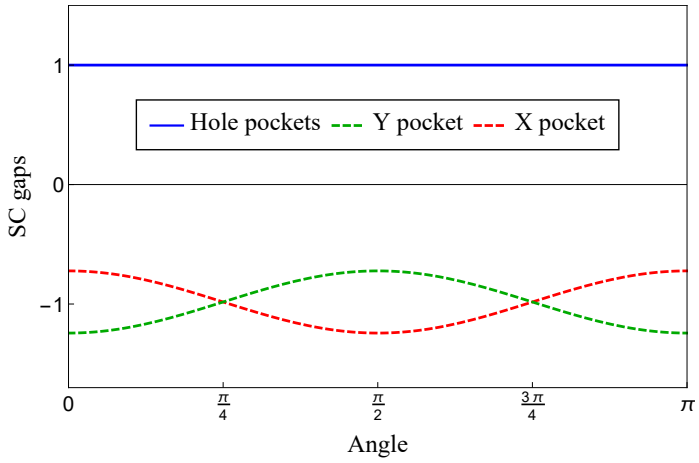

Figure 3.12: Superconducting gaps along the Fermi surfaces for the interactions on the weakly unstable fixed trajectory. The solid blue line is the gap Δ_h on the two hole pockets, the dashed lines are the gaps on the electron pockets – the green one is the gap on the Y pocket and red one is on the X pocket. The angle is counted anti-clockwise from k_x direction. We set $m_h/m_e = 1$, $A_0 = 0.8$.

3.5.2 Orbital order parameter

Long-range orbital order in our RG analysis emerges as a $d-$wave Pomeranchuk order. Such an order leads to unequal occupations of d_{xz} and d_{yz} orbital states near hole and electron pockets, and also to unequal occupations of d_{xy} orbital states near X and Y electron pockets. The three B_{1g} order parameters in the orbital basis are $\Gamma_{1,e} = n^Y_{xz} - n^X_{yz}$, $\Gamma_{1,h} = n^\Gamma_{xz} - n^\Gamma_{yz}$, and $\Gamma_{2,e} = n^Y_{xy} - n^X_{xy}$. In our notations, $\Gamma_{1,e} = \Gamma_1 - \Gamma_3 = 2\Gamma_1, \Gamma_{2,e} = \Gamma_2 - \Gamma_4 = 2\Gamma_2$, and $\Gamma_{1,h} = \Gamma_6 - \Gamma_5 = 2\Gamma_6$. Transforming from orbital to band basis, we obtain for electron and hole densities

$$
\begin{aligned}
\langle f^\dagger_{1,k} f_{1,k}\rangle &\propto (\frac{A_0^2}{2}\Gamma_1 + (1-\frac{A_0^2}{2})\Gamma_2) + A_0^2\frac{\Gamma_1-\Gamma_2}{2}\cos 2\theta_e \\
&\equiv \Gamma_{a,e} + \Gamma_{b,e}\cos 2\theta_e \\
\langle f^{dag}_{2,k} f_{2,k}\rangle &\propto (\frac{A_0^2}{2}\Gamma_3 + (1-\frac{A_0^2}{2})\Gamma_4) + (A_0^2\frac{\Gamma_3-\Gamma_4}{2})cos2\theta_e \\
&= -(\frac{A_0^2}{2}\Gamma_1 + (1-\frac{A_0^2}{2})\Gamma_2) + A_0^2\frac{\Gamma_1-\Gamma_2}{2}\cos 2\theta_e \\
&= -\Gamma_{a,e} + \Gamma_{b,e}\cos 2\theta_e \\
\langle c^\dagger_k c_k\rangle &\propto \cos^2\theta_h\Gamma_5 + \sin^2\theta_h\Gamma_6 = -\cos 2\theta_h\Gamma_6
\end{aligned}
$$

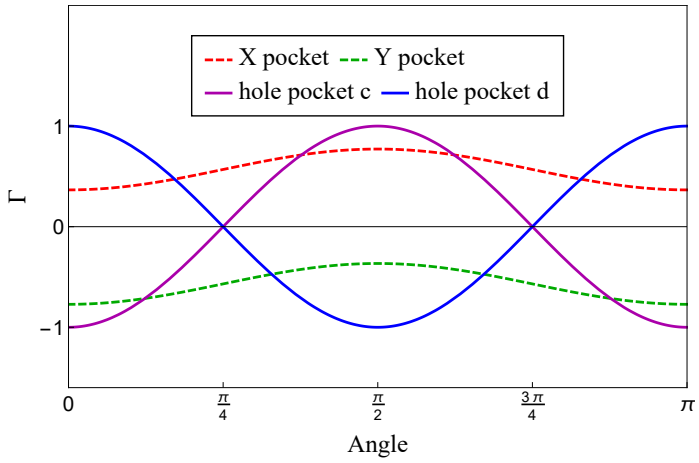

Figure 3.13: $d-$wave Pomeranchuk order parameters (Eq. 3.64) for interactions on the weakly unstable fixed trajectory. The order parameters on the hole pockets are shown by solid lines, and the ones on the electron pockets by dashed lines. The $\cos 2\theta$ form of order parameters on the hole pockets deform C_4-symmetric hole pockets into ellipses, with long axis along orthogonal directions on the two pockets. Almost constant order parameters of opposite sign on the two electron pockets make one pocket larger and the other smaller in the nematic phase (see Fig. 3.11). The angle θ is counted anti-clockwise from k_x direction. We use $m_h/m_e = 1$, $A_0 = 0.8$ to determine the order parameters on the electron pockets. The overall magnitude of the order parameters on the hole pockets was adjusted to be comparable to that on the electron pockets.

$$\langle d_k^\dagger d_k \rangle \propto \cos^2\theta_h \Gamma_6 + \sin^2\theta_h \Gamma_5 = \cos 2\theta_h \Gamma_6, \tag{3.64}$$

where $\Gamma_{a,e} = \Gamma_1 A_0^2/2 + \Gamma_2(1 - A_0^2/2)$ and $\Gamma_{b,e} = (\Gamma_1 - \Gamma_2)A_0^2/2$. We show the order parameters on hole and electron pockets in Fig. 3.13. Like in the superconducting case, we extract the relations between Γ_1, Γ_2, and Γ_6 from the matrix equation (3.54), i.e. from the solution which corresponds to the largest eigenvalue.

Exactly on the weakly unstable fixed trajectory the 3×3 matrix $M_{B_{1g}}$ decouples into the 2×2 set for Γ_1 and Γ_2 and a single equation for Γ_6, because ϵ_1 and ϵ_2 in (3.54) vanish. From the 2×2 set one can obtain the ratio $\Gamma_1/\Gamma_2 = \Gamma_{1,e}/\Gamma_{2,e}$. The ratio does depend on A_0, but is generally close to one (see Fig. 3.14). This result implies that the $d-$wave order parameters made out of d_{xz}/d_{yz} orbitals and d_{xy} orbitals at X and at Y pockets are nearly equal. This is very different from the behavior on the two stable fixed trajectories, where either Γ_1 or Γ_2 vanishes.

To obtain the ratios of the order parameters on hole and on electron pockets, e.g.

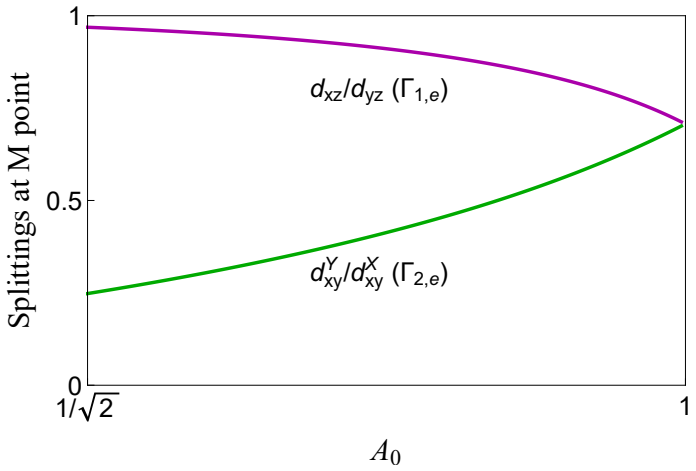

Figure 3.14: The orbital order parameters on the electron pockets $\Gamma_{1,e} = n^Y_{xz} - n^X_{yz} = 2\Gamma_1$ and $\Gamma_{2,e} = n^Y_{xy} - n^X_{xy} = 2\Gamma_2$ as functions of A_0 at fixed $m_h/m_e = 1$ for interactions on the weakly unstable fixed trajectory. Each order parameter determines the splitting of the corresponding bands at M point in the 2Fe BZ.

$\Gamma_6/\Gamma_1 = \Gamma_{1,h}/\Gamma_{1,e}$, one needs to include the fact that in reality the system approaches a fixed trajectory in the process of the RG flow, but is never strictly on the fixed trajectory, i.e., ϵ_1 and ϵ_2 are small but non-zero. Analyzing the RG flow towards the weakly unstable fixed trajectory, we find that $\Gamma_{1,h}/\Gamma_{1,e}$ is *negative* and its magnitude is large.

3.5.3 Implications for experiments

We now compare our theoretical results with the experiments on FeSe, where at ambient pressure a nematic order has been observed below $85K$, and superconductivity has been observed below $8K$. This sequence of transitions is consistent with the outcome of our RG analysis. We identify the nematic order with a spontaneous $d-$wave orbital order.

The most generic feature of $d-$wave orbital order is the elongation of the pockets due to breaking of C_4 lattice rotational symmetry down to C_2. This effect is particularly pronounced for the two hole pockets, which in the absence of orbital order are C_4-symmetric. Below the nematic transition, the pockets become elongated. In the 2Fe Brillouin zone, where ARPES experiments are performed, one pocket becomes elongated along one BZ diagonal and the other along the other zone diagonal (see Fig. 3.15). Such an elongation has been observed in ARPES experiments on FeSe by several groups [12, 86, 87]. In addition, there is an elongation of electron pockets as well. In the 2Fe BZ the X and the Y electron

pockets are centered at the same M point (Fig. 3.15). The two form an inner and outer pocket that touch each other in the absence of spin-orbit coupling, but split in the presence of such a coupling. The inner pocket predominantly consists of d_{xz} and d_{yz} orbital states, the outer pocket is predominantly made out out of d_{xy} orbital states. Above the nematic transition both inner and outer pockets are C_4-symmetric, but in the presence of orbital order each pocket is elongated along the diagonal directions (Fig. 3.15).

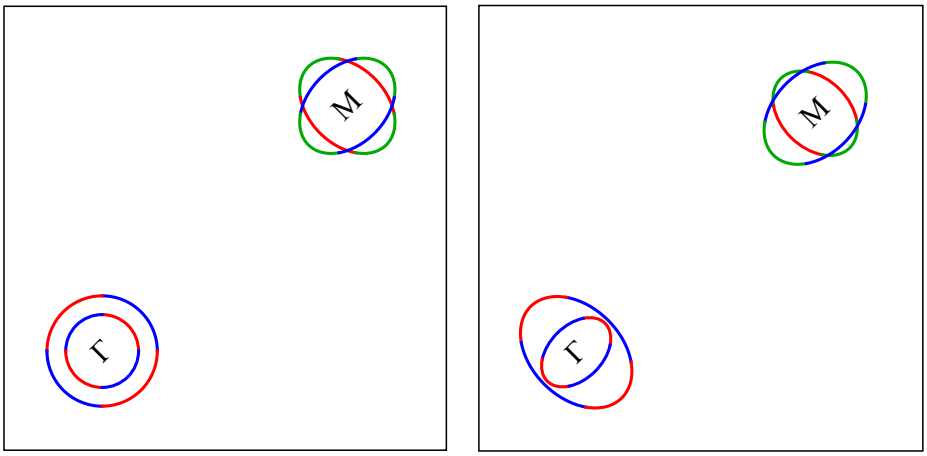

Figure 3.15: Left panel – Fermi surfaces in 2Fe Brillouin zone above the nematic transition. Each of the two hole pockets is C_4 symmetric. The two electron pockets are centered at $M = (\pi, \pi)$ and form an inner and outer pockets. The inner pocket predominantly consists of d_{xz} and d_{yz} orbital states, the outer pocket is predominantly made out out of d_{xy} orbital states. These pockets touch each other along $\tilde{k}_x = \pi$ and $\tilde{k}_y = \pi$ directions ($\tilde{\mathbf{k}}$ is the momentum in 2Fe BZ). Within our model, the location of the pockets in 2Fe BZ and their dispersion can be obtained by a simple folding, i.e, by changing momentum components k_x and k_y in the 1Fe BZ to $\tilde{k}_x = k_x + k_y$ and $\tilde{k}_y = k_y - k_x$. Spin-orbit interaction, however, splits the inner and the outer pockets. Right panel – the structure of hole and electron pockets in the nematic phase in the 2Fe BZ.

The orbital order also affects the states away from the Fermi surface, in particular the hierarchy of electronic states at high-symmetry Γ and M points in the 2Fe BZ. In the absence of orbital order, the states at M are doubly degenerate even in the presence of spin-orbit interaction [85] (left panel in Fig. 3.16). One degeneracy is between d_{xz} and d_{yz} states, another is between two d_{xy} states. In the 1Fe Brillouin zone one of the states in each subset comes from the pocket at X, another from the pocket at Y. In the presence of orbital order, these degenerate states split. The splitting of d_{xz}/d_{yz} states is $2\Gamma_{1,e}(= 4\Gamma_1)$, the splitting of d_{xy} states is $2\Gamma_{2,e}(= 4\Gamma_2)$. Assuming that one can extend the results of the

RG analysis to the high-symmetry points, one can compare the ratios of the two splittings between theory and experiment. In the RG analysis, either $\Gamma_{1,e}$ or $\Gamma_{2,e}$ vanish on the stable fixed trajectories, but the ratio of the two is close to one on the weakly unstable fixed trajectory (see Fig. 3.14).

ARPES data for $\Gamma_{1,e}/\Gamma_{2,e}$ from different groups [12, 87, 88, 86] are similar but not identical. We will use recent ARPES data from Ref. [12] for comparison. These authors have found that the magnitudes of the splittings within d_{xz}/d_{yz} and d_{xy} subsets are close to each other – each is about 15 meV. In our notations, this implies that $\Gamma_{1,e} \approx \Gamma_{2,e} \approx 7.5$ meV. Such near-equal splitting is not reproduced on the two stable fixed trajectories, but it is well reproduced on the weakly unstable fixed trajectory. We illustrate this in Figs. 3.16 and 3.17. We argue, based on this comparison, that the RG analysis does agree with the ARPES data on the electron pockets, if, indeed, the parameters for FeSe are such that the system is in the basin of attraction of the weakly unstable fixed trajectory.

The comparison with orbital order on the hole pockets requires more care. On one hand, Suzuki et al reported [89], based on their ARPES data, that the signs of the d_{xz}/d_{yz} order parameters on hole and electron pockets are opposite. This is consistent with the RG result that on the weakly unstable fixed trajectory, as we found that $\Gamma_{1,h}$ and $\Gamma_{1,e}$ have different signs [the same sign difference between $\Gamma_{1,h}$ and $\Gamma_{1,e}$ holds on the two stable fixed trajectories [11]]. On the other hand, our RG analysis yields a larger magnitude of $\Gamma_{1,h}$ than that of $\Gamma_{1,e}$, and, hence, a larger splitting at the Γ point than that at the M point. The authors of Ref. [12], meanwhile, argued that the splitting at Γ is comparable to that at M. However, when comparing our RG result for $\Gamma_{1,h}$ with the measured splitting at Γ, one has to bear in mind that our $\Gamma_{1,h}$ was obtained without spin-orbit coupling. Meanwhile, Ref. [12] found that the splitting at Γ largely survives above the nematic transition and hence is predominantly due to spin-orbit coupling, which is known to split the bands at Γ already in the absence of an orbital order [85]. The $\Gamma_{1,h} \sim 15$ meV was extracted from the ARPES data in Ref. [12] by detecting an additional splitting in the nematic phase at low T. Because of this, a meaningful comparison of the magnitude of $\Gamma_{1,h}$ between experiment and theory is only possible after the inclusion of spin-orbit interaction into the theoretical analysis.

3.6 Conclusion

In this communication we reported the results of the parquet RG study of competing instabilities in the full 2D four pocket, three orbital low-energy model for FeSCs. Our four-pocket

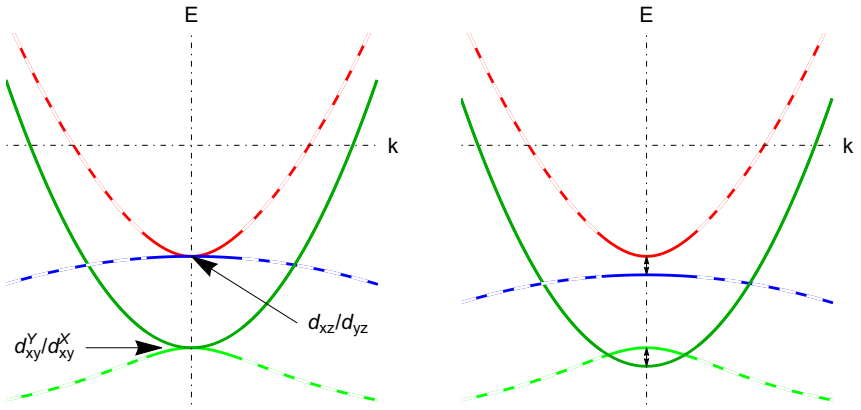

Figure 3.16: The splittings in the band dispersions near the M point in the 2Fe BZ for interaction on the weakly unstable fixed trajectory. The M point is taken as the origin of the coordinates and the cut is along $M - \Gamma$ ($k_x = k_y = k$). Left panel – above the nematic transition. Right panel – in the nematic phase. Solid and dashed lines describe excitations with near-pure and mixed orbital content, respectively.

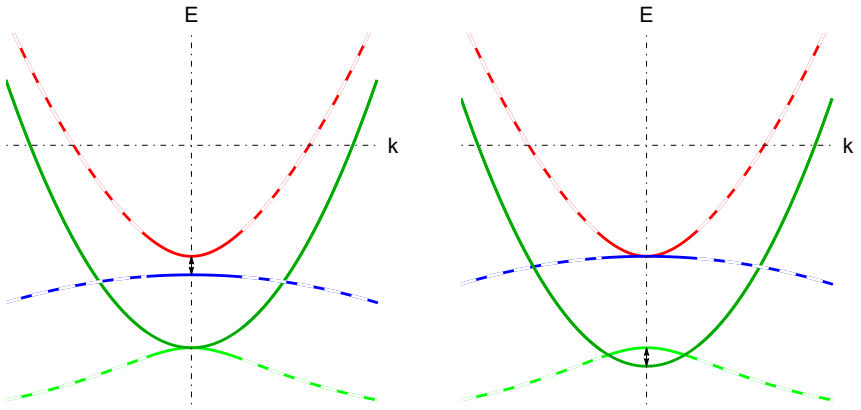

Figure 3.17: The same as in Fig. 3.16 but for interactions on one of the two stable fixed trajectories. In this situation either the splitting between d_{xz}/d_{yz} bands or the splitting between the two d_{xy} bands vanishes.

model consists of two Γ- centered hole pockets, made out of d_{xz} and d_{yz} orbitals, and two symmetry-related electron pockets centered at $X = (\pi, 0)$ and $Y = (0, \pi)$ points in the 1Fe BZ and made out of d_{yz}/d_{xy} and d_{xz}/d_{xy} orbitals, respectively. We derived and analyzed the RG flow of 30 couplings, which describe all symmetry-allowed interactions between low-

energy fermions. Despite that the number of couplings is large, we argued that there are only two stable fixed trajectories of the RG flow and one weakly unstable trajectory with a single unstable direction. On one stable trajectory the interactions involving d_{xz}/d_{yz} orbital components on electron pockets vanish relative to interactions involving d_{xy} components, on the other interactions involving d_{xy} orbital components vanish relative to d_{xz}/d_{yz} components. On the weakly unstable trajectory, interactions involving d_{xz}/d_{yz} and d_{xy} orbital states on electron pockets remain comparable. The behavior along the two stable fixed trajectories has been analyzed in Ref. [11]. In this work we analyzed the system behavior along the weakly unstable trajectory. We argued, based on the analysis of susceptibilities along this trajectory, that the leading instability upon lowering the temperature is towards a *three-component* d-wave orbital nematic order. Two orbital components are the differences between fermionic densities on d_{xz} and d_{yz} orbitals on hole pockets and on electron pockets, $\Gamma_{1,h} = n^{\Gamma}_{xz} - n^{\Gamma}_{yz}$, $\Gamma_{1,e} = n^{Y}_{xz} - n^{X}_{yz}$, the third one is the difference between the densities of d_{xy} orbitals on X and Y pockets, $\Gamma_{2,e} = n^{Y}_{xy} - n^{X}_{xy}$. In our RG analysis, the magnitudes of $\Gamma_{1,e}$ and $\Gamma_{2,e}$ turn out to be nearly equal, and the sign of $\Gamma_{1,h}$ is opposite to that of $\Gamma_{1,e}$. We applied the results to FeSe and found both qualitative and quantitative agreement with ARPES data [12, 87, 86, 89], specifically on the ratio of $\Gamma_{1,e}/\Gamma_{2,e}$. We argue, based on this agreement and the fact that Fermi surfaces in FeSe are all small, that the nematicity, observed in FeSe below $85K$ is likely the result of a spontaneous orbital order, which is captured by RG. The situation in other Fe-pnictides, where either hole or/and electron pockets are larger, is different, and there the nematic order is likely due to softening of composite spin fluctuations. This last scenario gives rise to a two-step magnetic transition into the stripe SDW state, with an intermediate Ising-nematic phase, in which C_4 symmetry is broken, but $O(3)$ spin-rotation symmetry remains intact.

3.7 Supplementary material

3.7.1 Details of RG analysis on fixed trajectories

As we wrote in Sec. 3.3.2, the solution of the parquet RG equations leads to a divergence of various couplings, which occurs in a universal way in the sense that the coupling ratios tend to constants. These constants characterize the different solutions - the fixed trajectories - of the flow. In the following we present the detailed solution of the parquet RG equations and the stability analysis of the resulting fixed trajectories.

3.7.1.1 Stable fixed trajectories

For the first fixed trajectory we rewrite all couplings in terms of the ratios $\gamma_i, \tilde{\gamma}_i$ as $u_i = \gamma_i u_1$, $\tilde{u}_i = \tilde{\gamma}_i u_1$. This leads to flow equations for the ratios $u_1 \frac{d\gamma_i}{dL} = \frac{d}{dL} u_i - \gamma_i \frac{d}{dL} u_1$ and analogously for $\tilde{\gamma}_i$. A fixed trajectory is set by conditions $\frac{d\gamma_i}{dL} = 0$. In our case

$$\begin{aligned}
\dot{u}_1 &= u_1^2 + u_3^2/C^2 \\
\tilde{\gamma}_1(1+\gamma_3^2/C^2) &= \tilde{\gamma}_1^2 + \tilde{\gamma}_3^2/\tilde{C}^2 \\
\gamma_2(1+\gamma_3^2/C^2) &= 2\gamma_2 - 2\gamma_2^2 \\
\tilde{\gamma}_2(1+\gamma_3^2/C^2) &= 2\tilde{\gamma}_1\tilde{\gamma}_2 - 2\tilde{\gamma}_2^2 \\
\gamma_3(1+\gamma_3^2/C^2) &= -2\gamma_3\gamma_5 - 2\tilde{\gamma}_3\gamma_7 - E(2\tilde{\gamma}_3\gamma_5 \\
&\quad + 2\gamma_3\gamma_7) - 2\gamma_3\gamma_4 + 4\gamma_3 - 2\gamma_2\gamma_3 \\
\tilde{\gamma}_3(1+\gamma_3^2/C^2) &= -2\gamma_3\gamma_7 - 2\tilde{\gamma}_3\gamma_6 - E(2\gamma_3\gamma_6 \\
&\quad + 2\tilde{\gamma}_3\gamma_7) - 2\tilde{\gamma}_3\gamma_4 + 4\tilde{\gamma}_1\tilde{\gamma}_3 - 2\tilde{\gamma}_2\tilde{\gamma}_3 \\
\gamma_4(1+\gamma_3^2/C^2) &= -2\gamma_3^2 - 2\tilde{\gamma}_3^2 - E(4\gamma_3\tilde{\gamma}_3) - 2\gamma_4^2 \\
\gamma_5(1+\gamma_3^2/C^2) &= -2\gamma_5^2 - 2\gamma_7^2 - E(4\gamma_5\gamma_7) - 2\gamma_3^2 \\
\gamma_6(1+\gamma_3^2/C^2) &= -2\gamma_7^2 - 2\gamma_6^2 - E(4\gamma_6\gamma_7) - 2\tilde{\gamma}_3^2 \\
\gamma_7(1+\gamma_3^2/C^2) &= -2\gamma_5\gamma_7 - 2\gamma_6\gamma_7 - E(2\gamma_5\gamma_6 + 2\gamma_7^2) \\
&\quad - 2\gamma_3\tilde{\gamma}_3.
\end{aligned} \tag{3.65}$$

The solutions for γ_i in Ref. [11] are reproduced by setting $\tilde{\gamma}_1 = \gamma_2 = \tilde{\gamma}_2 = \tilde{\gamma}_3 = \gamma_6 = \gamma_7 = 0$ to obtain

$$\begin{aligned}
\gamma_3(1+\gamma_3^2/C^2) &= -2\gamma_3\gamma_5 - 2\gamma_3\gamma_4 + 4\gamma_3 - 2\gamma_2\gamma_3 \\
\gamma_4(1+\gamma_3^2/C^2) &= -2\gamma_3^2 - 2\gamma_4^2 \\
\gamma_5(1+\gamma_3^2/C^2) &= -2\gamma_5^2 - 2\gamma_3^2
\end{aligned} \tag{3.66}$$

This leads to the following five solutions

(1) $\gamma_3 = \pm C\sqrt{-1 + 8C^2 + 4\sqrt{1 - C^2 + 4C^4}}$
$\gamma_4 = \gamma_5 = 1 - 2C^2 \pm \sqrt{1 - C^2 + 4C^4}$

(2) $\gamma_3 = 0, \gamma_4 = -\frac{1}{2}, \gamma_5 = -\frac{1}{2}$

(3) $\gamma_3 = 0, \gamma_4 = -\frac{1}{2}, \gamma_5 = 0$

(4) $\gamma_3 = 0, \gamma_4 = 0, \gamma_5 = -\frac{1}{2}$

(5) $\gamma_3 = 0, \gamma_4 = 0, \gamma_5 = 0$

Analyzing the stability as explained in the next section, we find that solutions (2)-(5) are unstable with more than one unstable direction. Additionally the negative sign in the expression for γ_4 and γ_5 in solution (1) also leads to several unstable directions. Regarding the remaining solution in (1), we anticipate that it is stable and that γ_3 retains a positive sign, because its initial value is positive for repulsive interactions. Therefore we obtain as a first stable fixed trajectory

$$\begin{aligned} u_1(L) &= \frac{1}{1+\gamma_3^2/C^2}\frac{1}{L_0-L}, \\ \gamma_3 &= +C\sqrt{-1+8C^2+4\sqrt{1-C^2+4C^4}}, \\ \gamma_4 &= \gamma_5 = 1-2C^2-\sqrt{1-C^2+4C^4}, \end{aligned} \tag{3.67}$$

which corresponds to Eq. (3.33) of the main text.

To obtain the second stable fixed trajectory, Eq. 3.34 in the main text, we write the couplings as $u_i = \gamma_i \tilde{u}_1$, $\tilde{u}_i = \tilde{\gamma}_i \tilde{u}_1$. One finds the same structure of equations as above (Eq. (3.66)) with γ_3 replaced by $\tilde{\gamma}_3$, γ_5 by γ_6, and C by $\tilde{C}$. The stability analysis then is analogous to the one for Eq. (3.66), and we obtain as second stable fixed trajectory

$$\begin{aligned} \tilde{u}_1(L) &= \frac{1}{1+\tilde{\gamma}_3^2/\tilde{C}^2}\frac{1}{L_0-L}, \\ \tilde{\gamma}_3 &= +\tilde{C}\sqrt{-1+8\tilde{C}^2+4\sqrt{1-\tilde{C}^2+4\tilde{C}^4}}, \\ \gamma_4 &= \gamma_6 = 1-2\tilde{C}^2-\sqrt{1-\tilde{C}^2+4\tilde{C}^4}. \end{aligned} \tag{3.68}$$

3.7.1.2 Weakly unstable fixed trajectory

Since in the case of the weakly unstable fixed trajectory the situation is more involved, we first consider the simpler case when $C = \tilde{C}$ (implying $A_0 = 1$). Then the parquet RG equations simplify to

$$\begin{aligned} u_1 &= \tilde{u}_1 \\ u_2 &= \tilde{u}_2 \end{aligned}$$

$$
\begin{aligned}
u_3 &= \tilde{u}_3 \\
u_5 &= u_6 \\
\dot{u}_1 &= u_1^2 + u_3^2/C^2 \\
\dot{u}_2 &= 2u_1u_2 - 2u_2^2 \\
\dot{u}_3 &= -2u_3u_5(1+E) - 2u_3u_7(1+E) \\
&\quad - 2u_3u_4 + 4u_1u_3 - 2u_2u_3 \\
\dot{u}_4 &= -4u_3^2(1+E) - 2u_4^2 \\
\dot{u}_5 &= -2u_5^2 - 2u_7^2 - E(4u_5u_7) - 2u_3^2 \\
\dot{u}_7 &= -4u_5u_7 - E(2u_5^2 + 2u_7^2) - 2u_3^2.
\end{aligned} \tag{3.69}
$$

We again reformulate these equations in terms of $u_i = \gamma_i u_1$ and determine the ratios γ_i. We solve the resulting algebraic set of equations numerically. We find that solutions with $\gamma_3 = 0$ are truly unstable and as above $\gamma_3 < 0$ cannot be reached with repulsive initial conditions. For $\gamma_3 > 0$ and varying C and E, we find two solutions. One of them exhibits only one unstable directions, while the second one is more unstable. For example, when $m_h/m_e = 1$ and $A_0 = 1$, we get $C = \sqrt{\frac{3}{2}}$ and $E = \frac{1}{3}$, and the two solutions are $\gamma_2 = 0$ and

$$
\begin{aligned}
&\gamma_3 = 9.66, \gamma_4 = -14.81, \gamma_5 = \gamma_6 = -5.55, \gamma_7 = -5.55; \\
&\gamma_3 = 9.66, \gamma_4 = -14.81, \gamma_5 = \gamma_6 = -29.27, \gamma_7 = 18.16
\end{aligned} \tag{3.70}
$$

In this case the first fixed trajectory has one unstable direction and the second fixed trajectory has three such directions.

Also in the general case, when $\tilde{C} \neq C$, there are two solutions for $\gamma_3 > 0$. Both are unstable with one and three unstable directions. We call the solution with only one unstable direction, the weakly unstable fixed trajectory. Explicitly the solutions for general $\tilde{C} \neq C$ are determined by

$$
\begin{aligned}
&\tilde{\gamma}_1 = 1, \quad \gamma_2 = \tilde{\gamma}_2 = 0, \quad \tilde{\gamma}_3 = \frac{\tilde{C}}{C}\gamma_3 \\
&\gamma_3 = \sqrt{-C^2\left[\left(1 + E\frac{\tilde{C}}{C} + \alpha\left(\frac{\tilde{C}}{C} + E\right)\right)2\gamma_5 + 2\beta\left(\frac{\tilde{C}}{C} + E\right)\gamma_6 + 2\gamma_4 - 3\right]} \\
&\gamma_4 = -\frac{1}{2}\left(c_1 - 3 + \frac{c_2}{a_1\gamma_5 + b_1\gamma_6 + c_3}\right) \\
&\gamma_7 = \alpha\gamma_5 + \beta\gamma_6,
\end{aligned} \tag{3.71}
$$

where γ_5 and γ_6 are given by the solution of the following two equations of third order

$$
\begin{aligned}
&(-a_1^2 + a_1 x_1)\gamma_5^3 + (-2a_1 b_1 + b_1 x_1 + a_1 z_1)\gamma_5^2\gamma_6 + (-a_1 - a_1 c_1 - a_1 c_3 - 2a_1^2 C^2 + c_3 x_1)\gamma_5^2 \\
&+ (-b_1^2 + a_1 y_1 + b_1 z_1)\gamma_5\gamma_6^2 + (-b_1 - b_1 c_1 - b_1 c_3 - 4a_1 b_1 C^2 + c_3 z_1)\gamma_5\gamma_6 \\
&+ (-c_2 - c_3 - c_1 c_3 - 2a_1 c_1 C^2 - 2a_1 c_3 C^2)\gamma_5 + b_1 y_1 \gamma_6^3 + (-2b_1^2 C^2 + c_3 y_1)\gamma_6^2 \\
&+ (-2b_1 c_1 C^2 - 2b_1 c_3 C^2)\gamma_6 + (-2c_2 C^2 - 2c_1 c_3 C^2) = 0 \\
&a_1 x_2 \gamma_5^3 + (-a_1^2 + b_1 x_2 + a_1 z_2)\gamma_5^2\gamma_6 + (-2a_1^2 \tilde{C}^2 + c_3 x_2)\gamma_5^2 + (-2a_1 b_1 + a_1 y_2 + b_1 z_2)\gamma_5\gamma_6^2 \\
&+ (-a_1 - a_1 c_1 - a_1 c_3 - 4a_1 b_1 \tilde{C}^2 + c_3 z_2)\gamma_5\gamma_6 + (-2a_1 c_1 \tilde{C}^2 - 2a_1 c_3 \tilde{C}^2)\gamma_5 + (-b_1^2 + b_1 y_2)\gamma_6^3 \\
&+ (-b_1 - b_1 c_1 - b_1 c_3 - 2b_1^2 \tilde{C}^2 + c_3 y_2)\gamma_6^2 + (-c_2 - c_3 - c_1 c_3 - 2b_1 c_1 \tilde{C}^2 - 2b_1 c_3 \tilde{C}^2)\gamma_6 \\
&+ (-2c_2 \tilde{C}^2 - 2c_1 c_3 \tilde{C}^2) = 0
\end{aligned}
\tag{3.72}
$$

In these expressions, we introduced the parameters

$$
\begin{aligned}
\alpha &= -(1 + E\frac{\tilde{C}}{C})/(\frac{\tilde{C}}{C} - \frac{C}{\tilde{C}}) \\
\beta &= (1 + E\frac{C}{\tilde{C}})/(\frac{\tilde{C}}{C} - \frac{C}{\tilde{C}}) \\
a_1 &= -2((1 + E\frac{\tilde{C}}{C}) + \alpha(\frac{\tilde{C}}{C} + E)) \\
b_1 &= -2\beta(\frac{\tilde{C}}{C} + E) \\
c_1 &= 3 + 4C^2(1 + \frac{\tilde{C}^2}{C^2} + 2E\frac{\tilde{C}}{C}) \\
c_2 &= 4C^2(1 + \frac{\tilde{C}^2}{C^2} + 2E\frac{\tilde{C}}{C})(4C^2(1 + \frac{\tilde{C}^2}{C^2} + 2E\frac{\tilde{C}}{C}) - 1) \\
c_3 &= 4 - 4C^2(1 + \frac{\tilde{C}^2}{C^2} + 2E\frac{\tilde{C}}{C}) \\
x_1 &= -2(1 + \alpha^2 + 2\alpha E) \\
y_1 &= -2\beta^2; \\
z_1 &= -(4\alpha\beta + 4\beta E) \\
x_2 &= -2\alpha^2 \\
y_2 &= -2(1 + \beta^2 + 2\beta E) \\
z_2 &= -(4\alpha\beta + 4\alpha E)
\end{aligned}
\tag{3.73}
$$

As we said, there are two solutions for γ_5 and γ_6, which we obtain numerically with A_0 and m_h/m_e as parameters. One of them leads to the weakly unstable trajectory with a single unstable direction and the other leads to the solution with three unstable directions.

3.7.2 Stability analysis

As we have explained in App. 3.7.1, the calculation of fixed trajectories can conveniently be done by transforming the parquet RG equations for the couplings to equations for the ratios $\gamma_i, \tilde{\gamma}_i$. The ratios are determined by choosing one of the relevant couplings, e.g. u_1, and rewriting the other couplings as $u_i = \gamma_i u_1$ and $\tilde{u}_i = \tilde{\gamma}_i u_1$. We can hence analyze the stability of different fixed trajectories in terms of the flow equations for the ratios. Therefore we consider small deviations of γ_i from their values on a fixed trajectory and determine whether these deviations increase or decrease during the RG flow. We label the flow equations for the ratios as $\beta_i = \frac{d}{dL}\gamma_i$, $\tilde{\beta}_i = \frac{d}{dL}\tilde{\gamma}_i$, and the deviations from a fixed trajectory as $\delta = \gamma - \gamma^{fixpoint}$. Linearizing the flow equations for small deviations from a fixed trajectory we obtain

$$\begin{pmatrix} \dot{\tilde{\delta}}_1 \\ \dot{\delta}_2 \\ \dot{\tilde{\delta}}_2 \\ \dot{\delta}_3 \\ \dot{\tilde{\delta}}_3 \\ \dot{\delta}_4 \\ \dot{\delta}_5 \\ \dot{\delta}_6 \\ \dot{\delta}_7 \end{pmatrix} = \begin{pmatrix} \frac{\partial\tilde{\beta}_1}{\partial\tilde{\gamma}_1} & \frac{\partial\tilde{\beta}_1}{\partial\gamma_2} & \cdots & \frac{\partial\tilde{\beta}_1}{\partial\gamma_7} \\ \frac{\partial\beta_2}{\partial\tilde{\gamma}_1} & \frac{\partial\beta_2}{\partial\gamma_2} & \cdots & \frac{\partial\beta_2}{\partial\gamma_7} \\ \vdots & \vdots & \ddots & \vdots \\ \frac{\partial\beta_7}{\partial\tilde{\gamma}_1} & \frac{\partial\beta_7}{\partial\gamma_2} & \cdots & \frac{\partial\beta_7}{\partial\gamma_7} \end{pmatrix} \begin{pmatrix} \tilde{\delta}_1 \\ \delta_2 \\ \tilde{\delta}_2 \\ \delta_3 \\ \tilde{\delta}_3 \\ \delta_4 \\ \delta_5 \\ \delta_6 \\ \delta_7 \end{pmatrix} \tag{3.74}$$

The eigenvalues of the stability matrix $\partial\beta_i/\partial\gamma_i$ at γ_i taken on the fixed trajectory determine if deviations grow or flow back to a given fixed trajectory. A positive eigenvalue signals growing deviations, and therefore an unstable direction corresponding to the eigenvector of the positive eigenvalue. Attaining such an unstable fixed trajectory requires fine tuning of initial conditions, and with more positive eigenvalues, more initial couplings must be fined-tuned. Only if all eigenvalues are negative, deviations in every direction will decrease during the flow. This is what happens for a stable fixed trajectory.

For example for the stable fixed trajectory of Eq. (3.33) (i.e. Eq. (3.67) in the supplementary material), the eigenvalues for the stability matrix are $-4u_1$, $-4(2C^2+\sqrt{1-C^2+4C^4})u_1$,

$-4(2C^2+\sqrt{1-C^2+4C^4})u_1$, $-4(2C^2+\sqrt{1-C^2+4C^4})u_1$, $-4(2C^2-\frac{1}{2}+\sqrt{1-C^2+4C^4})u_1$, $-2(1+2C^2+\sqrt{1-C^2+4C^4}\pm C\sqrt{-1+8C^2+4\sqrt{1-C^2+4C^4}})u_1$ and $-(1+8C^2+4\sqrt{1-C^2+4C^4}\pm\sqrt{-15+32C^2+16\sqrt{1-C^2+4C^4}})u_1$. Since u_1 is positive, these eigenvalues are negative for any C, i.e. the fixed trajectory is stable. Analogously we determine that the fixed trajectory of Eq. (3.34) (Eq. (3.68) in the supplementary material) is stable and that the weakly unstable fixed trajectory Eq. (3.35) (Eq. (3.71) in the supplementary material) has merely one unstable direction. Furthermore we find that this single unstable direction is weak in the sense that the corresponding eigenvalue is small.

3.7.3 Subleading ordering tendencies

In the main text, we have discussed instabilities towards superconducting order, $(\pi,0)$ and $(0,\pi)$ SDWs, and Pomeranchuk order in the A_{1g} and B_{1g} channel. We also considered further instabilities regarding CDW order, SDW order with momentum transfer (π,π) and Pomeranchuk order in the A_{2g} and B_{2g} channel. However, we found them to be subleading. We discuss the details in the following.

3.7.3.1 Charge density wave (CDW) channel at $(0,\pi)$ and $(\pi,0)$

A CDW instability breaks the translational symmetry of the lattice and is characterized by particle-hole order parameters at finite momenta, $(0,\pi)$ and $(\pi,0)$.

In this case, we define the auxiliary complex test fields as follows,

$$\begin{aligned} &H_{CDW} = \\ &\sum_{k\sigma}[\delta_1^{(0)}\psi^\dagger_{1,\sigma}(k)\psi_{5,\sigma}(k)+\delta_{1'}^{(0)}\psi^\dagger_{1,\sigma}(k)\psi_{6,\sigma}(k) \\ &\quad+\delta_2^{(0)}\psi^\dagger_{2,\sigma}(k)\psi_{5,\sigma}(k)+\delta_{2'}^{(0)}\psi^\dagger_{2,\sigma}(k)\psi_{6,\sigma}(k) \\ &\quad+\delta_3^{(0)}\psi^\dagger_{3,\sigma}(k)\psi_{6,\sigma}(k)+\delta_{3'}^{(0)}\psi^\dagger_{3,\sigma}(k)\psi_{5,\sigma}(k) \\ &\quad+\delta_4^{(0)}\psi^\dagger_{4,\sigma}(k)\psi_{6,\sigma}(k)+\delta_{4'}^{(0)}\psi^\dagger_{4,\sigma}(k)\psi_{5,\sigma}(k)+h.c.] \end{aligned} \tag{3.75}$$

The parquet RG equations describing the renormalization of the real and imaginary parts of these vertices are

$$\begin{aligned} \frac{d}{dL}\delta^{re}_{1(1')} &= \delta^{re}_{1(1')}(u_1-2u_2-\frac{u_3}{C}) \\ \frac{d}{dL}\delta^{im}_{1(1')} &= \delta^{im}_{1(1')}(u_1-2u_2+\frac{u_3}{C}) \end{aligned}$$

$$\frac{d}{dL}\delta^{re}_{2(2')} = \delta^{re}_{2(2')}(\tilde{u}_1 - 2\tilde{u}_2 - \frac{\tilde{u}_3}{\tilde{C}})$$
$$\frac{d}{dL}\delta^{im}_{2(2')} = \delta^{im}_{2(2')}(\tilde{u}_1 - 2\tilde{u}_2 + \frac{\tilde{u}_3}{\tilde{C}}) \tag{3.76}$$

where we have already used the equivalences of Eq. (3.31) to simplify the expressions. The vertices $\delta_{3(3')}$ and $\delta_{4(4')}$ satisfy the same parquet RG equations as $\delta_{1(1')}$ and $\delta_{2(2')}$, respectively, due to the C_4 symmetry explained below Eq. (5.14).

We perform the same procedure as in the main text, i.e. we take the fixed-trajectory solutions for the couplings as input for the Eqs. (3.76), which allows to solve for the vertices. The vertices, in turn, determine the susceptibilities and signal the appearance or the absence of the corresponding order. For the stable fixed trajectory in Eq. (3.33), we then obtain

$$\delta^{re}_1(L) = \delta^{re,(0)}_1 (\frac{L_0}{L_0 - L})^{\beta^{re}_{CDW,1}}$$
$$\beta^{re}_{CDW,1} = \frac{1 - \gamma_3/C}{1 + \gamma_3^2/C^2}\,. \tag{3.77}$$

The parquet RG equation satisfied by the susceptibility reads

$$\frac{d\chi^{re}_{CDW,1}}{dL} = [\frac{\delta^{re}_1}{\delta^{re,(0)}_1}]^2\,. \tag{3.78}$$

With Eq. (3.77) on the stable fixed trajectory, this leads to

$$\chi^{re}_{CDW,1}(L) = \frac{L_0^{2\beta^{re}_{CDW,1}}}{1 - 2\beta^{re}_{CDW,1}}(L_0 - L)^{-\alpha^{re}_{CDW,1}}\,, \tag{3.79}$$

where the scaling exponent of the susceptibility is

$$\alpha^{re}_{CDW,1} = 2\beta^{re}_{CDW,1} - 1\,. \tag{3.80}$$

Similarly, we determine $\alpha^{re}_{CDW,2} = \alpha^{im}_{CDW,2} = 0$ and $\alpha^{im}_{CDW,1} = 2\beta^{im}_{CDW,1} - 1$, where $\beta^{im}_{CDW,1} = \frac{1+\gamma_3/C}{1+\gamma_3^2/C^2}$. Furthermore, as can be seen in (3.76), we find $\alpha^{re,im}_{CDW,i} = \alpha^{re,im}_{CDW,i'}$.

We now perform the same analysis for the second stable fixed trajectory and the weakly unstable fixed trajectory. For the first stable fixed trajectory in Eq. (3.33), we obtain the susceptibility exponents

$$\alpha^{re}_{CDW,1} = 2\frac{1 - \gamma_3/C}{1 + \gamma_3^2/C^2} - 1$$

$$\alpha^{im}_{CDW,1} = 2\frac{1+\gamma_3/C}{1+\gamma_3^2/C^2} - 1$$
$$\alpha^{re}_{CDW,2} = 0$$
$$\alpha^{im}_{CDW,2} = 0 \tag{3.81}$$

Furthermore we find that $\alpha^{re,im}_{CDW,1} = \alpha^{re,im}_{CDW,1'} = \alpha^{re,im}_{CDW,3} = \alpha^{re,im}_{CDW,3'}$, and $\alpha^{re,im}_{CDW,2} = \alpha^{re,im}_{CDW,2'} = \alpha^{re,im}_{CDW,4} = \alpha^{re,im}_{CDW,4'}$. Among the different exponents in Eq. (3.81), the largest one is $\alpha^{im}_{CDW,1}$. As a result the leading CDW instability is characterized by the order parameter $\langle\psi_1^\dagger\psi_5 - \psi_5^\dagger\psi_1\rangle$. Similarly the order parameters $\langle\psi_1^\dagger\psi_6 - \psi_6^\dagger\psi_1\rangle$, $\langle\psi_3^\dagger\psi_5 - \psi_5^\dagger\psi_3\rangle$, and $\langle\psi_3^\dagger\psi_6 - \psi_6^\dagger\psi_3\rangle$ lead to the same exponent on our level of approximation and are thus equivalent candidates for the instability.

The susceptibility exponents of the second stable fixed trajectory (3.34) are

$$\alpha^{re}_{CDW,1} = 0$$
$$\alpha^{im}_{CDW,1} = 0$$
$$\alpha^{re}_{CDW,2} = 2\frac{1-\tilde{\gamma}_3/\tilde{C}}{1+\tilde{\gamma}_3^2/\tilde{C}^2} - 1$$
$$\alpha^{im}_{CDW,2} = 2\frac{1+\tilde{\gamma}_3/\tilde{C}}{1+\tilde{\gamma}_3^2/\tilde{C}^2} - 1. \tag{3.82}$$

In this case the roles of the d_{xz}/d_{yz} and d_{xy} orbitals on electron pockets are interchanged, and the largest exponent is $\alpha^{im}_{CDW,2}$. Correspondingly, the leading CDW instability is characterized by the order parameter, $\langle\psi_2^\dagger\psi_5 - \psi_5^\dagger\psi_2\rangle$, which is equivalent to the order parameters $\langle\psi_2^\dagger\psi_6 - \psi_6^\dagger\psi_2\rangle$, $\langle\psi_4^\dagger\psi_5 - \psi_5^\dagger\psi_4\rangle$, and $\langle\psi_4^\dagger\psi_6 - \psi_6^\dagger\psi_4\rangle$.

For the weakly unstable fixed trajectory, Eq. (3.35), we find

$$\alpha^{re}_{CDW,1} = 2\frac{1-\gamma_3/C}{1+\gamma_3^2/C^2} - 1$$
$$\alpha^{im}_{CDW,1} = 2\frac{1+\gamma_3/C}{1+\gamma_3^2/C^2} - 1$$
$$\alpha^{re}_{CDW,2} = 2\frac{1-\tilde{\gamma}_3/\tilde{C}}{1+\tilde{\gamma}_3^2/\tilde{C}^2} - 1 = \alpha^{re}_{CDW,1}$$
$$\alpha^{im}_{CDW,2} = 2\frac{1+\tilde{\gamma}_3/\tilde{C}}{1+\tilde{\gamma}_3^2/\tilde{C}^2} - 1 = \alpha^{im}_{CDW,1}, \tag{3.83}$$

where we used that $\gamma_3/C = \tilde{\gamma}_3/\tilde{C}$ for this fixed trajectory. The largest exponent in the

CDW channel is again $\alpha^{im}_{CDW,1}$.

In summary we find that for all three fixed trajectories, the largest exponent occurs for charge current operators. The corresponding exponent $\alpha_{CDW} \equiv 2\frac{1+\gamma_3/C}{1+\gamma_3^2/C^2} - 1$ is the same as in the SDW channel, i.e. $\alpha_{CDW} = \alpha_{SDW}$. The reason is that $\gamma_2 = \tilde{\gamma}_2 = 0$ on the fixed trajectories. However, if γ_2 and $\tilde{\gamma}_2$ are non-zero and small, we can see in Eq. (3.76) that SDW wins over CDW.

3.7.3.2 Spin density wave and charge density wave at (π, π)

Additionally, we consider SDW and CDW channels with momentum transfer (π, π). The corresponding coupling to fermion bilinears is given by

$$\begin{aligned} H_{SDW,(\pi,\pi)} = \sum_k [& \boldsymbol{s}^{(0)}_{1,3} \cdot \psi^\dagger_{1,\alpha}(k) \boldsymbol{\sigma}_{\alpha,\beta} \psi_{3,\beta}(k) \\ & + \boldsymbol{s}^{(0)}_{2,4} \cdot \psi^\dagger_{2,\alpha}(k) \boldsymbol{\sigma}_{\alpha,\beta} \psi_{4,\beta}(k) \\ & + \boldsymbol{s}^{(0)}_{1,4} \cdot \psi^\dagger_{1,\alpha}(k) \boldsymbol{\sigma}_{\alpha,\beta} \psi_{4,\beta}(k) + h.c.] \end{aligned} \tag{3.84}$$

and

$$\begin{aligned} H_{CDW,(\pi,\pi)} = \sum_{k\sigma} [& \delta^{(0)}_{1,3} \psi^\dagger_{1,\sigma}(k) \psi_{3,\sigma}(k) \\ & + \delta^{(0)}_{2,4} \psi^\dagger_{2,\sigma}(k) \psi_{4,\sigma}(k) \\ & + \delta^{(0)}_{1,4} \psi^\dagger_{1,\sigma}(k) \psi_{4,\sigma}(k) + h.c.] \end{aligned} \tag{3.85}$$

The RG equations for the vertices then are

$$\begin{aligned} \frac{ds^{re,im}_{1,3}}{dL} &= \pm \frac{A_e^{'}}{A_e} u_5 \\ \frac{ds^{re,im}_{2,4}}{dL} &= \pm \frac{A_e^{''}}{\bar{A}_e} u_6 \\ \frac{ds^{re,im}_{1,4}}{dL} &= \pm \frac{A_e^{'''}}{\tilde{A}_e} E u_7 \end{aligned} \tag{3.86}$$

and

$$\frac{d\delta^{re,im}_{1,3}}{dL} = \frac{ds^{im,re}_{1,3}}{dL}$$

$$\frac{d\delta^{re,im}_{2,4}}{dL} = \frac{ds^{im,re}_{2,4}}{dL}$$
$$\frac{d\delta^{re,im}_{1,4}}{dL} = \frac{ds^{im,re}_{1,4}}{dL} \tag{3.87}$$

We calculate the exponents of the susceptibilities for this SDW and CDW order similarly as before. We find that all exponents are smaller than zero. The result for the largest exponent is shown in Fig. 3.10 in the main text as $\alpha_{SDW'(CDW')}$.

3.7.3.3 Pomeranchuk instability in A_{2g} and B_{2g} channel

The order parameters in the A_{2g} and B_{2g} Pomeranchuk channel couple to the combination of vertices $\Gamma^{re(im)}_{1,2} = \Gamma_{1,2} \pm \Gamma^*_{1,2}$, $\Gamma^{re(im)}_{3,4} = \Gamma_{3,4} \pm \Gamma^*_{3,4}$ and $\Gamma^{re(im)}_{5,6} = \Gamma_{5,6} \pm \Gamma^*_{5,6}$ as defined in Eq. (3.51). Let us recall that the indices $1-4$ label states on electron and 5-6 states on hole pockets. In the A_{2g} channel the vertices are renormalized according to

$$\begin{aligned}
\Gamma^{re}_{1,2} &= -4Eu_7\Gamma^{re}_{1,2} + \Gamma^{re,(0)}_{1,2} \\
\Gamma^{re}_{3,4} &= -4Eu_7\Gamma^{re}_{3,4} + \Gamma^{re,(0)}_{3,4} \\
\Gamma^{re}_{5,6} &= -2u_4\Gamma^{re}_{5,6} + \Gamma^{re,(0)}_{5,6}\,.
\end{aligned} \tag{3.88}$$

On the weakly unstablefixed trajectory Eq. (3.35), the susceptibilities in the A_{2g} channel diverge as

$$\begin{aligned}
\chi^e_{A_{2g}} &\propto (L^e_{A_{2g}} - L)^{-1}, \\
\chi^h_{A_{2g}} &\propto (L^h_{A_{2g}} - L)^{-1},
\end{aligned} \tag{3.89}$$

and the divergence occurs on electron and hole pockets at scales $L^e_{A_{2g}}$ and $L^h_{A_{2g}}$, respectively,

$$\begin{aligned}
L^e_{A_{2g}} &= L_0 + \frac{4E\gamma_7}{1+\gamma_3^2/C^2} \\
L^h_{A_{2g}} &= L_0 + \frac{2\gamma_4}{1+\gamma_3^2/C^2}\,.
\end{aligned} \tag{3.90}$$

We see that $L^e_{A_{2g}}$ is larger than $L_{B_{1g}}$, i.e. it is subleading to the B_{1g} channel. However, the critical scale in the B_{1g} and A^h_{2g} Pomeranchuk channel are formally the same.

But if we consider that the flow will only be close to and not exactly on the weakly unstable fixed trajectory, ϵ_1 and ϵ_2 will be small and non-zero. Then the B_{1g} critical scale

always appears before the A_{2g}^h critical scale.

In the B_{2g} channel, the vertices are renormalized by

$$\begin{aligned}\Gamma_{1,2}^{im} &= \Gamma_{1,2}^{im,(0)} \\ \Gamma_{3,4}^{im} &= \Gamma_{3,4}^{im,(0)} \\ \Gamma_{5,6}^{im} &= 2u_4\Gamma_{5,6}^{im} + \Gamma_{5,6}^{im,(0)}.\end{aligned} \tag{3.91}$$

In this channel the vertices on electron pockets are not renormalized, while the vertex involving the hole pockets is reduced since $u_4 < 0$. As a result, there is no instability in the B_{2g} Pomeranchuk channel.

Chapter 4

A 5-pocket model for iron-based superconductors – a parquet renormalization group study

4.1 Introduction

The interplay between superconductivity, magnetism, and nematicity is the key physics of Fe-based superconductors (FeSCs) [109, 59, 113, 110, 111, 112]. In some FeSCs, e.g., 1111 and 122 systems, undoped materials display a stripe magnetic order below a certain T_N and a nematic order at slightly higher temperatures, while superconductivity emerges upon doping, when magnetic order gets weaker. In other systems, like 111 LiFeAs and 11 FeSe, superconductivity emerges without long-ranged magnetism already in undoped systems. Besides, FeSe displays an orbital order above the superconducting (SC) T_c [114]. The issue for the theory is to understand whether these seemingly different behaviors can be understood within the same framework.

In this communication we report the results of our analysis, which connects different classes of FeSCs. We study the competition between superconductivity, magnetism, and nematicity in the most generic five-pocket (5p) model for FeSCs with full orbital content of low-energy excitations. To do this, we use the machinery of analytical parquet renormalization group (pRG) [115]. This approach, along with complementary numerical functional RG [116, 117, 118, 119], has been argued [116, 120, 121, 117, 118, 119, 122, 123, 111, 24] to be the most unbiased way to analyze competing orders in an itinerant electron system.

The 5p model consists of three hole pockets, of which two are centered at $\Gamma = (0, 0)$ in the 1Fe Brillouin zone and one is centered at $M = (\pi, \pi)$, and two electron pockets centered at $Y = (0, \pi)$ and $X = (\pi, 0)$ (see the right panel in Fig. 4.1). The two Γ-centered hole pockets are made out of d_{xz} and d_{yz} orbitals, the hole pocket at M is made out of d_{xy} orbitals. The electron pockets are made out of $d_{xz}(d_{yz})$ and d_{xy} orbitals [141, 125].

For such an electronic configuration, there are 40 different 4-fermion interaction terms, allowed by C_4 symmetry [126] (without the hole pocket at M, this number is 30 [45]). If one departs from the model with only local interactions, the bare values of all 40 interactions are linear combinations of inter- and intra-orbital Hubbard and Hund terms U, U', J and J'. However, the 40 interactions flow to different values under pRG, which implies that the system self-generates non-local interactions. The flow of the interactions is obtained by solving differential equations that encode series of coupled vertex renormalizations. The running interactions are then used as input to determine susceptibilities in different channels. This way one can monitor a simultaneous build-up of different correlations taking into account their mututal feedback, which turns out to be crucial in our study.

The main result of pRG analysis is the emergent universality. It means that 40 microscopic interactions flow towards a *limited number* of fixed trajectories (FT), where the

ratios of different interactions become universal numbers. Each fixed trajectory has a basin of attraction in the space of bare interaction parameters. This allows us to explain the rich behaviors of the different FeSCs within a unifying description. In practical terms a simultaneous build-up of different correlations holds in the window of energies between a fraction of W and a scale comparable to the Fermi energy, E_F. At smaller energies, interactions in different channels evolve independent on each other. The range between W and E_F should be wide enough, otherwise the pRG flow ends before the system reaches one of the FTs [127].

4.2 Summary of our results

We found four stable FTs. For the first two stable FTs, the interactions within the subset of the two Γ-centered hole pockets and the two electron pockets become dominant, i.e., the 5p model effectively reduces to the four-pocket model (4p). For the other two stable FTs, the 5p model reduces to an effective 3-pocket model (3p) consisting of two electron pockets and the M-hole pocket. On each of two stable 4p FTs or 3p FTs the system behavior is described by an even simpler effective model because interactions involving fermions from either d_{xz}/d_{yz} or d_{xy} orbitals become dominant. We label these models as $4p_1$, $3p_1$, and $4p_2$, $3p_2$, respectively. We illustrate the four cases and present the phase diagram in Fig. 4.1. We then computed susceptibilities in different channels [128]. We found that the interplay between spin-density-wave (SDW) magnetism and superconductivity is the same in all four effective models. Namely, the SDW susceptibility is the largest at intermediate energies and pushes SC and orbital susceptibilities up. However, in the process of the pRG flow the SC susceptibility overtakes the SDW one, and the feedback from SC fluctuations halts the increase of the SDW susceptibility (see Fig. 4.3(b)). As a consequence, already the undoped system develops superconductivity rather than SDW magnetism, if indeed the pRG flow runs over a wide enough range of energies. This result could not be obtained within RPA and is entirely due to the feedback from increasing SC fluctuations on the SDW channel. In all cases superconductivity is of s^{+-} type, with sign change between the gaps on hole and electron pockets. In 4p models the susceptibility towards C_4-breaking orbital order also grows, and its exponent is larger than that for superconductivity [111], i.e., the system first develops a spontaneous orbital order. In 3p models orbital fluctuations are much weaker, and orbital order does not have enough "space" to develop.

We found that SDW magnetism does develop before superconductivity and/or orbital order if the FT is not reached within the range of pRG flow. The type of SDW order is

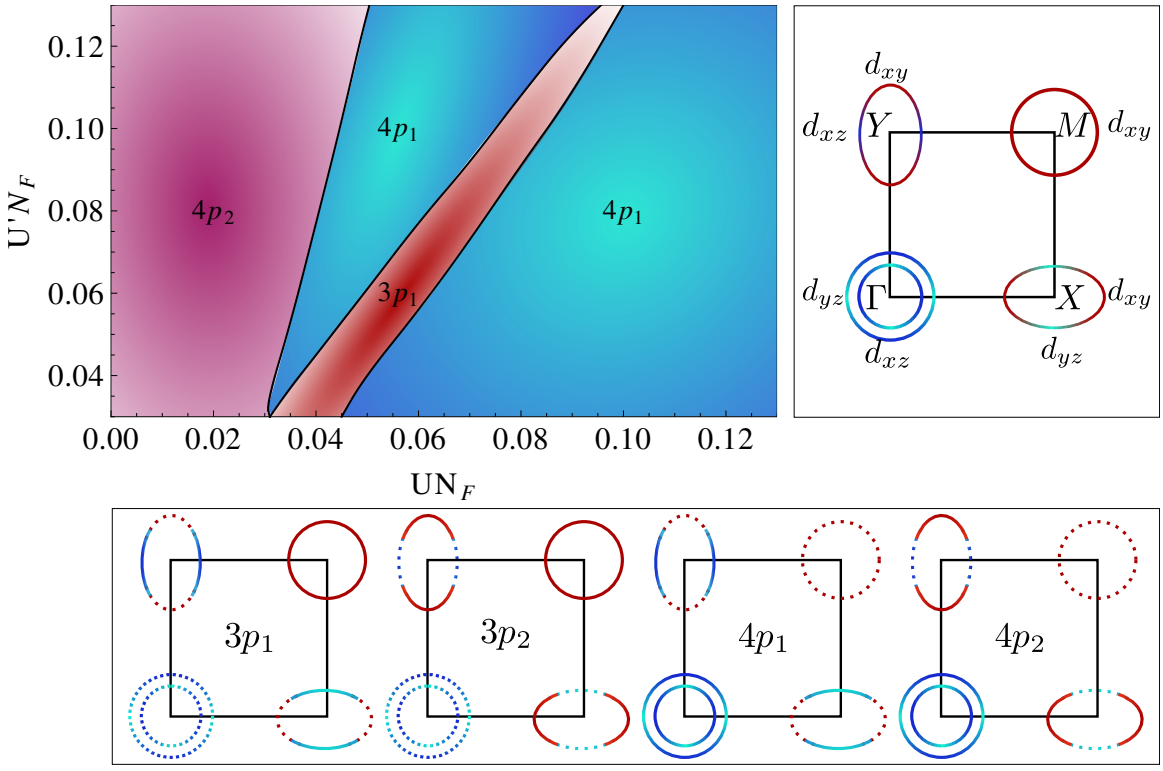

Figure 4.1: Upper panel: Right – main orbital content of excitations near Fermi surfaces (presented by different colors). Left – regions of different system behavior of the full 5-pocket model, indicated by the type of the effective model. In the ranges marked $3p_{1,2}$, the dominant interactions at low energies are within the subset of the two electron pockets and the $M = (\pi, \pi)$-hole pocket. In the ranges marked $4p_{1,2}$, the dominant interactions are between fermions near the Γ-centered hole pockets and electron pockets. The index $1, 2$ distinguishes if interactions involving d_{xz}/d_{yz} or d_{xy} orbital components on the electron pockets are dominant. For illustrative purposes, the bare model is set to have local Hubbard and Hund interactions – intraorbital U, interorbital U', J and J'. We set $J = 0.025/N_F$, $J' = 0.03/N_F$, where N_F is the density of states on the FSs (assumed to be equal on all FSs for simplicity), and varied U and U' as two independent parameters. Lower panel: Graphic representations of $3p_{1,2}$ and $4p_{1,2}$ models. Fermionic states, for which interactions become the largest in the process of pRG flow, are shown by solid lines.

different for the 3p and the 4p models. In 3p models SDW order is a C_4-breaking stripe order [33, 129], while in 4p models it is C_4 preserving double-Q order [130, 131] (a symmetric combination of $(\pi, 0)$ and $(0, \pi)$ magnetic orders). This last result, in combination with pRG, implies a clear separation between the magnetic and orbital scenario for nematicity in FeSCs. Namely, in 4p models, the SDW scenario for Ising-nematic order does not work

because double-Q SDW preseves the symmetry between X and Y directions, and, simultaneously, orbital fluctuations are strong. In 3p models, orbital fluctuations are weak, and, simultaneously, SDW *stripe* fluctuations favor vestigial Ising-nematic spin order [132].

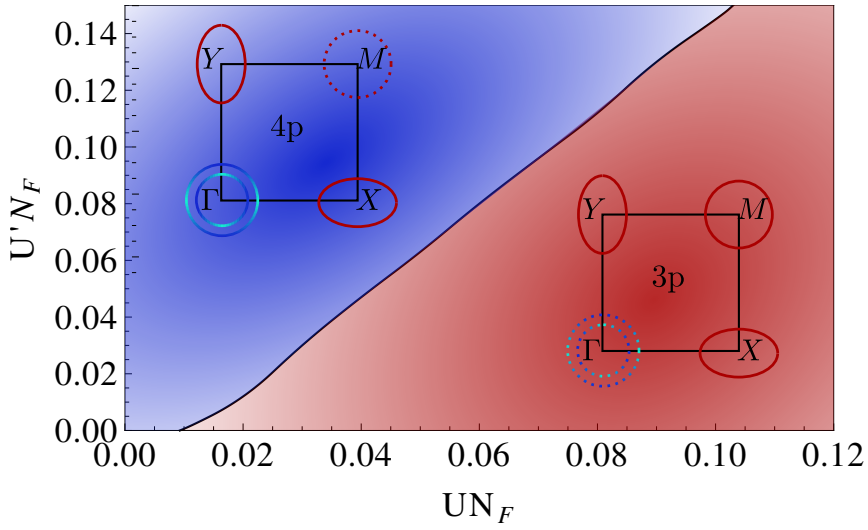

Figure 4.2: Two different regions of system behavior indicated by fixed trajectories of the pRG flow for the toy model with electron pockets made entirely of d_{xy}, for different values of U, U' (treated as two independent parameters) and $J = J' = 0.03/N_F$. In the region labeled as 3p the interactions within the subset of the two electron pockets and the $M = (\pi, \pi)$-hole pocket become dominant at low energies. In the region labeled as 4p interactions involving fermions from the two Γ-centered hole pockets and the two electron pockets become dominant.

In the remainder of this Letter we present the details of our study. The full analysis of the set of 40 pRG equations is quite involved, so to demonstrate the separation into 4p or 3p behavior at low energies, we first analyze a toy model, in which we approximate the orbital composition of the two electron pockets as pure d_{xy}. We then extend the analysis to the full 5-pocket model.

4.3 Toy model with d_{xy} electron pockets

As we said, the kinetic term describes fermionic excitations around the five Fermi surfaces, i.e. $H = H^{\Gamma} + H^{X} + H^{Y} + H^{M}$. The symmetry-allowed interaction terms contain 14 interactions U_i within the subset of the two electron and the two Γ-centered hole pockets and 7 interactions U_{in} involving fermions near the M-hole pocket, so the total number

of the interactions is 21. We present the Hamiltonian and the full set of pRG equations for a generic dispersion near hole and electron FSs in the Supplementary Material (SM). The pRG analysis shows that six interactions flow to zero and five increase with smaller exponents than the other ten. The pRG flow of the remaining ten interactions determines the FTs. We show these ten interactions in the inset of Fig. 4.3(a). The pRG equations for these interactions are ($u_i = U_i N_F$)

$$\begin{aligned}
&\dot{u}_1 = u_1^2 + u_3^2,\ \dot{u}_{1n} = u_{1n}^2 + u_{3n}^2 \\
&\dot{u}_2 = 2u_2(u_1 - u_2),\ \dot{u}_{2n} = 2u_{2n}(u_{1n} - u_{2n}) \\
&\dot{u}_3 = 2u_3(2u_1 - u_2 - u_5) - 2u_3u_4 - u_{3n}u_{5n} \\
&\dot{u}_{3n} = 2u_{3n}(2u_{1n} - u_{2n} - u_5) - u_{3n}u_{4n} - 2u_3u_{5n} \\
&\dot{u}_4 = -2u_4^2 - 2u_3^2 - 2u_{5n}^2, \dot{u}_{4n} = -u_{4n}^2 - 2u_{3n}^2 - 2u_{5n}^2 \\
&\dot{u}_5 = -2u_5^2 - 2u_3^2 - u_{3n}^2, \\
&\dot{u}_{5n} = -2u_4u_{5n} - u_{4n}u_{5n} - 2u_3u_{3n}
\end{aligned} \tag{4.1}$$

The derivatives are with respect to $L = \log W/E$, where E is the running scale.

We searched for FTs of Eq. (4.20) by selecting one divergent interaction (specifically u_1 or u_{1n}), writing other interactions as $u_i = \gamma_i u_1$, $u_{in} = \gamma_{in} u_1$ (or $u_i = \gamma_i u_{1n}$, $u_{in} = \gamma_{in} u_{1n}$), and solving the set of equations for $L-$independent γ_i, γ_{in}. We found two stable FTs: one with

$$u_1 = \frac{1}{1+\gamma_3^2}\frac{1}{L_0 - L}, \tag{4.2}$$

and $\gamma_{in} = \gamma_2 = 0$, $\gamma_3 = \pm\sqrt{15}, \gamma_4 = \gamma_5 = 3$, and the other with

$$u_{1n} = \frac{1}{1+\gamma_{3n}^2}\frac{1}{L_0 - L} \tag{4.3}$$

and $\gamma_1 = \gamma_2 = \gamma_3 = \gamma_4 = \gamma_{2n} = \gamma_{5n} = 0$, $\gamma_{3n} = \pm(3 + 2\sqrt{6}), \gamma_{4n} = 2\gamma_5 = -\sqrt{6}$. In Eqs. (4.2), (4.3) L_0 is the scale at which interactions diverge and the system develops a long-range order, as we show below. For the first stable FT all γ_{in} involving the M pocket vanish, so the 5-pocket model effectively reduces to the 4p model. For the second stable FT the situation is the opposite – interactions involving the two Γ-centered hole pockets vanish compared to other interactions, i.e., the 5p model effectively reduces to the 3p model. We checked the stability of the 4p FT and the 3p FT by expanding around them and verified

that all eigenvalues are negative. Whether the system flows to one FT or the other is determined by the bare values of the interactions (see Fig.4.2).

We next use the running interactions as inputs and compute the susceptibilities in different channels, χ_j. We describe the computational procedure in the SM and here list the results. The potentially divergent parts of the susceptibilities in SC and SDW channels are $\chi_i \propto (L_0 - L)^{2\beta_i - 1}$ (i = SDW, SC). Along 4p FT and 3p FT, the exponents are $\beta_{SDW}^{(4p)} = 0.30, \beta_{SC}^{(4p)} = 0.86$, $\beta_{SDW}^{(3p)} = 0.43, \beta_{SC}^{(3p)} = 0.72$. We see that in both cases $\beta_{SC} > 1/2$ while $\beta_{SDW} < 1/2$, i.e. χ_{SC} diverges at $L = L_0$, while χ_{SDW} remains finite, despite that it was the largest at the beginning of the pRG flow. This implies that the system develops SC order but not SDW order. We show the flow of the susceptibilities in Fig. 4.3(b). For both 4p and 3p models, we found that the largest $\beta_{SC} > 0$ corresponds to the s^{+-} gap structure, with opposite sign of the gap on hole and electron pockets [133]

We also analyzed the susceptibility χ_P in the d-wave Pomeranchuk channel. An instability in this channel leads to spontaneous orbital order [113, 111], i.e., non-equal densities of fermions on d_{xz} and d_{yz} orbitals. For the 4p model we found that $\beta_P^{(4p)} = 1$ is larger than $\beta_{SC}^{(4p)}$, i.e., orbital order can precede the SC transition [111]. We found no d_{xz}/d_{yz} orbital order for the 3p model because the electron and the M pockets have d_{xy} character [134].

4.4 Full 5-pocket model

The analysis of the full 5-pocket model with d_{xz}/d_{xy} and d_{yz}/d_{xy} orbital content of the electron pockets is more involved as one has to analyze the set of 40 coupled differential equations for the interactions (see SM). We searched for FTs with the same procedure as in the toy model. Amazingly enough, we found much the same behavior. Namely, the 5p model effectively becomes either a 4p or a 3p model. The new feature, not present in the toy model, is that in each case there are now two stable FTs, on which the system behavior is described by even more restricted $3p_{1,2}$ and $4p_{1,2}$ models. For $3p_1$ and $4p_1$ models interactions involving fermions from d_{xz} (d_{yz}) orbitals on the electron pockets become dominant, for $3p_2$ and $4p_2$ models interactions of d_{xy} orbitals on the electron pockets become dominant. We verified that these four FTs are stable with respect to small deviations. We show the phase diagram in Fig. 4.1.

The interplay between SDW and SC is the same in all four effective models and is similar to that in the toy model. Namely, the SDW susceptibility is the largest at the beginning, but in the process of the flow SC susceptibility diverges faster, and the feedback from SC fluctuations halts the growth of SDW susceptibility. As a result, even at zero

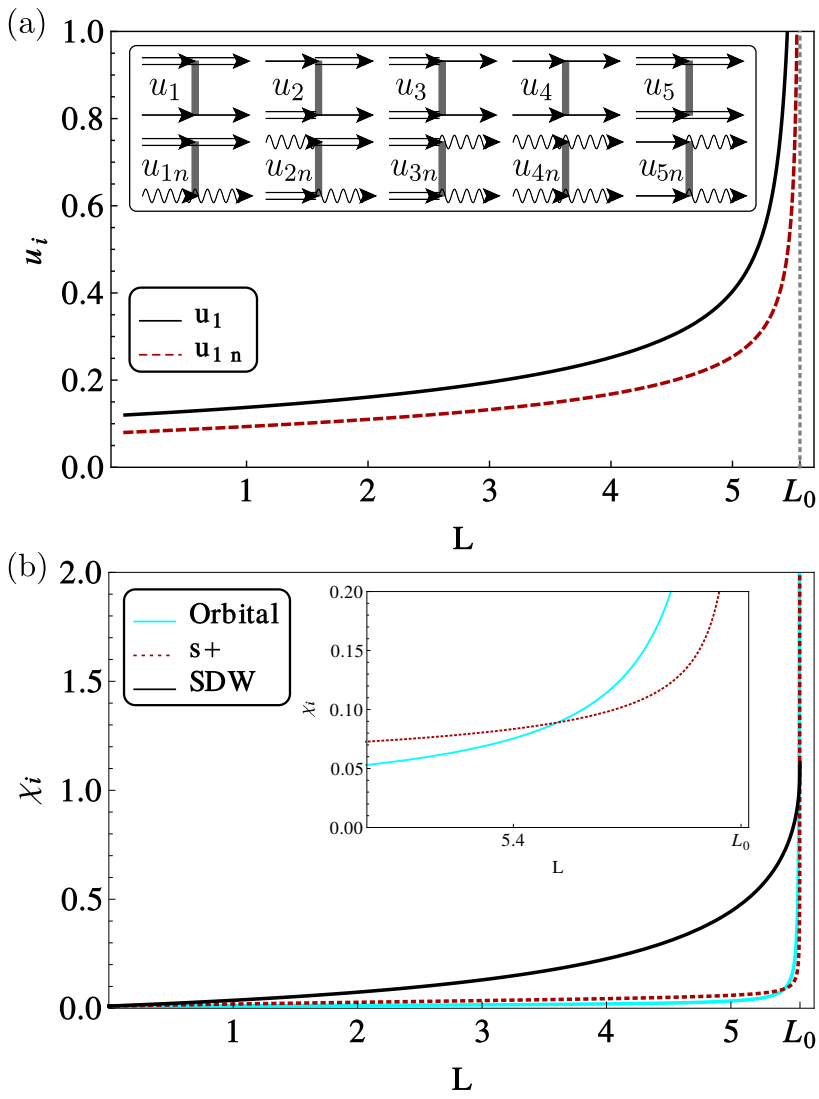

Figure 4.3: (a) Representative RG flow towards the 4p FT in the toy model for the interactions u_1 and u_{1n}. The inset shows the 10 relevant interactions of the toy model, where double lines represent electron pockets, wavy lines the M-centered hole pocket and solid single lines the Γ-centered hole pockets. Bare values are $U = 0.08/N_F$, $U' = 0.12/N_F$, $J = J' = 0.03/N_F$. The RG parameter L is $\log W/E$, where W is the bandwidth and E is running energy/temperature. The system undergoes an instability into an ordered state (SDW, SC, or orbital order) at $L = L_0$. (b) Corresponding flow of the SDW, SC s^{+-} and orbital susceptibilities. Near $L = L_0$ the SC and the orbital susceptibilities keep increasing, while the SDW susceptibility remains finite. The inset shows orbital and SC susceptibilities at the end of the flow.

doping the system develops s^{+-} SC order but no SDW order. Orbital fluctuations are, however, different in 4p and 3p models, again in similarity to the toy model. If the pRG flow is towards $4p_1$ or $4p_2$ models, orbital fluctuations also get strong and χ_P diverges with the largest exponent, i.e., the system develops a spontaneous orbital order prior to SC [136]. If the flow is towards 3p model, orbital fluctuations are much weaker and do not develop for not too large W/E_F. If E_F is larger than $E_0 \sim We^{-L_0}$, the pRG flow ends before χ_{SC} and/or χ_P wins over χ_{SDW}. In this situation, the system develops SDW order at smaller doping and SC order at larger dopings [127]. For the 4p model an SDW order is a double-Q order, maintaining the symmetry between X and Y directions[130, 131], while for the 3p model SDW order is a stripe, breaking this symmetry. [33, 129]. Combining this with pRG results, we find that, if the pRG flow is towards one of the two 4p models, the nematicity emerges as a spontaneous orbital order. If the flow is towards one of the 3p models, the nematicity emerges due to stripe fluctuations as a composite Ising-nematic spin order.

4.5 Applications to FeSCs and conclusions

Our results have several implications for FeSCs. First, the pRG analysis shows that SC order may develop instead of long-ranged magnetism already in undoped materials, not only when SDW order is destroyed by doping. This is consistent with the behavior in LiFeAs and FeSe [164]. In systems with smaller regions of the pRG flow (larger bare interactions or larger E_F) SDW order develops first, and SC develops only upon doping. Second, pRG analysis shows that in 4p models orbital order develops first, SC develops at a lower T, and SDW order does not develop down to $T = 0$. This is consistent with the observed behavior in FeSe at ambient pressure [114]. The third result is the separation between orbital and magnetic scenarios for nematicity in 4p and 3p models. Whether the system flows towards 3p or 4p effective model at low energies depends on the microscopic Hubbard and Hund parameters (see Figs. 4.1, 4.2) as well as the parameters of fermionic dispersions (see SM).

In this Letter we analyzed the competition between SDW, SC, and orbital order in the full 5-pocket model for FeSCs. We used pRG techniques and included into consideration the orbital composition of hole and electron pockets in terms of d_{xz}, d_{yz}, and d_{xy} orbitals. The total number of symmetry-allowed interactions between low-energy fermions is 40, yet we found the system behavior is amazingly simple – depending on initial values of the interactions and quasiparticle masses the system flows to one of four stable FTs. For two of these FTs, the system behavior at low energies is the same as if the the M-pocket was absent (4p model), for the other two the system behavior is the same as if the two Γ-centered hole

pockets were absent (3p model). In all cases s^{+-} SC wins over SDW if E_F is small enough, and SDW wins if E_F is larger. In the parameter range where the pRG flow is towards the effective 4p model, the system develops spontaneous orbital order, which then is the origin of nematicity. When the pRG flow is towards the effective 3p model, a spontaneous orbital order does not develop, and nematicity is associated with Ising-nematic spin order. The phase diagram in Fig. 4.1 describes the behavior found in all four families of FeSCs – 1111, 122, 111 and 11 systems, and in this respect our findings provide a unified description of the competition between SDW, SC, and orbital orders in all FeSCs.

4.6 Supplemental Material

4.6.1 3-orbital, 5-band model

4.6.1.1 Kinetic part of the Hamiltonian

We use as an input the fact that the low-energy excitations near all 5 Fermi surfaces are composed out of three orbitals – d_{xz}, d_{yz}, and d_{xy}. We perform calculations in the 1-Fe unit cell and neglect the dispersion in the third direction and the processes with momentum non-conservation by (π, π) (the ones which hybridize the pockets).

One way to obtain the dispersion of low-energy excitations is to use the tight-binding model in the orbital basis, restrict with d_{xz}, d_{yz}, and d_{xy} orbitals, and expand around the high-symmetry points in the Brillouin zone, where different electron and hole pockets are located (cf. Fig. 4.4). Another way to obtain low-energy dispersions is to identify the symmetry properties around the Fermi level and construct the invariants to leading order in the deviations from the symmetry points[45]. The two approaches are equivalent to quadratic order in the deviations near the centra of the pockets ($\Gamma = (0,0)$ for two hole pockets, $M = (\pi, \pi)$ for the third hole pocket, and $X = (\pi, 0)$ and $Y = (0, \pi)$ for the two electron pockets). The effective low-energy Hamiltonian reads

$$H_0 = \sum_{\mathbf{k},\sigma} \Big[\psi^\dagger_{\Gamma,\boldsymbol{k},\sigma} h_\Gamma(\boldsymbol{k}) \psi_{\Gamma,\boldsymbol{k},\sigma} + \psi^\dagger_{X,\boldsymbol{k},\sigma} h_X(\boldsymbol{k}) \psi_{X,\boldsymbol{k},\sigma} + \psi^\dagger_{Y,\boldsymbol{k},\sigma} h_Y(\boldsymbol{k}) \psi_{Y,\boldsymbol{k},\sigma} + \psi^\dagger_{M,\boldsymbol{k},\sigma} h_M(\boldsymbol{k}) \psi_{M,\boldsymbol{k},\sigma} \Big], \tag{4.4}$$

where

$$h_\Gamma(\boldsymbol{k}) = \begin{pmatrix} \epsilon_\Gamma + \frac{k^2}{2m_\Gamma} + ak^2 \cos 2\theta_k & ck \sin 2\theta_k \\ ck \sin 2\theta_k & \epsilon_\Gamma + \frac{k^2}{2m_\Gamma} + ak^2 \cos 2\theta_k \end{pmatrix}$$

$$h_{X/Y}(\boldsymbol{k}) = \begin{pmatrix} \epsilon_1 + \frac{k^2}{2m_1} \pm a_1 k^2 \cos 2\theta_k & -iv_{X/Y}(\boldsymbol{k}) \\ iv_{X/Y}(\boldsymbol{k}) & \epsilon_3 + \frac{k^2}{2m_3} \pm a_3 k^2 \cos 2\theta_k \end{pmatrix}$$
$$h_M(\boldsymbol{k}) = \epsilon_M - \frac{k^2}{2m_M} \tag{4.5}$$

where $v_X(k) = 2vk\sin\theta$, $v_Y(k) = 2vk\cos\theta$ and $\theta_k = \arctan\frac{k_y}{k_x}$. Here and below the term A/B (in, e.g., $h_{X/Y}$) means "either A or B". The spinors in Eq. (4.4) are defined as $\psi_{\Gamma,\boldsymbol{k},\sigma} = (d_{yz,\boldsymbol{k},\sigma}, d_{xz,\boldsymbol{k},\sigma})^T$, $\psi_{X,\boldsymbol{k},\sigma} = (d_{yz,\boldsymbol{X}+\boldsymbol{k},\sigma}, d_{xy,\boldsymbol{X}+\boldsymbol{k},\sigma})^T$,$\psi_{Y,\boldsymbol{k},\sigma} = (d_{xz,\boldsymbol{Y}+\boldsymbol{k},\sigma}, d_{xy,\boldsymbol{Y}+\boldsymbol{k},\sigma})^T$ and $\psi_{M,\boldsymbol{M}+\boldsymbol{k},\sigma} = d_{xy,\boldsymbol{k},\sigma}$. Below we shorten notations to $d_{yz,\boldsymbol{k},\sigma} = d_{1,\boldsymbol{k},\sigma}$, $d_{xz,\boldsymbol{k},\sigma} = d_{2,\boldsymbol{k},\sigma}$, $d_{yz,\boldsymbol{X}+\boldsymbol{k},\sigma} = f_{1,\boldsymbol{k},\sigma}$, $d_{xz,\boldsymbol{Y}+\boldsymbol{k},\sigma} = f_{2,\boldsymbol{k},\sigma}$, $d_{xy,\boldsymbol{X}+\boldsymbol{k},\sigma} = f_{31,\boldsymbol{k},\sigma}$, $d_{xy,\boldsymbol{Y}+\boldsymbol{k},\sigma} = f_{32,\boldsymbol{k},\sigma}$, and $d_{xy,\boldsymbol{k},\sigma} = d_{3,\boldsymbol{k},\sigma}$. In these notations, the spinors are $\psi_{\Gamma,\boldsymbol{k},\sigma} = (d_{1,\boldsymbol{k},\sigma}, d_{2,\boldsymbol{k},\sigma})^T$, $\psi_{X/Y,\boldsymbol{k},\sigma} = (f_{1/2,\boldsymbol{k},\sigma}, f_{31/32,\boldsymbol{k},\sigma})^T$ and $\psi_{M,\boldsymbol{M}+\boldsymbol{k},\sigma} = d_{3,\boldsymbol{k},\sigma}$.

To make RG analysis more tractable we made several simplifications in Eq. (4.5). For Γ-centered hole pockets we set $a = c$. Then the transformation from the orbital to the band basis is given by

$$\begin{pmatrix} d_{1,\boldsymbol{k},\sigma} \\ d_{2,\boldsymbol{k},\sigma} \end{pmatrix} = \begin{pmatrix} \cos\theta_k & \sin\theta_k \\ -\sin\theta_k & \cos\theta_k \end{pmatrix} \begin{pmatrix} c_{\boldsymbol{k},\sigma} \\ d_{\boldsymbol{k},\sigma} \end{pmatrix}, \tag{4.6}$$

and the dispersions of fermions $c_{\boldsymbol{k},\sigma}$ and $d_{\boldsymbol{k},\sigma}$ are isotropic in $\mathbf{k}$:

$$\epsilon_{c/d,\boldsymbol{k},\sigma} = -\frac{k^2}{2m_{c/d}} \tag{4.7}$$

where $m_{c/d}^{-1} = m_\Gamma^{-1} \pm 2a$. The two hole Fermi surfaces are obviously circular. The fermionic Green's functions in the orbital representation are related to $G_{c/d}(i\omega, \boldsymbol{k}) = (i\omega - \epsilon_{c/d,k} - \mu)^{-1}$ in the band representation as

$$\begin{aligned} G_{d_1,d_1}(i\omega,\boldsymbol{k}) &= G_c(i\omega,\boldsymbol{k})\cos^2\theta + G_d(i\omega,\boldsymbol{k})\sin^2\theta \\ G_{d_2,d_2}(i\omega,\boldsymbol{k}) &= G_c(i\omega,\boldsymbol{k})\sin^2\theta + G_d(i\omega,\boldsymbol{k})\cos^2\theta \\ G_{d_1,d_2}(i\omega,\boldsymbol{k}) &= G_{d_2,d_1}(i\omega,\boldsymbol{k}) \\ &= [G_d(i\omega,\boldsymbol{k}) - G_c(i\omega,\boldsymbol{k})]\sin\theta\cos\theta \end{aligned} \tag{4.8}$$

A third hole pocket arises around the M-point in the Brillouin zone. Here the transformation from orbital to band basis is trivial, because the spectral weight comes entirely from the d_{xy} orbital. The dispersion is given in Eq. (4.5), and the corresponding Green's function is $G_M(i\omega, \boldsymbol{k}) = (i\omega + k^2/(2m_M) - \epsilon_M)^{-1}$. The presence of this hole pocket is material

dependent and relatively small changes in the system parameters may sink this pocket below the Fermi level (at least at $k_z = 0$, when k_z dispersion is included). However, such a pocket is definitely present in, e.g., hole-doped $K_xBa_{1-x}Fe_2As_2$ and LiFeAs, which motivates to include it into our model.

For electron pockets, the diagonalization of h_X (h_Y) gives two bands, of which only one crosses the Fermi level and forms the electron pocket around X (Y). The electron pockets at X and Y are related by C_4 symmetry, i.e. they map onto each other under a rotation by $\pi/2$. Due to the non-diagonal hybridization $v_{X/Y}(k)$, the transformation from orbital to band basis is not a simple rotation. Nevertheless, it can be expressed through

$$\begin{pmatrix} e_{1/2} \\ \bar{e}_{1/2} \end{pmatrix} = e^{i\phi} \begin{pmatrix} e^{i\phi_1} \cos\varphi_{1/2,\theta} & e^{i\phi_2} \sin\varphi_{1/2,\theta} \\ -e^{-i\phi_2} \sin\varphi_{1/2,\theta} & e^{-i\phi_1} \cos\varphi_{1/2,\theta} \end{pmatrix} \begin{pmatrix} f_{1/2} \\ f_{31/32} \end{pmatrix}, \tag{4.9}$$

where $e_{1/2} = e_{1,\boldsymbol{k},\sigma}, e_{2,\boldsymbol{k},\sigma}$ and $\bar{e}_{1/2}$ are operators for band fermions near the electron pockets, and the functions $\varphi_{1/2,\theta}$ and $\phi_{1/2}$ depend on the system parameters and determine the relative spectral weight of xz/yz and xy orbitals. We set $e_{1/2}$ to describe the electrons in the band that crosses the Fermi level. The dispersion of these fermions is $\xi_{e1} = k_x^2/(2m_{ex}) + k_y^2/(2m_{ey}) - \mu_e, \xi_{e2} = k_x^2/(2m_{ey}) + k_y^2/(2m_{ex}) - \mu_e$. For simplicity we assume $m_{ex} = m_{ey} = m_e$, i.e., set $\xi_{e1} = \xi_{e2} = \xi_e = k^2/(2m_e) - \mu_e$. We checked that keeping m_{ex} and m_{ey} different will not change the pRG equations, once we properly rescale the couplings.

The electron propagator in orbital representation is expressed in terms of low energy fermions as

$$\begin{aligned} G_{f_{1/2},f_{1/2}}(i\omega,\boldsymbol{k}) &= G_{e1/e2}(i\omega,\boldsymbol{k}) \cos^2\varphi_{1/2,\theta} \\ G_{f_{31/32},f_{31/32}}(i\omega,\boldsymbol{k}) &= G_{e1/e2}(i\omega,\boldsymbol{k}) \sin^2\varphi_{1/2,\theta} \\ G_{f_{1/2},f_{31/32}}(i\omega,\boldsymbol{k}) &= G_{f_{31/32},f_{1/2}}(i\omega,\boldsymbol{k})^* \\ &= G_{e1/e2}(i\omega,\boldsymbol{k}) e^{i(\phi_1-\phi_2)} \cos\varphi_{1/2,\theta} \sin\varphi_{1/2,\theta}, \end{aligned} \tag{4.10}$$

where $G_{e1/e2}(i\omega,\boldsymbol{k}) = (i\omega - \xi_e)^{-1}$ (k is counted from X in G_{e1} and from Y in G_{e2}).

4.6.1.2 The toy model

In the toy model, which we analyze in the main text prior to the full one, we approximate the orbital content of the two electron pockets as pure d_{xy}. In this case, the electron dispersions are already diagonal in the orbital basis, i.e. orbital and band representations are identical. Our notation for the electron operators is, in this approximation, $\psi_{X/Y,\boldsymbol{k},\sigma} = f_{1/2,\boldsymbol{k}}$, where 1/2 just labels the pockets. This toy model allows us to study the impact of the fifth pocket in a transparent way. Furthermore, we expect that the toy model already captures

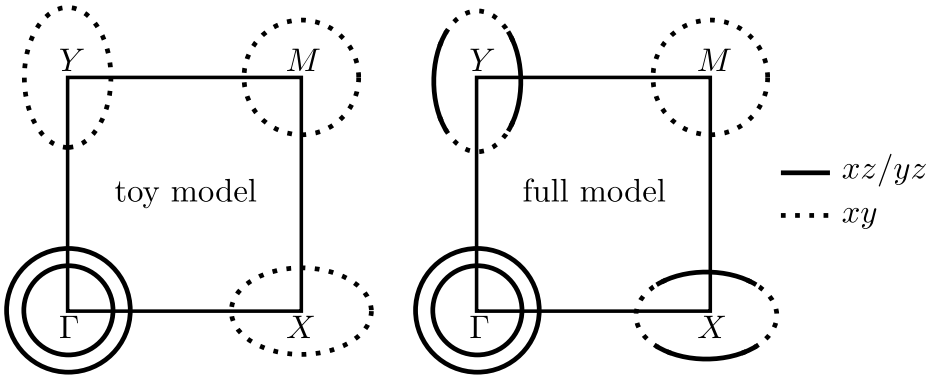

Figure 4.4: The two 5-pocket models that we consider. The toy and the full model differ in the orbital content of electron pockets. For the full model, the electron pocket at X has contributions from d_{yz} and d_{xy} orbitals and the one at Y has contributions from d_{xz} and d_{xy} orbitals. For the toy model, we approximated these pockets as consisting exclusively of d_{xy} orbital.

a substantial portion of the physics of the full model because adiabatically changing the tight-binding parameters of the underlying lattice model, one can move the spectral weight from $d_{xz}(d_{yz})$ to d_{xy} orbital everywhere on the electron pockets. There are, however, several features of the full model, which are not captured by the toy model. These are caused by the interactions which involve both xz/yz and xy-orbital states on the electron pockets.

4.6.1.3 Interactions

4.6.1.3.1 The toy model

As we said in the main text, the total number of different interactions between low-energy fermions in the toy model is 21. Of them 14 interactions involve fermions near the two Γ-centered hole pockets and the two electron pockets, and 7 involve fermions near the third hole pocket. In terms of the spinor components defined above, the 14 interaction terms are

$$\begin{aligned} H_I^{4ps} = & U_1 {\sum}' \left[f_{1\sigma}^\dagger f_{1\sigma} d_{1\sigma'}^\dagger d_{1\sigma'} + f_{2\sigma}^\dagger f_{2\sigma} d_{2\sigma'}^\dagger d_{2\sigma'} \right] \\ & + \bar{U}_1 {\sum}' \left[f_{2\sigma}^\dagger f_{2\sigma} d_{1\sigma'}^\dagger d_{1\sigma'} + f_{1\sigma}^\dagger f_{1\sigma} d_{2\sigma'}^\dagger d_{2\sigma'} \right] \\ & + U_2 {\sum}' \left[f_{1\sigma}^\dagger d_{1\sigma} d_{1\sigma'}^\dagger f_{1\sigma'} + f_{2\sigma}^\dagger d_{2\sigma} d_{2\sigma'}^\dagger f_{2\sigma'} \right] \\ & + \bar{U}_2 {\sum}' \left[f_{1\sigma}^\dagger d_{2\sigma} d_{2\sigma'}^\dagger f_{1\sigma'} + f_{2\sigma}^\dagger d_{1\sigma} d_{1\sigma'}^\dagger f_{2\sigma'} \right] \end{aligned}$$

$$
\begin{aligned}
&+\frac{U_3}{2}\sum{}'\left[f^\dagger_{1\sigma}d_{1\sigma}f^\dagger_{1\sigma'}d_{1\sigma'}+f^\dagger_{2\sigma}d_{2\sigma}f^\dagger_{2\sigma'}d_{2\sigma'}+h.c.\right]\\
&+\frac{\bar{U}_3}{2}\sum{}'\left[f^\dagger_{1\sigma}d_{2\sigma}f^\dagger_{1\sigma'}d_{2\sigma'}+f^\dagger_{2\sigma}d_{1\sigma}f^\dagger_{2\sigma'}d_{1\sigma'}+h.c.\right]\\
&+\frac{U_4}{2}\sum{}'\left[d^\dagger_{1\sigma}d_{1\sigma}d^\dagger_{1\sigma'}d_{1\sigma'}+d^\dagger_{2\sigma}d_{2\sigma}d^\dagger_{2\sigma'}d_{2\sigma'}\right]\\
&+\frac{\bar{U}_4}{2}\sum{}'\left[d^\dagger_{1\sigma}d_{2\sigma}d^\dagger_{1\sigma'}d_{2\sigma'}+d^\dagger_{2\sigma}d_{1\sigma}d^\dagger_{2\sigma'}d_{1\sigma'}\right]\\
&+\tilde{U}_4\sum{}'d^\dagger_{1\sigma}d_{1\sigma}d^\dagger_{2\sigma'}d_{2\sigma'}+\tilde{\tilde{U}}_4\sum{}'d^\dagger_{1\sigma}d_{2\sigma}d^\dagger_{2\sigma'}d_{1\sigma'}\\
&+\frac{U_5}{2}\sum{}'\left[f^\dagger_{1\sigma}f_{1\sigma}f^\dagger_{1\sigma'}f_{1\sigma'}+f^\dagger_{2\sigma}f_{2\sigma}f^\dagger_{2\sigma'}f_{2\sigma'}\right]\\
&+\frac{\bar{U}_5}{2}\sum{}'\left[f^\dagger_{1\sigma}f_{2\sigma}f^\dagger_{1\sigma'}f_{2\sigma'}+f^\dagger_{2\sigma}f_{1\sigma}f^\dagger_{2\sigma'}f_{1\sigma'}\right]\\
&+\tilde{U}_5\sum{}'f^\dagger_{1\sigma}f_{1\sigma}f^\dagger_{2\sigma'}f_{2\sigma'}+\tilde{\tilde{U}}_5\sum{}'f^\dagger_{1\sigma}f_{2\sigma}f^\dagger_{2\sigma'}f_{1\sigma'},
\end{aligned}
\tag{4.11}
$$

where the sum $\sum'$ denotes the summation over spin σ,σ', momenta $\boldsymbol{k}_1+\boldsymbol{k}_2-\boldsymbol{k}_3-\boldsymbol{k}_4=0$ and includes the normalization factor $1/N$. The other 7 couplings are

$$
\begin{aligned}
H_I^{5p}=&\,U_{1n}\sum{}'\left[d^\dagger_{3\sigma}d_{3\sigma}f^\dagger_{1\sigma'}f_{1\sigma'}+d^\dagger_{3\sigma}d_{3\sigma}f^\dagger_{2\sigma'}f_{2\sigma'}\right]\\
&+U_{2n}\sum{}'\left[d^\dagger_{3\sigma}f_{1\sigma}f^\dagger_{1\sigma'}d_{3\sigma'}+d^\dagger_{3\sigma}f_{2\sigma}f^\dagger_{2\sigma'}d_{3\sigma'}\right]\\
&+\frac{U_{3n}}{2}\sum{}'\left[d^\dagger_{3\sigma}f_{1\sigma}d^\dagger_{3\sigma'}f_{1\sigma'}+d^\dagger_{3\sigma}f_{2\sigma}d^\dagger_{3\sigma'}f_{2\sigma'}+h.c.\right]\\
&+\frac{U_{4n}}{2}\sum{}'d^\dagger_{3\sigma}d_{3\sigma}d^\dagger_{3\sigma'}d_{3\sigma'}\\
&+U_a\sum{}'\left[d^\dagger_{3\sigma}d_{3\sigma}d^\dagger_{1\sigma'}d_{1\sigma'}+d^\dagger_{3\sigma}d_{3\sigma}d^\dagger_{2\sigma'}d_{2\sigma'}\right]\\
&+U_b\sum{}'\left[d^\dagger_{3\sigma}d_{1\sigma}d^\dagger_{1\sigma'}d_{3\sigma'}+d^\dagger_{3\sigma}d_{2\sigma}d^\dagger_{2\sigma'}d_{3\sigma'}\right]\\
&+\frac{U_c}{2}\sum{}'\left[d^\dagger_{3\sigma}d_{1\sigma}d^\dagger_{3\sigma'}d_{1\sigma'}+d^\dagger_{3\sigma}d_{2\sigma}d^\dagger_{3\sigma'}d_{2\sigma'}+h.c.\right]
\end{aligned}
\tag{4.12}
$$

The interactions of the toy model are sketched in Fig. 4.5. Each single interaction term in Eq. (4.11) and Eq. (4.12) obeys the C_4 symmetry separately, which is why they do not need to flow equally under RG.

The bare values of the 21 couplings are expressed in terms of the parameters of the microscopic model for intra-orbital and inter-orbital interactions between fermions. The

commonly used model approximates all interactions as local in real space:

$$\begin{aligned} H_I = & U \sum_{i,\mu} n_{i,\mu,\uparrow} n_{i,\mu,\downarrow} + \frac{U'}{2} \sum_{i,\mu \neq \mu'} n_{i,\mu} n_{i,\mu'} \\ & + \frac{J}{2} \sum_{i,\mu \neq \mu'} \sum_{\sigma,\sigma'} d^\dagger_{i,\mu,\sigma} d^\dagger_{i,\mu',\sigma'} d_{i,\mu',\sigma'} d_{i,\mu,\sigma} \\ & + \frac{J'}{2} \sum_{i,\mu \neq \mu'} \sum_{\sigma,\sigma'} d^\dagger_{i,\mu,\sigma} d^\dagger_{i,\mu,\sigma'} d_{i,\mu',\sigma'} d_{i,\mu',\sigma}. \end{aligned} \tag{4.13}$$

Here the sums run over the sites i, the spin components σ, and the three orbitals $\mu = xy, xz, yz$. The density operator on site i in orbital μ is labeled by $n_{i,\mu} = \sum_\sigma n_{i,\mu,\sigma}$ and $n_{i,\mu,\sigma} = d^\dagger_{i,\mu,\sigma} d_{i,\mu,\sigma}$. The interactions in Eq. (4.13) involve the Hubbard interaction U between electrons on the same orbital, the onsite repulsion U' between electrons in different orbitals, the Hund's rule coupling J and the pair-hopping term J'.

By comparing with Eq. (4.13), we obtain the bare values of the 21 couplings

$$\begin{aligned} U &= U_4 = U_5 = \bar{U}_5 = \tilde{U}_5 = \tilde{\tilde{U}}_5 = U_{1n} = U_{2n} = U_{3n} = U_{4n} \\ U' &= U_1 = \bar{U}_1 = \tilde{U}_4 = U_a \\ J &= U_2 = \bar{U}_2 = \tilde{\tilde{U}}_4 = U_b \\ J' &= U_3 = \bar{U}_3 = \bar{U}_4 = U_c \end{aligned} \tag{4.14}$$

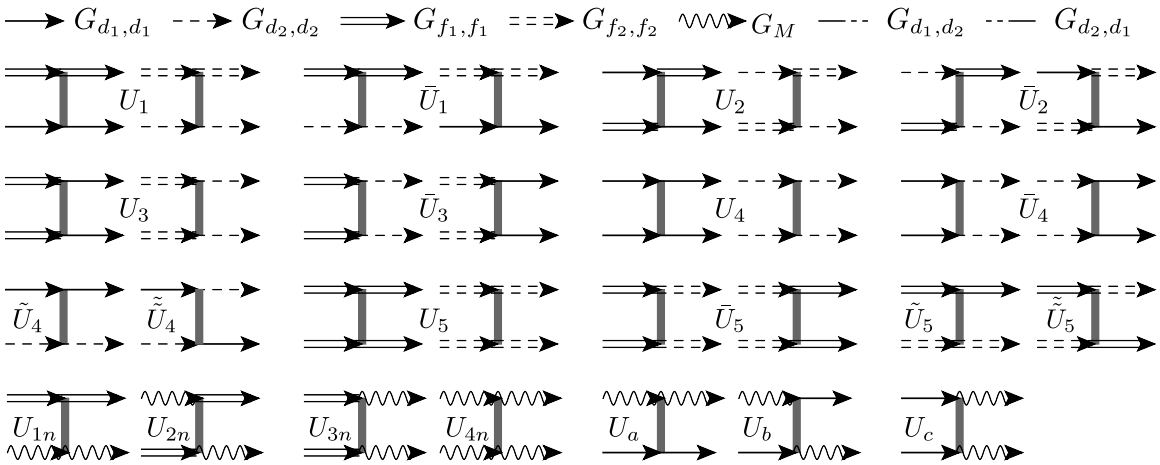

Figure 4.5: Diagrammatic representation of the 21 interaction terms in the toy model. Each interaction term is invariant under C_4 rotation.

Like we sad in the main text, the 21 interactions all flow to different values under pRG. This implies that the system self-generates longer-ranged interactions as one progressively integrates out fermions with higher energies.

4.6.1.3.2 The full model

In the full model with d_{xz}/d_{xy} and d_{yz}/d_{xy} orbital content of fermions near the electron pockets, 23 more couplings are allowed by symmetry, what increases the total number of the C_4-symmetric interaction terms to 44. 40 interactions involve pairs of fermions, with each pair near either Γ, X, Y, or M point. The 4 additional interactions involve fermions one near each of these points. Of the 23 new couplings, 13 are obtained by substituting f_1 and f_2 by f_{31} and f_{32} in Eqs. (4.11) and (4.12):

$$\begin{aligned}
H_I^{(1)} = & V_1 {\sum}' \left[f^\dagger_{31\sigma} f_{31\sigma} d^\dagger_{1\sigma'} d_{1\sigma'} + f^\dagger_{32\sigma} f_{32\sigma} d^\dagger_{2\sigma'} d_{2\sigma'} \right] \\
& + \bar{V}_1 {\sum}' \left[f^\dagger_{32\sigma} f_{32\sigma} d^\dagger_{1\sigma'} d_{1\sigma'} + f^\dagger_{31\sigma} f_{31\sigma} d^\dagger_{2\sigma'} d_{2\sigma'} \right] \\
& + V_2 {\sum}' \left[f^\dagger_{31\sigma} d_{1\sigma} d^\dagger_{1\sigma'} f_{31\sigma'} + f^\dagger_{32\sigma} d_{2\sigma} d^\dagger_{2\sigma'} f_{32\sigma'} \right] \\
& + \bar{V}_2 {\sum}' \left[f^\dagger_{31\sigma} d_{2\sigma} d^\dagger_{2\sigma'} f_{31\sigma'} + f^\dagger_{32\sigma} d_{1\sigma} d^\dagger_{1\sigma'} f_{32\sigma'} \right] \\
& + \frac{V_3}{2} {\sum}' \left[f^\dagger_{31\sigma} d_{1\sigma} f^\dagger_{31\sigma'} d_{1\sigma'} + f^\dagger_{32\sigma} d_{2\sigma} f^\dagger_{32\sigma'} d_{2\sigma'} + h.c. \right] \\
& + \frac{\bar{V}_3}{2} {\sum}' \left[f^\dagger_{31\sigma} d_{2\sigma} f^\dagger_{31\sigma'} d_{2\sigma'} + f^\dagger_{32\sigma} d_{1\sigma} f^\dagger_{32\sigma'} d_{1\sigma'} + h.c. \right] \\
& + \frac{V_5}{2} {\sum}' \left[f^\dagger_{31\sigma} f_{31\sigma} f^\dagger_{31\sigma'} f_{31\sigma'} + f^\dagger_{32\sigma} f_{32\sigma} f^\dagger_{32\sigma'} f_{32\sigma'} \right] \\
& + \frac{\bar{V}_5}{2} {\sum}' \left[f^\dagger_{31\sigma} f_{32\sigma} f^\dagger_{31\sigma'} f_{32\sigma'} + f^\dagger_{32\sigma} f_{31\sigma} f^\dagger_{32\sigma'} f_{31\sigma'} \right] \\
& + \tilde{V}_5 {\sum}' f^\dagger_{31\sigma} f_{31\sigma} f^\dagger_{32\sigma'} f_{32\sigma'} + \tilde{\bar{V}}_5 {\sum}' f^\dagger_{31\sigma} f_{32\sigma} f^\dagger_{32\sigma'} f_{31\sigma'} \\
& + V_{1n} {\sum}' \left[d^\dagger_{3\sigma} d_{3\sigma} f^\dagger_{31\sigma'} f_{31\sigma'} + d^\dagger_{3\sigma} d_{3\sigma} f^\dagger_{32\sigma'} f_{32\sigma'} \right] \\
& + V_{2n} {\sum}' \left[d^\dagger_{3\sigma} f_{31\sigma} f^\dagger_{31\sigma'} d_{3\sigma'} + d^\dagger_{3\sigma} f_{32\sigma} f^\dagger_{32\sigma'} d_{3\sigma'} \right] \\
& + \frac{V_{3n}}{2} {\sum}' \left[d^\dagger_{3\sigma} f_{31\sigma} d^\dagger_{3\sigma'} f_{31\sigma'} + d^\dagger_{3\sigma} f_{32\sigma} d^\dagger_{3\sigma'} f_{32\sigma'} + h.c. \right] \qquad (4.15)
\end{aligned}$$

Further six couplings come from interactions involving xy and xz/yz orbital states on the electron pockets

$$H_I^{(2)} = V_a {\sum}' \left[f^\dagger_{31\sigma} f_{31\sigma} f^\dagger_{1\sigma'} f_{1\sigma'} + f^\dagger_{32\sigma} f_{32\sigma} f^\dagger_{2\sigma'} f_{2\sigma'} \right]$$

$$
\begin{aligned}
&+ \bar{V}_a \sum{}' \left[f^\dagger_{32\sigma} f_{32\sigma} f^\dagger_{1\sigma'} f_{1\sigma'} + f^\dagger_{31\sigma} f_{31\sigma} f^\dagger_{2\sigma'} f_{2\sigma'} \right] \\
&+ V_b \sum{}' \left[f^\dagger_{31\sigma} f_{1\sigma} f^\dagger_{1\sigma'} f_{31\sigma'} + f^\dagger_{32\sigma} f_{2\sigma} f^\dagger_{2\sigma'} f_{32\sigma'} \right] \\
&+ \bar{V}_b \sum{}' \left[f^\dagger_{31\sigma} f_{2\sigma} f^\dagger_{2\sigma'} f_{31\sigma'} + f^\dagger_{32\sigma} f_{1\sigma} f^\dagger_{1\sigma'} f_{32\sigma'} \right] \\
&+ \frac{V_c}{2} \sum{}' \left[f^\dagger_{31\sigma} f_{1\sigma} f^\dagger_{31\sigma'} f_{1\sigma'} + f^\dagger_{32\sigma} f_{2\sigma} f^\dagger_{32\sigma'} f_{2\sigma'} + h.c. \right] \\
&+ \frac{\bar{V}_c}{2} \sum{}' \left[f^\dagger_{31\sigma} f_{2\sigma} f^\dagger_{31\sigma'} f_{2\sigma'} + f^\dagger_{32\sigma} f_{1\sigma} f^\dagger_{32\sigma'} f_{1\sigma'} + h.c. \right]
\end{aligned} \tag{4.16}
$$

We show these interactions graphically in Fig. 4.6. Note that, in contrast to the simplified model, $f_{1/2}$ now labels fermions with yz/xz orbital content, whereas $f_{31,32}$ labels fermions with xy orbital content.

Finally there are four additional interactions that, in contrast to the previous 40 interactions, involve fermions near each of the four high-symmetry points Γ, X, Y, M. In explicit form, these interactions are

$$
\begin{aligned}
H_I^{(3)} = &W_1 \sum{}' \left[f^\dagger_{1\sigma} d_{3\sigma} f^\dagger_{32\sigma'} d_{1\sigma'} + f^\dagger_{2\sigma} d_{3\sigma} f^\dagger_{31\sigma'} d_{2\sigma'} + h.c. \right] \\
&+ W_2 \sum{}' \left[f^\dagger_{31\sigma} d_{3\sigma} f^\dagger_{2\sigma'} d_{2\sigma'} + f^\dagger_{32\sigma} d_{3\sigma} f^\dagger_{1\sigma'} d_{1\sigma'} + h.c. \right] \\
&+ W_3 \sum{}' \left[f^\dagger_{1\sigma} d_{1\sigma} d^\dagger_{3\sigma'} f_{32\sigma'} + f^\dagger_{2\sigma} d_{2\sigma} d^\dagger_{3\sigma'} f_{31\sigma'} + h.c. \right] \\
&+ W_4 \sum{}' \left[f^\dagger_{31\sigma} d_{2\sigma} d^\dagger_{3\sigma'} f_{2\sigma'} + f^\dagger_{32\sigma} d_{1\sigma} d^\dagger_{3\sigma'} f_{1\sigma'} + h.c. \right]
\end{aligned} \tag{4.17}
$$

We checked explicitly that these four additional interactions do not affect the behavior near each of the four stable fixed trajectories, which we obtained by solving the pRG equations for 40 couplings (see Sec. 4.6.2.2). This is what we presented in the main text. We also verified that these additional interactions do not generate new fixed trajectories, if the bare values of these interactions are within certain limits. Outside these limits, the 4 additional interactions may, in principle, move the system towards a new stable fixed trajectory. We did not explore this possibility here and in the following we neglect these four additional interactions.

Like we did for the toy model, we express the bare values of the 40 couplings in terms

of U, U', J, J'. We have

$$\begin{aligned} U &= U_1 = U_2 = U_3 = U_4 = U_5 = \bar{U}_5 = U_{4n} = V_5 = \bar{V}_5 \\ &= \tilde{V}_5 = \tilde{\bar{V}}_5 = V_{1n} = V_{2n} = V_{3n} \\ U' &= \bar{U}_1 = \tilde{U}_4 = \tilde{U}_5 = U_{1n} = U_a = V_a = \bar{V}_a = V_1 = \bar{V}_1 \\ J &= \bar{U}_2 = \tilde{\bar{U}}_4 = \tilde{\bar{U}}_5 = U_{2n} = U_b = V_b = \bar{V}_b = V_2 = \bar{V}_2 \\ J' &= \bar{U}_3 = \bar{U}_4 = \bar{U}_5 = U_{3n} = U_c = V_c = \bar{V}_c = V_3 = \bar{V}_3. \end{aligned} \tag{4.18}$$

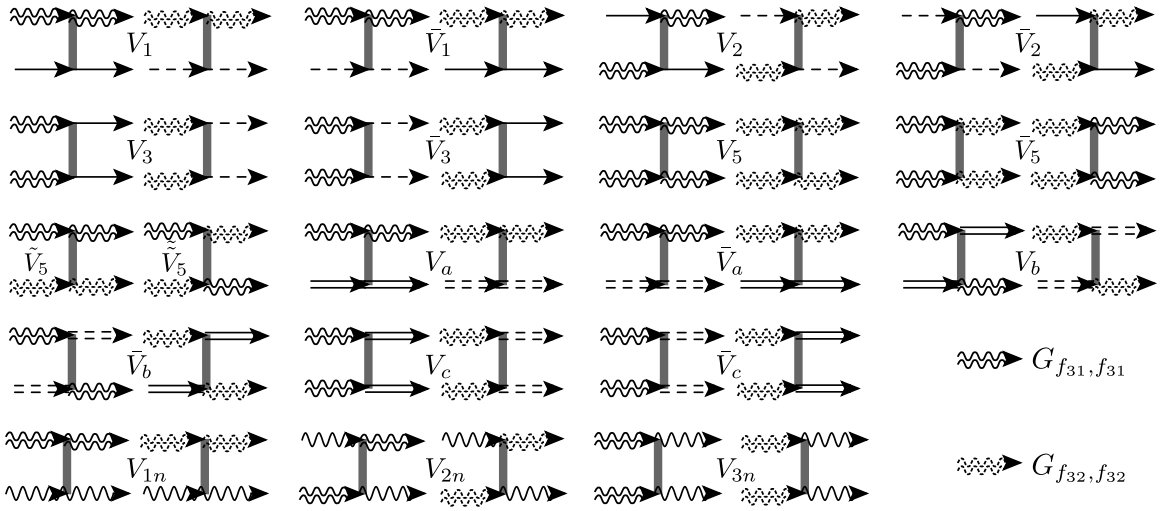

Figure 4.6: Additional interactions allowed by C_4 symmetry in the full model.

4.6.2 Analytic parguet RG for 5-pocket model

We employ a pRG approach to study the hierarchy of the orders that the system develops at low energies. The pRG procedure allows us to see how the susceptibilities in different ordering channels evolve as the system flows to low energies, including their mutual feedback. In the pRG procedure, one integrates out fermions with energies down to a progressively smaller running energy E and observes how the couplings vary as E gets smaller. We describe this flow of interactions in terms of the RG scale $L = \log \Lambda/E$, where Λ is the UV-cutoff, generally of the order of the bandwidth. The logarithmic energy scale L appears due to the fact that the polarization bubbles in the particle-particle channel at zero total momentum *and* the particle-hole channel at momenta $(\pi, 0)$ and $(0, \pi)$ are logarithmical. As a result of the integration procedure, we obtain coupled differential equations

-the flow equations- for all the interactions, describing their evolution with L. We solve for the running couplings $U_i(L)$ and use these solutions as inputs to calculate susceptibilities in different ordering channels (SDW, CDW, superconducting and Pomeranchul channels). An instability in a particular channel is signaled by the divergence of the corresponding susceptibility at a scale L_{cr}. Below we show the details of pRG analysis for the toy model and the full model. We recall that pRG analysis works when E is larger than the Fermi energy, i.e., when $L < L_F = \log \Lambda / E_F$ (see, e.g., Ref. [127]). If $L_{cr} < L_F$, the pRG analysis works all the way to the leading instability. If $L_{cr} > L_F$, pRG analysis allows one to determine the largest susceptibility at $L = L_F$. It is likely (although not guaranteed) that this susceptibility will diverge first at a lower energy.

4.6.2.1 PRG for the toy model

4.6.2.1.1 PRG equations and fixed trajectories

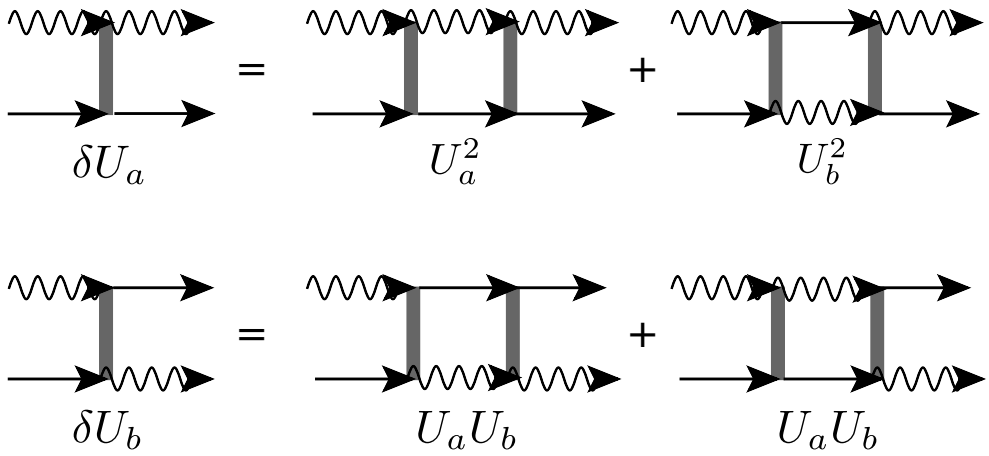

Figure 4.7: Diagrammatic representation of the 1-loop renormalizations of the interactions U_a and U_b. They decouple from the remaining interactions and are representative for the subgroup of interactions flowing to zero.

We derive the pRG equations by collecting all possible one-loop diagrams that contribute to logarithmic renormalization of each of the interactions. The procedure has been described Ref. [111] (for a simplified 4-pocket, two-orbital model) and in Ref. [127] for 3-pocket, one-orbital model. We follow the same line of reasoning as in these works. We obtain the pRG equations for our 5-pocket model by combining and modifying pRG equations from these two models.

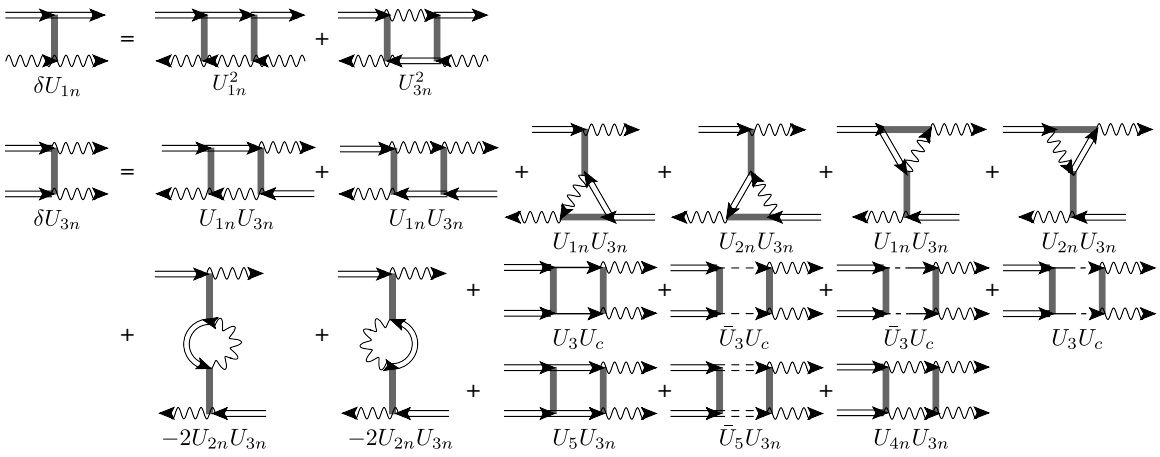

Figure 4.8: Diagrammatic representation of the 1-loop renormalization of the interactions U_{1n} and U_{3n}.

Like in Ref. [111] we find that pRG equations for 6 combinations of the couplings $(\tilde{U}_4 \pm \tilde{\tilde{U}}_4)$, $(\tilde{U}_5 \pm \tilde{\tilde{U}}_5)$ and $(\tilde{U}_a \pm \tilde{\tilde{U}}_b)$ decouple from other RG equations, and these combinations all flow to zero if their bare values are positive, which is the case for $U' \geq J$. We assume that this inequality holds. If it does not hold, the system may develop a superconducting instability in the spin-triplet A_{2g} channel (Ref. [139]). Representative diagrams for the renormalizations of the couplings from this group of 6 are shown in Fig. 4.7. The 6 pRG equations are:

$$\begin{aligned} 4\pi \frac{d}{dL}\left(\tilde{U}_4 \pm \tilde{\tilde{U}}_4\right) &= -c_{pp}^{(1)}\left(\tilde{U}_4 \pm \tilde{\tilde{U}}_4\right)^2 \\ 4\pi \frac{d}{dL}\left(\tilde{U}_5 \pm \tilde{\tilde{U}}_5\right) &= -c_{pp}^{(2)}\left(\tilde{U}_5 \pm \tilde{\tilde{U}}_5\right)^2 \\ 4\pi \frac{d}{dL}\left(U_a \pm U_b\right) &= -c_{pp}^{(3)}\left(U_a \pm U_b\right)^2, \end{aligned} \tag{4.19}$$

where $c_{pp}^{(1)} = \frac{1}{8}(m_c + m_d + 12\frac{m_c m_d}{m_c+m_d} \pm \frac{(m_c-m_d)^2}{m_c+m_d})$, $c_{pp}^{(2)} = m_e$ and $c_{pp}^{(3)} = \frac{m_M m_c}{m_M+m_c} + \frac{m_M m_d}{m_M+m_d}$. The pRG equations for the other remaining 15 couplings are

$$\begin{aligned} 4\pi \frac{d}{dL} U_1 &= A(U_1^2 + U_3^2) \\ 4\pi \frac{d}{dL} \bar{U}_1 &= A(\bar{U}_1^2 + \bar{U}_3^2) \\ 4\pi \frac{d}{dL} U_{1n} &= A_n(U_{1n}^2 + U_{3n}^2) \\ 4\pi \frac{d}{dL} U_2 &= 2AU_2(U_1 - U_2) \end{aligned}$$

$$
\begin{aligned}
4\pi\frac{d}{dL}\bar{U}_2 &= 2A\bar{U}_2(\bar{U}_1-\bar{U}_2)\\
4\pi\frac{d}{dL}U_{2n} &= 2A_nU_{2n}(U_{1n}-U_{2n})\\
4\pi\frac{d}{dL}U_3 &= 2AU_3(2U_1-U_2)-A_e(U_3U_5+\bar{U}_3\bar{U}_5)\\
&\quad -A_h(U_3U_4+\bar{U}_3\bar{U}_4)-A_h^-(U_3\bar{U}_4+\bar{U}_3U_4)-A_MU_{3n}U_c\\
4\pi\frac{d}{dL}\bar{U}_3 &= 2A\bar{U}_3(2\bar{U}_1-\bar{U}_2)-A_e(\bar{U}_3U_5+U_3\bar{U}_5)\\
&\quad -A_h(\bar{U}_3U_4+U_3\bar{U}_4)-A_h^-(U_3U_4+\bar{U}_3\bar{U}_4)-A_MU_{3n}U_c\\
4\pi\frac{d}{dL}U_{3n} &= 2A_nU_{3n}(2U_{1n}-U_{2n})-A_eU_{3n}(U_5+\bar{U}_5)\\
&\quad -A_MU_{3n}U_{4n}-(A_h+A_h^-)(U_3+\bar{U}_3)U_c\\
4\pi\frac{d}{dL}U_4 &= -A_h(U_4^2+\bar{U}_4^2)-2A_h^-U_4\bar{U}_4-A_e(U_3^2+\bar{U}_3^2)\\
&\quad -A_MU_c^2\\
4\pi\frac{d}{dL}\bar{U}_4 &= -2A_hU_4\bar{U}_4-A_h^-(U_4^2+\bar{U}_4^2)-2A_eU_3\bar{U}_3\\
&\quad -A_MU_c^2\\
4\pi\frac{d}{dL}U_{4n} &= -A_MU_{4n}^2-2A_eU_{3n}^2-2(A_h+A_h^-)U_c^2\\
4\pi\frac{d}{dL}U_5 &= -A_e(U_5^2+\bar{U}_5^2)-A_h(U_3^2+\bar{U}_3^2)-2A_h^-U_3\bar{U}_3\\
&\quad -A_MU_{3n}^2\\
4\pi\frac{d}{dL}\bar{U}_5 &= -2A_eU_5\bar{U}_5-2A_hU_3\bar{U}_3-A_h^-(U_3^2+\bar{U}_3^2)\\
&\quad -A_MU_{3n}^2\\
4\pi\frac{d}{dL}U_c &= -(A_h+A_h^-)(U_4+\bar{U}_4)U_c-A_MU_{4n}U_c\\
&\quad -A_3(U_3+\bar{U}_3)U_{3n}.
\end{aligned}
\tag{4.20}
$$

As an example, the one-loop diagrams that renormalize U_{1n} and U_{3n} are presented in Fig. 4.8. The numerical prefactors in the r.h.s. of pRG equations are $A=\frac{m_em_c}{m_e+m_c}+\frac{m_em_d}{m_e+m_d}$, $A_n=\frac{m_Mm_e}{m_M+m_e}$, $A_e=m_e$, $A_h=\frac{3}{8}(m_c+m_d)+\frac{1}{2}\frac{m_cm_d}{m_c+m_d}$, $A_h^-=\frac{1}{8}\frac{(m_c-m_d)^2}{m_c+m_d}$ and $A_M=m_M$. Note that the contribution $A_h^-=(m_c-m_d)^2/(8(m_c+m_d))$ comes from the G_{d_1,d_2} the propagator for fermions near the $\Gamma-$centered hole pockets (see Eq.(4.8)).

To proceed, we note that, if $U_i=\bar{U}_i$, then $d_LU_i=d_L\bar{U}_i$. We have checked that

the trajectory with this property is a stable one. We searched for other potential stable fixed trajectories, but did not find one. Hence we set $U_i = \bar{U}_i$. We further introduce the dimensionless couplings $u_{1,2} = A/(4\pi)U_{1,2}$, $u_3 = A/(4\pi)aU_3$, $u_4 = A_h/(4\pi)U_4$, $u_5 = A_e/(4\pi)U_5$, $u_{1n,2n} = A_n/(4\pi)U_{1n,2n}$, $u_{3n} = A_n/(4\pi)a_nU_{3n}$, $u_{4n} = A_M/(4\pi)U_{4n}$ and $u_{5n} = \sqrt{A_MA_h}/(4\pi)U_c$ and define $a = \sqrt{A_hA_e}/A$ and $a_n = \sqrt{A_MA_e}/A_n$ and $b = 1 + A_h^-/A_h$. Then we obtain the pRG equations

$$
\begin{aligned}
\dot{u}_1 &= u_1^2 + \frac{u_3^2}{a^2} \\
\dot{u}_{1n} &= u_{1n}^2 + \frac{u_{3n}^2}{a_n^2} \\
\dot{u}_2 &= 2u_2(u_1 - u_2) \\
\dot{u}_{2n} &= 2u_{2n}(u_{1n} - u_{2n}) \\
\dot{u}_3 &= 2u_3(2u_1 - u_2 - u_5) - 2bu_3u_4 - u_{3n}u_{5n} \\
\dot{u}_{3n} &= 2u_{3n}(2u_{1n} - u_{2n} - u_5) - u_{3n}u_{4n} - 2bu_3u_{5n} \\
\dot{u}_4 &= -2bu_4^2 - 2u_3^2 - 2u_{5n}^2 \\
\dot{u}_{4n} &= -u_{4n}^2 - 2u_{3n}^2 - 2bu_{5n}^2 \\
\dot{u}_5 &= -2u_5^2 - 2bu_3^2 - u_{3n}^2 \\
\dot{u}_{5n} &= -2bu_4u_{5n} - u_{4n}u_{5n} - 2u_3u_{3n},
\end{aligned}
\tag{4.21}
$$

which we presented in the main text for $a = a_n = b = 1$.

4.6.2.1.2 The solution of PRG equations

To simplify the analysis we assume $m_c \approx m_d$ and neglect the contribution from A_h^-, i.e. set $A_h^- = 0$. We searched for different fixed trajectories of Eq. (4.20) along which the couplings diverge, but their ratios tend to fixed values. This can be seen in Fig. 4.9. Accordingly, we single out one of the coupling, say u_0, and write all other couplings as

$$u_i = \gamma_i u_0, \tag{4.22}$$

Along the fixed trajectory, u_0 flows to infinity, but γ_i tend to finite values. Solving for the fixed trajectory of the set of coupled pRG equations, Eq. (4.20), then reduces to finding the fixed point solution of

$$\beta_i := \partial_L \gamma_i = \frac{1}{u_i}(\partial_L u_i - \gamma_i \partial_L u_0) = 0. \tag{4.23}$$

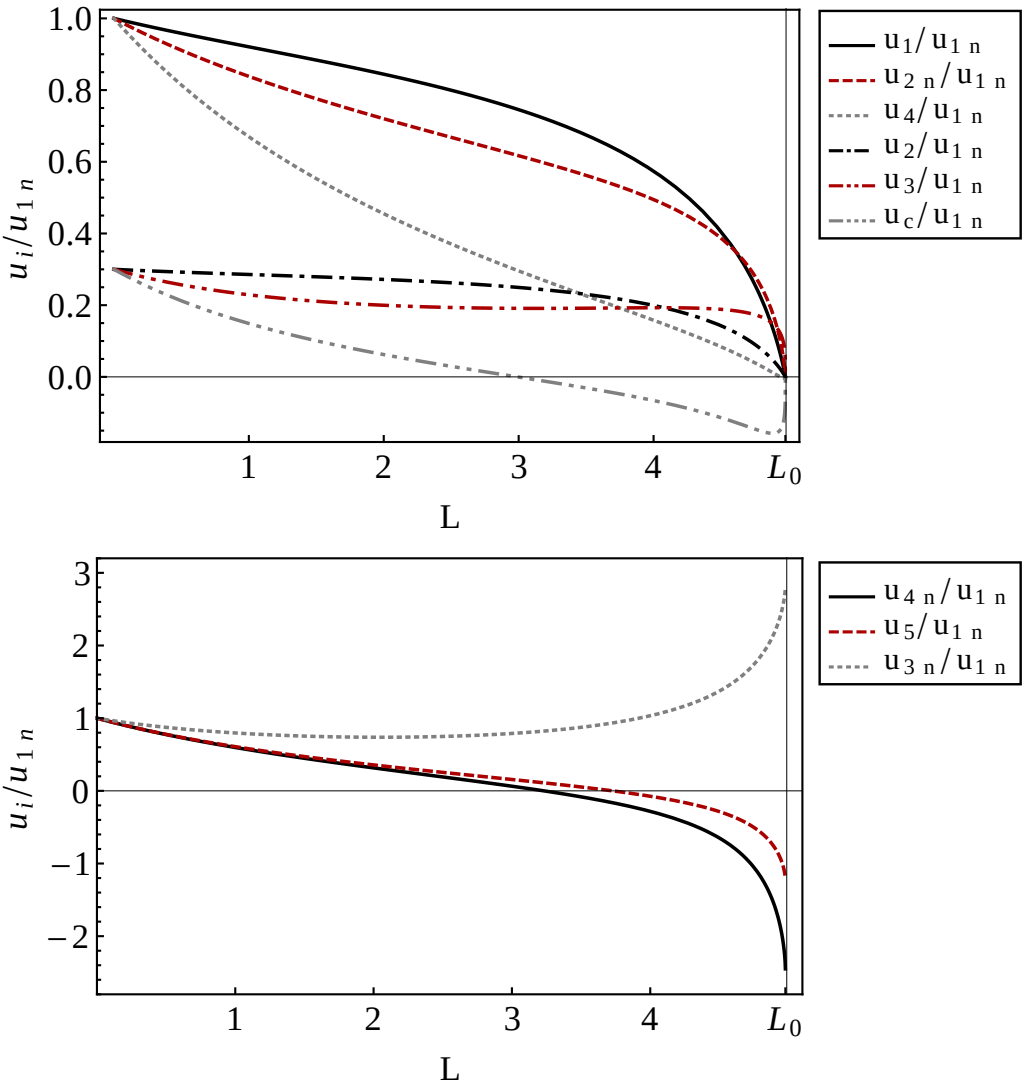

Figure 4.9: Ratios of couplings for the flow to the 3-pocket fixed trajectory (3p) in the toy model for bare values $U = U' = 0.1/N_F$, $J = J' = 0.03/N_F$ and $a = a_n = 1$, N_F is the density of states on the FSs. All ratios tend to zero (upper penal), except for those within the triad of electron pockets and the $M-$centered hole pocket.

The fixed trajectory is stable if small perturbations around the fixed point do not grow, i.e. the stability matrix $\partial\beta_i/\partial\gamma_j|_{\gamma^*}$, which describes the linearized flow around the fixed point, should have only negative eigenvalues. For the toy model we find two stable fixed trajectories, separated by a fixed point solution with a single unstable direction. In the

main text we labeled the two stable fixed trajectories as effective 4-pocket model (4p) and effective 3-pocket mode (3p). The behavior of the couplings along these two stable fixed trajectories is

(1) 4p

$$\begin{aligned} u_i &= \gamma_i u_1 \\ u_1 &= \frac{1}{1+\gamma_3^2/a^2}\frac{1}{L_0-L} \\ \gamma_2 &= \gamma_{1n} = \gamma_{2n} = \gamma_{3n} = \gamma_{4n} = \gamma_c = 0 \\ \gamma_3 &= \pm a\sqrt{8a^2 - 1 + 4\sqrt{1-a^2+4a^4}} \\ \gamma_4 &= \gamma_5 = 1 - 2a^2 - \sqrt{1-a^2+4a^4} \end{aligned} \tag{4.24}$$

(2) 3p

$$\begin{aligned} u_i &= \gamma_i u_{1n} \\ u_{1n} &= \frac{1}{1+\gamma_{3n}^2/a_n^2}\frac{1}{L_0-L} \\ \gamma_{2n} &= \gamma_c = \gamma_1 = \gamma_2 = \gamma_3 = \gamma_4 = 0 \\ \gamma_{3n} &= \pm a_n\sqrt{4a_n^2 - 1 + 2\sqrt{4-2a_n^2+4a_n^4}} \\ \gamma_{4n} &= 2\gamma_5 = 2 - 2a_n^2 - \sqrt{4-2a_n^2+4a_n^4} \end{aligned} \tag{4.25}$$

Because the bare values for γ_3, γ_{3n} are positive, the system reaches the stable FT with positive γ_3, γ_{3n}. We see that along the stable fixed trajectories, either all γ_i for interactions with the $\Gamma-$centered hole pockets vanish (3p), or all γ_i for the interactions with the third hole pocket at M vanish (4p). This does not mean that the interactions themselves vanish, it only means that these interactions do not grow as fast as other interactions. These couplings actually still increase under pRG but with exponents smaller than one. This means that, to leading order, the system flows to either 4-pocket model (4p) or 3-pocket model (3p). However the subleading terms still have an impact on the emergent order, as they determine how the order parameter behaves at the remaining hole pocket(s).

The third, weakly unstable fixed trajectory is symmetry-enhanced in the sense that $u_1 = u_{1n}$, and $u_3/a = u_{3n}/a_n$. Along this trajectory all ratios (except for γ_2, γ_{2n}) attain

finite values. Specifically, we obtain

$$
\begin{aligned}
u_i &= \gamma_i u_1 \\
u_1 &= \frac{1}{1+\gamma_3^2/a^2}\frac{1}{L_0 - L} \\
\gamma_{1n} = \gamma_1 &= 1 \quad \frac{\gamma_{3n}}{a_n} = \pm\frac{\gamma_3}{a} \quad \gamma_2 = \gamma_{2n} = 0 \\
\gamma_3 &= \sqrt{8a^4 - a^2 + 4a^2a_n^2 + a^2\sqrt{15 + (8a^2 + 4a_n^2 - 1)^2}} \\
\gamma_5 &= 1 - a_n^2 - 2a^2 - \sqrt{1 + a_n^4 - a^2 + 4a^4 + a_n^2(4a^2 - \frac{1}{2})} \\
\gamma_c &= \pm a_n \frac{2a - \sqrt{2\gamma_3^2 a_n^2 + 4a^2(1+\gamma_3^2)}}{a_n^2 + 2a^2} \\
\gamma_4 &= \pm\frac{a_n}{2a}\gamma_c + \frac{\gamma_3^2}{4a^2} - \frac{3}{4} \\
\gamma_{4n} &= \mp\frac{2a}{a_n}\gamma_c + \gamma_5
\end{aligned}
\tag{4.26}
$$

For $a = a_n = 1$ γ_i in (4.26) reduce to

$$
\begin{aligned}
&\gamma_3 = \pm\gamma_{3n} \quad \gamma_4 = \gamma_{4n} = \pm\gamma_c \\
&\gamma_3 = \sqrt{11 + 2\sqrt{34}} \quad \gamma_4 = -\frac{1}{3}(4 + \sqrt{34}) \\
&\gamma_5 = -2 - \sqrt{\frac{17}{2}}
\end{aligned}
\tag{4.27}
$$

Like we said, this fixed trajectory has one unstable direction when we consider deviations from it. We verified that, depending on the sign of deviation along the unstable direction, the system flows either to one or to the other stable fixed trajectory. We present the phase diagram for different bare values in the main text and here present the result of our study of the stability regimes of 4p and 3p at various a_n/a in Fig.4.10.

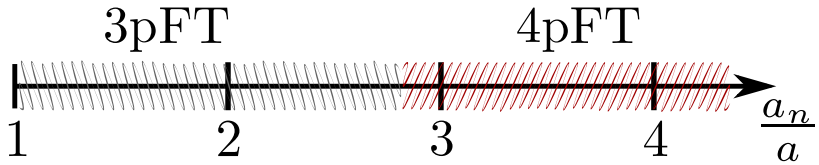

Figure 4.10: Fixed trajectory at the end of the flow for different values of a_n/a. 3pFT (4pFT) denotes the effective 3p (4p) model. Bare values are $U = U', J = J'$ and $J/U = 0.3$.

4.6.2.1.3 Susceptibilities

To decide which order wins and develops at low energies, we introduce vertices Γ_i that describe the coupling between fermions and order parameters. The vertices in turn determine the susceptibilities in the corresponding ordering channel, whose divergence would signal a phase transition. Here we focus on SDW, CDW, and SC channels. The analysis of the susceptibilities in the Pomeranchuk channels is discussed afterwards.

The vertices are renormalized by the corresponding polarization bubbles and diverge with a certain exponent when the running couplings approach the fixed trajectory, as $\Gamma_i \propto (L_0 - L)^{-\beta}$. The susceptibilities

$$\chi_i - \chi_0 \propto \int_L dL' \Gamma_i^2(L'), \tag{4.28}$$

then behave as $\chi \propto (L_0 - L)^{1-2\beta} + \text{const}$. In order to diverge the vertex exponent must satisfy $\beta \geq 1/2$. The one-loop renormalization of the vertices are shown in Fig. 4.11. In analytic form, the pRG equations for the vertices in the SDW and CDW channels are

$$\begin{aligned}
\partial_L \Gamma^{\Gamma}_{SDW} &= \left(u_1 + \frac{u_3}{a}\right) \Gamma^{\Gamma}_{SDW} \\
\partial_L \Gamma^{M}_{SDW} &= \left(u_{1n} + \frac{u_{3n}}{a_n}\right) \Gamma^{M}_{SDW} \\
\partial_L \Gamma^{\Gamma}_{CDW} &= \left(u_1 - 2u_2 - \frac{u_3}{a}\right) \Gamma^{\Gamma}_{CDW} \\
\partial_L \Gamma^{M}_{CDW} &= \left(u_{1n} - 2u_{2n} - \frac{u_{3n}}{a_n}\right) \Gamma^{M}_{CDW}.
\end{aligned} \tag{4.29}$$

By inserting the values for the fixed trajectories, we obtain the exponents β_i:

$$\begin{aligned}
\beta^{(4p)}_{SDW} &= \frac{1 + \gamma_3/a}{1 + \gamma_3^2/a^2} \quad \beta^{(4p)}_{CDW} = \frac{1 - \gamma_3/a}{1 + \gamma_3^2/a^2} \\
\beta^{(3p)}_{SDW} &= \frac{1 + \gamma_{3n}/a_n}{1 + \gamma_{3n}^2/a_n^2} \quad \beta^{(3p)}_{CDW} = \frac{1 - \gamma_{3n}/a_n}{1 + \gamma_{3n}^2/a_n^2}.
\end{aligned} \tag{4.30}$$

Note that γ_3, γ_{3n} also depend on a, a_n in these expressions. The exponents attain their maximal values at $a = 1, a_n = 1$ with $\beta^{(4p)}_{SDW} \approx 0.30$, $\beta^{(4p)}_{CDW} \approx -0.18$ and $\beta^{(3p)}_{SDW} \approx 0.43$, $\beta^{(3p)}_{CDW} \approx -0.20$. These values do not lead to a divergent susceptibility, i.e. the corresponding order does not develop if the normal state becomes unstable before the Fermi energy is reached.

The pRG flow of the vertices in the particle-particle channel obeys

$$\partial_L \begin{pmatrix} \Gamma^e_{SC} \\ \Gamma^\Gamma_{SC} \\ \Gamma^M_{SC} \end{pmatrix} = \begin{pmatrix} -2u_5 & -2u_3 & -2u_{3n} \\ -2u_3 & -2u_4 & -2u_c \\ -u_{3n} & -u_c & -u_{4n} \end{pmatrix} \begin{pmatrix} \Gamma^e_{SC} \\ \Gamma^\Gamma_{SC} \\ \Gamma^M_{SC} \end{pmatrix}, \tag{4.31}$$

where we have absorbed different prefactors into Γ_{SC} as $\sqrt{A_h/A_e}\Gamma^\Gamma_{SC} \to \Gamma^\Gamma_{SC}$, $\sqrt{A_M/A_e}\Gamma^M_{SC} \to \Gamma^M_{SC}$. For 4pFT and 3pFT, this set reduces to a 2x2 matrix, and the diagonalization of Eq. (4.31) yields in these two cases

$$\begin{aligned} \beta^{(4p)}_{SC,+-/++} &= \frac{-\gamma_4 - \gamma_5 \pm \sqrt{(\gamma_4 - \gamma_5)^2 + 4\gamma_3^2/a^2}}{1 + \gamma_3^2/a^2} \\ \beta^{(3p)}_{SC,+-/++} &= \frac{-\gamma_{4n} - 2\gamma_5 \pm \sqrt{(\gamma_{4n} - 2\gamma_5)^2 + 8\gamma_{3n}^2/a_n^2}}{1 + \gamma_{3n}^2/a_n^2}. \end{aligned} \tag{4.32}$$

The largest eigenvalues correspond to the s_{+-} superconducting state and satisfy $\beta_{SC,+-} > 1/2$. For $a = a_n = 1$ they are $\beta^{(4p)}_{SC,+-} = 0.86$, and $\beta^{(3p)}_{SC,+-} = 0.72$. Because these β_{SC} are larger than $1/2$, we find that the system develops superconductivity at low energies rather than SDW or CDW order. From the analysis of the fixed trajectory we can infer that the gap changes sign either between the electron pockets and the two $\Gamma-$centered hole pockets (for 4p), or between the electron pockets and the $M-$centered hole pocket (for 3p). In both cases, this is conventional s^{+-} gap structure.

To determine the sign of the superconducting gap on the remaining hole pocket(s), we must include the residual interactions (the once which diverge with smaller exponents). To do this and to verify our analytical reasoning, we solved the set of pRG equations for the couplings and the set of the vertices in the SC channel, Eq. (4.31), numerically. We find two positive (attractive) and one negative eigenvalue in the SC channel. The negative one obviously corresponds to repulsive interaction in s^{++} channel. The positive eigenvalues correspond to s^{+-} gap structure. For the largest positive eigenvalue along the 3p FT or 4p FT the gap(s) on the remaining hole pocket(s) align such that the sign of the gap on all three hole pockets is the same (and opposite to the gap sign on the two electron pockets). This is the "conventional" s^{+-} gap structure. However, the size of the vertex, which is related to the gap size, on the residual pocket is smaller than on the dominant pockets. The smaller positive eigenvalue along the 3p FT or the 4p FT actually starts negative at small L and then changes the sign in the process of the RG flow. For the 4p FT, the gap structure that corresponds to this eigenvalue has the same sign of the gap on the $M-$centered hole pocket

as on the electron pockets, i.e., there is one sign of the gap on the two $\Gamma-$centered hole pockets and another sign on the other three pockets. For the 3p FT and for this eigenvalue, the sign of the gap on the $\Gamma-$centered hole pockets and on the electron pockets is the same, and opposite to that on the $M-$ hole pocket. The gap structure of this kind was proposed in Ref. [133] and termed as "orbital anti-phase". Our RG analysis shows that along the fixed trajectory such a state is subleadng to a conventional s^{+-}. Finally, we computed the gap structure along the weakly unstable FT of Eq. (4.26) and found that it is also a conventional s^{+-}. We do not find d-wave order.

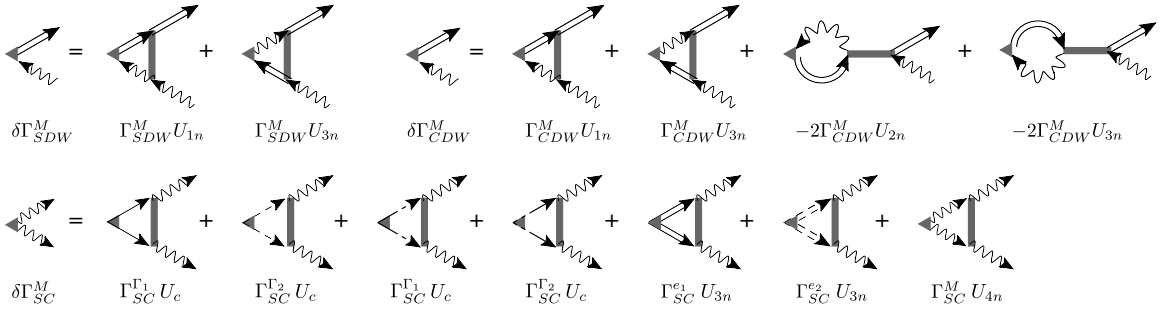

Figure 4.11: Diagrammatic representation of the 1-loop renormalization of representative SDW, CDW, and SC vertices. In the RG equations of the superconducting vertices, only the combinations $\Gamma^{\Gamma}_{SC} := \Gamma^{\Gamma_1}_{SC} + \Gamma^{\Gamma_2}_{SC}, \Gamma^{e}_{SC} := \Gamma^{e_1}_{SC} + \Gamma^{e_2}_{SC}$ appear.

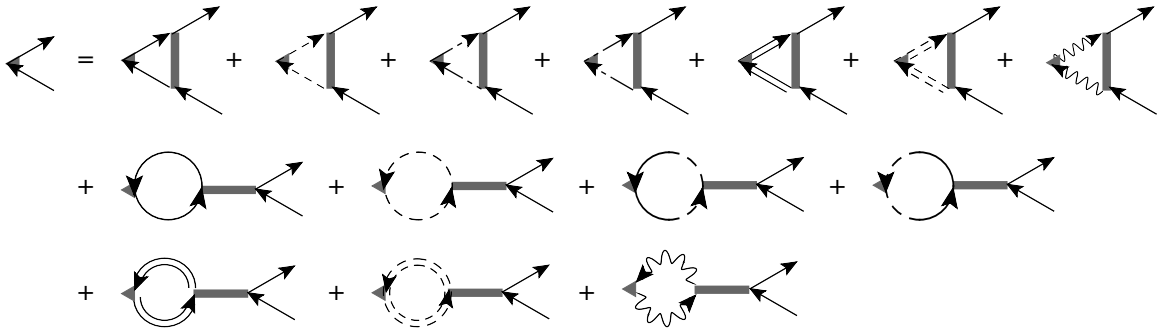

Figure 4.12: Diagrammatic representation of the 1-loop renormalization of a representative Pomeranchuk vertex corresponding to the orbital density n_{xz}. The polarization bubbles are not logarithmic as they involve two identical propagators.

To analyze orbital ordering, we calculate the vertices and susceptibilities in the Pomeranchuk channel with the orbital densities $n_\mu = d^\dagger_\mu d_\mu$ as order parameters. The analysis is somewhat different than before because the polarization bubbles that renormalize the Pomeranchuk vertices are not logarithmically divergent as can be seen in Fig. 4.12 . How-

ever, the scale-dependence of the interaction provides a logarithmic renormalization. Summing only logarithmic terms then leads to pRG equations in the Pomeranchuk channel of the form $\partial_L \Gamma_\mu \propto \Gamma_\mu^0 \partial_L u$, i.e. $\Gamma_\mu \propto \Gamma_\mu^0 (1+u)$. Since the couplings flow as $u \propto (L_0 - L)^{-1}$, the Pomeranchuk vertex grows with exponent $\beta_\mu = 1$ and overtakes the SC vertex at the end of the flow. Note however that the renormalization of the Pomeranchuk vertex develops when the couplings become of order one so that corrections to 1-loop RG may contribute. Explicitly the pRG equation of the Pomeranchuk channel for the toy model reads

$$\frac{d}{dL}\begin{pmatrix} \Gamma^\Gamma_{xz} \\ \Gamma^\Gamma_{yz} \\ \Gamma^X_{xy} \\ \Gamma^Y_{xy} \\ \Gamma^M_{xy} \end{pmatrix} = -2\frac{d}{dL} M \begin{pmatrix} \Gamma^\Gamma_{xz} \\ \Gamma^\Gamma_{yz} \\ \Gamma^X_{xy} \\ \Gamma^Y_{xy} \\ \Gamma^M_{xy} \end{pmatrix}, \tag{4.33}$$

where

$$M = \begin{pmatrix} u_4 & 0 & \frac{A_e}{A}(2u_1 - u_2) & \frac{A_e}{A}(2u_1 - u_2) & 0 \\ 0 & u_4 & \frac{A_e}{A}(2u_1 - u_2) & \frac{A_e}{A}(2u_1 - u_2) & 0 \\ \frac{A_h}{A}(2u_1 - u_2) & \frac{A_h}{A}(2u_1 - u_2) & u_5 & 0 & \frac{A_M}{A_n}(2u_{1n} - u_{2n}) \\ \frac{A_h}{A}(2u_1 - u_2) & \frac{A_h}{A}(2u_1 - u_2) & 0 & u_5 & \frac{A_M}{A_n}(2u_{1n} - u_{2n}) \\ 0 & 0 & \frac{A_e}{A_n}(2u_{1n} - u_{2n}) & \frac{A_e}{A_n}(2u_{1n} - u_{2n}) & u_{4n} \end{pmatrix} \tag{4.34}$$

where we have omitted the irrelevant couplings (Eq. (4.19)) and set $m_c = m_d$. As has been already obtained in Ref. [111], the leading instability in the Pomeranchuk channel along the 4pFT is in the d-wave channel with non-equal densities $n_{xz} - n_{yz}$. Along the 3pFT an instability with different densities on the electron pockets $n_{xy}(X) - n_{xy}(Y) \neq 0$ develops, which also breaks C_4 symmetry. Such an order splits one of the band degeneracies of the electron bands in the folded Brillouin zone.

Finally, we comment on the system behavior in a situation when the system does not reach a fixed trajectory before the RG scale L becomes comparable to $L_F = \log \Lambda / E_F$. Because the susceptibility in the SDW channel is the largest over a wide range of L, it is most likely that in this situation the system develops an SDW order. We compared the behavior of SDW vertices involving fermions from one of the electron pockets and either fermions from $\Gamma-$centered hole pockets (Γ^Γ_{SDW}) or from the $M-$pocket (Γ^M_{SDW}). We found that $\Gamma^M_{SDW} > \Gamma^\Gamma_{SDW}$ if the flow is towards the 3pFT, and $\Gamma^\Gamma_{SDW} > \Gamma^M_{SDW}$ if the flow is

towards the 4pFT. This implies that in the first case SDW order predominantly involves the triad of two electron pockets and the M hole pockets, while in the second case it involves two electron pockets and two Γ-centered hole pockets.

4.6.2.2 PRG for full 5-pocket model

4.6.2.2.1 PRG equations and fixed trajectories

We now move to the full 5-band model with xz/yz orbital content on the electron pockets. Like we said, in this case we have 19 more couplings (the total number of the couplings is 40). The couplings $\tilde{U}_4, \tilde{\tilde{U}}_4, \tilde{U}_5, \tilde{\tilde{U}}_5, U_a, U_b$ do not couple to additional terms and continue to flow to zero under pRG. We find six additional couplings $\tilde{V}_5$, $\tilde{\tilde{V}}_5$, $V_a, V_b, \bar{V}_a, \bar{V}_b$ that flow to zero. The corresponding pRG equations are

$$\begin{aligned} 4\pi\frac{d}{dL}\left(\tilde{V}_5 \pm \tilde{\tilde{V}}_5\right) &= -c_{pp}^{(4)}\left(\tilde{V}_5 \pm \tilde{\tilde{V}}_5\right)^2 \\ 4\pi\frac{d}{dL}\left(V_a \pm V_b\right) &= -c_{pp}^{(5)\pm}\left(V_a \pm V_b\right)^2 \\ 4\pi\frac{d}{dL}\left(\bar{V}_a \pm \bar{V}_b\right) &= -c_{pp}^{(6)}\left(\bar{V}_a \pm \bar{V}_b\right)^2, \end{aligned} \tag{4.35}$$

where

$$\begin{aligned} c_{pp}^{(4)} &= \frac{1}{L}\int d\omega \int d^2k G_{f_{31},f_{31}} G_{f_{32},f_{32}} \\ c_{pp}^{(5)\pm} &= \frac{1}{L}\int d\omega \int d^2k (G_{f_{31},f_{31}} G_{f_1,f_1} \pm G_{f_{31},f_1} G_{f_1,f_{31}}) \\ c_{pp}^{(6)} &= \frac{1}{L}\int d\omega \int d^2k G_{f_{31},f_{31}} G_{f_2,f_2} \end{aligned} \tag{4.36}$$

For the other couplings we make the same conjecture as for the toy model, i.e., assume that for stable and weakly unstable fixed trajectories $U_i = \bar{U}_i, V_i = \bar{V}_i$. The one-loop RG equations for the remaining dimensionless couplings are

$$\begin{aligned} \dot{u}_1 &= u_1^2 + \frac{u_3^2}{a^2} \\ \dot{u}_{1n} &= u_{1n}^2 + \frac{u_{3n}^2}{a_n^2} \\ \dot{u}_2 &= 2u_2(u_1 - u_2) \end{aligned}$$

$$
\begin{aligned}
\dot{u}_{2n} &= 2u_{2n}(u_{1n} - u_{2n}) \\
\dot{u}_3 &= 2u_3(2u_1 - u_2 - u_5) - 2bu_3u_4 - u_{3n}u_c \\
&\quad - 2v_3v_c - 2H(u_3v_c + v_3u_5) \\
\dot{u}_{3n} &= 2u_{3n}(2u_{1n} - u_{2n} - u_5) - u_{3n}u_{4n} - 2bu_3u_c \\
&\quad - 2v_{3n}v_c - 2H(u_{3n}v_c + v_{3n}u_5) \\
\dot{u}_4 &= -2bu_4^2 - 2u_3^2 - 2u_c^2 - 2v_3^2 - 4Hu_3v_3 \\
\dot{u}_{4n} &= -u_{4n}^2 - 2u_{3n}^2 - 2bu_c^2 - 2v_{3n}^2 - 4Hu_{3n}v_{3n} \\
\dot{u}_5 &= -2u_5^2 - 2bu_3^2 - u_{3n}^2 - 2v_c^2 - 4Hu_5v_c \\
\dot{u}_c &= -2bu_4u_c - u_{4n}u_c - 2u_3u_{3n} \\
&\quad - 2v_3v_{3n} - 2H(v_3u_{3n} + v_{3n}u_3) \\
\dot{v}_1 &= v_1^2 + \frac{v_3^2}{c^2} \\
\dot{v}_{1n} &= v_{1n}^2 + \frac{v_{3n}^2}{c_n^2} \\
\dot{v}_2 &= 2v_2(v_1 - v_2) \\
\dot{v}_{2n} &= 2v_{2n}(v_{1n} - v_{2n}) \\
\dot{v}_3 &= 2v_3(2v_1 - v_2 - v_5) - 2bv_3u_4 - v_{3n}u_c \\
&\quad - 2u_3v_c - 2H(v_3v_c + u_3v_5) \\
\dot{v}_{3n} &= 2v_{3n}(2v_{1n} - v_{2n} - v_5) - v_{3n}u_{4n} - 2bv_3u_c \\
&\quad - 2u_{3n}v_c - 2H(v_{3n}v_c + u_{3n}v_5) \\
\dot{v}_5 &= -2v_5^2 - 2bv_3^2 - v_{3n}^2 - 2v_c^2 - 4Hv_5v_c \\
\dot{v}_c &= -2bv_3u_3 - 2v_5v_c - 2u_5v_c \\
&\quad - 2v_{3n}u_{3n} - 2H(v_c^2 + v_5u_5),
\end{aligned}
\tag{4.37}
$$

where the additional parameters are

$$
c = \frac{\sqrt{A_hA_e'}}{A'} \quad c_n = \frac{\sqrt{A_MA_e'}}{A_n'} \quad H = \frac{A_e^a}{\sqrt{A_eA_e'}}
$$

$$
A_e = \frac{1}{L}\frac{1}{(2\pi)^2}\int d\omega \int d^2k G_{f_1,f_1}G_{f_1,f_1} = m_e\int \frac{d\theta}{2\pi}\cos^4\varphi_1
$$

$$
A_e' = \frac{1}{L}\frac{1}{(2\pi)^2}\int d\omega \int d^2k G_{f_{31},f_{31}}G_{f_{31},f_{31}}
$$

$$
\begin{aligned}
&= m_e \int \frac{d\theta}{2\pi} \sin^4 \varphi_1 \\
A' &= \frac{1}{L} \frac{1}{(2\pi)^2} \int d\omega \int d^2k G_{f_{31},f_{31}} G_{d_1,d_1} \\
&= 2 \int \frac{d\theta}{2\pi} \sin^2 \varphi_1 \left(\frac{m_c m_e}{m_c + m_e} \cos^2 \theta + \frac{m_d m_e}{m_d + m_e} \sin^2 \theta \right) \\
A'_n &= \frac{1}{L} \frac{1}{(2\pi)^2} \int d\omega \int d^2k G_{f_{31},f_{31}} G_M \\
&= 2 \frac{m_M m_e}{m_M + m_e} \int \frac{d\theta}{2\pi} \sin^2 \varphi_1 \\
A^a_e &= \frac{1}{L} \frac{1}{(2\pi)^2} \int d\omega \int d^2k G_{f_1,f_{31}} G_{f_1,f_{31}} \\
&= m_e \int \frac{d\theta}{2\pi} \sin^2 \varphi_1 \cos^2 \varphi_1 .
\end{aligned} \tag{4.38}
$$

Interestingly, we find that the stable fixed trajectories of the full model lead to the same decoupling at low-energies into effective three or four pocket models, as in the toy model. In distinction to the toy model, however, now there are two 3p and two 4p effective models $(3_1, 3p_2, 4p_1, 4p_2)$. These four stable fixed trajectories are specified by

($4p_1$)

$$
\begin{aligned}
u_i &= \gamma_i u_1 \quad v_i = g_i u_1 \\
u_1 &= \frac{1}{1 + \gamma_3^2/a^2} \frac{1}{L_0 - L} \\
\gamma_3 &= \pm a \sqrt{8a^2 - 1 + 4\sqrt{1 - a^2 + 4a^4}} \\
\gamma_4 &= \gamma_5 = 1 - 2a^2 - \sqrt{1 - a^2 + 4a^4}
\end{aligned} \tag{4.39}
$$

($4p_2$)

$$
\begin{aligned}
u_i &= \gamma_i v_1 \quad v_i = g_i v_1 \\
v_1 &= \frac{1}{1 + g_3^2/c^2} \frac{1}{L_0 - L} \\
g_3 &= \pm c \sqrt{8c^2 - 1 + 4\sqrt{1 - c^2 + 4c^4}} \\
\gamma_4 &= g_5 = 1 - 2c^2 - \sqrt{1 - c^2 + 4c^4}
\end{aligned} \tag{4.40}
$$

($3p_1$)

$$
\begin{aligned}
u_i &= \gamma_i u_{1n} \quad v_i = g_i u_{1n} \\
u_{1n} &= \frac{1}{1+\gamma_{3n}^2/a_n^2}\frac{1}{L_0-L} \\
\gamma_{3n} &= \pm a_n \sqrt{4a_n^2 - 1 + 2\sqrt{4-2a_n^2+4a_n^4}} \\
\gamma_{4n} &= 2\gamma_5 = 2 - 2a_n^2 - \sqrt{4-2a_n^2+4a_n^4}
\end{aligned}
\tag{4.41}
$$

($3p_2$)

$$
\begin{aligned}
u_i &= \gamma_i v_{1n} \quad v_i = g_i v_{1n} \\
v_{1n} &= \frac{1}{1+g_{3n}^2/c_n^2}\frac{1}{L_0-L} \\
g_{3n} &= \pm c_n \sqrt{4c_n^2 - 1 + 2\sqrt{4-2c_n^2+4c_n^4}} \\
g_{4n} &= 2g_5 = 2 - 2c_n^2 - \sqrt{4-2c_n^2+4c_n^4}
\end{aligned}
\tag{4.42}
$$

All couplings not presented in the above formulas evolve with smaller exponents. Note that the ratios of the couplings in Eqs. (4.39-4.42) do not depend on the parameter H.

We see from Eqs. (4.39-4.40) that for $4p_1$ and $4p_2$ all interactions involving the M-centered hole pocket become subleading, like in the toy model. For $4pFT_1$ the interactions involving xz/yz orbital components on the electron pockets become leading compared to the interactions involving xy orbital components, i.e., to first approximation the two electron pockets can be approximated as xz/yz-pockets. For $4p_2$ the situation is opposite – the interactions involving xy orbital component on the electron pockets become dominant compared to the interactions involving xz/yz orbital components, i.e., to first approximation the two electron pockets can be approximated as xy pockets. These two fixed trajectories have been analyzed in Ref. [111]. The situation is equivalent for the $3p_1$ and $3p_2$, see Eqs. (4.41-4.42). In the first case, the interactions involving xz/yz orbital component on the electron pockets become leading, and in the second the interactions involving xy orbital component on the electron pockets become leading.

These different effective low-energy models are sketched in Fig. 1 in the main text. We also note that the behavior of different couplings along $4p_1$ and $4p_2$ are quite similar, see Eqs. (4.39, 4.40), and the same is true for the couplings along $3p_1$ and $3p_2$, Eqs. (4.41,4.42).

Whether the system flows to $4p_1$ or $4p_2$ (or to $3p_1$ or $3p_2$) depends on the initial values of the couplings.

The stable FTs are separated by several weakly unstable ones with only a single direction along which perturbations grow. For general a, a_n, c, c_n, and H we determined these FTs and checked their stability numerically. For $a = a_n = c = c_n = 1$ these weakly unstable FTs can be analyzed analytically. The FTs with only one unstable direction are (the notations are self-evident):

($4p_1$+$4p_2$)

$$\begin{aligned} &u_i = \gamma_i u_1 \quad v_i = g_i u_1 \\ &u_1 = v_1 \quad u_3 = v_3 \quad u_5 = v_5 = v_c \\ &u_1 = \frac{1}{1+\gamma_3^2/a^2}\frac{1}{L_0 - L} \\ &\gamma_3 = \pm\sqrt{15+16H+4\sqrt{15+30H+16H^2}} \\ &\gamma_4 = 2(H+1)\gamma_5 = -3-4H\sqrt{15+30H+16H^2} \end{aligned} \tag{4.43}$$

($3p_1$+$3p_2$)

$$\begin{aligned} &u_i = \gamma_i u_{1n} \quad v_i = g_i u_{1n} \\ &u_{1n} = v_{1n} \quad u_{3n} = v_{3n} \quad u_5 = v_5 = v_c \\ &u_{1n} = \frac{1}{1+\gamma_{3n}^2/a_n^2}\frac{1}{L_0 - L} \\ &\gamma_{3n} = \pm\sqrt{7+8H+4\sqrt{4+7H+4H^2}} \\ &\gamma_{4n} = 4(H+1)\gamma_5 = -2-4H-2\sqrt{4+7H+4H^2} \end{aligned} \tag{4.44}$$

($3p_1$+$4p_1$)

$$\begin{aligned} &u_i = \gamma_i u_1 \quad v_i = g_i u_1 \\ &u_1 = u_{1n} \quad u_3 = \pm u_{3n} \quad u_4 = u_{4n} = \pm u_c \\ &u_1 = \frac{1}{1+\gamma_3^2/a^2}\frac{1}{L_0 - L} \\ &\gamma_3 = \sqrt{11+2\sqrt{34}} \quad \gamma_4 = -\frac{1}{3}(4+\sqrt{34}) \\ &\gamma_5 = -2-\sqrt{\frac{17}{2}} \end{aligned} \tag{4.45}$$

($3p_2$+$4p_2$)

$$
\begin{aligned}
&u_i = \gamma_i v_1 \quad v_i = g_i v_1 \\
&v_1 = v_{1n} \quad v_3 = \pm v_{3n} \quad u_4 = u_{4n} = \pm u_c \\
&g_3 = \sqrt{11 + 2\sqrt{34}} \quad \gamma_4 = -\frac{1}{3}(4 + \sqrt{34}) \\
&g_5 = -2 - \sqrt{\frac{17}{2}}.
\end{aligned}
\tag{4.46}
$$

Again all couplings not listed in the formulas above have smaller exponents. A detailed analysis of the structure of weakly unstable FTs in the full 4-pocket model is presented in Ref. [136].

Finally there is a high-symmetry FT with two unstable directions. Along this FT all couplings are non-zero:

$$
\begin{aligned}
&u_i = \gamma_i u_1 \quad v_i = g_i u_1 \\
&u_1 = u_{1n} = v_1 = v_{1n} \quad u_3 = u_{3n} = v_3 = v_{3n} \\
&u_4 = h_{4n} = u_c \quad u_5 = v_5 = v_c \\
&u_1 = \frac{1}{1 + \gamma_3^2/a^2} \frac{1}{L_0 - L} \\
&\gamma_3 = \pm\sqrt{23 + 24H + 4\sqrt{34 + 69H + 36H^2}} \\
&\gamma_4 = \frac{4}{3}(H+1)\gamma_5 = -\frac{10}{3} - 4H - \frac{2}{3}\sqrt{34 + 69H + 36H^2}.
\end{aligned}
\tag{4.47}
$$

4.6.2.2.2 Susceptibilities

As in the toy model, we introduce vertices that couple to different order parameter fields to determine which order develops first at low energies. In the SDW channel, we now have four vertices

$$
\begin{aligned}
\partial_L \Gamma^{\Gamma,1}_{SDW} &= \left(u_1 + \frac{u_3}{a}\right) \Gamma^{\Gamma,1}_{SDW} \\
\partial_L \Gamma^{\Gamma,2}_{SDW} &= \left(v_1 + \frac{v_3}{c}\right) \Gamma^{\Gamma,2}_{SDW} \\
\partial_L \Gamma^{M,1}_{SDW} &= \left(u_{1n} + \frac{u_{3n}}{a_n}\right) \Gamma^{M,1}_{SDW} \\
\partial_L \Gamma^{M,2}_{SDW} &= \left(v_{1n} + \frac{v_{3n}}{c_n}\right) \Gamma^{M,2}_{SDW}
\end{aligned}
\tag{4.48}
$$

where indices $1, 2$ mean that the order parameters involve fermions on electron pockets with either $xz(yz)$ or xy orbital content, and indices Γ and M mean that the SDW order

parameter involves fermions from either $\Gamma-$centered or $M-$centered hole pockets. Using the values of the couplings along the FTs as inputs and solving these differential equations, we obtain $\Gamma^{(i)}_{SDW} \sim 1/(L_0 - L)^{\beta^{(i)}_{SDW}}$, with $\beta^{(i)}_{SDW} = (1 + \gamma_{3i}/a_i)/(1 + \gamma^2_{3i}/a^2_i)$, where $i = (\Gamma, 1; \Gamma, 2; M, 1; M, 2)$ and $\gamma_{3i} \in \{\gamma_3, g_3, \gamma_{3n}, g_{3n}\}$, $a_i \in \{a, a_n, c, c_n\}$. We verified that *all* β^i_{SDW} are smaller than 1/2, so that SDW order does not develop (if $L_0 < L_F$). The largest values are for $a = a_n = c = c_n = 1$: $\beta^{\Gamma,1}_{SDW} = \beta^{\Gamma,2}_{SDW} = 0.3$ and $\beta^{M,1}_{SDW} = \beta^{M,2}_{SDW} = 0.43$. These are the same values as in the toy model.

There are also four superconducting vertices: $\Gamma^{e,xz/yz}_{SC}, \Gamma^{e,xy}_{SC}, \Gamma^{\Gamma}_{SC}$, and Γ^{M}_{SC}. The RG equations for these vertices can be cast into the matrix equation

$$\partial_L \mathbf{\Gamma}_{SC} = -2 \begin{pmatrix} u_5 + Hv_c & v_c + Hu_5 & u_3 & u_{3n} \\ v_c + Hv_5 & v_5 + Hv_c & v_3 & v_{3n} \\ u_3 + Hv_3 & v_3 + Hu_3 & u_4 & u_c \\ \frac{u_{3n}+Hv_{3n}}{2} & \frac{v_{3n}+Hu_{3n}}{2} & \frac{u_c}{2} & \frac{u_{4n}}{2} \end{pmatrix} \mathbf{\Gamma}_{SC}, \tag{4.49}$$

where we introduced $\mathbf{\Gamma}_{SC} = (\Gamma^{e,xz/yz}_{SC}, \Gamma^{e,xy}_{SC}, \Gamma^{\Gamma}_{SC}, \Gamma^{M}_{SC})^T$ Along each FT the solution of Eq. (4.49) gives rise to s^{+-} gap structure on the contributing pockets. The exponents are

$$\begin{aligned} \beta^{(4p_1)}_{SC} &= \frac{-\gamma_4 - \gamma_5 + \sqrt{(\gamma_4 - \gamma_5)^2 + 4\gamma_3^2}}{1 + \gamma_3^2/a^2} \\ \beta^{(4p_2)}_{SC} &= \frac{-\gamma_4 - g_5 + \sqrt{(\gamma_4 - g_5)^2 + 4g_3^2}}{1 + g_3^2/c^2} \\ \beta^{(3p_1)}_{SC} &= \frac{-\gamma_{4n} - 2\gamma_5 + \sqrt{(\gamma_{4n} - 2\gamma_5)^2 + 8\gamma_{3n}^2}}{1 + \gamma_{3n}^2/a_n^2} \\ \beta^{(3p_2)}_{SC} &= \frac{-\gamma_{4n} - 2g_5 + \sqrt{(\gamma_{4n} - 2g_5)^2 + 8g_{3n}^2}}{1 + g_{3n}^2/c_n^2}. \end{aligned} \tag{4.50}$$

For $a = a_n = c = c_n$ we have $\beta^{(4p_1)}_{SC} = \beta^{(4p_2)}_{SC} = 0.86$ and $\beta^{(3p_1)}_{SC} = \beta^{(3p_2)}_{SC} = 0.72$, again as in the toy model. We checked that $\beta^{(i)}_{SC} \geq 1/2$ for all a, a_n, c, c_n, i.e., the superconducting susceptibility does diverge at $L = L_0$.

To determine the SC gap structure on all pockets, we need to include the residual interactions. We did this numerically. We found that, like in the toy model, the largest eigenvalue in the SC channel corresponds to a "conventional" s^{+-} gap structure, although the magnitude of the gap on the "secondary" pockets is small. Specifically, this means that for $4\mathrm{p}_1$ the gap magnitude is relatively small on the $M-$centered hole pocket and the

$xy-$part of the electron pockets, for $4p_2$ it is small (very small) on the $M-$centered hole pocket and the $xz/yz-$parts of the electron pockets. In the 3p case, the gap almost vanishes on both $\Gamma-$centered hole pockets, and the two 3p FTs differ in the gap magnitude on the xz/yz and xy portions of the electron pockets.

For the second largest eigenvalue the gap structure for the FTs, where the dominant interactions are within the same orbitals (i.e. $4pFT_1$ and $3pFT_2$), is the orbital-antiphase s^{+-} state, Ref. [133] ($\text{sign}(\Gamma_{SC}^{e,xz/yz}, \Gamma_{SC}^{e,xy}, \Gamma_{SC}^{\Gamma}, \Gamma_{SC}^{M}) = (+,-,-,+)$). For the FTs with dominant couplings between different orbitals ($4pFT_2$ and $3pFT_1$) the sign structure corresponds to "orbital-antiphase s^{++}" state ($\text{sign}(\Gamma_{SC}^{e,xz/yz}, \Gamma_{SC}^{e,xy}, \Gamma_{SC}^{\Gamma}, \Gamma_{SC}^{M}) = (+,-,+,-)$).

Chapter 5

Orbital order in FeSe iron-based superconductors – the case for vertex renormalization

5.1 Introduction

Orbital degrees of freedom turned out to play an important role for iron-based superconductors (FeSC). Studies of SDW magnetism and superconductivity in these materials found that the orbital composition of the states near the Fermi surface (FS) affects the structure of the fermionic spectrum in the spin-density-wave (SDW) phase [140] and the anisotropy of the superconducting gap [141, 142, 11]. Another example where different orbitals come into play is the tetragonal-to-orthorhombic phase transition observed in many FeSCs at $T = T_s$. Below T_s, the system spontaneously breaks C_4 lattice rotational symmetry down to C_2. This is similar to what happens in nematic liquid crystals, and, by analogy, the state below T_s is called nematic. Below T_s the occupation of d_{xz} and d_{yz} orbitals becomes unequal, i.e., the system develops an orbital order $\Gamma(|\mathbf{k}|) \propto \int d\theta_k (n_{xz}(\mathbf{k}) - n_{yz}(\mathbf{k}))$, where n_i is the density of orbital i and the integration is over the directions of $\mathbf{k}$ for a given $|\mathbf{k}|$. Above T_s, Γ_k vanishes by C_4 symmetry, but once C_4 symmetry is broken, by one reason or the other [143], $\Gamma(|\mathbf{k}|)$ becomes finite.

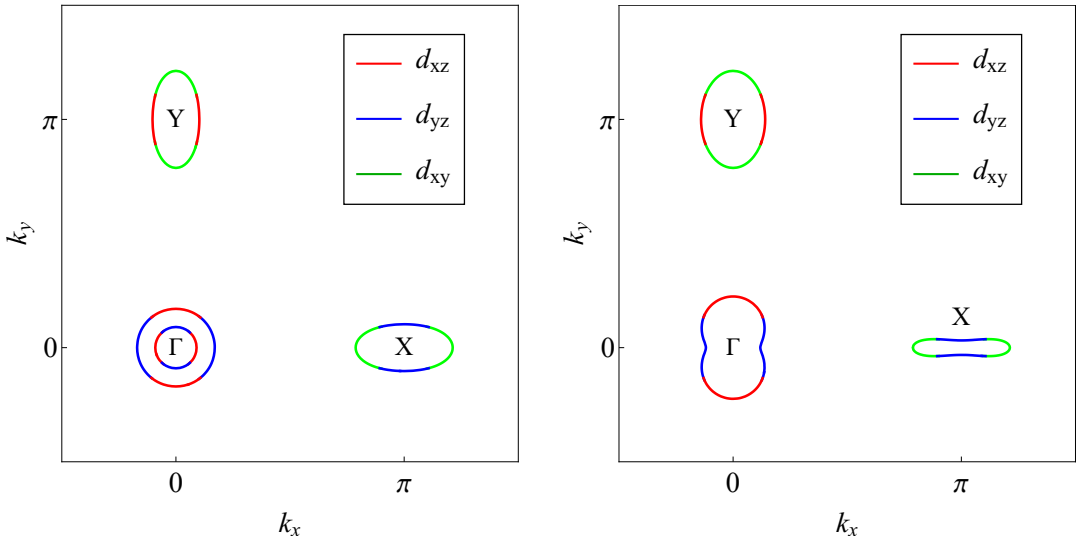

Figure 5.1: The Fermi surfaces in the 1Fe BZ with the leading orbital content encoded in color. The six ψ fields, marked in the figure, are introduced in Table 1. Left panel – the FSs in the tetragonal phase, right panel – the FSs in the nematic phase. The smaller hole pocket shrinks by orbital order and completely disappers once one include spin-orbit coupling. In FeSe, the size of the larger hole pocket depends on k_z and is the largest at $k_z = \pi$ (Ref. [154]). The parameters of the quadratic Hamiltonian used to obtain the Fermi surface are from Ref.[155]. The pockets are homogeneously enlarged to provide a better view.

In most FeSCs the range of nematic order is quite narrow as the system develops a stripe magnetic order almost immediately after the nematic order sets in. However, in FeSe (and in doped $FeSe_{1-x}S_x$) the regions of nematic and magnetic order are well separated in x ([145, 144])

In pure FeSe, the nematic order sets in at $T_s \approx 85K$, and magnetic order does not develop down to $T = 0$. This opens up an opportunity to extract the information about the structure of Γ from the analysis of the feedback effects on the electronic structure. The magnitude of Γ, extracted from ARPES, is $10 - 20meV$, much smaller than the fermionic bandwidth (see Refs [144, 151, 152, 146, 147, 148, 149, 150, 153] and the discussion below). In this case, the most relevant feedback from Γ on the electrons is for momentum components in the XY plane near $k_x = k_y = 0$ and $k_x = k_y = \pi$, where hole and electron pockets are located in the 2Fe Brillouin zone (2FeBZ). The pockets in FeSe are quite small, and $\Gamma(|\mathbf{k}|)$ near these pockets is well approximated by $\Gamma(0) = \Gamma_h$ and $\Gamma(|\pi|) = \Gamma_e$.

Manifestations of the orbital order in FeSe have been seen in Raman, STM, ARPES, and other experiments (see Ref. [144] for recent review on FeSe). STM data analysis within a single domain resolved one elliptical hole Fermi surface (FS) and one electron FS, whose form becomes peanut-like below T_s (Ref. [146]). In the 1FeBZ, where electron pockets are centered at $(0, \pi)$ and $(\pi, 0)$, the observed hole pocket is elongated towards $(0, \pi)$, and the observed electron pocket is centered at $(\pi, 0)$, and its smaller axis is along the Y direction (see Fig. 5.1b). ARPES data on single-domain samples [147, 148, 149, 150] show the same shape of the FSs. In multi-domain samples, ARPES shows the combination of FSs from different domains [154]. In the tetragonal phase above T_s, hole pockets are C_4 symmetric and electron pockets are elliptical (Fig. 5.1a). The changes from a C_4-symmetric to an elliptical shape for the hole pocket and from an elliptical to a peanut-like shape for the $(\pi, 0)$ electron pocket are due to orbital order. Adding Γ_h and Γ_e terms to the hopping Hamiltonian in orbital representation and transforming from orbital to band basis, one obtains [146, 155] that the observed shapes of the pockets are reproduced if $\Gamma_h > 0$ and $\Gamma_e < 0$, i.e., the orbital order changes sign between hole and electron pockets.

In this communication we address the issue how the sign change between Γ_e and Γ_h can be understood theoretically. For this, we derive and analyze the self-consistent equation for d-wave orbital order Γ. We argue that at mean-field level, the set of coupled equations for Γ_h and Γ_e contains the single effective interaction $U_0 = 5J - U$, where U and J are Hubbard and Hund local interactions. The orbital order either does not develop, when $U_0 > 0$, or does develop, if $U_0 < 0$ and its magnitude is strong enough, but the solution necessarily yields equal sign of Γ_e and Γ_h (d^{++} channel). We next include into the analysis

the fact that the couplings flow away from their bare values (used in mean-field analysis), when we progressively integrate out contributions of fermions with higher energies. This flow is captured within parquet renormalization group analysis (pRG) [156] or functional RG [157]. The pRG flow splits U_0 into two different interactions U_a and U_b. We show that this splitting gives rise to a non-zero coupling in another channel for orbital ordering, this time with Γ_e and Γ_h of opposite signs (d^{+-} channel). This is similar to how the coupling in the s^{+-} pairing channel emerges due to small inter-pocket pairing interaction on top of strong Hubbard repulsion. We show that the coupling in this new orbital channel is attractive, regardless of the sign of the bare U_0, and exceeds the coupling in the d^{++} channel. Our results are summarized in Figs. 5.3, 5.4.

Our approach is similar to earlier works [11, 24], which also found an attraction in the d^{+-} channel, but differs in detail. The authors of [11] analyzed self-consistent equations for Γ_h and Γ_e in the C_4 symmetric regime using the values of the interactions U_a and U_b near the fixed trajectory, i.e., at the very end of the pRG flow. Here we consider the evolution of U_a and U_b without assuming closeness to a fixed trajectory. This is a more realistic approach, given that in practice pRG only runs over a finite window of energies. We show that the d^{+-} channel becomes attractive from the very beginning of the pRG flow. The authors of [24] considered the case of large U/J and obtained sign-changing d^{+-} orbital order by selecting a particular combination of RPA and Aslamazov-Larkin type diagrams for the renormalization of the Hubbard interaction. We consider arbitrary U/J and treat vertex renormalizations within pRG, which accounts on equal footing for vertex renormalizations in particle-hole and particle-particle channels. Another explanation for the sign change between Γ_e and Γ_h has been put forward in Ref. [158]. It is based on the earlier study[159], which showed that the self-energy due to spin fluctuation exchange has opposite sign near Γ and near X/Y, and shrinks both hole and electron pockets. The authors of [158] argued (on a semi-phenomenological level) that the X/Y anisotropy of spin fluctuations below T_s leads to $\mathrm{sgn}(\Gamma_e) = -\mathrm{sgn}(\Gamma_h)$. Our approach is complimentary to that work: the authors of [158] included the X/Y anisotropy of the effective interaction but not orbital order. We, on the contrary, include orbital order into fermionic propagators, but neglect nematicity-induced changes of the interactions. We emphasize that both approaches lead to the sign change of the nematic splitting.

We also consider how orbital order affects the energies of d_{xz} and d_{yz} orbitals E_{xz} and E_{yz} at $(0, \pi)$ and $(\pi, 0)$ points in the 1FeBZ (the M point in the 2FeBZ). In absence of orbital order, the two energies are degenerate even in the presence of spin-orbit coupling[160]. A non-zero Γ_e breaks the degeneracy. To first order in Γ_e, the energies split – E_{xz} increases

by $\Gamma_e/2$ and E_{yz} decreases by $\Gamma_e/2$. Observation of this splitting has been reported by Fedorov et al [151]. However, this group argued that the d_{xz}/d_{yz} splitting appears on top of a larger effect – a simultaneous change of the temperature dependence of E_{xz} and E_{yz} below T_s. According to Refs. [151, 154], both energies become smaller in magnitude. This observation is consistent with the later result by the same group [154] that they can resolve both electron pockets within a single domain, and both pockets have peanut-like form. A simultaneous change of the temperature dependence of E_{xz} and E_{yz} below T_s has also been reported in [152]. Later, however, Watson et al. argued [148] that they can only observe d_{yz} orbital at the M point (in addition to d_{xy}). If this is the case, then the observed T dependence below T_s can be due to the expected first-order correction in Γ_e. To address this issue, we computed the corrections to E_{xz} and E_{yz} to second order in Γ_e and Γ_h. The Γ_e^2 and Γ_h^2 terms are the same for E_{xz} and E_{yz} and, if these terms are large, they can overtake the $\pm\Gamma_e/2$ splitting already at small Γ_i. We found that the second order contribution accounts only for a small correction to $\pm\Gamma_e/2$ and, moreover, the correction is of the wrong sign. If both E_{xz} and E_{yz} indeed become smaller in magnitude below T_s, as the authors of Refs [151, 154] argue, this is due to some other physics than the one we consider here.

ψ_i	Pocket	Orbital	ψ_i	Pocket	Orbital	ψ_i	Pocket	Orbital
ψ_1	Y	d_{xz}	ψ_3	X	d_{yz}	ψ_5	Γ	d_{yz}
ψ_2	Y	d_{xy}	ψ_4	X	d_{xy}	ψ_6	Γ	d_{xz}

Table 5.1: Affiliation of ψ_i with a pocket and an orbital.

5.2 Mean-field analysis

We consider a model with two hole pocket near $(0,0)$ in the tetragonal phase (H-pockets) and two electron pockets near $(0,\pi)$ and $(\pi,0)$ in the 1FeBZ (Y and X pockets). The hole pockets are made out of d_{xz} and d_{yz} orbitals, the X pocket is made out of d_{yz} and d_{xy} orbitals and the Y pocket is made out of d_{xz} and d_{yz} (Refs. [141, 45]). We introduce six spices of fermions: $\psi_1,\dots,\psi_6$, see Tab 5.1 and two $d-$wave d_{xz}/d_{yz} orbital order parameters $\Gamma_h = \langle\psi_6^\dagger\psi_6 - \psi_5^\dagger\psi_5\rangle$ and $\Gamma_e = \langle\psi_1^\dagger\psi_1 - \psi_3^\dagger\psi_3\rangle$. For simplicity, we neglect d-wave orbital order on the d_{xy} orbital (the $\psi_2^\dagger\psi_2 - \psi_4^\dagger\psi_4$ term, Refs. [160, 14, 15]). At the mean-field level, the self-consistent equations for Γ_h and Γ_e are obtained by adding up Hartree and Fock diagrams for different orbitals (Fig. 5.2a). To first order in the orbital order parameter, the self-energies are $\Sigma_{xz}^H = \Sigma_{h,0} + \Gamma_h/2$, $\Sigma_{yz}^H = \Sigma_{h,0} - \Gamma_h/2$, $\Sigma_{xz}^Y = \Sigma_{e,0} + \Gamma_e/2$, $\Sigma_{yz}^X = \Sigma_{e,0} - \Gamma_e/2$,

where $\Sigma_{h,0}$ and $\Sigma_{e,0}$ are the self-energies in the absence of orbital order. Evaluating the diagrams and taking the difference $\Sigma^H_{xz} - \Sigma^H_{yz} = \Gamma_h$, $\Sigma^Y_{xz} - \Sigma^X_{yz} = \Gamma_e$, we obtain self-consistent equations for Γ_h, Γ_e in the form [161]

$$\Gamma_h = U_a \left(n^H_{xz} - n^H_{yz} \right) + U_b \left(n^Y_{xz} - n^X_{yz} \right)$$
$$\Gamma_e = U_a \left(n^Y_{xz} - n^X_{yz} \right) + U_b \left(n^H_{xz} - n^H_{yz} \right) \tag{5.1}$$

Here each density n_i is the momentum integral over the corresponding Fermi function. We find, to leading order in Γ_i, $n^H_{xz} - n^H_{yz} = A_h \Gamma_h$ and $n^Y_{xz} - n^X_{yz} = A_e \Gamma_e$. To obtain the prefactors A_h and A_e, we used the orbitally-resolved low-energy model from Ref. [45] for the kinetic energy, converted from orbital to band basis, and computed the momentum integrals of the Fermi functions for different bands, weighted by the "coherent" factors associated with the change of the basis. We present the details of the calculations in [162] and here state the result: both A_h and A_e are negative, and their ratio $\gamma = A_e/A_h$ depends on the parameters in the kinetic energy and is, in general, of order one. Using the band structure parameters that fit the ARPES and STM data, we obtained $\gamma \sim 0.2$ (see [162]).

The interactions U_a and U_b are linear combinations of seven different interactions involving d_{xz} and d_{yz} orbital states near momenta where FSs are located. We show these seven interactions in Fig. 5.2b. In terms of these interactions, $U_a = U_5 - 2\tilde{U}_5 + \tilde{\tilde{U}}_5$[163] and $U_b = 2(U_1 - \bar{U}_1) - (U_2 - \bar{U}_2)$ (labels are as in Fig. 5.2b). The bare values of the seven couplings are $U_5^{(0)} = U_1^{(0)} = U_2^{(0)} = U, \tilde{U}_5^{(0)} = \bar{U}_1^{(0)} = U', \tilde{\tilde{U}}_5^{(0)} = \bar{U}_2^{(0)} = J$. As a result, the bare $U_a^{(0)}$ and $U_b^{(0)}$ are the same: $U_a^{(0)} = U_b^{(0)} = U_0 = U + J - 2U'$. If we take $U' = U - 2J$ (Ref. [141]), we obtain $U_0 = 5J - U$. Substituting $U_a = U_b = U_0$ into (5.1), we obtain that the only possible solution of the self-consistent set is $\Gamma_h = \Gamma_e$ (sign-preserving d^{++} orbital order), and this order develops if the eigenvalue $\lambda^{++} = U_0(A_h + A_e) > 1$. The solution with the opposite sign of Γ_e and Γ_h does not emerge at the mean-field level.

5.3 Beyond mean-field

We now go beyond mean-field and include into consideration that the seven interactions, which contribute to U_a and U_b, flow to different values as one progressively integrates out fermions with higher energies. This flow can be captured within pRG and comes from mutual vertex renormalizations of the total of 30 different interactions between low-energy fermions on d_{xz}, d_{yz}, and d_{xy} orbitals [45, 11, 14, 15]. The flow equations have been derived in [14, 15], and we use the results of that work to obtain the flow of U_a and U_b. The results

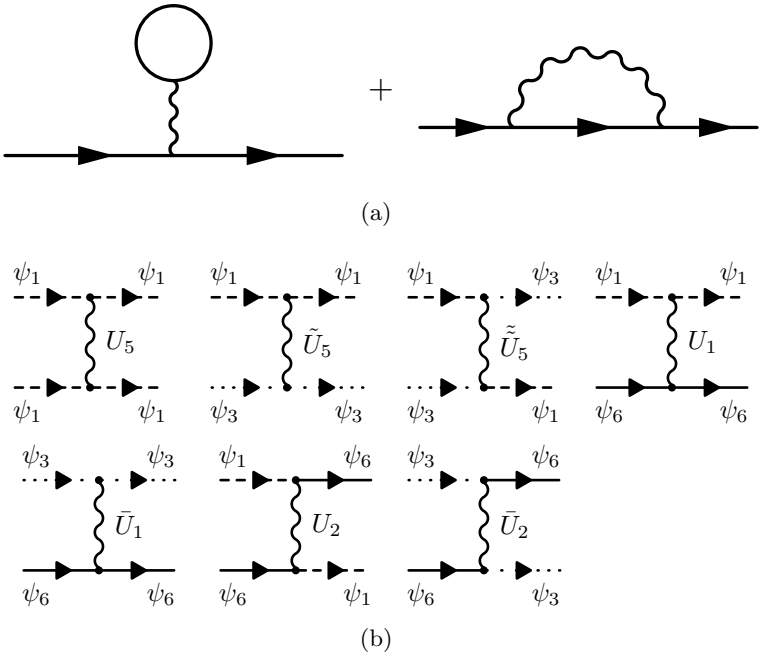

Figure 5.2: a) Hartree and Fock self-energy diagrams; b) Examples of the interaction terms which contribute to Hartree-Fock self-energies. The U_5 terms in the first row also act on hole pockets (ψ_5, ψ_6). Each diagram has symmetry-equivalents. $(\psi_1 \leftrightarrow \psi_3,\ \psi_5 \leftrightarrow \psi_6)$. The self-energy beyond mean-field has been computed using dressed interactions, which we obtained using pRG scheme. In a direct perturbation theory, this amounts to summing up infinite series of self-energy diagrams, including RPA and Aslamazov-Larkin diagrams.

are shown in Fig.5.3. We see that U_a and U_b become different from U_0, and $U_b > U_a$, irrespective of whether $U_0 > 0$ or $U_0 < 0$. Solving for the eigenfunctions and eigenvalues of Eq. (5.1) when U_a and U_b are different, we obtain an eigenfunction $\Gamma^{++} = \Gamma_h + \alpha_+ \Gamma_e$ with the eigenvalue λ^{++} and $\Gamma^{+-} = \Gamma_h + \alpha_- \Gamma_e$ with the eigenvalue λ^{+-}, where

$$\alpha_\pm = -\frac{1-\gamma}{2}\frac{U_a}{U_b} \pm \sqrt{\left(\frac{1-\gamma}{2}\right)^2 \frac{U_a^2}{U_b^2} + \gamma} \tag{5.2}$$

$$\lambda^{++,+-} = -|A_h| \left[\frac{1+\gamma}{2} U_a \pm U_b \sqrt{\left(\frac{1-\gamma}{2}\right)^2 \frac{U_a^2}{U_b^2} + \gamma} \right]$$

We see that $\alpha_+ > 0$ and $\alpha_- < 0$, i.e., the eigenfunction Γ^{++} describes sign-preserving d^{++} orbital order and Γ^{+-} describes sign-changing d^{+-} order. We plot the corresponding eigenvalues λ^{++} and λ^{+-} in Fig. 5.4. We see that λ^{+-} becomes positive (i.e., attractive)

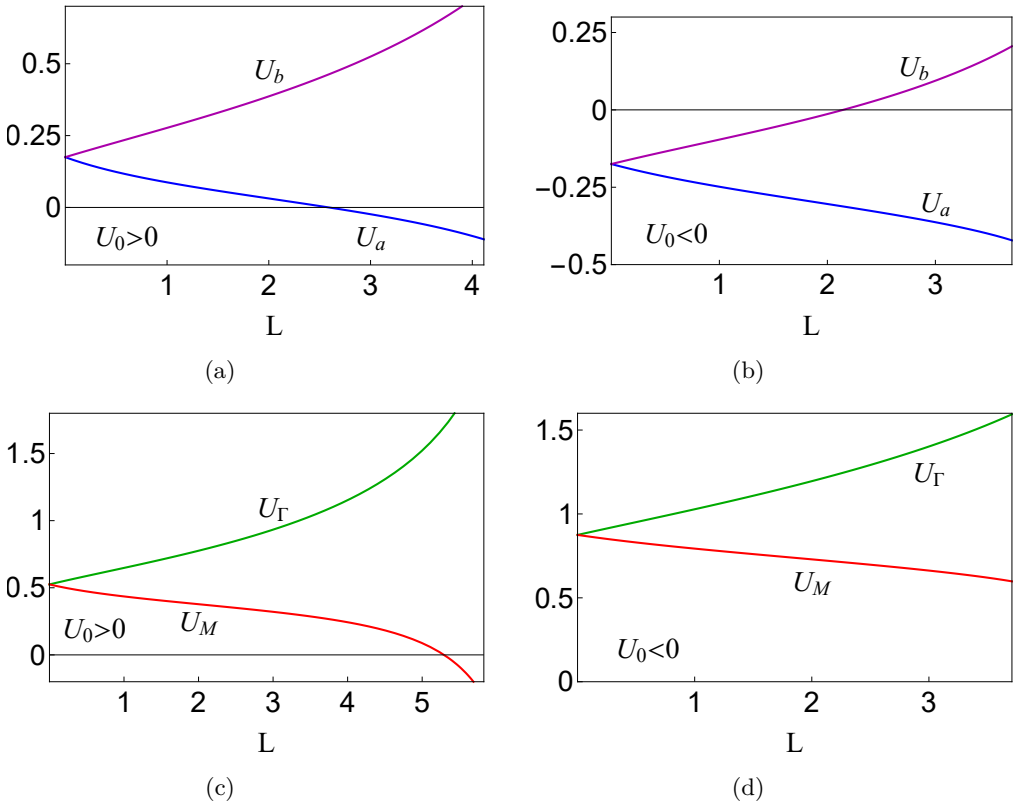

Figure 5.3: Panels (a) and (b) – the pRG flow of the couplings U_a and U_b for the case when the bare $U_a^{(0)} = U_b^{(0)} = U_0 = 5J - U$ is positive in (a) and negative in (b) (we set $J/U = 0.3$ and 0.1, respectively). Panels (c) and (d) – the flow of the couplings U_M and U_Γ in Eq. (5.3). The parameter $L = log\frac{W}{E}$, where W is of order bandwidth and E is the running energy. The larger L is, the more high energy states are integrated out. We used $m_h U/(4\pi) = 0.35$ where m_h is the mass of the dispersion near the hole pocket.

for any sign of U_0, once we include the pRG flow of the interactions. We emphasize that this holds even if the flow runs only over a small range of energies. For an instability towards a sign-changing orbital order, the flow needs to run over a finite range of energies to reach $\lambda^{+-} > 1$.

For $U_0 > 0$, the coupling in the λ^{++} channel is repulsive, i.e., d^{+-} orbital order is the only solution of Eq. (5.1). For $U_0 < 0$, the d^{++} channel is attractive at the bare level, but we see from Fig. 5.4c,d that it becomes sub-leading once U_b changes sign under pRG (see Fig. 5.3b). The attraction in d^{+-} orbital channel for $U_0 < 0$ was earlier obtained in Ref. [24] who used a combination of RPA spin and charge channels and Aslamazov-Larkin diagrams to

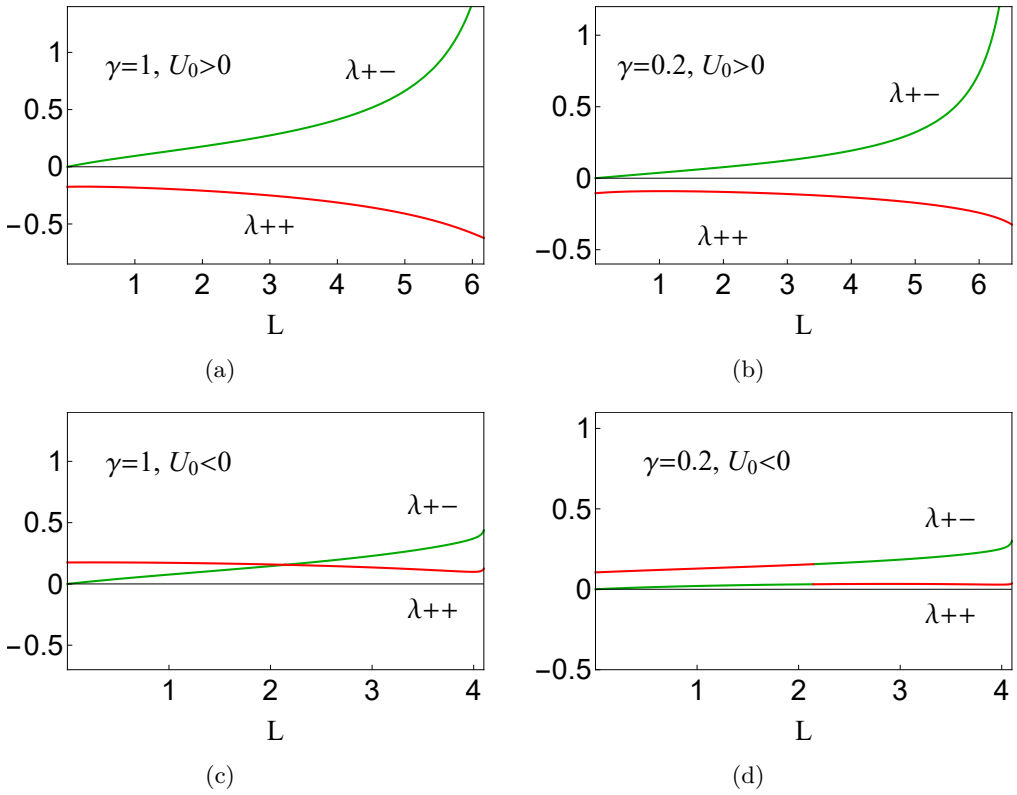

Figure 5.4: The flow of the dimensionless couplings λ^{++} in sign-preserving d^{++} channel (green) and λ^{+-} in sign-changing d^{+-} channel (red). Notations are as in Fig. 5.3. Panels (a) and (b) - the flow for the case $U_0 = 5J - U > 0$ for two values of the parameter $\gamma = A_e/A_h$ (see text). Panels (c) and (d) – the same for $U_0 < 0$. The sign-changing d^{+-} channel becomes dominant once U_b changes sign near $L = 2$. . For $\gamma \neq 1$, the couplings jump by finite values when U_b passes through zero.

separate U_a and U_b. In distinction with Ref. [24], here we account for the renormalization of U_a and U_b systematically, in an order-by-order treatment (as pRG is), through all channels including the pairing channel. Like we said, we found that λ^{+-} becomes positive already at the very beginning of the pRG flow, when the renormalization of $U_{a,b}$ can be obtained within a direct perturbative expansion. In particular, the condition $U_0 < 0$ is not required [164]. We note in this regard that our computation of the self-energy, using the diagrams in Fig. 5.2a with the dressed interactions obtained within the pRG scheme, is diagrammatically equivalent to summing up infinite series of contributions to the self-energy, including both RPA and Aslamazov-Larkin diagrams.

5.4 Temperature variations of E_{xz} and E_{yz}.

We now analyze how the energies E_{xz} at $(0,\pi)$ and E_{yz} at $(\pi,0)$ vary with increasing orbital order (in the 2FBZ these are energies of d_{xz}/d_{yz} orbitals at M). To first order in Γ_e, the two energies just split: $E_{xz} = E_{e,0} + \Gamma_e/2$ and $E_{yz} = E_{e,0} - \Gamma_e/2$, where $E_{e,0} < 0$ is the energy in the absence of the nematic order [45, 160]. Our goal is to go beyond the first order in Γ_e and check if there is a large common term of order $\Gamma^2_{e,h}$. A large positive $\Gamma^2_{e,h}$ term would be consistent with Refs. [151, 154]. The authors of these papers argued, based on interpretation of their ARPES data, that the magnitude of both E_{xz} and E_{yz} are reduced in the nematic phase.

To check this possibility, we computed the self-energies Σ^Y_{xz} and Σ^X_{yz} to order Γ^2. We We did not do the full self-consistent calculation to this order, as it would require to include the self-energy to order Γ^2 into the densities $n^H_{xz}, n^H_{yz}, n^Y_{xz}$, and n^X_{yz}. Rather, we evaluated the "source" term in the self-energy $\Sigma_{so}(\Gamma)$, which comes from keeping $O(\Gamma_{h,e})$ terms in the self-energy, but expanding the densities to order $\Gamma^2_{h,e}$. The the common self-energy for Σ^Y_{xz} and Σ^X_{yz} below the nematic transition is proportional to $\Sigma_{so}(\Gamma) - \Sigma_{so}(0)$. We find

$$\Sigma_{so}(\Gamma) = U_M(n^Y_{xz} + n^X_{yz}) + U_\Gamma(n^H_{xz} + n^H_{yz}) \tag{5.3}$$

and $U_M = U_5 + 2\tilde{U}_5 - \tilde{\tilde{U}}_5$ and $U_\Gamma = 2(U_1 + \bar{U}_1) - (U_2 + \bar{U}_2)$. The bare value of U_M and U_Γ are again equal, each is $U + 2U' - J$ ($= 3U - 5J$ if $U' = U - 2J$), but under pRG, U_Γ becomes larger than U_M, as we show in Fig. 5.3 c,d. The common densities are $(n^H_{xz} + n^H_{yz}) = n_{h,0} + B_h\Gamma^2_h, (n^Y_{xz} + n^X_{yz}) = n_{e,0} + B_e\Gamma^2_e$, where $n_{i,0}$ labels the density for $\Gamma_i = 0$. We find (see [162] for details) $B_h < 0$ and $|B_e| \leq |B_h|$. In this situation, the common correction to E^Y_{xz} and E^X_{yz} is negative. Given that $E_{e,0}$ is also negative, we see the common self-energy makes the two energies more negative. Furthermore, the magnitude of B_h is at most of order $1/T_s$, hence near T_s, when $\Gamma_{h,e}$ are small, the self-energy to second order in Γ_i is a small correction to the first-order $\pm\Gamma_i/2$ term. This is inconsistent with the interpretation of the data in Refs. [151, 154].

5.5 Conclusions.

In this communication we presented the solution of self-consistent equations for d-wave nematic order parameters on d_{xz}/d_{yz} orbitals. We argued that at a mean-field level the only solution possible is sign-preserving d^{++} nematic order Γ (same sign of Γ_e and Γ_h) when the bare coupling $U_0 < 0$. We went beyond mean-field and included the flow of the

couplings under pRG. Then we found an attraction in d^{+-} channel for which Γ_e and Γ_h have opposite sign, in agreement with STM and ARPES data. We argued that d^{+-} orbital order becomes the leading instability for either sign of bare U_0. We also computed the common self-energy for d_{xz} and d_{yz} orbitals at the center of electron pockets to second order in Γ to check whether we can reproduce the results of Refs. [151, 154] that the energies E^Y_{xz} and E^X_{yz} simultaneously get smaller by magnitude in the nematic phase. We obtained a much smaller self-energy and of opposite sign than the one which is needed. If the interpretation of the data in[151, 154] is correct, it has to be due to a self-energy with vertices beyond our RG analysis.

5.6 Supplemental Material

5.6.1 Orbitally-resolved low-energy model

We use an effective orbitally-resolved, low-energy model to describe excitations near the Fermi pockets in FeSe. The model can be constructed by expanding the hopping integrals near the centers of hole and electron pockets [45]. We will work in the "theoretical" 1FeBZ, where the hole pockets are centered at $\Gamma = (0, 0)$, and the electron pockets are centered at $X = (\pi, 0)$ and $Y = (0, \pi)$. The two Γ-centered pockets are made out of d_{xz} and d_{yz} orbitals, the X pocket is made out of d_{yz} and d_{xy} orbitals and the Y pocket is made out of d_{xz} and d_{xy} (Refs. [141, 45]), as shown in Fig. 5.1. The dispersion in the physical 2FeBZ can be obtained by folding the 1FeBZ along its diagonal. Under the folding, the points Y and X both become $M = (\pi, \pi)$.

We introduce six spices of fermions: $\psi_1, \ldots, \psi_6$. Fermions ψ_1 and ψ_2 describe d_{xz} and d_{xy} excitations near the electron pocket at Y, ψ_3 and ψ_4 describe d_{yz} and d_{xy} excitations near the X pocket, and ψ_5 and ψ_6 describe d_{xz} and d_{yz} excitations near the hole pockets at Γ. The assignment is summarized in Tab 5.1 and sketched in Fig. 5.1.

The quadratic Hamiltonian for states close to the hole pocket is

$$H^\Gamma = \sum_{\boldsymbol{k},\sigma} \left(\psi^\dagger_{5\sigma}(\boldsymbol{k}), \psi^\dagger_{6\sigma}(\boldsymbol{k})\right) h_\Gamma(\boldsymbol{k}) \begin{pmatrix} \psi_{5\sigma}(\boldsymbol{k}) \\ \psi_{6\sigma}(\boldsymbol{k}) \end{pmatrix} \tag{5.4}$$

with

$$h_\Gamma(\boldsymbol{k}) = \begin{pmatrix} \epsilon_h - \frac{k^2}{2m_h} + \frac{b}{2}(k_x^2 - k_y^2) - \Gamma_h & ck_xk_y \\ ck_xk_y & \epsilon_h - \frac{k^2}{2m_h} - \frac{b}{2}(k_x^2 - k_y^2) + \Gamma_h \end{pmatrix}, \tag{5.5}$$

In the tetragonal phase, $\Gamma_h = 0$. In the orthorhombic phase at $T < T_s$, Γ_h has a finite

value.

To make the formulas more compact, we assume $b = c$. Then in the tetragonal phase the hole pockets are circular, with energies $\epsilon^{tet}_{c,d} = \epsilon_h - (k^2/(2m_h))(1 \pm bm_h)$. The band operators c_k and d_k of the inner and outer hole pocket are related to $\psi_5(k)$ and $\psi_6(k)$ by a rotation

$$c_k = -\sin\theta_\Gamma(k)\psi_5(k) + \cos\theta_\Gamma(k)\psi_6(k), \quad d_k = \cos\theta_\Gamma(k)\psi_5(k) + \sin\theta_\Gamma(k)\psi_6(k) \tag{5.6}$$

where $\theta_\Gamma(k)$ corresponds to the polar angle along a hole pocket, counted from the k_x-axis.

In the orthorhombic (nematic) phase, the dispersion of hole-like excitations is altered to

$$\epsilon^{nem}_{c,d} = \epsilon_h - k^2/(2m_h) \mp \sqrt{b^2k^4 + 4\Gamma_h^2 - 4bk\Gamma_h\cos\theta}. \tag{5.7}$$

The transformation to band basis can still be viewed as a rotation, like in Eq. (5.6), but the rotation angle $\phi_\Gamma(k)$ no conger coincides with $\theta_\Gamma(k)$ and is expressed as [143, 155]

$$\tan\phi_\Gamma(k) = \frac{\sin 2\theta_\Gamma(k)}{\cos 2\theta_\Gamma(k) - 2\Gamma_h/(bk^2)} \tag{5.8}$$

The excitations near the electron pockets are described by

$$H^{Y,X} = \sum_{\boldsymbol{k},\sigma} \left(\psi^\dagger_{1,3\sigma}(\boldsymbol{k}), \psi^\dagger_{2,4\sigma}(\boldsymbol{k})\right) h_{Y,X}(\boldsymbol{k}) \begin{pmatrix} \psi_{1,3\sigma}(\boldsymbol{k}) \\ \psi_{2,4\sigma}(\boldsymbol{k}). \end{pmatrix} \tag{5.9}$$

with

$$h_{Y,X}(\boldsymbol{k}) = \begin{pmatrix} \epsilon_1 + \frac{k^2}{2m_1} \pm \frac{a_1}{2}(k_x^2 - k_y^2) \pm \Gamma_e & -\sqrt{2}ivk_{x/y} \\ \sqrt{2}ivk_{x/y} & \epsilon_2 + \frac{k^2}{2m_2} \pm \frac{a_2}{2}(k_x^2 - k_y^2) \end{pmatrix} \tag{5.10}$$

where the upper sign is for the Y pocket and the lower for the X pocket. In the tetragonal phase $\Gamma_e = 0$, in the orthorhombic phase it is finite. The parameters $v, \epsilon_{1,2}$, $a_{1,2}$, and $m_{1,2}$ can be determined by fitting the band structure to ARPES data. For FeSe they are given in the supplemental of Ref. [155]. In the band basis, this gives two branches around the X point and two branches around the Y point. Only one dispersion from each pair crosses the Fermi level and forms the electron pocket at X or Y.

In the tetragonal phase the energies of the bands that cross the Fermi level are given by $\epsilon^{tet}_{X,Y} = \frac{1}{2}(C_1^{X,Y} + C_2^{X,Y}) + \frac{1}{2}\sqrt{(C_1^{X,Y} - C_2^{X,Y})^2 + 8v^2k^2_{y,x}}$ with $C_i^{X,Y} = \epsilon_i + k^2/(2m_i) \mp a_i/2(k_x^2 - k_y^2)$. The bands that do not cross the Fermi level have energies $\tilde{\epsilon}^{tet}_{X,Y} = \frac{1}{2}(C_1^{X,Y} + C_2^{X,Y}) - \frac{1}{2}\sqrt{(C_1^{X,Y} - C_2^{X,Y})^2 + 8v^2k^2_{y,x}}$. The conversion from orbital to band basis can be

again written as rotation

$$e_{X,Y} = \mp i \cos\phi_{X,Y}\psi_{3,1} + \sin\phi_{X,Y}\psi_{4,2}, \quad \tilde{e}_{X,Y} = \pm i \sin\phi_{X,Y}\psi_{3,1} + \cos\phi_{X,Y}\psi_{4,2} \tag{5.11}$$

where e_i labels the band that forms the electron pocket and $\tilde{e}_i$ the one that does not cross the Fermi level. However, the angle $\phi_{X,Y}$ does not coincide with the polar angle along an electron pocket. To a good approximation, $\cos\phi_{X,Y} = A\sin\theta_{X,Y}$ and $\sin\phi_{X,Y} = \sqrt{1 - A^2\sin^2\theta_{X,Y}}$, where $\theta_{X(Y)}$ is the polar angle measured along $\Gamma - X$ ($\Gamma - Y$) and $1/\sqrt{2} < A < 1$ is a constant[155, 14, 15].

In the orthorhombic phase, the energies of the bands that cross the Fermi level become

$$\epsilon^{nem}_{X,Y} = \frac{1}{2}(C_1^{X,Y} + C_2^{X,Y} \mp \Gamma_e) + \frac{1}{2}\sqrt{(C_1^{X,Y} - C_2^{X,Y} \mp \Gamma_e)^2 + 8v^2k_{y,x}^2}. \tag{5.12}$$

The transformation from orbital to band space can still be written as in (5.11), but the relations between $\phi_{X,Y}$ and $\theta_{X,Y}$ change to $\cos\phi_{X,Y} = A_{X,Y}\sin\theta_{X,Y}$ and $\sin\phi_{X,Y} = \sqrt{1 - A_{X,Y}^2\sin^2\theta_{X,Y}}$ with $A_{X,Y} = A(1 \mp \frac{\Gamma_e}{\Delta E}(1 - A^2\sin^2\theta_{X,Y}))$ and $\Delta E = \tilde{\epsilon}^{tet}_X(k_F^X)$, where k_F^X is the Fermi wave vector of the electron pocket at X (Ref. [155]). In the following, we approximate $A_{X,Y}$ by their average values along the electron FSs: $A_{X,Y} = A(1 \mp \beta\Gamma_e)$ with $\beta = (1 - A^2/2)/\Delta E$. The constant ΔE is given by $\tilde{\epsilon}^0_X(k_F^X)$, where k_F^X is the Fermi wave vector of the electron pocket at X.

There are 30 symmetry-allowed interactions between six fermion species ψ_i [45, 14, 15]. We assume that interactions involving d_{xy} fermions are small, by one reason or the other (e.g., by applying full pRG to the full model with 30 couplings [14, 15]), and focus on the interaction terms which involve fermions from d_{xz} and d_{yz} orbitals. These interactions are

$$\begin{aligned}
H_{int} =& U_1 \sum{}' \left[\psi^\dagger_{1\sigma}\psi_{1\sigma}\psi^\dagger_{6\sigma'}\psi_{6\sigma'} + \psi^\dagger_{3\sigma}\psi_{3\sigma}\psi^\dagger_{5\sigma'}\psi_{5\sigma'}\right] \\
&+ \bar{U}_1 \sum{}' \left[\psi^\dagger_{1\sigma}\psi_{1\sigma}\psi^\dagger_{5\sigma'}\psi_{5\sigma'} + \psi^\dagger_{3\sigma}\psi_{3\sigma}\psi^\dagger_{6\sigma'}\psi_{6\sigma'}\right] \\
&+ U_2 \sum{}' \left[\psi^\dagger_{1\sigma}\psi_{6\sigma}\psi^\dagger_{6\sigma'}\psi_{1\sigma'} + \psi^\dagger_{3\sigma}\psi_{5\sigma}\psi^\dagger_{5\sigma'}\psi_{3\sigma'}\right] \\
&+ \bar{U}_2 \sum{}' \left[\psi^\dagger_{1\sigma}\psi_{5\sigma}\psi^\dagger_{5\sigma'}\psi_{1\sigma'} + \psi^\dagger_{3\sigma}\psi_{6\sigma}\psi^\dagger_{6\sigma'}\psi_{3\sigma'}\right] \\
&+ \frac{U_4}{2} \sum{}' \left[\psi^\dagger_{5\sigma}\psi_{5\sigma}\psi^\dagger_{5\sigma'}\psi_{5\sigma'} + \psi^\dagger_{6\sigma}\psi_{6\sigma}\psi^\dagger_{6\sigma'}\psi_{6\sigma'}\right] \\
&+ \tilde{U}_4 \sum{}' \psi^\dagger_{5\sigma}\psi_{5\sigma}\psi^\dagger_{6\sigma'}\psi_{6\sigma'} + \tilde{\bar{U}}_4 \sum{}' \psi^\dagger_{5\sigma}\psi_{6\sigma}\psi^\dagger_{6\sigma'}\psi_{5\sigma'} \\
&+ \frac{U_5}{2} \sum{}' \left[\psi^\dagger_{1\sigma}\psi_{1\sigma}\psi^\dagger_{1\sigma'}\psi_{1\sigma'} + \psi^\dagger_{3\sigma}\psi_{3\sigma}\psi^\dagger_{3\sigma'}\psi_{3\sigma'}\right]
\end{aligned}$$

$$+\tilde{U}_5 \sum{}' \psi^\dagger_{1\sigma}\psi_{1\sigma}\psi^\dagger_{3\sigma'}\psi_{3\sigma'}$$
$$+\tilde{\tilde{U}}_5 \sum{}' \psi^\dagger_{1\sigma}\psi_{3\sigma}\psi^\dagger_{3\sigma'}\psi_{1\sigma'} \tag{5.13}$$

The summation is over spin components and over momenta, under the constraint of momentum conservation. These interactions describe all symmetry-allowed scattering processes between d_{xz} and d_{yz} fermions near electron and hole pockets. We omitted pair hopping terms because they do not play a role in the following.

If we use the microscopic model with local Hubbard-Hund interactions, the interaction parameters are [14, 15]

$$\begin{aligned} U_1 &= U_2 = U_4 = U_5 = U, \\ \bar{U}_1 &= \tilde{U}_4 = \tilde{U}_5 = U', \\ \bar{U}_2 &= \tilde{\tilde{U}}_4 = \tilde{\tilde{U}}_5 = J, \end{aligned} \tag{5.14}$$

5.6.2 Self-consistent equations for Γ_h and Γ_e

To obtain the self-consistent equations for the nematic order parameters Γ_h and Γ_e, we evaluate the Hartree and Fock diagrams for the self-energies Σ_{xz} and Σ_{yz} near hole and electron pockets. In orbital basis, these self-energies contribute to the diagonal terms in Eqs. (5.5) and (5.10). Each self-energy contains a piece from the tetragonal phase and a piece which depends on Γ_e and Γ_h. To first order in the orbital order, $\Sigma^\Gamma_{xz} = \Sigma^\Gamma_{tet} + \Gamma_h/2$ and $\Sigma^\Gamma_{yz} = \Sigma^\Gamma_{tet} - \Gamma_h/2$, where Σ^Γ_{tet} is the self-energy at the Γ point in the tetragonal phase. At momenta close, but not equal to Γ, the self-energy acquires some k-dependence already in the tetragonal phase, but this dependence is small and irrelevant for our purposes, and we neglect it. Taking the difference between the two self-energies, we obtain $\Sigma^\Gamma_{xz} - \Sigma^\Gamma_{yz} = \Gamma_h$. Similarly, $\Sigma^Y_{xz} - \Sigma^X_{yz} = \Gamma_e$. Evaluating the diagrams for the self-energies then leads to

$$\begin{aligned} \Gamma_h &= U_{a4}\left(n^\Gamma_{xz} - n^\Gamma_{yz}\right) + U_b\left(n^Y_{xz} - n^X_{yz}\right) \\ \Gamma_e &= U_{a5}\left(n^Y_{xz} - n^X_{yz}\right) + U_b\left(n^\Gamma_{xz} - n^\Gamma_{yz}\right), \end{aligned} \tag{5.15}$$

The differences $n^\Gamma_{xz} - n^\Gamma_{yz}$ and $n^Y_{xz} - n^X_{yz}$ vanish in the tetragonal phase and are proportional to Γ_h and Γ_e, respectively. Eq. (5.15) then becomes a self-consistent set of linarized equations for Γ_h and Γ_e. Solving the set, one obtains T_s and the ratio Γ_e/Γ_h near T_s. We assume

that the sign of Γ_e/Γ_h will not change at a smaller T, when non-linear terms in the r.h.s. of (5.15) become relevant.

The interaction terms in (5.15) are $U_{a5} = U_5 - 2\tilde{U}_5 + \tilde{\tilde{U}}_5$, $U_{a4} = U_4 - 2\tilde{U}_4 + \tilde{\tilde{U}}_4$ and $U_b = 2(U_1 - \bar{U}_1) - (U_2 - \bar{U}_2)$. If we use the local Hubbard-Hund model Eq. (5.14), we obtain $U_{a5} = U_{a4} = U_b = U + J - 2U'$. However, the couplings become different once we include vertex corrections to U_{a5}, U_{a4}, and U_b. In the main text we present the results for the dressed couplings assuming that the running U_{a5} and U_{a4} remain equal, i.e., the running $U_{a5} = U_{a4} = U_a$. Here we present the results for a generic case when only bare $U_{a5} = U_{a4}$, but the running couplings are different. The running couplings U_{a5} and U_{a4} follow each other, and their ratio tends to constant r, whose value depends on system parameters [14, 15]. Below we use $U_{a5} = U_a$ and $U_{a4} = rU_a$, when we will be using the dressed couplings.

The fermionic densities are the integrals over momentum and sums over Matsubara frequencies of the corresponding Green's functions: $(n^\Gamma_{xz} - n^\Gamma_{yz}) = T\sum_{\omega_m}\int d^k/(2\pi)^2 (G^\Gamma_{xz}(k,\omega_m) - G^\Gamma_{yz}(k,\omega_m))$ and $(n^Y_{xz} - n^X_{yz}) = T\sum_{\omega_m}\int d^k/(2\pi)^2 (G^Y_{xz}(k,\omega_m) - G^X_{yz}(k,\omega_m))$. To evaluate the integrals, we transfer the Green's functions to the band basis and express the result in terms of the corresponding Fermi functions. One can check that in the tetragonal phase the self-energies Γ^Γ_{tet} and $\Gamma^{X,Y}_{tet}$ come from states not confined to the FSs, however the additional terms in the orthorhombic phase, proportional to Γ_h and Γ_e, come from the states near Γ, X, or Y points. In explicit form, we obtain near hole pockets

$$
\begin{aligned}
&(n^\Gamma_{xz} - n^\Gamma_{yz}) \\
&= \int \frac{d^2k}{(2\pi)^2} \cos 2\phi_H \Big(n_F(\epsilon^{nem}_c) - n_F(\epsilon^{nem}_d) \Big) = A_h \Gamma_h \\
A_h &= -\int \frac{d^2k}{(2\pi)^2} \left[\frac{2}{bk_F^2} \sin^2 2\theta \Big(n_F(\epsilon^{tet}_c) - n_F(\epsilon^{tet}_d) \Big) \right. \\
&\left. + \frac{1}{T} \cos^2 2\theta \left(\frac{e^{\epsilon^{tet}_c/T}}{\left(1 + e^{\epsilon^{tet}_c/T}\right)^2} + \frac{e^{\epsilon^{tet}_d/T}}{\left(1 + e^{\epsilon^{tet}_d/T}\right)^2} \right) \right] + \mathcal{O}(\Gamma_h^2)
\end{aligned}
\tag{5.16}
$$

where n_F is the Fermi distribution function and the expressions for $\epsilon^{tet}_c = \epsilon^{tet}_c(k)$ and $\epsilon^{tet}_d = \epsilon^{tet}_d(k)$ are given above. We recall that $c-$operators describe the inner hole pocket and $d-$operators describe the outer hole pocket. Accordingly, $\epsilon^{tet}_c \le \epsilon^{tet}_d$, so that $n_F(\epsilon^{tet}_c) \ge n_F(\epsilon^{tet}_d)$. As a result, both terms in the last line in (5.16) have the same sign, hence $A_h < 0$. We used this in the main text.

Similarly, fermionic densities in the vicinity of the electron pockets are given by

$$
\begin{aligned}
&(n^Y_{xz} - n^X_{yz}) \\
&= \int \frac{d^2k}{(2\pi)^2} \left[\cos^2\phi_Y n_F(\epsilon_Y) - \cos^2\phi_X n_F(\epsilon_X)\right] \\
&= \int \frac{d^2k}{(2\pi)^2} \left[A^2(1+\beta\Gamma_e)^2 \sin^2\theta_Y n_F(\epsilon^{nem}_Y) - A^2(1-\beta\Gamma_e)^2 \sin^2\theta_X n_F(\epsilon^{nem}_X)\right] = A_e\Gamma_e \\
&A_e = A^2 \int \frac{d^2k}{(2\pi)^2} \cos^2\theta \left[2\beta n_F(\epsilon^{tet}_Y) - \frac{1}{T} f_Y(k) \frac{e^{\epsilon^{tet}_Y/T}}{\left(1+e^{\epsilon^{tet}_Y/T}\right)^2}\right] + \mathcal{O}(\Gamma_e^2). \qquad (5.17)
\end{aligned}
$$

Here, the function $f_Y(k)$ is obtained when expanding the band energies to linear order in Γ_e, e.g., $\epsilon^{nem}_Y = \epsilon^{tet}_Y + f_Y(k)\Gamma_e/2$ with $f_Y(k) = 1 + (C^Y_1 - C^Y_2)/\sqrt{(C^Y_1 - C^Y_2)^2 + 8v^2k_x^2}$. To check the sign of A_e we evaluate the momentum integral in the last line in (5.17) analytically by setting $a_{1,2} = v = 0$ in (5.10). We obtain

$$
A_e = A^2 \frac{m_e}{2\pi} \left(\beta|\epsilon_1| + \beta T \ln\left(1 + e^{-|\epsilon_1|/T}\right) - \frac{1}{1+e^{-|\epsilon_1|/T}}\right) \qquad (5.18)
$$

For FeSe, $\beta|\epsilon_1| \sim 1/4$. For such β, A_e is negative. We then determine A_e numerically, using the full quadratic Hamltonian in (5.10) and the values of parameters for FeSe as given in Ref. [155]. We again obtain that A_e is negative. We used that $A_e < 0$ in the main text. The magnitudes of A_h and A_e are comparable, but A_h is larger: we found numerically $\gamma = A_e/A_h \approx 0.2$.

Using these results, we can write the self-consistent equations on Γ_h and Γ_e as

$$
\begin{aligned}
\Gamma_h &= -|A_h| \left(rU_a\Gamma_h + \gamma U_b \Gamma_e\right) \\
\Gamma_e &= -|A_h| \left(\gamma U_a \Gamma_e + U_b \Gamma_h\right). \qquad (5.19)
\end{aligned}
$$

In the main term we presented this equation and its solution (see below) for $r = 1$.

The two eigenmodes of the set (5.19) are

$$
\Gamma_h + \alpha_\pm \Gamma_e = \lambda^{++,+-}(\Gamma_h + \alpha_\pm \Gamma_e) \qquad (5.20)
$$

with

$$\alpha_{\pm} = -\frac{r-\gamma}{2}\frac{U_a}{U_b} \pm \sqrt{\left(\frac{r-\gamma}{2}\right)^2 \frac{U_a^2}{U_b^2} + \gamma} \tag{5.21}$$
$$\lambda^{++,+-} = -|A_h| \left[\frac{r+\gamma}{2} U_a \pm U_b \sqrt{\left(\frac{r-\gamma}{2}\right)^2 \frac{U_a^2}{U_b^2} + \gamma} \right],$$

5.6.3 Common part of the self-energies to order $\Gamma_{h,e}^2$

We now show the details of the evaluation of the common part of the self-energies Σ_{xz}^Y and Σ_{yz}^X to second order in $\Gamma_{h,e}$. We can isolate the quadratic terms by evaluating $\Sigma_2 = \Sigma_{xz}^Y + \Sigma_{yz}^X - 2\Sigma^{tet}$. The common self-energy Σ_2 is given by

$$\Sigma_2 = U_M(n_{xz}^Y + n_{yz}^X) + U_\Gamma(n_{xz}^\Gamma + n_{yz}^\Gamma) \tag{5.22}$$

where $U_M = U_5 + 2\tilde{U}_5 - \tilde{\tilde{U}}_5$ and $U_\Gamma = 2(U_1 + \bar{U}_1) - (U_2 + \bar{U}_2)$. The sums of the densities in the vicinity of the hole pockets are

$$\begin{aligned}
&(n_{xz}^\Gamma + n_{yz}^\Gamma) \\
&= \int \frac{d^2k}{(2\pi)^2} \left(n_F(\epsilon_c^{nem}) + n_F(\epsilon_d^{nem})\right) + n_{tet}^\Gamma \\
&= \Gamma_h^2 \int \frac{d^2k}{(2\pi)^2} \sum_{i=c,d} e^{\epsilon_i^{tet}/T} \left[\sigma_i \frac{1}{Tbk_F^2} \frac{1}{\left(1+e^{\epsilon_i^{tet}/T}\right)^2} + \frac{1}{2T^2}\cos^2\theta \frac{e^{\epsilon_i^{tet}/T}-1}{\left(1+e^{\epsilon_i^{tet}/T}\right)^3} \right] + n_{tet}^\Gamma \\
&= -\Gamma_h^2 \left[\frac{bm_h^2}{1-b^2m_h^2} \frac{1}{2\pi bk_F^2} \left(\tanh\left(1+\frac{\epsilon_h}{2T}\right)\right) + \frac{1}{8T\cosh^2\frac{\epsilon_h}{2T}} \right] + n_{tet}^\Gamma
\end{aligned} \tag{5.23}$$

where $\sigma_i = 1(-1)$ for $i = c(d)$, ϵ_h is defined after Eq. (5.5), and n_{tet}^Γ is the density around hole pockets in the tetragonal phase. We define $(n_{xz}^H + n_{yz}^H) = n_{tet}^\Gamma + B_h\Gamma_h^2$. Then

$$B_h = -\left[\frac{bm_h^2}{1-b^2m_h^2} \frac{1}{2\pi bk_F^2} \left(\tanh\left(1+\frac{\epsilon_h}{2T}\right)\right) + \frac{1}{8T\cosh^2\frac{\epsilon_h}{2T}} \right] \tag{5.24}$$

We see that $B_h < 0$. We use this in the main text. The densities around electron pockets are

$$(n_{xz}^Y + n_{yz}^X)$$

$$
\begin{aligned}
&= \int \frac{d^2k}{(2\pi)^2} \left[\cos^2\phi_Y n_F(\epsilon_Y) + \cos^2\phi_X n_F(\epsilon_X)\right] \\
&= \int \frac{d^2k}{(2\pi)^2} \left[A^2(1+\beta\Gamma_e)^2 \sin^2\theta_Y n_F(\epsilon_Y^{nem}) + A^2(1-\beta\Gamma_e)^2 \sin^2\theta_X n_F(\epsilon_X^{nem})\right] \\
&\approx A^2\Gamma_e^2 \int \frac{d^2k}{(2\pi)^2} \sin^2\theta \left[2f_Y^{(2)}(k) n_F'(\epsilon_Y^{tet}) + \frac{1}{4} f_Y^2(k) n_F''(\epsilon_Y^{tet}) + \beta f_Y(k) n_F'(\epsilon_Y^{tet})\right] \\
&+ (1+\beta^2\Gamma_e^2) n_{tet}^{X,Y} \qquad (5.25)
\end{aligned}
$$

In this formula, we used the symmetry between the expressions for the densities at X and Y for $\Gamma_e = 0$ and expanded to second order in Γ_e. We defined f_Y and $f_Y^{(2)}$ by writing $\epsilon_Y^{nem} = \epsilon_Y^{tet} + \Gamma_e/2 f_Y(k) + \Gamma_e^2 f_Y^{(2)}(k)$, where f_Y is given below Eq. (5.17), and $f_Y^{(2)} = 2v^2k_x^2/\sqrt{(C_1^Y - C_2^Y)^2 + 8v^2kx^2}$. We then define $(n_{xz}^Y + n_{yz}^X) = n_{tet}^{X,Y} + B_e\Gamma_e^2$ and compute B_e numerically using the parameters for FeSe from Ref. [155]). We find $B_e < 0$ and $|B_e| < |B_h|$. We use this in the main text.

As we said in the main text, this calculation is not fully self-consistent because we evaluated the "source" term by keeping the terms linear in Γ_h and Γ_e in the orbital Hamiltonian and expanding the densities to order $\Gamma_{h,e}^2$. For a full self-consistent calculation, we should have included also terms of order $\Gamma_{h,e}^2$ into the orbital Hamiltonian, expanded to order $\Gamma_{e,h}^2$ and then solved self-consistently for the prefactor of the Γ_e^2 term near the electron pockets. However, the Γ_e^2 term only appears because of the source term. The prefactor is then proportional to the source term and has the same sign. This is what we used in the main text.

Chapter 6

Conclusion

Nematic phase and magnetic phase are discovered near superconductivity in the phase diagram of iron-based superconductors. Nematic phase can be thought as a phase where electrons organize themselves to lie along a specific direction. The originally equivalent directions in the material, a and b, become nonequivalent (C_4 symmetry is broken macroscopically). Magnetism mostly appear in the form of stripe spin density waves in these materials. A natural question to ask is how these phases are related to superconductivity. To understand the mechanism of superconductivity and why the T_c is high in these materials, people need to study all these phases. Our works systematically investigated the interplay between these phases and especially the occurrence and trails of nematic phase in iron-based superconductors.

We first verify our starting point, the itinerant scenario approach, by comparing results with quantum Monte Carlo simulations, one of the most unbiased numerical calculations. The agreement of the predicted orders in both calculations give us confidence in the starting point we use, and proceed to more complex models.

We then study 4-pockets and 5-pockets models with RG. From our RG calculation in 4-pockets model, with parameters most probably suited to FeSe family, we found that, when the temperature is lowered, the first instability that occurs is orbital order (nonequal occupation for originally degenerate orbitals), which we argued to be the origin of nematic phase in this material, and that superconductivity develops at a lower temperature. These results are consistent with experiments. We find effective models corresponding to three kinds of orbital orders. This can be directly compared to experiments. Evidences from spectroscopic experiments seem to point to one of the solutions. From results of 5-pockets models, we find two effective models under RG flow at low temperatures(depending on parameters). We argue that different kinds of iron-based superconductors and their phases can be understood within our framework in a simple and unified way. The occurrence of both orbital order and superconductivity is due to the "push" from magnetic fluctuations. One of the models implies that compounds with large Fermi energy, such as LaOFeAs, develops stripe magnetic order first when lowering the temperature. The nematic phase observed in this material is argued to be what people call Ising-nematic order, which is a vestigial order of stripe magnetic order.

Finally we dig deeper into the nematic phase in FeSe systems. There is further discovery about the nematic phase (orbital order) in FeSe recently from the scan tunneling microscopy and Angle-resolved photoemission spectroscopy experiments. We study the structure of the orbital order and be able to explain the observed sign difference in orbital order based on the effect of renormalization of vertices in d-wave orbital channel. The effect cannot

be explained with commonly used mean-field analysis. Therefore, the renormalization of interactions in the materials, captured in our model, turns out to be crucial to explain the observed effect.

Bibliography

[1] H. K. Onnes, Commun. Phys. Lab. 12,120, (1911).

[2] Meissner, W.; Ochsenfeld, R. (1933). "Ein neuer Effekt bei Eintritt der Supraleitfahigkeit". Naturwissenschaften. 21 (44): 787-788

[3] Bednorz, J. George, and K. Alex Muller, Ten Years of Superconductivity: 1980-1990, Springer Netherlands, 1986. 267-271.

[4] Y. Kamihara, et al. Journal of the American Chemical Society 130.11 (2008): 3296-3297.

[5] J. Bardeen, L. N. Cooper, and J. R. Schrieffer, Physical Review 108.5 (1957): 1175.

[6] High-temperature superconductivity in iron-based materials, Johnpierre Paglione and Richard L. Greene, Nature Physics volume 6, pages 645-658 (2010)

[7] D.S. Inosov et al Nature Physics 6, 178-181(2010)

[8] Rafael M Fernandes and Andrey V Chubukov, Rep. Prog. Phys. 80 (2017) 014503

[9] M. D. Watson, T. K. Kim, A. A. Haghighirad, S. F. Blake, N. R. Davies, M. Hoesch, T. Wolf, and A. I. Coldea, Phys. Rev. B 92, 121108(R) (2015)

[10] Philipp T. Dumitrescu, Maksym Serbyn, Richard T. Scalettar, and Ashvin Vishwanath Phys. Rev. B 94, 155127

[11] A.V. Chubukov, M. Khodas, and R.M. Fernandes, Phys. Rev. X 6, 041045.

[12] A. Fedorov, A. Yaresko, T. K. Kim, E. Kushnirenko, E. Haubold, T. Wolf, M. Hoesch, A. Grueneis, B. Buechner, and S. V. Borisenko, Scientific Reports 6, 36834 (2016)

[13] Andrey V. Chubukov and Rui-Qi Xing Phys. Rev. B 93, 165141(2016)

[14] R.-Q. Xing, L. Classen, M. Khodas, A. V. Chubukov, Phys. Rev. B **95**, 085108 (2017);

[15] L. Classen, R.-Q. Xing, M. Khodas, and A. V. Chubukov, Phys. Rev. Lett. 118, 037001 (2017)

[16] Rui-Qi Xing, Laura Classen, and Andrey V. Chubukov Phys. Rev. B 98, 041108(R)(2018)

[17] I.I. Mazin, D.J. Singh, M.D. Johannes, M.H. Du, Phys. Rev. Lett. 101, 057003 (2008); P. J. Hirschfeld, M. M. Korshunov, and I. I. Mazin, Rep. Prog. Phys. 74, 124508 (2011).

[18] K. Kuroki, S. Onari, R. Arita, H. Usui, Y. Tanaka, H. Kontani, and H. Aoki, Phys. Rev. Lett. 101, 087004 (2008); K. Kuroki et al Phys. Rev. B 79, 224511 (2009).

[19] A. F. Kemper, T A Maier, S. Graser, H.-P. Cheng, P. J. Hirschfeld and D J Scalapino New Journal of Physics **12**, 073030 (2010); S. Graser, T. A. Maier, P. J. Hirschfeld, and D. J. Scalapino, New Journal of Physics 11, 025016 (2009).

[20] A. V. Chubukov, D. V. Efremov, and I. Eremin, Phys. Rev. B 78, 134512 (2008); A. V. Chubukov, Annu. Rev. Condens. Matter Phys. 3, 57, (2012); Physica C **469**, 640 (2009); S. Maiti and A. V. Chubukov, Phys. Rev. B **82**, 214515 (2010).

[21] R. M. Fernandes, A. V. Chubukov, J. Knolle, I. Eremin, and J. Schmalian, Phys. Rev. B 85, 024534 (2012).

[22] R. M. Fernandes and J. Schmalian, Phys. Rev. B 82, 014521 (2010).

[23] R. M. Fernandes, A. V. Chubukov, and J. Schmalian, Nature Phys. 10, 97 (2014).

[24] S. Onari, and H. Kontani, Phys. Rev. Lett. 109, 137001 (2012).

[25] W. Lv, and P. Phillips, Phys. Rev. B 84, 174512 (2011); W-C. Lee, and P. Phillips, Phys. Rev. B 86, 245113 (2012).

[26] F. Krüger, S. Kumar, J. Zaanen, and J. van den Brink, Phys. Rev. B 79, 054504 (2009).

[27] C. C. Lee, W. G. Yin, and W. Ku, Phys. Rev. Lett. 103, 267001 (2009).

[28] Qimiao Si and E. Abrahams, Phys. Rev. Lett. 101, 076401 (2008).

[29] Chen Fang, B. A. Bernevig, and Jiangping Hu, Eur. Phys. Lett. 86, 67005 (2009).

[30] L. de' Medici, G. Giovannetti, and M. Capone, Phys. Rev. Lett. 112, 177001 (2014).

[31] B. Valenzuela, E. Bascones, and M. J. Calderon, Phys. Rev. Lett. 105, 207202 (2010).

[32] Z. P. Yin, K. Haule, and G. Kotliar, Nature Physics 7, 294-297 (2011).

[33] I. Eremin and A. V. Chubukov, Phys. Rev. B 81, 024511 (2010).

[34] P. Dai, J. Hu, and E. Dagotto, Nature Phys. 8, 7 (2012).

[35] F. Hardy, A. E. Böhmer, D. Aoki, P. Burger, T. Wolf, P. Schweiss, R. Heid, P. Adelmann, Y. X. Yao, G. Kotliar, J. Schmalian, and C. Meingast, Phys. Rev. Lett. 111, 027002 (2013); J. S. Kim, E. G. Kim, G. R. Stewart, X. H. Chen, and X. F. Wang, Phys. Rev. B 83, 172502 (2011); H. Fukazawa, T. Saito, Y. Yamada, K. Kondo, M. Hirano, Y. Kohori, K. Kuga, A. Sakai, Y. Matsumoto, S. Nakatsuji, K. Kihou, A. Iyo, C. H. Lee, and H. Eisaki, J. Phys. Soc. Jpn. 80, SA118 (2011);M. Abdel-Hafiez, S. Aswartham, S. Wurmehl, V. Grinenko, C. Hess, S.-L. Drechsler, S. Johnston, A. U. B. Wolter, B. Büchner, H. Rosner, and L. Boeri, Phys. Rev. B 85, 134533 (2012);S. L. Bud'ko, Y. Liu, T. A. Lograsso, and P. C. Canfield, Phys. Rev. B 86, 224514 (2012).

[36] V. Grinenko, D. V. Efremov, S.-L. Drechsler, S. Aswartham, D. Gruner, M. Roslova, I. Morozov, K. Nenkov, S. Wurmehl, A. U. B. Wolter, B. Holzapfel, and B. Büchner, Phys. Rev. B 89, 060504(R) (2014).

[37] Z. P. Yin, K. Haule, G. Kotliar, Nature Physics 7, 294-297 (2011).

[38] S. Ducatman, N. B. Perkins, and A. V. Chubukov, Phys. Rev. Lett. 109, 157206 (2012); S. Ducatman, R. M. Fernandes, and N. B. Perkins, Phys. Rev. B 90, 165123 (2014).

[39] W. Bao, Y. Qiu, Q. Huang, M.A. Green, P. Zajdel, M.R. Fitzsimmons, M. Zhernenkov, S. Chang, M. Fang, B. Qian, K.E. Vehstedt, J. Yang, H.M. Pham, L. Spinu, and Z.Q. Mao, Phys. Rev. Lett. 102, 247001 (2009)

[40] A. V. Chubukov, R. M. Fernandes, and J. Schmalian, Phys. Rev. B 91, 201105 (2015).

[41] I. Gallais, and I. Paul, Comptes Rendus Physique 17, 113-139 (2016) and references therein.

[42] M. Khodas and A. V. Chubukov Phys. Rev. B 86, 144519 (2012)

[43] R. Applegate , R. R. P. Singh, C-C. Chen, and T. P. Devereaux, Phys. Rev. B 85, 054411 (2012).

[44] S. Raghu, X.-L. Qi, C.-X. Liu, D. J. Scalapino, and S.-C. Zhang, Phys. Rev. B77, 220503 (2008)

[45] V. Cvetkovic and O. Vafek, Phys. Rev. 88, 134510 (2013). See also Fernandes, R. M. and Vafek, O., Phys. Rev. B 90, 214514 (2014).

[46] I.A. Nekrasov, Z.V. Pchelkina, M.V. Sadovskii, JETP Letters, 88, 144 (2008); A. Kutepov, K. Haule, S. Y. Savrasov, and G. Kotliar, Phys. Rev. B 82, 045105 (2010).

[47] H. Yamase, and R. Zeyher, Phys. Rev. B 88, 180502(R) (2013); H. Yamase and R. Zeyher, arXiv:1503.07646.

[48] C. Platt, C. Honerkamp, W. Hanke, New J. Phys. 11, 055058 (2009); C. Platt, W. Hanke, and R. Thomale, Advances in Physics 62, 453-562 (2013); Fan Yang, Fa Wang, and Dung-Hai Lee, Phys. Rev. B 88, 100504 (2013).

[49] K. Binder and D. P. Landau, Phys. Rev. B 21, 1941 (1980); J. Yin and D. P. Landau, Phys. Rev. E 80, 051117 (2009).

[50] W. L. McMillan, Phys. Rev. 167, 331(1968); N. N. Bogolubov, V. V. Tolmachev, and D. V. Shirkov, Report for the Consultants Bureau, (1959).

[51] D. C. Johnston, Adv. Phys. **59**, 803 (2010).

[52] A. V. Chubukov, Annu. Rev. Condens. Matter Phys. **3**, 57 (2012).

[53] Z. P. Yin, K. Haule, and G. Kotliar, Nature Phys. **10**, 845 (2014).

[54] R. M. Fernandes, A. V. Chubukov and J. Schmalian, Nature Phys. **10**, 97 (2014).

[55] H. Yamase, and R. Zeyher, Phys. Rev. B **88**, 180502(R) (2013);

[56] P. M. R. Brydon, J. Schmiedt and C. Timm, Phys. Rev. B **84**, 214510 (2011).

[57] R. M. Fernandes, A. V. Chubukov, J. Knolle, I. Eremin, and J. Schmalian, Phys. Rev. B **85**, 024534 (2012).

[58] V. Stanev, and P. B. Littlewood, Phys. Rev. B **87**, 161122(R) (2013).

[59] S. Liang, A. Moreo and E. Dagotto, Phys. Rev. Lett. **111**, 047004 (2013).

[60] M. N. Gastiasoro, B. M. Andersen, Phys. Rev. B **92**, 140506(R) (2015).

[61] A. Hinojosa, J. Cai and A.V. Chubukov, Phys. Rev. B **93**, 075106 (2016).

[62] I. Gallais, and I. Paul, Comptes Rendus Physique **17**, 113-139 (2016);

[63] Z. Wang and A. H. Nevidomskyy, Journal of Physics: Condensed Matter **27**, 225602 (2015);

[64] V. K. Thorsmølle, M. Khodas, Z. P. Yin, C. Zhang, S. V. Carr, P. Dai, and G. Blumberg, Phys. Rev. B **93**, 054515 (2016)

[65] J.-H. Chu, J. G. Analytis, K. De Greve, P. L. McMahon, Z. Islam, Y. Yamamoto, and I. R. Fisher, Science **329**, 824 (2010).

[66] M. A. Tanatar, E. C. Blomberg, A. Kreyssig, M. G. Kim, N. Ni, A. Thaler, S. L. Bud'ko, P. C. Canfield, A. I. Goldman, I. I. Mazin, and R. Prozorov, Phys. Rev. B **81**, 184508 (2010).

[67] J.-H. Chu, H.-H. Kuo, J. G. Analytis, and I. R. Fisher, Science **337**, 710 (2012).

[68] S. Kasahara et. al., Nature **486** 382 (2012).

[69] L. Ma, G. F. Chen, D.-X. Yao, J. Zhang, S. Zhang, T.-L. Xia, and W. Yu, Phys. Rev. B **83**, 132501 (2011).

[70] X. Lu, J. T. Park, R. Zhang, H. Luo, A. H. Nevidomskyy, Q. Si, and P. Dai, Science **345**, 657 (2014).

[71] A. Dusza, A. Lucarelli, F. Pfuner, J.-H. Chu, I. R. Fisher, and L. Degiorgi, Europhys. Lett. **93**, 37002 (2011).

[72] I. R. Fisher, L. Degiorgi, and Z. X. Shen, Rep. Prog. Phys. **74**, 124506 (2011).

[73] T. M. McQueen, A. J. Williams, P. W. Stephens, J. Tao, Y. Zhu, V. Ksenofontov, F. Casper, C. Felser, and R. J. Cava, Phys. Rev. Lett. **103**, 057002 (2009).

[74] M. G. Kim *et. al.* Phys. Rev. B **83**, 134522 (2011)

[75] M. Yi *et. al*, Proc. Natl. Acad. Sci. USA **6878** (2011).

[76] H. Miao *et. al*, Phys. Rev. B **89**, 220503(R) (2014).

[77] P. Chandra, P. Coleman and A. I. Larkin, Phys. Rev. Lett. **64**, 88, (1990); C. Fang, H. Yao, W-F. Tsai, J. Hu, and S. A. Kivelson, Phys. Rev. B **77**, 224509 (2008); C. Xu, M. Muller, and S. Sachdev, Phys. Rev. B **78**, 020501(R) (2008).

[78] F. Wang, S. A. Kivelson, and D.-H. Lee, Nat. Phys. **11**, 959 (2015).

[79] J. K. Glasbrenner *et. al*, Nat. Phys. **11**, 953 (2015).

[80] S-H. Baek, D. V. Efremov, J. M. Ok, J. S. Kim, J. van den Brink, and B. Büchner, Nature Materials **14**, 210 (2015).

[81] A. E. Böhmer, T. Arai, F. Hardy, T. Hattori, T. Iye, T. Wolf, H. v. Löhneysen, K. Ishida, and C. Meingast, Phys. Rev. Lett. **114**, 027001 (2015).

[82] Q. Wang *et. al.*, Nature Materials, **15** 159 (2016).

[83] K. Kothapalli, *et al* arXiv:1603.04135 (2016).

[84] J. P. Sun, *et. al.*, Nat. Commun. **7**, 12146 (2016).

[85] R. M. Fernandes and O. Vafek, Phys. Rev. B **90**, 214514 (2014).

[86] P. Zhang *et al.*, Phys. Rev. B **91**, 214503 (2015);

[87] M. D. Watson, T. K. Kim, A. A. Haghighirad, N. R. Davies, A. McCollam, A. Narayanan, S. F. Blake, Y. L. Chen, S. Ghannadzadeh, A. J. Schofield, M. Hoesch, C. Meingast, T. Wolf, and A. I. Coldea, Phys. Rev. B **91**, 155106 (2015).

[88] L. Fanfarillo, J. Mansart, P. Toulemonde, H. Cercellier, P. Le Fevre, F. Bertran, B. Valenzuela, L. Benfatto, and V. Brouet, arXiv:1605.02482.

[89] Y. Suzuki, T. Shimojima, T. Sonobe, A. Nakamura, M. Sakano, H. Tsuji, J. Omachi, K. Yoshioka, M. Kuwata-Gonokami, T. Watashige, R. Kobayashi, S. Kasahara, T. Shibauchi, Y. Matsuda, Y. Yamakawa, H. Kontani, and K. Ishizaka, Phys. Rev. B **92**, 205117 (2015).

[90] W. Metzner, C. Castellani, and C. Di Castro, Adv. Phys. **47**, 317 (1998); M. Salmhofer, Commun. Math. Phys. **194**, 249 (1998).

[91] K. LeHur and T. M. Rice, Ann. Phys. **324**, 1452 (2009).

[92] C. Platt, C. Honerkamp, and W. Hanke, New J. Phys. **11**, 055058 (2009).

[93] C. Platt, W. Hanke, and R. Thomale, Advances in Physics **62**, 453-562 (2013).

[94] F. Yang, F. Wang, and D.-H. Lee, Phys. Rev. B **88**, 100504 (2013).

[95] I.T. Diatlov, V.V. Sudakov, K.A. Ter-Martirosian, JETP, **5**, 631 (1957).

[96] Y.A. Bychkov, L.P. Gor'kov and I. Dzyaloshinskii, Sov. Phys. JETP **23**, 489 (1966).

[97] I. Affleck, Nucl. Phys. B **257**, 397 (1985).

[98] C. Bourbonnais and L.G. Caron, Int. J. Mod. Phys. **B5**, 1033 (1991); A.T. Zheleznyak, V.M. Yakovenko, and I.E. Dzyaloshinskii, Phys. Rev. B **55**, 3200 (1997); L. Nandkishore, L. Levitov, and A.V. Chubukov, Nature Phys. **8**, 158 (2012).

[99] Y. Lemonik, I. L. Aleiner, V. I. Fal'ko, Phys. Rev. B 85, 245451 (2012); J. M. Murray and O. Vafek, Phys. Rev. B **89**, 201110(R) (2014).

[100] A. V. Chubukov, D. V. Efremov, and I. Eremin, Phys. Rev. B **78**, 134512 (2008); D. Podolsky, H-Y. Kee, Y. B. Kim, Europhysics Letters **88**, 17004 (2009); S. Maiti and A. V. Chubukov, Phys. Rev. B **82**, 214515 (2010).

[101] L. D. Landau and E. M. Lifshitz, Statistical Physics (Pergamon Press, 1980), Vol. 2.

[102] M. Randeria, J.-M. Duan, and L.-Y. Shieh, Phys. Rev. Lett. **62**, 981 (1989); Phys. Rev. B **41**, 327 (1990).

[103] A. V. Chubukov, I. Eremin, and D. V. Efremov, Phys. Rev. B **93**, 174516 (2016).

[104] O. Vafek and A.V. Chubukov, in preparation.

[105] W. Metzner, M. Salmhofer, C. Honerkamp, V. Meden, and K. Schönhammer, Rev. Mod. Phys. **84**, 299 (2012) and references therein;

[106] M. Khodas and A.V. Chubukov, Phys. Rev. B **94**, 115159 (2016).

[107] C.J. Halboth and W. Metzner, Phys. Rev. Lett. **85**, 5162 (2000).

[108] C. Honerkamp, M. Salmhofer, and T. M. Rice, Eur. Phys. J. **B 27**, 127 (2002); C. Husemann and W Metzner, Phys. Rev. B **86**, 085113 (2012).

[109] Fernandes, R. M. Chubukov, A. V. and Schmalian, J. Nature Phys. 10, 97 (2014); P. C. Canfield and S. L. Bud'ko, Annu. Rev. Condens. Matter Phys. 1, 27 (2010).

[110] see, e.g., A.V. Chubukov, in "Iron-based Superconductivity", Springer Series in Materials Science, Vol. 211, pp. 255-329, (2015); Luca de' Medici, *ibid* pp. 409-441, (2015).

[111] A.V. Chubukov, M. Khodas, and R.M. Fernandes, arXiv:1602.05503.

[112] Cvetkovic, V. and Tesanovic, Z., Phys. Rev. B 80, 024512 (2009);

[113] Yamase, H. and Zeyher, R., Phys. Rev. B 88, 180502(R) (2013); Lee, C. C., Yin, W. G. and Ku, W. Phys. Rev. Lett. 103, 267001 (2009); Kruger, F. S., Kumar, J., Zaanen, J. and van den Brink, Phys. Rev. B 79, 054504 (2009); Valenzuela, B., Bascones, E. and Calderon, M. J.Phys. Rev. Lett. 105, 207202 (2010). Lv, W. and Phillips, P., Phys. Rev. B 84, 174512 (2011); Lee, W-C. and Phillips, P. W. Phys. Rev. B 86, 245113 (2012); Applegate, R., Singh, R. R. P., Chen, C-C. and Devereaux, T. P. Phys. Rev. B 85, 054411 (2012); Stanev, V. and Littlewood, P. B., Phys. Rev. B 87, 161122(R) (2013); Dumitrescu, P. T., Serbyn, M., Scalettar, R. T., and Vishwanath, A, Phys. Rev. B 94, 155127 (2015); Baek, S.-H., Efremov, D. V., Ok, J. M., Kim, J. S., van den Brink, J. and Buchner, B. Nat Mater 14, 210 (2015); Gallais, I. and Paul, I. Comptes Rendus Physique 17, 113-139 (2016); Wang, Z., and Nevidomskyy, A. H., Journal of Physics: Condensed Matter bf 27, 225602 (2015); ThorsmÃžlle, V. K., Khodas, M., Yin, Z.P., Zhang, C., Carr, S.V., Dai, P., and Blumberg, G., Phys. Rev. B 93, 054515 (2016)

[114] Watson, M. D., Kim, T. K., Haghighirad, A. A., Davies, N. R., McCollam, A., Narayanan, A., Blake, S. F., Chen, Y. L., Ghannadzadeh, S., Schofield, A. J., Hoesch, M., Meingast, C., Wolf, T. and Coldea, A. I., Phys. Rev. B 91, 155106 (2015); Y. Suzuki, T. Shimojima, T. Sonobe, A. Nakamura, M. Sakano, H. Tsuji, J. Omachi, K. Yoshioka, M. Kuwata-Gonokami, T. Watashige, R. Kobayashi, S. Kasahara, T. Shibauchi, Y. Matsuda, Y. Yamakawa, H. Kontani, and K. Ishizaka, Phys. Rev. B 92, 205117 (2015); Zhang, Y., *et al.* arXiv: 1503.01556; Zhang, P. *et al.* Phys. Rev. B 91, 214503 (2015); Kothapalli, K. *et al*, arXiv:1603.04135 (2016); Fedorov, A, Yaresko, A, Kim, T. K., Kushnirenko, E. Haubold, E, Wolf, T., Hoesch, M., Gruneis, A., Buchner, B., and Borisenko S. preprint.

[115] see e.g., A.T. Zheleznyak, V.M. Yakovenko, and I.E. Dzyaloshinskii, Phys. Rev. B 55, 3200 (1997) and references therein.

[116] Metzner, W., Castellani, C. and Di Castro, C. Adv. Phys. 47, 317 (1998); Salmhofer M., Commun. Math. Phys. 194, 249 (1998).

[117] Platt, C., Honerkamp, C., and Hanke, W., New J. Phys. 11, 055058 (2009);

[118] Platt, C., Hanke, W. and Thomale, R., Advances in Physics 62, 453-562 (2013).

[119] Yang, F., Wang, F., and Lee, D.-H., Phys. Rev. B 88, 100504 (2013).

[120] LeHur, K. and Rice, T. M., Ann. Phys. 324, 1452 (2009).

[121] Nandkishore,L., Levitov,L., and Chubukov, A.V., Nature Phys. 8, 158 (2012); Kiesel, M., Platt, C. Hanke, W., Abanin, D.A., and Thomale R., Phys. Rev. B 86, 020507 (2012).

[122] Chubukov, A. V., Efremov, D. V. and Eremin, Phys. Rev. B 78, 134512 (2008)

[123] D. Podolsky, H-Y. Kee, Y. B. Kim, Europhysics Letters 88, 17004 (2009); Maiti, S and Chubukov, A. V. Phys. Rev. B 82,214515 (2010).

[124] see. e.g., Kemper, A. F., Maier, T. A., Graser, S., Cheng, H.-P., Hirschfeld, P. J. and Scalapino, D. J. New Journal of Physics 12, 073030 (2010) and references therein.

[125] see, e.g., V. Brouet, M. Fuglsang Jensen, Ping-Hui Lin, A. Taleb-Ibrahimi, P. Le FÃšvre, F. Bertran, Chia-Hui Lin, Wei Ku, D. Colson, and A. Forget, Phys. Rev. B 86, 075123 (2012).

[126] See Supplementary Material for detail. The 40 interactions involve pairs of fermions, each near either Γ, X, Y or M point. There are 4 additional interactions involving fermions near each of these points. These additional interactions do not affect the behavior near the four stable fixed trajectioris that we found within the space of 40 couplings, as we explicitly verified. We neglect these additional interactions in our analysis.

[127] see e.g. S. Maiti, A. Chubukov, Phys. Rev. B, 82, 214515 (2010) for a detailed explanation

[128] A similar procedure has been used in the RG studies of other problems: see, e.g., Metzner, W., Salmhofer, M., Honerkamp C., Meden, V., and Schoenhammer K., Rev. Mod. Phys. 84, 299 (2012) and references therein; Lemonik Y., Aleiner, I.L., and Fal'ko V.L., Physical Review B 85, 245451 (2012); Murray, J. M., and Vafek, O., Phys. Rev. B 89, 201110(R) (2014).

[129] Chandra, P., Coleman, P., and Larkin, A. I., Phys. Rev. Lett. 64, 88, (1990); Fang, C., Yao, H., Tsai, W-F., Hu, J. and Kivelson, S. A. Phys. Rev. B 77, 224509 (2008); Xu, C., Muller, M., and Sachdev, S., Phys. Rev. B 78, 020501(R) (2008).

[130] R.M. Fernandes, M. Khodas, and A.V. Chubukov, in preparation.

[131] M.N., Gastiasoro, I. Eremin, R.M. Fernandes, and B.M. Andersen, arXiv:1607.04711

[132] R. M. Fernandes, A.V. Chubukov, J. Knolle, I. Eremin, and J. Schmalian, Phys. Rev. B 85, 024534 (2012).

[133] For the 3p case, the subleading eigenfunction (smaller $\beta_{SC} > 0$) describes the orbital-antiphase state with the gap sign on the M pocket opposite to that on the other four pockets, see Yin, Z. P., Haule, K., and Kotliar, G., Nature Phys. 10, 845 (2014).

[134] We call orbital order the symmetry breaking between d_{xz} and d_{yz} orbitals. Another C_4- symmetry breaking term is the difference in the occupations of d_{xy} orbitals at X and Y in the 1FeBZ [135]. Such an order is present in our $3p_2$ model and $4p_2$ models.

[135] R. M. Fernandes and O. Vafek, Phys. Rev. B 90, 214514 (2014).

[136] For the application of the full 4p model to FeSe see R. Xing, L. Classen, M. Khodas, and A.V. Chubukov, arXiv:1611.03912

[137] SC not preceded by SDW already at zero doping has been detected in a fRG analysis of a 4-pocket model and contrasted with the reported lack of such tendency in 5-pocket models [138]. We argue that the outcome of the pRG flow is qualitatively the same in both cases, only in the 5-pocket model the SC susceptibility overcomes the SDW susceptibility at smaller energies, i.e. after a longer RG flow.

[138] R. Thomale, C. Platt, W. Hanke, B. A. Bernevig, Phys. Rev. Lett. 106, 187003 (2011).

[139] O. Vafek and A.V. Chubukov, in preparation.

[140] Ying Ran, Fa Wang, Hui Zhai, Ashvin Vishwanath, Dung-Hai Lee, Phys. Rev. B 79, 014505 (2009).

[141] S. Graser, T. A. Maier, P. J. Hirschfeld, and D. J. Scalapino, New J. Phys. 11, 025016 (2009).

[142] Naoya Arakawa, Masao Ogata, J. Phys. Soc. Jpn. 80, 074704 (2011)

[143] R. M. Fernandes and A. V. Chubukov, Rep. Prog. Phys. **80**, 014503 (2017).

[144] see e.g., Anna E. Böhmer, Andreas Kreisel, Journal of Physics: Condensed Matter 30, 023001 (2017) and references therein.

[145] K. Matsuura, Y. Mizukami, Y. Arai, Y. Sugimura, N. Maejima, A. Machida, T. Watanuki, T. Fukuda, T. Yajima, Z. Hiroi, K. Y. Yip, Y. C. Chan, Q. Niu, S. Hosoi, K. Ishida, K. Mukasa, S. Kasahara, J.-G. Cheng, S. K. Goh, Y. Matsuda, Y. Uwatoko, and T. Shibauchi, Nature Communications, 8 1143 (2017).

[146] P. O. Sprau, A. Kostin, A. Kreisel, A. E. BÃ¶hmer, V. Taufour, P. C. Canfield, S. Mukherjee, P. J. Hirschfeld, B. M. Andersen, and J. C. Seamus Davis, Science **357**, 6346 (2017).

[147] H. C. Xu, X. . Niu, D. F. Xu, J. Jiang, Q. Yao, Q. Y. Chen, Q. Song, M. Abdel-Hafiez, D. A. Chareev, A. N. Vasiliev, Q. S. Wang, H. L. Wo, J. Zhao, R. Peng, and D. L. Feng, Phys. Rev. Lett. **117**, 157003 (2016) T. Hashimoto, Y. Ota, H. Q. Yamamoto, Y. Suzuki, T. Shimojima, S. Watanabe, C. Chen, S. Kasahara, Y. Matsuda, T. Shibauchi, K. Okazaki, and S. Shin, Nat. Comm. **9**, 282 (2018);

[148] M. D Watson, A. A. Haghighirad, L. C. Rhodes, M. Hoesch, T. K. Kim, New J. Phys. **19**, 103021 (2017)

[149] Y. Suzuki, T. Shimojima, T. Sonobe, A. Nakamura, M. Sakano, H. Tsuji, J. Omachi, K. Yoshioka, M. Kuwata-Gonokami, T. Watashige, R. Kobayashi, S. Kasahara, T. Shibauchi, Y. Matsuda, Y. Yamakawa, H. Kontani, and K. Ishizaka, Phys. Rev. B **92**, 205117 (2015).

[150] Xingjiang Zhou, private communication

[151] A. Fedorov, et al., Scientific Reports **6**, 36834(2016).

[152] A. Coldea and M. Watson, Annual Review of Condensed Matter Physics 9, 125 (2018).

[153] In some earlier studies, see e.g., Ref. [158] a larger magnitude of $\Gamma_e \sim 50meV$ has been reported. The authors of later studies argued [151, 152, 148] that $50meV$ is the difference between the energies of d_{xz}/d_{yz} and d_{xy} orbitals.

[154] Y. S. Kushnirenko, A. V. Fedorov, E. Haubold, S. Thirupathaiah, T. Wolf, S. Aswartham, I. Morozov, T. K. Kim, B. Buchner, and S. V. Borisenko, arXiv:1802.08668.

[155] J. Kang, R.M. Fernandes, and A.V. Chubukov, arXiv:1802.01048.

[156] A.V. Chubukov, Annul. Rev. Cond. Mat. Phys.3, 13.1 (2012).

[157] Fa Wang, Hui Zhai, Ying Ran, Ashvin Vishwanath, Dung-Hai Lee, Physical Review Letters, 102, 047005 (2009); Christian Platt, Werner Hanke, Ronny Thomale, Advances in Physics 62, 453-562 (2013).

[158] L. Fanfarillo, J. Mansart, P. Toulemonde, H. Cercellier, P. Le Fevre, F. Bertran, B. Valenzuela, L. Benfatto, V. Brouet, Phys. Rev. B **94**, 155138 (2016)

[159] L. Ortenzi, E. Cappelluti, L. Benfatto and L. Pietronero, Phys. Rev. Lett. **103**, 046404 (2009).

[160] R. M. Fernandes and O. Vafek, Phys. Rev. B **90**, 214514(2014)

[161] In principle, the r.h.s. of Eq. (5.1) also contains the term $n^Y_{xy} - n^X_{xy}$ as this difference has a piece linear in Γ_e. However this term turns out to be numerically smaller than $n^Y_{xz} - n^X_{yz}$ already at a bare level and we neglect it. Another reason to neglect the contribution from d_{xy} orbital is that for $U > U'$, interactions involving fermions from d_{xy} orbital flow under pRG to progressively smaller values than the ones involving fermions from d_{xz}/d_{yz} orbital. The smallness of the interactions involving d_{xy} orbital also follows from other treatments [Z. P. Yin, K. Haule, G. Kotliar, Nature Materials **10**, 932 (2011); L. de' Medici, G. Giovannetti, M. Capone, Phys. Rev. Lett. **112**, 177001 (2014); E. Bascones, B. Valenzuela, and M. J. Calderon, Phys. Rev. B **86**, 174508 (2012); L. Fanfarillo, G. Giovannetti, M. Capone, E. Bascones, Phys. Rev. B **95**, 144511 (2017)].

[162] See Supplementary Material

[163] In principle, one has to distinguish between interactions on hole and electron pockets for U_a. However, they differ only by a factor [14, 15]. To smplify the presentation, in the main text we set U_a to be equal on hole and electron pockets. We discuss a generic case in [162].

[164] The authors of [24] found that the attraction in d^{+-} channel holds also for $U_0 > 0$ (H. Kontani, private communication).